THE CONTRIBUTION OF OPTICAL COHERENCE TOMOGRAPHY TO INTERVENTIONAL CARDIOLOGY:

Methodological Considerations and Clinical Application

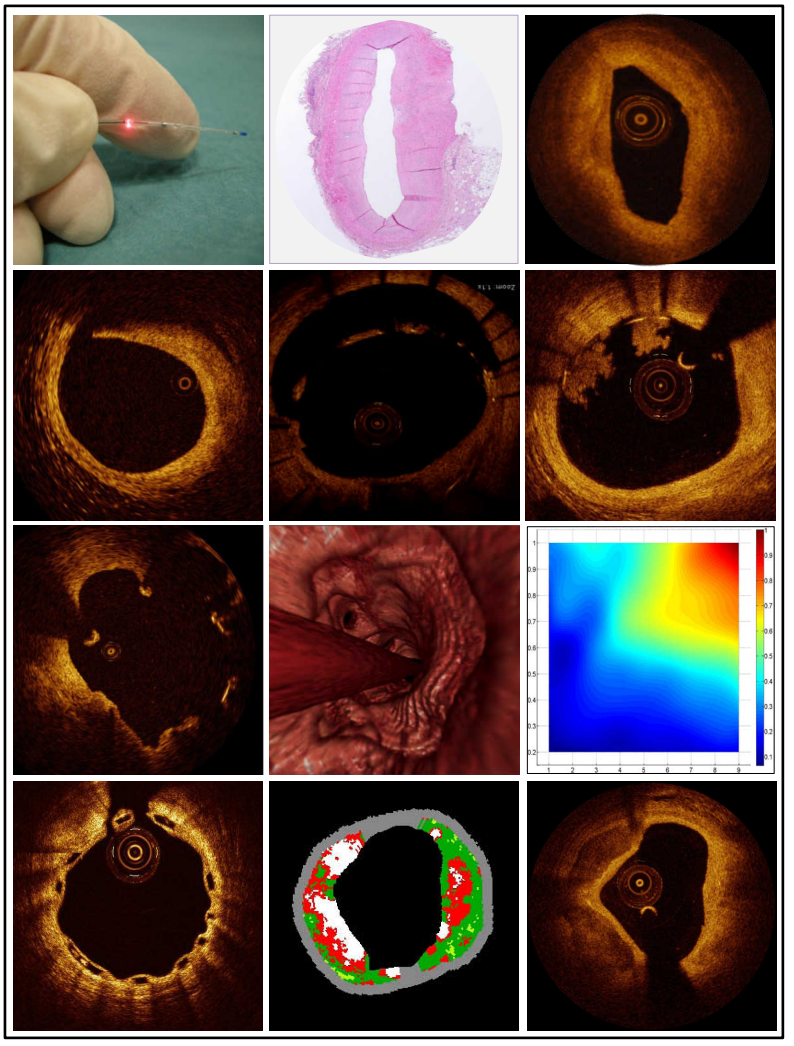

Maria D. Radu

The Contribution of Optical Coherence Tomography to Interventional Cardiology: Methodological Considerations and Clinical Application

Maria D. Radu

The Contribution of Optical Coherence Tomography to Interventional Cardiology: Methodological Considerations and Clinical Application

De bijdrage van optische coherentie tomografie in interventionele cardiologie: methodologische overwegingen en klinische toepassingen

Thesis

to obtain the degree of Doctor from the
Erasmus University Rotterdam
by command of the rector magnificus
Prof.dr. H.A.P. Pols
and in accordance with the decision of the Doctorate Board

The public defence shall be held on
Wednesday the 3rd of December, 2014 at 9:30 o'clock

by

Maria D. Radu
born in Stockholm, Sweden

DOCTORAL COMMITTEE

Promoter	Prof.dr. P.W. Serruys
Inner committee	Assoc. Prof. E. Regar Prof. P. de Feyter Prof. S. Windecker
Co-promotors	Dr. H. Kelbæk Dr. H.M. García-García

To my loving parents
and brothers

And God said, "Let there be light",
and there was light.
Genesis 1:3

TABLE OF CONTENTS

* Indicates equal contributorship

INTRODUCTION

INTRODUCTION

Since the beginning of interventional cardiology, coronary angiography has been the reference tool for assessing the severity of coronary lesions and guide stent implantation. With growing knowledge about the pathophysiology of atherothrombosis and stent failure it became of interest to visualise *in vivo* different processes taking place at the level of the coronary vessel wall for the purpose of improving cardiovascular outcomes. [1, 2] Intracoronary imaging techniques overcome the lumenographic limitations of angiography by enabling a histology-like cross-sectional view of the vessel wall and implanted devices. Although intravascular ultrasound (IVUS) has provided valuable insights into the dynamic nature of atherosclerosis and the causes of stent failure, the technology has a limited axial resolution (100-250 μm) and poor ability to differentiate between various tissue components. [3, 4] Intracoronary optical coherence tomography (OCT) has opened the door to a new world in interventional cardiology. With a near-histological resolution of 10-20 μm, this near-infrared light-based technology offers a significantly improved visualisation of plaque and stent-related features. [5, 6] However, only after its introduction did we realise how much the technology differs from IVUS beyond the level of resolution: in terms of aspects related to the use of light rather than sound, affecting tissue and stent characterisation and resulting in a unique array of artefacts; but also as a consequence of the significantly increased amount of data and its hierarchical nature requiring an adjustment of the qualitative-, quantitative- and statistical methods for an appropriate utilisation of the technology. This thesis will provide an insight into the development of these methods and their clinical application.

The first chapter reviews the history, principles and limitations of the OCT technology, and evaluates the consequence of the need to flush the vessel during image acquisition in terms of the clinical feasibility and safety. For successfully utilising OCT in research and clinics, it is necessary to understand the OCT image in order to recognise a variety of phenomena that can distort it and mimic pathology: these will be reviewed and discussed in detail.

The main part of this thesis relates to the application of OCT in the imaging of coronary devices – ultimately, for the prevention of stent thrombosis. ***Chapter 2*** describes the characterisation with OCT of strut apposition and coverage within conventional metallic stents, specifically illustrating how the methods have developed over time to allow the assessment of morphological features previously unseen by IVUS and histology, while

at the same time taking into account the inability of OCT to depict the entire metallic strut thickness.

In ***chapter 3***, we evaluate vascular healing following coronary intervention with drug-eluting stents (DES). The newly defined *protruding struts* and specifically the associated *coronary evaginations* are investigated with respect to their occurrence, predictors and mechanisms. Whether these can induce flow disturbances in the respective lesions is also tested. Whilst coronary evaginations can be seen at follow-up, edge dissections represent vascular injury at baseline – in some studies related to early stent thrombosis. Due to their dramatic appearance by OCT, even when angiographically not flow-limiting, we have revisited the natural history and clinical impact of these lesions.

Although DES have effectively reduced the rates of restenosis [7, 8], they are associated with drawbacks that need yet to be addressed. In addition to late/very late stent thrombosis and the potential disposition of the metallic and polymeric material to induce chronic inflammatory reactions [9, 10]; the "caging" effect related to the permanent nature of the metallic stents interferes with normal vascular physiology. [11] Everolimus-eluting bioresorbable vascular scaffolds (BVS) have been introduced as a promising alternative to metallic DES. Being composed primarily of poly-L-lactide which is slowly degraded by hydrolysis, the goal of this device is to provide a temporary scaffold which allows restoration of physiological, pharmacological and biological vascular functions once the polymer is resorbed. When imaged with OCT and compared with metallic stents, the BVS presents important differences related to the optical translucent polymeric struts, necessitating a different analysis methodology. [12]

Chapter 4 describes how OCT can be used to evaluate BVS in scaffold-overlap regions, and the nature of "white dots", as well as the relationship between OCT and histology for quantitative measurements.

In ***chapter 5***, we assess with serial OCT the vascular healing processes following implantation of BVS, and compare measureable changes within the scaffold itself between OCT, IVUS and IVUS-virtual histology. Additionally, we discuss the potential role of the neointima not only as a temporary protection for the scaffold, but also as a plaque shield once the scaffold is resorbed.

Finally, in ***chapter 6***, the goal to comprehensively review how OCT visualises atherosclerosis is used as a starting point for discussing important physical differences and

terminological confusions between OCT, histology and IVUS, as well as the limitations of OCT for tissue characterisation and how these can be overcome using multimodality imaging.

In conclusion, the aims of this thesis are:

- To demonstrate the systematic interpretation of OCT findings related to metallic stent implantation and atherosclerotic plaques, with consideration of important artefacts and fundamental differences between OCT and histology;
- To illustrate the development and application of methods to evaluate the acute effects of stent implantation and the vascular responses taking place thereafter; and
- To specifically assess the occurrence, predictors, mechanisms and haemodynamic effects of coronary evaginations; the natural history of edge dissections; and various aspects of vascular healing following BVS implantation.

INTRODUCTIE

Coronair angiografie is van af het begin van de interventie cardiologie de referentie techniek voor het vaststellen van de ernst en uitgebreidheid van coronaire laesies en voor het begeleiden van stent implantatie. Met de toenemende kennis van de pathofysiologie van atherosclerose en stent disfunctie werd het ook interessant om verschillende *in vivo* pathofysiologische processen te bestuderen die plaats vinden in de vaatwand, met als doel de cardiovasculaire prognose te verbeteren. [1, 2] Intra coronaire beeldvormende technieken zoals intravasculair ultrageluid (IVUS) of optische coherentie tomografie (OCT) kennen niet de beperkingen van de lumenografie van coronair angiografie doordat zij in staat zijn een op pathologie/histogie gelijkende dwarsdoorsnede van de vaatwand en van de ge-implanteerde stents of "scaffolds " te genereren. IVUS heeft waardevolle inzichten in de dynamiek van atherosclerose en de oorzaken van stent disfunctie gegeven, echter de techniek is beperkt door de beperkte axiale resolutie (100-250 µm) en de geringe mogelijkheid om verschillende weefsel componenten te onderscheiden. [3, 4] OCT heeft de deur geopend naar een nieuwe wereld in de interventie cardiologie. Deze op bijna infrarood licht gebaseerde techniek met een resolutie van 10-20µm die bijna de histologie benaderd, is in staat om een significante verbetering te geven van de coronaire plaque en stent karakteristieken. [5, 6] Maar, pas na de introductie van deze techniek begonnen we ons te realiseren dat OCT zeer grote verschillen toont met IVUS, niet alleen wat betreft de resolutie maar bovenal het gebruik van licht in plaats van geluid. Licht genereert andere weefsel en stent eigenschappen, inclusief nieuwe artefacten, terwijl de enorme toename van data samenhangend met hierarchische aspecten anpassing vereist van kwalitatieve, kwantitatieve en statistische methoden voor een correct gebruik van de technologie. Dit proefschrift verschaft inzicht in de ontwikkeling van deze methoden en van de klinische toepassing.

Het eerste hoofdstuk geeft een overzicht van de geschiedenis, principes en beperkingen van de OCT technologie en bespreekt de consequentie van de noodzaak om het vat bloedvrij te maken door het schoon te spoelen gedurende de beeld acquisitie in termen van uitvoerbaarheid en veiligheid. Om OCT goed te kunnen begrijpen is het noodzakelijk dat men de beelden correct kan interpreteren en dat men de verschillende fenomenen kan herkennen die de beeldvorming verstoren en zelfs op pathologie kunnen lijken: dit alles wordt uitgebreid opnieuw bekeken en in detail besproken.

Het belangrijkste deel van dit proefschrift betreft de toepassing van OCT voor het afbeelden van coronaire stents en "scaffolds" met het ultieme doel de preventie van stent trombose. In ***hoofdstuk 2*** wordt beschreven hoe we stent appositie en de bekleding

van metalen stents met OCT moeten beoordelen. Specifiek wordt ingegaan hoe deze methodes zich in de tijd hebben ontwikkeld, met de nadruk op het detecteren van morfologische kenmerken die niet mogelijk waren met IVUS of histologie. Ook worden de tekortkomingen van OCT besproken met betrekking tot het afbeelden van complete metalen stents met name van de stent "strut" dikte.

In ***hoofdstuk 3*** evalueren we het vasculaire genezings proces na coronaire interventie met "drug-eluting stents" (DES). We introduceren een specfiek fenomeen: "protruding struts" en de daarmee samenhangende "coronary evaginations" (uitstulpingen). De frequentie, de voorspelling en ontstaanswijze worden besproken. De mogelijkheid dat deze uitstulpingen bloedstroom storingen kunnen veroorzaken wordt getest. Coronaire uitstulpingen worden gezien bij vervolg onderzoek en stentrand dissecties onmiddellijk na implantatie ten gevolge van vasculaire beschadiging; deze worden in sommige studies gerelateerd met vroege stent trombose. Omdat deze laesies er zo dramatisch uit zien, zelfs indien ze niet stroom belemmerend zijn, was voor ons de reden om het natuurlijke beloop en klinische gevolgen te bestuderen.

DES zijn effectief in het reduceren van re-stenosen [7, 8], maar ze hebben ook nadelen, die ook bespreking behoeven zoals late en zeer late trombose, chronische ontsteking [9, 10], het "kooi" effect ten gevolge van de blijvende aard van de metalen stent daarmee de normale fysiologie van de vaatwand verstorend. [11] "Everolimus-eluting bioresorbable vascular scaffolds" (BVS) zijn een veelbelovend alternatief voor de metalen stent. Ze zijn samengesteld uit poly-l-lactide, dat langzaam degradeert door hydrolyse. Het doel van deze tijdelijke "scaffold" is dat na resorptie van de "scaffold" er een herstel van de fysiologische, farmacologische en biologische vaatwand functies kan optreden. OCT van de BVS is duidelijk verschillend van DES door de optische doorlaatbaar-heid van de BVS. Dit maakt een andere analyse noodzakelijk. [12]

In ***hoofdstuk 4*** wordt beschreven hoe OCT kan worden gebruikt voor de evaluatie van de BVS daar waar de "struts" overlappen, voor de bestudering van de "white dots" en de relatie van de kwantitatieve metingen tussen OCT en histologie.

In ***hoofdstuk 5*** onderzoeken we middels serieel OCT het vasculaire genees proces na implantatie van een BVS en de vergelijking van de meetbare veranderingen binnen de "scaffold" tussen OCT, IVUS en IVUS-VH (virtuele histologie). Bovendien bespreken we de potentiele rol van de neointima die niet allen kan dienen als een tijdelijke bescherming van de BVS maar ook kan fungeren als een plaque schild nadat de BVS is geresorbeerd.

In ***hoofdstuk 6*** wordt uitgebreid behandeld hoe OCT atherosclerose afbeeld en we bespreken belangrijke fysische verschillen en verwarrende terminologie zoals dit kan optreden tussen OCT, histologie en IVUS. De beperkingen van OCT voor weefsel classificatie worden belicht en ook hoe dit kan worden ondervangen met het gebruik van meerdere afbeeld technieken.

Concluderend, de doelen van dit proefschrift zijn:

- De demonstratie van een systematische interpretatie van OCT van metalen stents, en atherosclerotische plaques, rekening houdend met de fundamentele verschillen tussen OCT en histologie;
- De illustratie van de ontwikkelingen en toepassing van methodes om de acute effecten van stent implantatie en de daarmee samenhangende vaatwand reactie te bestuderen; en
- De specifieke vaststelling van de frequentie, voorspellers en ontstaanswijze en hemodynamische effecten van "coronary evaginations", het natuurlijk beloop van stentrand dissecties, en de verschillende aspecten van het vasculaire genees proces na BVS implantatie.

REFERENCES

1. Muller JE, Abela GS, Nesto RW, Tofler GH. Triggers, acute risk factors and vulnerable plaques: the lexicon of a new frontier. *J Am Coll Cardiol.* 1994;23(3):809-813.
2. Schwartz RS, Huber KC, Murphy JG, Edwards WD, Camrud AR, Vlietstra RE, Holmes DR. Restenosis and the proportional neointimal response to coronary artery injury: results in a porcine model. *J Am Coll Cardiol.* 1992;19(2):267-274.
3. Mintz GS, Painter JA, Pichard AD, Kent KM, Satler LF, Popma JJ, Chuang YC, Bucher TA, Sokolowicz LE, Leon MB. Atherosclerosis in angiographically "normal" coronary artery reference segments: an intravascular ultrasound study with clinical correlations. *J Am Coll Cardiol.* 1995;25(7):1479-1485.
4. Jensen LO, Thayssen P, Pedersen KE, Stender S, Haghfelt T. Regression of coronary atherosclerosis by simvastatin: a serial intravascular ultrasound study. *Circulation.* 2004;110(3):265-270.
5. Yabushita H, Bouma BE, Houser SL, Aretz HT, Jang IK, Schlendorf KH, Kauffman CR, Shishkov M, Kang DH, Halpern EF, Tearney GJ. Characterization of human atherosclerosis by optical coherence tomography. *Circulation.* 2002;106(13):1640-1645.
6. Bouma BE, Tearney GJ, Yabushita H, Shishkov M, Kauffman CR, DeJoseph Gauthier D, MacNeill BD, Houser SL, Aretz HT, Halpern EF, Jang IK. Evaluation of intracoronary stenting by intravascular optical coherence tomography. *Heart.* 2003;89(3):317-320.
7. Morice MC, Serruys PW, Sousa JE, Fajadet J, Ban Hayashi E, Perin M, Colombo A, Schuler G, Barragan P, Guagliumi G, Molnar F, Falotico R. A randomized comparison of a sirolimus-eluting stent with a standard stent for coronary revascularization. *N Engl J Med.* 2002;346(23):1773-1780.
8. Kastrati A, Mehilli J, Pache J, Kaiser C, Valgimigli M, Kelbaek H, Menichelli M, Sabate M, Suttorp MJ, Baumgart D, Seyfarth M, Pfisterer ME, Schomig A. Analysis of 14 trials comparing sirolimus-eluting stents with bare-metal stents. *N Engl J Med.* 2007;356(10):1030-1039.
9. Finn AV, Joner M, Nakazawa G, Kolodgie F, Newell J, John MC, Gold HK, Virmani R. Pathological correlates of late drug-eluting stent thrombosis: strut coverage as a marker of endothelialization. *Circulation.* 2007;115(18):2435-2441.
10. John MC, Wessely R, Kastrati A, Schomig A, Joner M, Uchihashi M, Crimins J, Lajoie S, Kolodgie FD, Gold HK, Virmani R, Finn AV. Differential healing responses in polymer- and nonpolymer-based sirolimus-eluting stents. *JACC Cardiovasc Interv.* 2008;1(5):535-544.
11. Ormiston JA, Serruys PW. Bioabsorbable coronary stents. *Circ Cardiovasc Interv.* 2009;2(3):255-260.
12. Serruys PW, Onuma Y, Ormiston JA, de Bruyne B, Regar E, Dudek D, Thuesen L, Smits PC, Chevalier B, McClean D, Koolen J, Windecker S, Whitbourn R, Meredith I, Dorange C, Veldhof S, Miquel-Hebert K, Rapoza R, Garcia-Garcia HM. Evaluation of the second generation of a bioresorbable everolimus drug-eluting vascular scaffold for treatment of de novo coronary artery stenosis: six-month clinical and imaging outcomes. *Circulation.* 2010;122(22):2301-2312.

CHAPTER 1 INTRODUCTION TO OPTICAL COHERENCE TOMOGRAPHY

1.1 Principles of intravascular optical coherence tomography.

Radu MD, Räber L, van Soest G, Garcia-Garcia HM, Serruys PW.

The Clinical Atlas of OCT. PCR Publishing. May 2012.

Please see separate electronic application, chapter 1

CHAPTER 1 INTRODUCTION TO OPTICAL COHERENCE TOMOGRAPHY

1.2 Long-term safety and feasibility of three-vessel multimodality intravascular imaging in patients with ST-elevation myocardial infarction – From the IBIS-4 (Integrated Biomarker and Imaging Study) substudy.

Taniwaki M, **Radu MD**, Garcia-Garcia HM, Heg D, Kelbæk H, Holmvang L, Moschovitis A, Noble S, Pedrazzini G, Saunamäki K, Dijkstra J, Landmesser U, Wenaweser P, Meier B, Stefanini GG, Roffi M, Lüscher TF, Windecker S, Räber L.

Submitted.

Long-term safety and feasibility of three-vessel multimodality intravascular imaging in patients with ST-elevation myocardial infarction
The IBIS-4 (Integrated Biomarker and Imaging Study) substudy

Masanori Taniwaki, MD*; Maria D. Radu, MD, PhD||; Hector M. Garcia-Garcia, MD, PhD†; Dik Heg, PhD∫; Henning Kelbæk, MD, DMSci||; Lene Holmvang, MD, DMSci||; Aris Moschovitis, MD*; Stephane Noble, MD‡; Giovanni Pedrazzini, MD§; Kari Saunamäki, MD, DMSci||; Jouke Dijkstra, MD#, Ulf Landmesser, MD¶; Peter Wenaweser, MD*; Bernhard Meier, MD*; Giulio G Stefanini, MD*; Marco Roffi, MD‡; Thomas F. Lüscher, MD¶; Stephan Windecker, MD*; Lorenz Räber, MD*

* Bern University Hospital, Bern, Switzerland
|| Rigshospitalet, Copenhagen, Denmark
† ErasmusMC, Rotterdam, the Netherlands
‡ University Hospital, Geneva, Switzerland
§ Cardiocentro, Lugano, Switzerland
¶ Cardiovascular Center, University Hospital Zurich, Zurich, Switzerland
∫ Clinical Trial Unit, University of Bern, Switzerland
Leiden University Medical Center, Leiden, Netherlands

Correspondence: Lorenz Räber, MD
Department of Cardiology
Swiss Cardiovascular Center Bern
Bern University Hospital
3010 Bern, Switzerland
e-mail: lorenz.raeber@insel.ch
Tel. +41 31 632 09 29
Fax. +41 31 632 19 28

The IBIS4 trial was supported by the Swiss National Science Foundation, and is registered at: http://www.clinicaltrials.gov/ct2/show/NCT00617084

ABSTRACT

Aim: We assessed the feasibility and the procedural and long-term safety of Intracoronary (i.c) imaging for documentary purposes with optical coherence tomography (OCT) and intravascular ultrasound (IVUS) in patients with acute ST-elevation myocardial infarction (STEMI) undergoing primary PCI in the setting of IBIS-4 study.

Methods and Results: IBIS4 (NCT00962416) is a prospective cohort study conducted at five European centers including 103 STEMI patients who underwent serial three-vessel coronary imaging during primary PCI and at 13 months. The feasibility parameter was successful imaging, defined as the number of pullbacks suitable for analysis. Safety parameters included the frequency of peri-procedural complications, and major adverse cardiac events (MACE), a composite of cardiac death, myocardial infarction (MI) and any clinically-indicated revascularization at 2 years. Clinical outcomes were compared with the results from a cohort of 485 STEMI patients undergoing primary PCI without additional imaging. Imaging of the infarct-related artery at baseline (and follow-up) was successful in 92.2% (96.6%) of patients using OCT and in 93.2% (95.5%) using IVUS. Imaging of the non-infarct-related vessels was successful in 88.7% (95.6%) using OCT and in 90.5% (93.3%) using IVUS. Periprocedural complications occurred less than 2.0% of OCT and none during IVUS. There were no differences throughout 2 years between the imaging and control group in terms of MACE (16.7% vs 13.3%, adjusted HR1.40, 95%CI0.77-2.52, p=0.27).

Conclusions: Multi-modality three-vessel i.c. imaging in STEMI patients undergoing primary PCI is consistent a high degree of success and can be performed safely without impact on cardiovascular events at long-term follow-up.

KEYWORDS

Optical coherence tomography, intravascular ultrasound, ST-segment elevation myocardial infarction

ABBREVIATIONS AND ACRONYMS

ARC = Academic Research Consortium
CI = Confidence interval
DES = Drug-eluting stent
MACE = Major adverse cardiac event
MI = Myocardial infarction
ST = Stent thrombosis
TLF = Target lesion failure
TLR = Target lesion revascularization
IVUS = Intravascular ultrasound
IVUS-VH = IVUS-virtual histology
OCT = Optical coherence tomography
PCI = Percutaneous coronary intervention
STEMI = ST-elevation myocardial infarction

INTRODUCTION

Multimodality intracoronary (i.c.) imaging using optical coherence tomography (OCT), grayscale intravascular ultrasound (IVUS), and IVUS-virtual histology (IVUS-VH) provides means to characterize coronary atherosclerosis and optimize stent implantation in a comprehensive manner. Based on near-infrared light, OCT visualizes in great detail the vascular luminal integrity, thrombus, and characteristics of plaque vulnerability and facilitates the detection of geographical miss, stent strut malapposition and edge dissections following stent implantation.[1] Although the resolution of IVUS is an order of magnitude lower than OCT, the technology provides a greater penetration depth and therefore the ability to assess plaque volume.[2] IVUS-VH is based on radiofrequency analysis and has been proposed as a method to assist the evaluation of plaque composition, particularly necrotic core.[3] The combined use of these sound- and light-based modalities theoretically increases the accuracy to detect "vulnerable" plaques [4,5] and may thus provide a complete platform to exploit future treatment targets. Additionally, these technologies have the potential to improve cardiovascular outcomes by optimizing percutaneous coronary intervention (PCI), particularly in STEMI patients.[6]

Nevertheless, the use of intracoronary imaging catheters may be accompanied by procedural complications including injury of the endothelium, which may increase the risk of short- and long-term events. Despite an increasing use of intracoronary imaging in daily practice, there is insufficient data on the feasibility and safety of multimodality imaging. We therefore aimed to analyse the feasibility and short- and long-term safety of patients enrolled in the IBIS-4 imaging study, a prospective, observational multicenter study with the objective to assess the arterial healing after biolimus-eluting stent implantation versus bare metal stent implantation and to investigate the changes in atherosclerosis on the background of a high intensity statin therapy in the two non-infarct related arteries. [7]

METHODS

Study population

IBIS 4 (NCT00962416) is a prospective cohort study nested into the COMFORTABLE-AMI, a trial comparing the safety and efficacy of a biolimus-eluting stent with a bare metal stent in 1161 STEMI patients undergoing primary PCI at 11 international centers.[8] A total of 103 patients were enrolled in this imaging study using OCT, IVUS and IVUS-VH to assess the arterial healing response following stent implantation and to quantify changes

in atherosclerotic plaque characteristics in non-infarct related arteries in the presence of high dose statin therapy (rosuvastatin 40mg daily).

Patients enrolled in the COMFORTABLE-AMI trial were eligible for participating in the IBIS 4 study when the following criteria were met: age< 90 years, haemodynamic stability allowing the administration of nitroglycerine, preserved renal function (GFR >30ml/min), ≥TIMI II flow of the infarct-related artery at the end of the intervention, and a coronary anatomy considered suitable for intracoronary imaging (e.g. absence of vessel tortuosity).

Following PCI, multimodality imaging with OCT followed by IVUS/IVUS-VH was performed, first addressing the treated culprit lesion, and then the two non-infarct related arteries. Care was taken to maintain an activated clotting time >250 seconds, and prior to each pullback, i.c. nitroglycerine (200μg) was administered to achieve maximal vasodilatation. After complete acquisition, imaging pullbacks were analyzed offline by an independent CoreLab (Cardialysis B.V., Rotterdam). Operators were strongly recommended not to optimize the treatment result based on the post-procedural i.c. imaging result.

All patients were scheduled for repeat angiography and the same three vessel multimodality imaging protocol at 13 months. In total, they were followed up to 2 years, and events were recorded at 30 days, 1 year, and 2 years. Per protocol, all patients received rosuvastatin 40mg once daily throughout the 13 month follow-up period.

The control group of the present study consisted of 485 patients who were simultaneously enrolled in the COMFORTABLE-AMI study at the five imaging centers, but who did not undergo imaging although they formally fulfilled the inclusion criteria for the imaging sub-study. All patients provided written informed consent for the participation in both the COMFORTABLE-AMI study and IBIS 4.

OCT

OCT images were acquired using the frequency domain (FD) C7 console system (Lightlab, St. Jude, Westford, MA) and the Dragonfly catheter at a pullback speed of 20mm/sec. Blood clearance was achieved using the non-obstructive technique with a power injector applying flushing rates of 3-6 ml/sec depending on vessel size. The regions of interest included in the culprit vessel: at least 5mm of the proximal and distal reference vessel segments; and as much as possible of the proximal non-infarct-related arteries, though a minimum of 40mm as measured from the respective ostia.

IVUS

IVUS-images were acquired with the Volcano s5 system (Volcano Corp., Rancho Cordova, CA) and the 2.9 French Eagle Eye catheter, which uses a 20 MHz transducer, at a pullback rate of 0.5mm/sec. The regions of interest were the same as for OCT, as were the storage of pullbacks and transfer to Corelab for further offline analysis.

Antithrombotic therapy regimen

All patients were loaded with aspirin (≥250 mg) prior to the procedure. In centers where prasugrel was available, an initial dose of 60 mg (including patients preloaded with clopidogrel) was given followed by a daily maintenance dose of 10 mg. If prasugrel was not available or contraindicated, clopidogrel was administered at a loading dose of 600 mg, followed by 75mg twice daily for seven days, followed by a maintenance dose of 75 mg daily. Dual antiplatelet therapy was prescribed for the duration of 13 months.

Feasibility parameters

Feasibility was defined as the acquisition of a pullback with sufficient image quality for independent CoreLab analysis, e.g. allowing the acquisition of ≥70% of the region of interest and satisfactory blood clearing with visibility of ≥3 quadrants in ≥70% of the pullback length.

Safety parameters

The following procedural complications (directly related to the imaging or within 24 hours of the procedure) were prospectively collected: coronary artery dissection (angiographic) or vessel perforation, ventricular fibrillation, symptomatic brady- or tachyarrythmia, thrombus formation, spasm and air embolism.

The primary clinical safety endpoint was a composite of cardiac death, myocardial infarction and any clinically indicated revascularization. Secondary safety endpoints included death, cardiac death, myocardial infarction, Academic research consortium (ARC-)-defined definite- and definite or probable stent thrombosis and major bleeding events according to the Bleeding-ARC (BARC) definition. All definitions of endpoints used in this study have been previously reported.[9] Any revascularization refers to all revascularizations (target-lesion revascularization (TLR), target-vessel revascularization (TVR), and non-TVR). Acute renal failure was defined as an absolute increase in serum creatinine of >1.5 fold from baseline or a glomerular filtration rate decrease of >25% within 72 hours.

Data management

Independent study monitors verified source data according to a prespecified monitoring plan. Data were stored in a central online database. Follow-up appointments were scheduled at 30 days, 1 year and 2 years, and patients were questioned about the occurrence of angina, any adverse events. All events were independently adjudicated by a clinical event committee.

Statistical analysis

Categorical variables are presented as counts with percentages and compared using chi-square or Fisher's tests, and continuous variables as means with standard deviations or medians and interquartile ranges, and compared using the Student t-test and Mann-Whitney U-test, respectively. Lesion-level data were analyzed using general or generalized linear mixed models, nesting lesions within patient identifiers, wherever applicable. Time-to-first event or composite events were analyzed using Cox's regression analysis comparing the Imaging group and the control group (at 30 days, 1 year and 2 years of follow-up), both crude (presented with Kaplan-Meier graphs), and adjusted (using inverse-probability of treatment weighting (IPTW), where the treatment is the imaging performed). IPTW was calculated using the following baseline variables: age, gender, body mass index, diabetes, hypertension, hypercholesterolemia, current smoker, renal insufficiency, anemia, pain onset within 6h, Killip II, resuscitation, left ventricular ejection fraction, treatment of a bifurcation lesion, small vessel ≤2.5mm diameter, long lesion ≥20mm length, SYNTAX score, TIMI flow pre-procedure, after 20 times multiple imputation of missing data using chained equations (IPTW Adjusted Cox's Regressions weight the patients by their IPTW and are based on 20 imputed data-sets). Sensitivity crude and IPTW adjusted Cox's regression analyses were conducted on the primary outcome, stratifying patients according to whether they received clopidogrel loading or prasugrel/double loading during the index procedure. Similarly, event rates at discharge were analysed using Crude or IPTW Adjusted Poisson Regressions with robust error variances and reported as Risk Ratios RR with 95% confidence intervals (95%CI). P-values from Fisher's tests are reported in case of zero events. All statistical analyses were performed with Stata 12.1 (StataCorp, Texas, USA) and differences were considered significant at $\alpha=0.05$.

RESULTS

A total of 103 STEMI patients undergoing primary PCI were included at 5 European centers into the IBIS 4 imaging study between September 2009 and January 2011.

Feasibility of multimodality intracoronary imaging

The feasibility of OCT, grayscale IVUS, and IVUS-VH at baseline and follow-up imaging is shown in **Table 1**. Imaging of the infarct-related artery at baseline (and follow-up) was successful in 92.2% (96.6%) patients using OCT, 93.2% (95.5%) patients using grayscale IVUS and 88.3% (94.3%) patients using IVUS-VH. Imaging of the non-infarct related artery at baseline (and follow-up) was successful in 88.7% (95.6%) patients using OCT, 90.5% (93.3%) patients using grayscale IVUS and 83.1% (92.6%) patients using IVUS-VH, respectively. Failure of OCT imaging was mainly related to insufficient image quality due to incomplete vessel flushing but also due to difficulties to advance the OCT catheter in the non-infarct related artery. IVUS-VH imaging failure was mainly caused by technical problems with the ECG transmission for gating of the acquisition, and by the use of manual- instead of automatic pullback.

Procedural complications

In the setting of primary PCI, 2 out of 103 (1.9%) OCT pullback acquisitions resulted in a complication at baseline, and 1 out of 91 (1.1%) at follow-up. Specifically, a dissection at the proximal stent edge was caused by the tip of the OCT imaging catheter in one of the cases at baseline; whereas the other two complications (one at baseline, one at follow-up) consisted of ventricular fibrillation induced by vessel flushing with contrast. Complications were managed by additional stent implantation in the former case, and successful defibrillation in the other cases, without further sequelae. IVUS imaging was performed without complications; and there were no cases of i.c. related thrombus formation, perforation, air embolism, or mechanical device failure or spasm.

Safety analysis

A total of 103 imaging patients were compared to a cohort of 485 control patients.
Baseline clinical characteristics of the two groups are shown in **Table 3**. Imaging patients were younger, more frequently male, had a higher BMI and were less likely to have hypercholesterolemia compared to patients not undergoing i.c. imaging. Imaging patients were more often resuscitated prior to hospital admission. Prognostically important characteristics like diabetes, Killip classification and left ventricular function were similar. Procedural characteristics are shown in **Table 4**. Other than a lower maximal

Table 1 Feasibility of OCT, IVUS, and IVUS-VH at baseline and 13 months follow-up

	Infarct-related vessel			Non-infarct-related vessel		
	OCT	IVUS	IVUS-VH	OCT	IVUS	IVUS-VH
Baseline						
Number of patients		103			103	
Number of vessels available for imaging	103	103	103	204	201	201
Successful imaging	**95 (92.2)**	**96 (93.2)**	**91 (88.3)**	**181 (88.7)**	**181 (90.5)**	**172 (83.1)**
Unsuccessful imaging	**8 (7.8)**	**7 (6.8)**	**12 (11.7)**	**23 (11.3)**	**20 (9.5)**	**29 (14.4)**
Failure to cross lesion	1 (1.0)	3 (2.9)	3 (2.9)	11 (5.4)	9 (4.5)	9 (4.5)
Technical problem§	0	1 (1.0)	6 (5.8)	0	3 (1.5)	12 (6.0)
Insufficient quality for analysis	6 (5.8)	2 (1.9)	2 (1.9)	10 (4.9)	6 (3.0)	6 (3.0)
Patient compliance ǁ	1 (1.0)	1 (1.0)	1 (1.0)	2 (1.0)	2 (1.0)	2 (1.0)
Follow-up						
Number of patients		91			91	
Total number of vessels available for imaging	91	91	91	185	183	183
Not obtained as at baseline#	2	2	2	25	20	20
Successful imaging*	**86 (96.6)**	**85 (95.5)**	**84 (94.3)**	**153 (95.6)**	**152 (93.3)**	**150 (92.6)**
Unsuccessful imaging	**3 (3.4)**	**4 (3.4)**	**5 (5.6)**	**7 (4.4)**	**9 (5.5)**	**11 (7.3)**
Failure to cross lesion	2 (2.2)	2 (2.2)	2 (2.2)	0	1 (0.6)	1 (0.6)
Technical problem§	0	2 (1.1)	3 (3.4)	1 (0.6)	5 (3.1)	7 (4.3)
Insufficient quality for analysis	1 (1.1)	0	0	3 (1.9)	1 (0.6)	1 (0.6)
Patient compliance ǁ	0	0	0	3 (1.9)	2 (1.2)	2 (1.2)

Values are number (%) or mean ± SD.
OCT, optical coherence tomography; IVUS, intravascular ultrasound; VH, virtual histology;
#Not investigated at follow-up as no baseline was available
*The success rate at follow-up = successful imaging /(total number of vessel available – number of not obtained as at baseline)
§Technical problem is defined as manual pullback or DVD defect or ECG trigger missing.
ǁPatient compliance is defined as preterm termination of the imaging procedure due to patient discomfort in view of the prolonged catheterization time.

balloon pressure and a higher amount of contrast used, there were no significant differences between groups. Antithrombotic medication prior or during the procedure and at hospital discharge is shown in **Table 5**. Imaging patients more frequently (58.3% vs. 32.7%, p<0.001) received a concomitant loading dose of prasugrel in addition to clopidogrel and were more frequently discharged with prasugrel as compared with control patients (77.5% vs. 52.1%, p<0.001), the proportion of patients on double antiplatelet therapy at discharge, however, was similar.

Table 2 Complications related to imaging procedure (per patient)

	Baseline		Follow-up	
	OCT N=103	IVUS N=103	OCT N=91	IVUS N=91
Dissection	1 (1.0)	0	0	0
Ventricular fibrillation	1 (1.0)	0	1 (1.1)	0
Symptomatic brady- or tachyarrhythmia	0	0	0	0
Thrombus formation	0	0	0	0
Perforation	0	0	0	0
Air embolism	0	0	0	0
Total	**2 (1.9)**	**0**	**1 (1.1)**	**0**

Values are number (%). OCT, optical coherence tomography; IVUS, intravascular ultrasonography.

Short and long term outcomes of patients undergoing intracoronary imaging

Table 6 presents clinical outcomes at 30 days, 1 year and 2 years. The primary endpoint MACE was similar for patients undergoing i.c. imaging and controls at 2 years (16.7% vs 13.3%, adjusted HR=1.4, 95%CI 0.77–2.52, p=0.27) (**Figure 1**). Similarly, no differences in the individual endpoints including death, myocardial infarction and any revascularization were observed at two years. Two recurrent myocardial infarctions were noted in the imaging group within 30 days. One event was related to an early stent thrombosis four days after stent implantation in a calcified ostial RCA lesion due to stent underexpansion. The second event occurred in a patient who was readmitted with cardiogenic shock due to ischemic mitral regurgitation with documentation of stent thrombosis. There was no significant difference in the rate of acute renal failure at 30 days between 2 groups (1% vs. 1.9%, adjusted HR=0.68, 95%CI 0.09-5.37, p=0.72). Revascularization of non-infarct related arteries (clinically indicated non-TVR) is an important surrogate for lesion progression potentially related to i.c. imaging. Non-TVR occurred at a similar frequency in the imaging (9.0%) and control group (4.8%, HR=1.70, 95%CI 0.76-3.81, p=0.20). Similarly, there was no difference in the frequency of any clinically indicated revascularization (**Table 6**).

To investigate whether the observed differences in the use of P2Y12 inhibitors were responsible similar MACE rates, we performed a sensitivity analysis for the primary endpoint MACE. We found hazards to be consistent for both groups at any time point of follow-up when separately comparing patients receiving a clopidogrel loading dose (imaging vs. control group, adjusted 2 year HR 1.18, 95%CI 0.39-3.61, p=0.77) and those receiving either prasugrel or a double loading dose separately (adjusted 2 year HR 1.67 95%CI 0.81-3.43, p=0.16) (**Appendix Table S1**).

Table 3 Baseline clinical characteristics

	Imaging group (n=103)	Control group (n=485)	P value
Age (yrs)	58.2 ± 10.5	61.5 ± 12.2	0.012
Male gender	93 (90.3)	385 (79.4)	0.008
BMI – kg/m^2	27.8 ± 4.2	26.8 ± 4.0	0.019
Cardiovascular risk factors			
Diabetes	13 (12.6)	65 (13.4)	1.00
Hypertension	48 (46.6)	212 (43.7)	0.66
Hypercholesterolemia	42 (40.8)	259 (53.7)	0.022
Current smoker	48 (46.6)	242 (50.4)	0.52
Family history of CAD	31 (31.0)	130 (27.3)	0.46
Renal failure	1 (1.0)	13 (2.7)	0.48
Previous MI	2 (1.9)	26 (5.4)	0.20
Previous CABG	0 (0.0)	13 (2.7)	0.14
Peak CK	1847 (1045-3494)	1652 (800-2814)	0.20
Peak CK-MB	187 (107-319)	160 (72-300)	0.20
Clinical presentation			
Time from symptom onset to balloon inflation, min	258 (170-472)	244 (164-422)	0.72
Time from arrival at hospital to balloon inflation, min	40 (30-56)	42 (30-63)	0.18
Killip class II, III, or IV	8 (7.8)	34 (7.0)	0.83
Resuscitation before hospital arrival	5 (4.9)	7 (1.4)	0.042
LVEF (%)	47.8 ± 9.4	48.6 ± 10.1	0.52

Values are expressed as mean ± SD or number (%).
BMI, body mass index; CAD, coronary artery disease; MI, myocardial infarction; PCI, percutaneous coronary intervention;
CABG, coronary artery bypass graft; CK, creatine kinase; LVEF, left ventricular ejection fraction.

DISCUSSION

This is the first report on the feasibility and safety of multimodality three-vessel intracoronary imaging in the setting of a prospective observational study in STEMI patients undergoing primary PCI. Less extensive intracoronary imaging may be used in daily clinical routine, a situation for which our findings are also applicable.

The following major findings apply to this study:

Table 4 Baseline procedural characteristics

	Imaging group (n=103)	Control group (n=485)	P value
No of lesions treated in infarct vessel	121	542	
Infarct vessel location			0.24*
Left main coronary artery	1 (1.0)	1 (0.2)	
Left anterior descending artery	46 (44.7)	184 (38.0)	
Left circumflex artery	18 (17.5)	68 (14.0)	
Right coronary artery	38 (36.9)	229 (47.3)	
Baseline TIMI flow			0.51*
0 or 1	73 (60.8)	351 (65.0)	
2	17 (14.2)	67 (12.4)	
3	30 (25.0)	122 (22.6)	
Lesion complexity			
Bifurcation lesion,no.	14 (13.6)	44 (9.1)	0.20*
Small vessel	14 (13.6)	67 (13.9)	1.00*
Long lesion	31 (30.1)	149 (31.0)	0.91*
SYNTAX MI Score	14.7 ± 6.7	14.5 ± 8.3	0.82*
Primary PCI procedure			
No. of stents per lesion	1.22 ± 0.51	1.30 ± 0.67	0.28*
Type of stent			
Biolimus-eluting stent	64 (52.9)	268 (49.8)	0.60*
Bare metal stent	57 (47.1)	274 (50.9)	0.57*
Stent length per lesion, mm	22.1 ± 10.5	24.1 ± 13.2	0.16*
Stent diameter, mm	3.25 ± 0.49	3.2 ± 0.7	0.36*
Direct stenting	24 (19.8)	127 (23.6)	0.31*
Maximal balloon pressure, atm	13.7 ± 2.9	14.9 ± 3.4	<0.001*
Thrombus aspiration performed	70 (68.0)	288 (59.5)	0.12
Intravenous vasopressors	2 (1.9)	14 (2.9)	1.00
TIMI flow post-procedure			0.76
0 or 1	0 (0.0)	3 (0.6)	
2	2 (1.7)	22 (4.1)	
3	119 (98.3)	516 (95.4)	
Total amount of contrast used during primary PCI, ml			
BL	268.3 ± 109.8	197.9 ± 88.8	<0.001
Total amount of contrast used for imaging, ml			
BL	174 ± 72	n.a.	
FUP	169 ± 83	n.a.	
Total time for primary PCI intervention, min	34.3 ± 18.5	36.2 ± 20.1	0.39
Total time used for imaging, min	44 ± 22	n.a.	

Data are expressed as number (%) unless otherwise specified.
* Mixed model p-value accounting for lesions nested within patient
IQR, interquartile range; SD, standard deviation; PCI, percutaneous coronary intervention; QCA, quantitative coronary angiography;
TIMI, thrombolysis in myocardial infarction; BL, baseline; FUP, follow-up; MI, myocardial infarction, n.a. not applicable

Table 5 Medication during the procedure and at discharge

	Imaging group (n=103)	Control group (n=485)	P value
Periprocedural medication			
Unfractionated heparin	101 (98.1)	478 (98.6)	0.66
Bivalirudin	6 (5.8)	29 (6.0)	1.00
Glycoprotein IIb/IIIa antagonists	54 (52.4)	241 (49.7)	0.67
Loading dose of clopidogrel and prasugrel			
Clopidogrel only (600mg)	26 (25.2)	251 (52.0)	<0.001
Prasugrel only (60mg)	17 (16.5)	68 (14.1)	0.54
Both	60 (58.3)	158 (32.7)	<0.001
No loading dose clopidogrel and prasugrel	0 (0.0)	6 (1.2)	0.60
Medication at discharge			
Aspirin	102 (100.0)	481 (99.8)	1.00
Clopidogrel	23 (22.5)	230 (47.7)	<0.001
Prasugrel	79 (77.5)	251 (52.1)	<0.001
Any dual antiplatelet therapy	102 (100.0)	480 (99.6)	1.00

Values are n (%).

1) Multimodality three-vessel i.c. imaging was consistent with high degree of success, confirming the feasibility even in the acute setting of primary PCI at centers with various level of expertise in i.c. imaging.
2) Periprocedural complications were rare (1.9 % per patient at baseline, 1.1% at follow-up), solely related to the imaging with OCT, and resolved without sequelae in all cases.
3) Rates of death and myocardial infarction at 30 days were similar between patients undergoing i.c. imaging and controls attesting to the procedural safety of three-vessel multimodality imaging.
4) Rates of MACE up to 2 years were low and similar for both groups indicating that diagnostic serial multimodality i.c. imaging is not associated with harm.

Feasibility

The present study demonstrates an overall high feasibility of both OCT and IVUS for imaging the infarct vessel, which did not differ between the baseline acute setting and the planned follow-up investigation at 13 months, suggesting that the acute presentation does not limit the success rate of i.c. imaging except in cases of hemodynamic instability or poor PCI result. As opposed to the infarct-related vessels, the success rates for evaluating non-infarct related arteries were lower. The principal reason for this was the caliber

Table 6 Clinical outcomes at discharge, 30 days, 1 year, and 2 years

			Crude		IPTW adjusted	
	Imaging group (n=103)	Control group (n=485)	Hazard Ratio(95% CI)	P value	Hazard Ratio(95% CI)	P value
Clinical events at 30 days ∫∫						
Death	1 (1.0)	8 (1.7)	0.59 (0.07-4.69)	0.62	1.20 (0.15-9.47)	0.86
Cardiac death	1 (1.0)	8 (1.7)	0.59 (0.07-4.69)	0.62	1.20 (0.15-9.47)	0.86
MI	2 (2.0)	5 (1.0)	1.89 (0.37-9.73)	0.45	2.66 (0.51-13.85)	0.25
Death or MI	3 (2.9)	13 (2.7)	1.09 (0.31-3.83)	0.89	1.79 (0.50-6.34)	0.37
Cardiac death or MI	3 (2.9)	13 (2.7)	1.09 (0.31-3.83)	0.89	1.79 (0.50-6.34)	0.37
Clinically indicated revascularization (any)	2 (2.0)	7 (1.5)	1.35 (0.28-6.50)	0.71	1.82 (0.37-8.85)	0.46
Clinically indicated non-TVR	0 (0.0)	1 (0.2)	2.34 (0.21-25.57)	1.00	.	.
Clinically indicated TVR	2 (2.0)	7 (1.5)	1.35 (0.28-6.50)	0.71	1.82 (0.37-8.85)	0.46
Clinically indicated TLR	2 (2.0)	7 (1.5)	1.35 (0.28-6.50)	0.71	1.82 (0.37-8.85)	0.46
MACE†	3 (2.9)	16 (3.3)	0.88 (0.26-3.03)	0.84	1.43 (0.41-4.98)	0.57
Definite ST	2 (2.0)	6 (1.2)	1.58 (0.32-7.82)	0.58	2.10 (0.42-10.50)	0.37
Definite or probable ST	2 (2.0)	11 (2.3)	0.86 (0.19-3.88)	0.84	1.22 (0.27-5.61)	0.79
Any major bleeding (BARC 3,4,5)	4 (3.9)	15 (3.1)	1.25 (0.42-3.78)	0.69	2.14 (0.57-7.69)	0.26
Acute renal failure	1 (1.0)	9 (1.9)	0.52 (0.07-4.12)	0.54	0.68 (0.09-5.37)	0.72
Clinical events at 1 year ∫∫						
Death	2 (2.0)	12 (2.5)	0.78 (0.17-3.48)	0.74	1.08 (0.21-5.45)	0.92
Cardiac death	2 (2.0)	10 (2.1)	0.93 (0.20-4.27)	0.93	1.29 (0.25-6.60)	0.76
MI	5 (4.9)	13 (2.8)	1.81 (0.65-5.08)	0.26	1.74 (0.57-5.29)	0.33
Death or MI	6 (5.9)	24 (5.0)	1.18 (0.48-2.88)	0.72	1.34 (0.50-3.56)	0.56
Cardiac death or MI	6 (5.9)	22 (4.6)	1.29 (0.52-3.17)	0.58	1.45 (0.54-3.89)	0.46
Clinically indicated revascularization (any)	6 (5.9)	29 (6.2)	0.96 (0.40-2.32)	0.93	0.89 (0.34-2.33)	0.82

Table 6 Clinical outcomes at discharge, 30 days, 1 year, and 2 years (continued)

			Crude		IPTW adjusted	
	Imaging group (n=103)	Control group (n=485)	Hazard Ratio(95% CI)	P value	Hazard Ratio(95% CI)	P value
Clincally indicated non-TVR	4 (4.0)	11 (2.4)	1.70 (0.54-5.34)	0.36	1.29 (0.39-4.25)	0.68
Clinically indicated TVR	3 (3.0)	22 (4.7)	0.63 (0.19-2.11)	0.45	0.77 (0.22-2.75)	0.69
Clinically indicated TLR	3 (3.0)	22 (4.7)	0.63 (0.19-2.11)	0.45	0.77 (0.22-2.75)	0.69
MACE†	7 (6.8)	39 (8.2)	0.83 (0.37-1.87)	0.66	0.90 (0.37-2.20)	0.83
Definite ST	3 (3.0)	8 (1.7)	1.77 (0.47-6.66)	0.40	2.01 (0.51-7.92)	0.32
Definite or probable ST	3 (3.0)	15 (3.1)	0.94 (0.27-3.25)	0.92	1.15 (0.31-4.17)	0.84
Any major bleeding (BARC 3,4,5)	5 (4.9)	23 (4.8)	1.02 (0.39-2.68)	0.97	1.60 (0.50-5.10)	0.43
Clinical events at 2 years ∫∫						
Death	2 (2.0)	19 (4.0)	0.49 (0.11-2.09)	0.33	0.68 (0.14-3.35)	0.64
Cardiac death	2 (2.0)	13 (2.7)	0.72 (0.16-3.17)	0.66	1.00 (0.20-5.02)	1.00
MI	5 (4.9)	21 (4.5)	1.11 (0.42-2.95)	0.83	1.07 (0.37-3.11)	0.90
Death or MI	6 (5.9)	39 (8.2)	0.72 (0.30-1.70)	0.45	0.82 (0.32-2.14)	0.69
Cardiac death or MI	6 (5.9)	33 (7.0)	0.85 (0.36-2.03)	0.72	0.97 (0.37-2.53)	0.95
Clinically indicated revascularization (any)	16 (15.9)	49 (10.6)	1.54 (0.87-2.70)	0.14	1.60 (0.86-2.96)	0.14
Clinically indicated non-TVR	9 (9.0)	22 (4.8)	1.93 (0.89-4.20)	0.096	1.70 (0.76-3.81)	0.20
Clinically indicated TVR	10 (10.0)	36 (7.8)	1.28 (0.64-2.58)	0.49	1.52 (0.71-3.26)	0.28
Clinically indicated TLR	9 (9.0)	34 (7.3)	1.22 (0.59-2.54)	0.60	1.46 (0.65-3.26)	0.36
MACE†	17 (16.7)	63 (13.3)	1.27 (0.74-2.16)	0.39	1.40 (0.77-2.52)	0.27
Definite ST	3 (3.0)	11 (2.3)	1.28 (0.36-4.58)	0.71	1.46 (0.38-5.51)	0.58
Definite or probable ST	3 (3.0)	20 (4.2)	0.70 (0.21-2.36)	0.56	0.85 (0.24-3.02)	0.80
Any major bleeding (BARC 3,4,5)	5 (4.9)	24 (5.0)	0.97 (0.37-2.55)	0.96	1.52 (0.48-4.83)	0.48

∫Data are number of first events (%) and rate ratios RR (95% CI) with p-values from Poisson Regressions Crude, or IPTW Adjusted, using robust error variances.
∫∫Data are number of first events (% from Kaplan-Meier life-tables) and hazard ratios HR (95% CI) with p-values from Cox's Regressions Crude, or IPTW Adjusted.
CI, confidence interval; † MACE, composite of all cardiac death, myocardial infarciton and any clinically indicated revascularization.

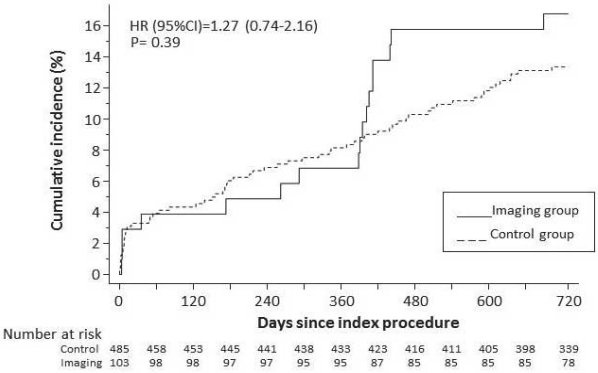

Figure 1. Cumulative incidence curve for MACE (cardiac death, MI and any clinically indicated revascularization) throughout 2 years. Continuous line indicates imaging group, dotted line indicates control group not undergoing imaging.

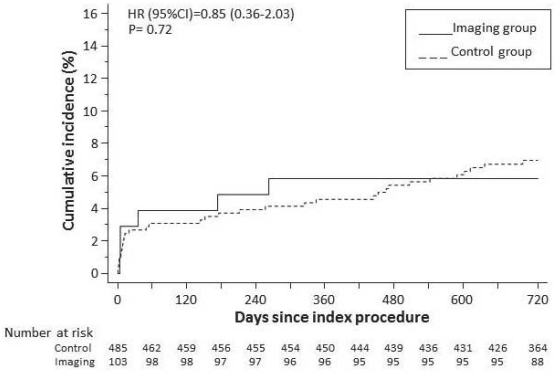

Figure 2. Cumulative incidence curve for the composite of cardiac death or MI throughout 2 years.

of some of the arteries, vessel tortuosity, and an untreated stenosis. This is however, not surprising since these features typically make part of the exclusion criteria in OCT studies. Nevertheless, as we aimed at a three-vessel evaluation in an already diseased patient population, with as few exclusion criteria as possible to minimize selection bias, these vessels were included yet still contribute to an overall high success rate. Studies investigating the feasibility of multimodality three-vessel i.c. imaging in STEMI patients undergoing primary PCI are lacking. Up until now, few studies performed three vessel (single modality) imaging with either OCT [10] or IVUS [11], however, these reports did not disclose the number of excluded patients related to imaging failures, thus only reported

the number of pullbacks excluded due to insufficient imaging quality and safety data is not available.

Periprocedural complications

Peri-procedural complications were rare and solely related to the use of OCT. In two out of 309 OCT pullbacks (0.6%), ventricular fibrillation occurred due to prolonged flushing with contrast media. Given the overall low frequency of ventricular fibrillation in this patient group presenting for primary PCI, and in view of the prompt restoration of sinus rhythm following defibrillation, OCT can be considered as a safe diagnostic tool. Nonetheless, physicians using this technology need to be aware about the potential of inducing ventricular fibrillation. The single dissection recorded at a proximal stent edge was related to the short monorail of the previous version of the dragonfly OCT catheter, which was difficult to advance in a vessel curvature.

The largest study with time-domain (TD-) OCT where peri-procedural complications were reported included 468 mainly stable coronary artery disease patients, and observed ventricular fibrillation in 1.1% of patients, air embolism in 0.6% and vessel dissection in 0.2% of patients. Only few data is available on the safety of FD-OCT [12, 13], which acquires images at frame rates at least 10 times faster than TD-OCT and results in an improved imaging quality. The marked simplification of the acquisition procedures and reduction in the required contrast volume has decreased the imaging procedure time and increased the imaging quality.[11] The absence of complications with the use of IVUS confirms the already known high degree of safety of this technique, and may be the result of device adaptations since the introduction of the technique in the early 1990s and the high degree of experience with its use. Conversely, OCT has been introduced only 15 years later. In our study, two participating study centers initiated the use of OCT only with the occasion of this study, which increases the applicability of the study results to a broader spectrum of centers performing i.c. imaging.

Short and long-term safety

We did not limit our analysis to peri-procedural complications and compared clinical outcome measures of safety between imaging patients and a control group. At 30 days, the composite endpoint cardiac death or MI occurred at a similar rate in imaging and non-imaging patients, further supporting the procedural and long-term safety of multimodality imaging for documentary purpose. Similarly, no difference in cardiac death or MI was noted at 1 and 2 years of follow-up.

Safety concerns related to imaging procedures in native coronary arteries are not limited to peri-procedural complications occurring during the first 30 days after imaging

but also apply to a hypothetical acceleration of atherosclerosis during long-term follow-up [14,15,16] Hypothetically, the introduction of imaging catheters solely for diagnostic purposes (IVUS: 2.9 French, OCT 2.7 French) may induce clinically silent endothelial injury as previously demonstrated in an experimental model[17]. The iatrogenic damage may trigger atherosclerotic disease progression by initiating clinically silent plaque ruptures with subsequent progression[18]. As non-infarct related arteries of STEMI patients are known to accommodate vulnerable plaques, and as they are potentially more sensitive to catheter-induced rupture than other lesions, we extended our evaluation to a long-term monitoring with a particular focus on repeat revascularization events in untreated segments.[11,10] Indicators of a disease progression in untreated vessel segments are the frequency of target vessel revascularizations (TVR) and the revascularizations occurring in the untreated vessels (non-target lesion revascularization, non-TVR). Throughout 2 years, TVR and non-TVR occurred in a similar frequency when comparing the imaging with the control group. Similar to our findings, the "Avasimibe and progression of coronary lesions assessed by IVUS" (A-PLUS trial) investigating i.c. imaging related atherosclerosis progression, found no evidence by quantitative coronary analysis of disease progression 24 months following IVUS investigation, as compared to control arteries of the same patients.[15]

OCT and IVUS require the placement of an i.c. guidewire and therefore, radiation exposure and contrast agents are important safety considerations. While we did not record the incremental radiation dosage required for three-vessel i.c. imaging, we did assess the amount of contrast agents used. OCT requires complete blood removal achieved by a proper contrast injection. In our study, the contrast use per pullback ranged between 15 and 30 ml per pullback and we used injection rates between 3.5 and 6 ml/sec. A total of 174 ml of contrast media was injected at baseline and 164 ml at follow-up. This relatively high number has to be interpreted in light of our IBIS-4 study protocol, which required the placement of a guidewire in two non-intervened vessels, the placement and documentation of the image wire for matching purpose, the acquisition of OCT pullbacks in three vessels and a documentary final angiography after both IVUS and OCT to confirm the absence of harm. Despite the higher contrast use in imaging patients, the risk of developing renal failure after primary PCI was low and similar for patients in the imaging and control group (1.0% vs. 1.9%, p=0.72). In addition, no difference was observed in the creatinine increase from admission to peak during the index hospitalization (7.2±9.2 µmol/L vs. 8.8±15.2 µmol/L, p=0.16).

Limitation

This study has some limitations. First of all, there is to date no clinical indication for the performance of multi-modality three vessel imaging during primary PCI. However, the results observed in the setting of a maximal i.c. imaging approach can be translated to less extensive imaging procedures in daily clinical routine, attesting to their feasibility and safety.

Despite the attempt to select a comparable control group, the decision to perform i.c. imaging was not random introducing some selection bias and probably including a lower risk population in the imaging study. Repeated manipulation with the infarct related artery could potentially lead to an increasing risk for micro-embolization. Whilst myocardial blush grade was not recorded, no difference in final TIMI-flow between the two groups were recorded. Although the presence of a myocardial infarction at baseline hypothetically masks the occurrence of a imaging induced peri-procedural myocardial infarction, we did not observe an increased risk at follow-up under stable conditions.

In addition, we did not assess the radiation dose in both groups. Nevertheless, the total radiation time inevitably increases as positioning of the coronary wire and imaging catheter has to be documented with both OCT and IVUS. The total number of patients investigated is limited considering the presence of a complex imaging protocol.

CONCLUSIONS

Multi-modality three-vessel i.c. imaging in the acute setting of STEMI and performed for documentary purposes is consistent with a high degree of success and can be performed safely without impact on cardiovascular events at long-term follow-up. This data provides reassurance on the feasibility and safety of intravascular imaging in daily routine, where a less extensive approach may be used.

REFERENCES

1. Tearney GJ, Regar E, Akasaka T, Adriaenssens T, Barlis P, Bezerra HG, et al. Consensus standards for acquisition, measurement, and reporting of intravascular optical coherence tomography studies: a report from the International Working Group for Intravascular Optical Coherence Tomography Standardization and Validation. J Am Coll Cardiol 2012;**59**:1058-72.
2. Mintz GS, Nissen SE, Anderson WD, Bailey SR, Erbel R, Fitzgerald PJ, et al. American College of Cardiology Clinical Expert Consensus Document on Standards for Acquisition, Measurement and Reporting of Intravascular Ultrasound Studies (IVUS). A report of the American College of Cardiology Task Force on Clinical Expert Consensus Documents. J Am Coll Cardiol 2001;**37**:1478-92.
3. Nair A, Kuban BD, Tuzcu EM, Schoenhagen P, Nissen SE, Vince DG. Coronary plaque classification with intravascular ultrasound radiofrequency data analysis. Circulation 2002;**106**:2200-6.
4. Sawada T, Shite J, Garcia-Garcia HM, Shinke T, Watanabe S, Otake H, et al. Feasibility of combined use of intravascular ultrasound radiofrequency data analysis and optical coherence tomography for detecting thin-cap fibroatheroma. Eur Heart J 2008;**29**:1136-46.
5. Trii S Nakazawa G, Ijichi T, Yoshikawa A, Ikari Y. Ex vivo assessment of plaque characteristics with optical frequency domain imaging; accuracy and pitfalls in diagnosis of lipid rich plaque. Abstract Presented at ESC 2013.
6. Witzenbichler B, Maehara A, Weisz G, Neumann FJ, Rinaldi MJ, Metzger DC, et al. Relationship between intravascular ultrasound guidance and clinical outcomes after drug-eluting stents: the assessment of dual antiplatelet therapy with drug-eluting stents (ADAPT-DES) study. Circulation 2014;**129**:463-70.
7. Räber L Taniwaki M, Zaugg S, Kelbaek H, Roffi M, Holmvang L et al. Effect of high-intensity statin therapy no atherosclerosis in non-infarct related coronary arteries (IBIS-4): a serial intravascular ultrasonography study. Eur Heart J 2014;in print.
8. Räber L, Kelbaek H, Ostojic M, Baumbach A, Heg D, Tuller D, et al. Effect of biolimus-eluting stents with biodegradable polymer vs bare-metal stents on cardiovascular events among patients with acute myocardial infarction: the COMFORTABLE AMI randomized trial. JAMA 2012;**308**:777-87.
9. Raber L, Kelbaek H, Ostoijc M, Baumbach A, Tuller D, von Birgelen C, et al. Comparison of biolimus eluted from an erodible stent coating with bare metal stents in acute ST-elevation myocardial infarction (COMFORTABLE AMI trial): rationale and design. EuroIntervention 2012;**7**:1435-43.
10. Kato K, Yonetsu T, Kim SJ, Xing L, Lee H, McNulty I, et al. Nonculprit plaques in patients with acute coronary syndromes have more vulnerable features compared with those with non-acute coronary syndromes: a 3-vessel optical coherence tomography study. Circ Cardiovasc Imaging 2012;**5**:433-40.
11. Hong MK, Mintz GS, Lee CW, Kim YH, Lee SW, Song JM, et al. Comparison of coronary plaque rupture between stable angina and acute myocardial infarction: a three-vessel intravascular ultrasound study in 235 patients. Circulation 2004;**110**:928-33.
12. Kataiwa H, Tanaka A, Kitabata H, Matsumoto H, Kashiwagi M, Kuroi A, et al. Head to head comparison between the conventional balloon occlusion method and the non-occlusion method for optical coherence tomography. Int J Cardiol 2011;**146**:186-90.

13. Imola F, Mallus MT, Ramazzotti V, Manzoli A, Pappalardo A, Di Giorgio A, et al. Safety and feasibility of frequency domain optical coherence tomography to guide decision making in percutaneous coronary intervention. EuroIntervention 2010;**6**:575-81.
14. Yamaguchi T, Terashima M, Akasaka T, Hayashi T, Mizuno K, Muramatsu T, et al. Safety and feasibility of an intravascular optical coherence tomography image wire system in the clinical setting. Am J Cardiol 2008;**101**:562-7.
15. Guedes A, Keller PF, L'Allier PL, Lesperance J, Gregoire J, Tardif JC. Long-term safety of intravascular ultrasound in nontransplant, nonintervened, atherosclerotic coronary arteries. J Am Coll Cardiol 2005;**45**:559-64.
16. Hausmann D, Erbel R, Alibelli-Chemarin MJ, Boksch W, Caracciolo E, Cohn JM, et al. The safety of intracoronary ultrasound. A multicenter survey of 2207 examinations. Circulation 1995;**91**:623-30.
17. Van der Giessen W. Intracoronary device insertion induces temporary, but stents induce chronic endothelial damage. Abstract Presented at ESC 2010.
18. Burke AP, Kolodgie FD, Farb A, Weber DK, Malcom GT, Smialek J, et al. Healed plaque ruptures and sudden coronary death: evidence that subclinical rupture has a role in plaque progression. Circulation 2001;**103**:934-40.

Appendix Table 1 Clinical outcomes at discharge, 30 days, 1 year, and 2 years of follow-up separated for clopidogrel loading and prasugrel loading/double loading

			Crude		IPTW adjusted	
	Imaging group	Control group	Hazard Ratio(95% CI)	P value	Hazard Ratio(95% CI)	P value
Clopidogrel loading						
Number of patient treated	26	251				
MACE at discharge	1 (3.8)	5 (2.0)	1.93 (0.23-15.97)	0.54	2.84 (0.35-23.13)	0.33
MACE at 30 days	2 (7.7)	11 (4.4)	1.80 (0.40-8.12)	0.44	2.15 (0.46-10.00)	0.33
MACE at 1 year	3 (11.5)	21 (8.5)	1.40 (0.42-4.68)	0.59	1.39 (0.38-5.12)	0.62
MACE at 2 years	4 (15.4)	33 (13.5)	1.18 (0.42-3.32)	0.76	1.18 (0.39-3.61)	0.77
Prasugrel loading or double loading						
Number of patient treated	77	226				
MACE at discharge	0 (0.0)	1 (0.4)	1.46 (0.13-15.88)	1.00		
MACE at 30 days	1 (1.3)	4 (1.8)	0.73 (0.08-6.56)	0.78	1.38 (0.16-12.13)	0.77
MACE at 1 year	4 (5.2)	15 (6.7)	0.77 (0.26-2.33)	0.65	0.78 (0.23-2.67)	0.70
MACE at 2 years	13 (17.3)	27 (12.3)	1.43 (0.74-2.77)	0.29	1.67 (0.81-3.43)	0.16

Values are % (n/N). MACE, major adverse cardiac event.

CHAPTER 1 INTRODUCTION TO OPTICAL COHERENCE TOMOGRAPHY

1.3 Artefacts with intracoronary optical coherence tomography.

Radu MD, Räber L, Serruys PW.

The Clinical Atlas of OCT. PCR Publishing. May 2012.

Please see separate electronic application, chapter 2

CHAPTER 2 METHODOLOGICAL CONSIDERATIONS IN THE APPLICATION OF OPTICAL COHERENCE TOMOGRAPHY FOR THE EVALUATION OF METALLIC STENTS

2.1 Optical coherence tomography for the assessment of intracoronary stents.

Radu MD*, Räber L*, Gomez-Lara J, Kelbæk H, Stefanini G, Jørgensen E, Helqvist S, Tellez A, Granada J, Saunamäki K, Serruys PW, Windecker S.

The Clinical Atlas of OCT. PCR Publishing. May 2012.

Please see separate electronic application, chapter 4

CHAPTER 2 METHODOLOGICAL CONSIDERATIONS IN THE APPLICATION OF OPTICAL COHERENCE TOMOGRAPHY FOR THE EVALUATION OF METALLIC STENTS

2.2 Strut apposition after coronary stent implantation visualised with optical coherence tomography.

Radu M, Jørgensen E, Kelbæk H, Helqvist S, Skovgaard L, Saunamäki K.

EuroIntervention. 2010;6:86-93.

Strut apposition after coronary stent implantation visualised with optical coherence tomography

Maria Radu[1]*, MD; Erik Jørgensen[1], MD; Henning Kelbæk[1], MD, DMSci; Steffen Helqvist[1], MD, DMSci; Lene Skovgaard[2], MSc; Kari Saunamäki[1], MD, DMSci

1. Department of Cardiology, The Heart Centre, Rigshospitalet, University of Copenhagen, Copenhagen, Denmark;
2. Department of Biostatistics, University of Copenhagen, Copenhagen, Denmark

The authors have no conflict of interest to declare.

This paper also includes accompanying supplementary data published at the following website: www.eurointervention.org

KEYWORDS
OCT, strut apposition, stent implantation, invasive imaging

Abstract

Aims: To describe different patterns of stent strut apposition, as visualised with optical coherence tomography.

Methods and results: Strut thicknesses were reconstructed according to the manufacturers' specifications. The stent area (SA) was measured by connecting the reconstructed abluminal surfaces of struts with a trace line, and the vessel wall area (VWA) was estimated from the abluminal strut surfaces, as well as from the lumen border, in cases of struts that were separated from the vessel wall by flush. Strut apposition was evaluated by comparing the SA- and VWA traces. We observed four patterns of strut apposition. Based on these, stent struts could be classified as: (I) apposed struts, (II) struts overlying the ostium of a side branch, (III) malapposed struts that were clearly separated from the vessel wall by flush, and (IV) pseudoapposed struts that were not separated from the vessel wall by visual estimate, but were malapposed in the sense that SA<VWA. Pseudoapposed struts were found in frames with "flower-shaped" lumen contours, and were often surrounded by structures of a lower signal intensity than the rest of the vessel wall.

Conclusions: For a detailed analysis of strut apposition with OCT, we reconstructed strut thicknesses and estimated stent- and vessel wall areas. With this method, we found four types of strut apposition, where pseudoapposed struts constitute a type of struts not previously described. The clinical importance of pseudoapposed struts remains to be settled.

** Corresponding author: Department of Cardiology, The Heart Centre, Rigshospitalet, University of Copenhagen, Section 2013, Blegdamsvej 9, DK-2100, Copenhagen, Denmark*
E-mail: maria_d_radu@yahoo.com

Introduction

The importance of refining stent implantation in coronary artery lesions was previously demonstrated using intravascular ultrasound (IVUS).[1] Accordingly, it became customary to deploy coronary stents at high pressure, since this improves stent expansion and apposition to the vessel wall.[2] Although IVUS- and histopathological reports have related stent strut malapposition to late thrombosis of drug-eluting stents (DES)[3,4], other studies have shown that malapposition may occur in up to 10% of DES without any clinical consequence.[5,6] The importance of strut malapposition therefore remains controversial.

Optical coherence tomography (OCT) is an infrared light-based imaging technique with a resolution of 10 µm, which is ten times higher than that of IVUS.[7] As a sensitive tool, OCT detects strut malapposition and thin strut coverages more often than IVUS.[8] Consequently, intracoronary OCT examination of stented areas might contribute to evaluate the clinical importance of strut malapposition.

At present, there is no consensus regarding the classification of strut apposition as visualised with OCT. It was recently suggested that strut apposition on OCT may be classified into three grades; embedded, protruding, and malapposed[9], where embedded and protruding struts are different degrees of apposed struts. In our work with OCT, we have encountered various morphological configurations of the stent/vessel wall complex that seem to be related to strut apposition. The objectives of this study were therefore (1) to describe the different morphological appearances of the stent/vessel wall complex at the frame level, and (2) to analyse whether these, by means of various quantitative parameters, are related to apposition at the strut level.

Methods

Patient population

The study included data from patients with coronary stents implanted at least two months prior to the OCT examinations. These were performed either as part of an elective diagnostic- or routine control angiography, or in connection with an angiography performed subacutely as part of the diagnostic program in acute coronary syndrome (ACS). Only examinations with a good image quality, defined as an adequate displacement of blood and visualisation of >70% of the vessel wall circumference, were included.

OCT image acquisition

The M2 OCT system (LightLab Imaging Inc., Westford, MA, USA) used in this study has been described previously.[10] We used occlusive or non-occlusive techniques to obtain blood displacement during OCT imaging. In brief, after crossing the stent with an angioplasty wire, an over-the-wire OCT occlusion balloon catheter (Helios™) or a Renegade™ catheter (Boston Scientific, Natick, MA, USA) was advanced distal to the stented segment, and the coronary wire was exchanged with the OCT image wire (ImageWire™). For the occlusive method, the OCT catheter was retracted proximally to the stented segment and the balloon was inflated at 0.5-0.7 atmospheres. For the non-occlusive method, the Renegade catheter was retracted into the guiding catheter. During image acquisition, coronary blood was displaced by manual infusion of saline or Visipaque (Iodixanol 320, GE Healthcare, Ireland) for the occlusive and non-occlusive set-up, respectively. Although the non-occlusive technique may imply a slightly higher intracoronary pressure during image acquisition compared to the occlusive technique, the potential change in areas of relevance for this study, is likely to be proportional for the different areas. We therefore assumed it unlikely that the choice of technique would influence strut apposition. Cross-sectional images were acquired at 15.4 frames/s, and we used an automated pullback system at 1.0 or 2.0 mm/s. Image acquisition was performed for a maximum of 40 seconds under careful monitoring of heart rhythm and haemodynamics.

OCT image analysis

Frames within the stented segment were examined at 1 mm intervals to identify recurring morphological patterns in the stent/vessel wall complex at the frame level. Because OCT visualises only the endoluminal surfaces of struts, strut thicknesses are underestimated by visual estimate.[11] To compensate for this, we reconstructed all strut thicknesses according to the manufacturers' specifications (Table 1) before evaluating strut apposition (Figure 1). Aspects influencing the appearance of struts on OCT, and thus the reconstruction of strut thicknesses, are considered in the online appendix (www.eurointervention.org).

The stent area (SA) was measured planimetrically by fitting a smooth curve through the trace points of the reconstructed abluminal strut surfaces (Figure 1A). If the lumen contour on visual estimation was located inside the stent area, the stent at this cross-sectional point was considered apposed. Thus, the best possible estimation of the vessel wall area (VWA) in contact with the stent, then equalled the SA. In cases of stent malapposition, the VWA was traced along points in the lumen contour located outside the stent contour (Figure 1B).

Table 1. Actual and reconstructed strut thicknesses of the stents analysed.

Stent	Metal strut	Polymer	Total thickness	Reconstructed strut thickness
Cypher Select	140	7	154	160
Taxus Liberté/Express	97	15	127	130
Endeavor Sprint	91	8 *	107	110
NIR, Palmaz-Schatz	102	-	102	100
Micro-Driver	91	-	91	90
CoStar	89	-	89	90
Multilink Vision	81	-	81	80

All values are in µm. *Average thickness of uneven endo- and abluminal polymers. Cypher Select/Palmaz-Schatz (Cordis Corp., Johnson & Johnson, Warren, NJ, USA); Taxus Liberté/Express (Boston Scientific Corp., Natick, MA, USA); Endeavor Sprint/Micro-Driver (Medtronic Vascular, Santa Rosa, CA, USA); NIR (Medinol, Boston Scientific, Tel Aviv, Israel); CoStar (Conor Medsystems, Menlo Park, CA, USA); Multilink Vision (Abbott Vascular, Redwood City, CA, USA).

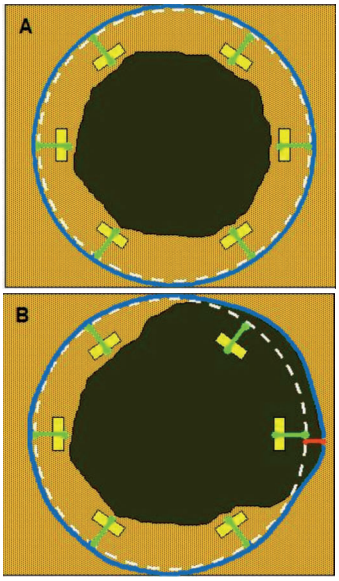

Figure 1. Schematic drawing of the methodology used for the OCT analysis. Yellow boxes represent the endoluminal surfaces of struts, as visualised by OCT. Actual strut thicknesses were reconstructed by drawing a trace line for every strut from the strongest endoluminal surface reflection a certain distance (exaggerated in the figure) in the abluminal direction (green traces), as specified by the stent manufacturer. White dotted lines represent the stent area (SA). Blue traces represent the best possible estimation of the vessel wall area (VWA), estimated from the SA in cases of apposed struts (panel A), or from the lumen contour in cases of clearly malapposed struts (panel B). For the purpose of clear visualisation, the VWA in panel A is depicted slightly outside the SA. Comparison of the abluminal strut surfaces with the VWA trace for every strut yields that struts are apposed in panel A, and malapposed at 1 and 3 o'clock in panel B. The interspace distance (red trace) for the malapposed struts was measured from the abluminal strut surface to the VWA trace.

Apposition to the vessel wall was evaluated for every strut by comparing the location of the reconstructed abluminal strut surface with the VWA trace line (Figure 1). A strut was defined as apposed if the abluminal strut surface was located outside the lumen contour and was tangent to the estimated VWA trace. In cases of malapposed struts, the distance between the abluminal strut surface and the VWA trace, interspace distance (ISD), was additionally measured (Figure 1B).

Statistical analysis

Statistical analysis was performed with SAS statistical package, version 9.2 (SAS Institute Inc., Cary, NC, USA), and the R statistical environment, version 2.10.0. Continuous data are presented as mean ± standard deviation or median and interquartile range (IQR), and categorical variables as percentages. Normality of the data was assessed by visual estimation of residual plots. Frequencies were compared with Fisher's exact test.

Given the hierarchical structure of the data (stent struts nested within frames nested within lesions), a multilevel model was applied to compare the interspace distance between relevant apposition classes, with variance components for "struts within frames" and "frames within lesions", using only strut apposition as a fixed factor. In order to have a good fit of the normal distribution, analysis was performed on a logarithmic scale.

Intra-observer reproducibility of the classification of strut apposition was assessed by calculating the Kappa coefficient. A two-tailed *p*-value of ≤0.05 was considered statistically significant for all analyses.

Results

Clinical-, stent- and procedural characteristics at OCT examination

Thirty-one patients with 31 lesions (37 stents) were included in the study. Clinical-, stent-, and procedural characteristics are shown in Table 2. The majority (87.1%) of stents were DES, and the median duration from implantation was 20 months (range 2-125 months). Eight patients had acute coronary syndrome (ACS) at the time of OCT examination, while the remaining 23 patients were examined in a stable clinical setting.

The non-occlusive technique was used in 13 patients, of which one developed ventricular fibrillation during image acquisition of a stent in the right coronary artery. Sinus rhythm was immediately restored after defibrillation. Otherwise there were no haemodynamic instabilities, arrhythmias, coronary dissections, subsequent myocardial infarctions, or deaths with any of the two methods used.

Qualitative assessment of the stent/vessel wall morphology

A total of 596 frames were analysed. We identified four morphological patterns of the stent/vessel wall complex, each of which were accompanied by distinct features of strut apposition.

Figure 2A shows a frame where the lumen contour is regular, circular, and located inside the SA. The VWA is estimated as VWA=SA, and we conclude that every single strut is well apposed to the vessel wall. This pattern of the stent/vessel wall complex was seen in 506 frames from all 31 lesions.

As an example of the second morphological pattern, Figure 2B shows three struts where the abluminal strut surfaces are not in touch with the vessel wall. Analysis of consecutive frames shows that the vessel wall "opens up" and "closes" (not shown) again behind these struts, indicating that struts are overlying the ostium of a side branch. This pattern was seen in 15 frames from 10 lesions. In Figure 2C$_1$ we see two struts that are clearly separated from the vessel wall by lumen extending behind them. Analysis of consecutive frames showed no signs suggestive of a side branch (not shown). Estimation of SA and VWA shows that VWA exceeds SA, and that abluminal strut surfaces at 10 o'clock are located

Table 2. Clinical-, stent- and procedural characteristics.

n=31 patients/lesions	n (%)
Patient characteristics	
Age (years)	65.3±8.8*
Male gender	22 (71.0)
Hypertension	22 (71.0)
Statin treatment	31 (100.0)
Diabetes mellitus	10 (32.3)
Smoker (current/former)	25 (80.6)
Family history of IHD	12 (38.7)
Clinical setting at OCT	
CAG control	6 (19.4)
Clinical indication	25 (80.6)
Stable angina	17 (54.8)
ACS presentation	8 (25.8)
Stent characteristics	
Average stent number per lesion	1.2±0.5
Duration from implantation (months)	20 (9–34)**
Stent type	
BMS	4 (12.9)
DES	27 (87.1)
Stent type, specified	
Cypher Select	13 (41.9)
Taxus Liberté	6 (19.4)
Taxus Express	2 (6.5)
Endeavor	5 (16.1)
CoStar	1 (3.2)
Micro-Driver	1 (3.2)
Multilink Vision	1 (3.2)
Palmaz-Schatz	1 (3.2)
NIR	1 (3.2)
Average stent diameter (mm)	2.9±0.4
Total stented length	20 (13–33)*
Lesion location	
Target vessel	
LAD	8 (25.8)
LCX	6 (19.4)
RCA	16 (51.6)
VG	1 (3.2)
Location	
Proximal	6 (19.4)
Mid	21 (67.7)
Distal	3 (9.7)
VG	1 (3.2)

* Mean ± standard deviation; ** Median (interquartile range); IHD: ischaemic heart disease; CAG: coronary angiography; ACS: acute coronary syndrome; BMS: bare metal stent; DES: drug-eluting stent; LAD: left anterior descending artery; LCX: left circumflex artery; RCA: right coronary artery; VG: vein graft

inside the VWA trace (Figure $2C_2$), indicating that struts are malapposed. This pattern was present focally in seven lesions (23 frames), predominantly at the edges, but also at the mid portions of the stents. The stents in question included an Endeavor stent (12 months after implantation), one Taxus Express stent (40 months after implantation), one NIR stent (100 months after implantation), and four Cypher stents (12, 15, 20 and 29 months after implantation).

In the last type of stent/vessel wall configuration, lumen contour is irregular and flower-shaped (Figure 2D). On first impression, struts look apposed to the vessel wall. After reconstruction of strut thicknesses and estimation of SA it appears that the lumen contour at several points exceeds the SA trace. Planimetrical estimation of the VWA from these outer points shows that SA is smaller than VWA, suggesting that the stent in this frame is malapposed although struts are not clearly separated from the vessel wall. Comparison of the location of the abluminal strut surfaces with the VWA trace suggests the presence of malapposed struts from 6 to 3 o'clock. Further, the regions in immediate approximation of these types of struts often displayed a lower signal brightness than the rest of the vessel wall (Figures 2D and 3A). The pattern where the VWA exceeds the SA, but where struts are not clearly separated from the vessel wall, was present to varying extents in 89 frames from 11 lesions, predominantly at the mid portions of the stents. The stents involved, and the time points from implantation were: Endeavor (three and 12 months), Taxus Express (40 and 51 months), Cypher (12, 15, 20, 29 and 41 months), Taxus Liberté (21 months), and NIR (100 months).

Based on these four patterns of stent/vessel wall morphology, strut apposition can be divided in four classes: (I) apposed struts, in frames where SA=VWA; (II) struts overlying the ostium of a side branch (SA=VWA); (III) malapposed struts, that are clearly separated from the vessel wall where SA<VWA; and (IV) struts that are not clearly separated from the vessel wall, but where SA<VWA. For the latter, we suggest the term "pseudoapposed" struts.

Quantitative assessment of strut apposition in relation to vessel wall and stent parameters

A total of 5,966 struts were analysed and classified according to the definition above. 5,592 struts were apposed, 20 were overlying the ostium of a side branch, 52 were malapposed, and 302 were pseudoapposed.

At the strut level, the interspace distance was 2.85 times higher for malapposed- compared to pseudoapposed struts (95% confidence limits [CI]: 2.29–3.56, p<0.0001), with a (geometrical) mean [95%CI] ISD of 101.1 µm [80.2–127.5] and 288.4 µm [213.4–389.9] for pseudo- and malapposed struts, respectively.

The overall intra-observer agreement in classification of strut apposition was very good (Kappa coefficient [95% CI]=0.94 [0.92–0.96]). Further, the absolute difference in ISD between two observations by the same observer was 0 µm, within ±10 µm and ±20 µm for 17%, 44% and 60% of paired observations, respectively.

The clinical importance of mal- and pseudoapposed struts

In total, mal- and pseudoapposed struts were present in 35% of patients (11 out of 31). Mal- and pseudoapposed struts were found in bare metal stents as well as DES, and were often present together in the same lesions (seven out of 11 lesions with pseudo- and/or malapposed struts). Patients with ACS had more frequently mal- and pseudoapposed struts than patients examined in a stable clinical setting (fraction [95% CI]: 75% [35–97] vs. 22% [7–44], respectively [p=0.012]).

Discussion

The main finding of the present study is the identification with OCT of a type of stent strut apposition not previously described. These struts were found in frames where the stent/vessel wall complex was irregular, tending to have a flower-shaped appearance. Estimation of

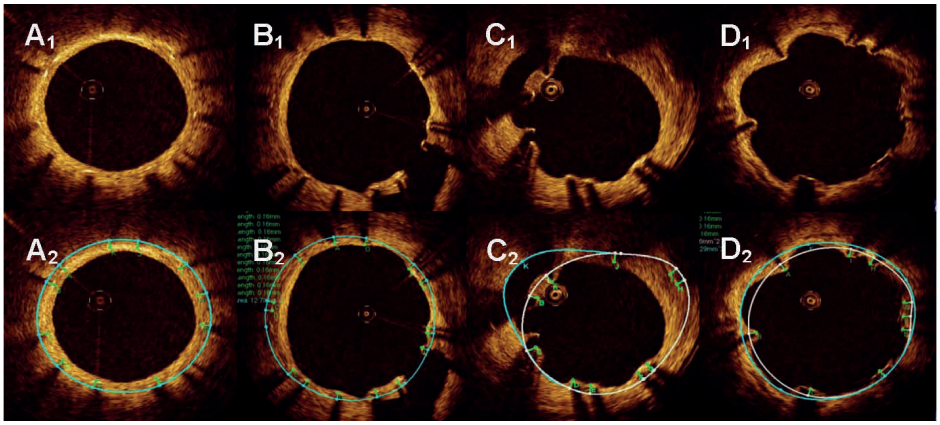

Figure 2. Morphological patterns of the stent/vessel wall complex. Green lines depict the reconstructed strut thicknesses, blue lines represent the vessel wall area (VWA) trace, and the white lines the stent area (SA) trace (A-D). In panels A2 and B2, the white lines are hidden behind the blue lines. Panel A shows apposed struts. In panel B, struts are overlying the ostium of a side branch at 4 to 6 o'clock. Panel C shows malapposed struts at 10 o'clock. In panel D, lumen is flower-shaped and struts are pseudoapposed at 6 to 3 o'clock. The regions in the vicinity of struts at 6 and 9 o'clock have a lower signal intensity than the rest of the vessel wall. Stent types and time points from implantation are: A: Cypher (41 months), B: Cypher (22 months), C and D: Cypher (15 months).

SA and VWA suggested they were malapposed, although not clearly separated from the vessel wall. Further, the region adjacent to these struts often displayed a lower signal brightness than the rest of the vessel wall. We propose that this category of struts be classified as "pseudoapposed" – a designation that refers to their lack of apparent separation from the vessel wall, as well as their malapposed appearance by closer examination. Since the detection of pseudoapposed struts is based on a methodology that estimates the location of the vessel wall, we find it relevant to comment on this methodology and how it relates to current approaches.

Reconstruction of strut thicknesses and estimation of stent and vessel wall areas

The underestimation of strut thicknesses on OCT may be addressed in different ways. One approach is to measure the distance from the endoluminal strut surface to the visible lumen- or vessel wall contour, and compare it with the actual strut thickness.[9,12] We addressed this issue by reconstructing the actual strut thickness for every strut, which allowed us to locate the abluminal surfaces of struts, and use them for estimation of other parameters. Compared to the method used by Tanigawa et al, our approach does not distinguish between apposed struts that are "protruding" from- and apposed struts that are "embedded" into the vessel wall. Importantly, a consistent use of this grading, requires a clear definition of the reference structure that is being referred to, which in turn requires consideration of the time point at which OCT is performed and the presence or not of a strut coverage. In the present study, we assumed apposed struts to be of the protruding type, in order not to overestimate apposition. In this way, it is unlikely that a protruding strut which is covered, will be mixed up with a pseudoapposed strut surrounded by material.

With other methodologies, the stent area is assessed from the leading endoluminal strut surface. We chose to estimate the SA from the reconstructed abluminal surfaces of struts because strut apposition refers to a contact between the vessel wall and the strut surface orienting towards it. In this way, the abluminal strut surfaces were used to estimate the dimensions of the vessel wall in contact with the stent (in cases of apposed struts), and in combination with the lumen contour, the vessel wall that was not in contact with the stent (in cases of malapposed struts), expressed as the VWA. Since the detection of pseudoapposed struts is dependent on the estimation of the abluminal SA and the VWA, these struts cannot be identified with the current approaches, because they do not estimate a parameter that is equivalent to the VWA used in this study. Until the importance of pseudoapposed struts is clarified, we find it relevant to reconstruct strut thicknesses when evaluating strut apposition, particularly in frames with an irregular lumen contour.

It should be emphasised that the VWA as we have estimated it with OCT, is different from that measured with IVUS at stent implantation and generally referred to as the "external elastic membrane (EEM) area". The EEM area refers to the border between the media and adventitia, and is used for the study of vessel remodeling behind the stent.[13] Due to a limited tissue penetration, OCT is rarely able to visualise the EEM when the vessel is significantly diseased. What the VWA with OCT actually represents depends on the strut apposition at stent implantation, and the occurrence or not of late vessel remodelling and stent recoil. Due to the lack of post-implantation OCT, this was not possible to evaluate in our study. Nevertheless, as with IVUS, serial estimation of the SA and the VWA with OCT may allow us to monitor changes in the stent and vessel wall over time, including the luminal part of vessel remodelling and stent recoil.

Strut malapposition with different imaging modalities and potential explanation of pseudoapposed struts

With IVUS, strut malapposition, also referred to as incomplete stent apposition, has been defined as a lack of contact between stent struts and the underlying vessel wall not overlying a side branch, with blood speckle between struts and the vessel wall.[13,14] With other OCT approaches, as well as with the one described here, struts were considered malapposed when the distance from its endoluminal surface to the vessel wall was greater than the actual thickness of the strut, indirectly including a separation of struts from the vessel wall by flush. Although no clear histopathological criteria have been defined for strut malapposition, histological images reveal that struts can be separated from the original vessel wall by material such as fibrin. In these cases the authors conclude that struts are malapposed.[4,15] Considering this, it is interesting to speculate whether these struts would have appeared malapposed or apposed, had they been examined with IVUS or OCT *in vivo*; and inversely, whether there is a risk that some struts on IVUS and OCT visualised *in vivo* can be classified as apposed, although they are in reality malapposed.

Although difficult to objectify, analysis of tissue texture is a novel and interesting aspect in the evaluation of coronary stents.[16,17] In the present study, we noticed that the structures in the vicinity of pseudoapposed struts often displayed a lower signal brightness than the rest of the vessel wall (Figures 2D and 3A). Considering that the variation in signal intensity on OCT is related to variations in backscatter- and attenuation coefficients between tissue components[18], the differences in signal brightness might indicate that the regions containing these struts are composed of various materials. On previously published histology images, it is not only evident that struts can be separated from the vessel wall by fibrin, but also that these fibrin deposits have a morphological shape that resembles that of the low-signal areas on OCT (Figure 3).[4,15] Moreover, some of these histological cross-sections exhibit a "flower-shaped" appearance of the lumen contour, reminding of the one observed with OCT in this study (Figure 4A1 and 4B1). Considering the proposed link between persistent fibrin deposition around struts and late stent thrombosis, it would be remarkable if OCT could visualise this *in vivo*. Whether the low-signal structures adjacent to some of the pseudoapposed struts on OCT may represent fibrin overlying components of the initial vessel wall; and whether pseudoapposed struts in some cases could actually be malapposed, would be interesting to investigate in comparison with histology.

It should be stressed that the flower-shaped appearance of the stent/vessel wall configuration in frames with pseudoapposed struts should not be mixed up with a similar pattern seen in both OCT images and histological sections, where the outer portion of the "petals" are created by stent struts rather than the vessel wall (Figure 4).[19] This phenomenon is probably a consequence of stent implantation at high pressure, stretching the vessel wall between struts.

We would also like to mention that struts overlying side branch ostia were included as part of the classification, as to describe their existence. Since the mechanism of non-apposition, as well as the potential consequence hereof is pathophysiologically different from that of malapposed struts, they cannot be compared. Struts overlying side branch ostia are therefore often excluded from studies involving analysis of strut apposition.[9]

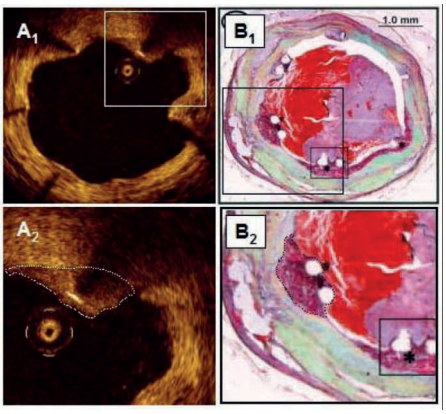

Figure 3. Area of low signal brightness around a strut on OCT morphologically resembling fibrin deposition from a histology image of late stent thrombosis. Panel A shows an OCT image from a Cypher stent, 12 months after implantation. The pseudoapposed strut at one o'clock (estimated SA and VWA not shown) is separated from the vessel wall by material that has a lower signal brightness than the rest of the vessel wall. Panel B shows a histology section from a Cypher stent with thrombosis 24 months after implantation (stained with Movat's pentachrome). Struts at 6 and 8 o'clock are separated from the vessel wall by fibrin. In panels A2 and B2, the morphological shapes of the low-signal area by OCT and fibrin deposit by histology, respectively, are marked. (B. from Finn et al; Circulation 2007. Reproduced with permission from Wolters Kluwer Health.)

Relevance of detecting pseudo- and malapposed struts with OCT

Although our study population was highly heterogeneous, it demonstrates that pseudoapposed struts can be found in many different stent types, at varying time points after implantation. In the present study, pseudoapposed struts were considerably more common than malapposed struts, and were frequently found in frames and lesions also containing malapposed struts. Both types of stent struts were found in stable as well as unstable clinical settings, albeit more frequently in ACS. Whether this could be related to mal- and pseudoapposed struts is difficult to evaluate from our small population, and requires larger, serial studies with OCT.

Strut malapposition has been related to late stent thrombosis, although the frequency of malapposed struts has varied between autopsy- and IVUS studies.[3,4] With histology, focus has mainly been on stent healing, where a lack of neointimal stent coverage and a persistent deposition of fibrin around struts has been associated with late stent thrombosis.[15] However, the importance of strut apposition for stent healing is not known, which may partly be related to the insufficient resolution of IVUS, precluding the

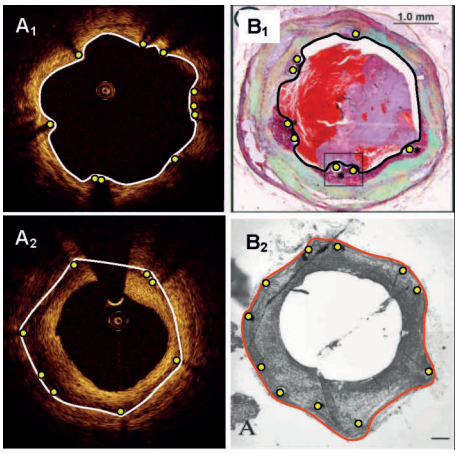

Figure 4. Two types of "flower configuration" in OCT images and histology sections. OCT images in panels A1 (Cypher, 15 months) and A2 (Cypher, 15 months) are potentially corresponding with histology sections in panels B1 (Cypher, 24 months) and B2 (MultiLink, 4 weeks, rabbit artery, stained with toluidine blue). Yellow circles represent struts. In panels A1 and B1, the lumen contours are traced with a white and black line, respectively. In panels A2 and B2, the boundaries of the original vessel walls to which struts are apposed, are traced with a white and red line, respectively. (Panel B1 from Finn et al; Circulation 2007, and B2 from Carlier et al; Circulation 2003. Reproduced with permission from Wolters Kluwer Health.)

visualisation of very thin strut coverages and thus the study of the relationship between strut healing and apposition. Thus far, OCT studies have indicated that malapposed struts were more frequently uncovered than struts that were apposed.[20,21] It is yet to be clarified whether the same is true for pseudoapposed struts.

Limitations

This study was a retrospective observational analysis. Due to the lack of post-implantation OCT data, it was not possible to evaluate whether mal- or pseudoapposition was present immediately after implantation or was acquired. Moreover, our study population was very heterogeneous and limited to a small number of cases, wherefore it was not possible to estimate the prevalence of pseudoapposed struts in different stent types, and at different time points after implantation.

Conclusion

For a detailed analysis of strut apposition with OCT, we used a methodology involving the reconstruction of strut thicknesses and estimation of stent- and vessel wall areas. With this method, we found four types of strut apposition, where pseudoapposed struts constitute a type of struts not previously described. These struts were found in frames with flower-shaped lumen contours, and were surrounded by structures of different signal intensities on OCT. The clinical importance of pseudoapposed struts remains to be settled.

References

1. Nakamura S, Colombo A, Gaglione A, Almagor Y, Goldberg SL, Maiello L, Finci L, Tobis JM. Intracoronary ultrasound observations during stent implantation. *Circulation* 1994;89:2026-2034.

2. Goldberg SL, Colombo A, Nakamura S, Almagor Y, Maiello L, Tobis JM. Benefit of intracoronary ultrasound in the deployment of Palmaz-Schatz stents. *J Am Coll Cardiol* 1994;24:996-1003.

3. Cook S, Wenaweser P, Togni M, Billinger M, Morger C, Seiler C, Vogel R, Hess O, Meier B, Windecker S. Incomplete stent apposition and very late stent thrombosis after drug-eluting stent implantation. *Circulation* 2007;115:2426-2434.

4. Joner M, Finn AV, Farb A, Mont EK, Kolodgie FD, Ladich E, Kutys R, Skorija K, Gold HK, Virmani R. Pathology of drug-eluting stents in humans: delayed healing and late thrombotic risk. *J Am Coll Cardiol* 2006;48:193-202.

5. Ako J, Morino Y, Honda Y, Hassan A, Sonoda S, Yock PG, Leon MB, Moses JW, Bonneau HN, Fitzgerald PJ. Late incomplete stent apposition after sirolimus-eluting stent implantation: a serial intravascular ultrasound analysis. *J Am Coll Cardiol* 2005;46:1002-1005.

6. Hoffmann R, Morice MC, Moses JW, Fitzgerald PJ, Mauri L, Breithardt G, Schofer J, Serruys PW, Stoll HP, Leon MB. Impact of late incomplete stent apposition after sirolimus-eluting stent implantation on 4-year clinical events: intravascular ultrasound analysis from the multicentre, randomised, RAVEL, E-SIRIUS and SIRIUS trials. *Heart* 2008;94:322-328.

7. Regar E, Schaar JA, Mont E, Virmani R, Serruys PW. Optical coherence tomography. *Cardiovasc Radiat Med* 2003;4:198-204.

8. Bouma BE, Tearney GJ, Yabushita H, Shishkov M, Kauffman CR, DeJoseph GD, MacNeill BD, Houser SL, Aretz HT, Halpern EF, Jang IK. Evaluation of intracoronary stenting by intravascular optical coherence tomography. *Heart* 2003;89:317-320.

9. Tanigawa J, Barlis P, Di MC. Intravascular optical coherence tomography: optimisation of image acquisition and quantitative assessment of stent strut apposition. *EuroIntervention* 2007;3:128-136.

10. Pinto TL, Waksman R. Clinical applications of optical coherence tomography. *J Interv Cardiol* 2006;19:566-573.

11. Kawase Y, Hoshino K, Yoneyama R, McGregor J, Hajjar RJ, Jang IK, Hayase M. In vivo volumetric analysis of coronary stent using optical coherence tomography with a novel balloon occlusion-flushing catheter: a comparison with intravascular ultrasound. *Ultrasound Med Biol* 2005;31:1343-1349.

12. Gonzalo N, Garcia-Garcia HM, Serruys PW, Commissaris KH, Bezerra H, Gobbens P, Costa M, Regar E. Reproducibility of quantitative optical coherence tomography for stent analysis. *EuroIntervention* 2009;5:224-232.

13. Mintz GS, Nissen SE, Anderson WD, Bailey SR, Erbel R, Fitzgerald PJ, Pinto FJ, Rosenfield K, Siegel RJ, Tuzcu EM, Yock PG. American College of Cardiology Clinical Expert Consensus Document on Standards for Acquisition, Measurement and Reporting of Intravascular Ultrasound Studies (IVUS). A report of the American College of Cardiology Task Force on Clinical Expert Consensus Documents. *J Am Coll Cardiol* 2001;37:1478-1492.

14. Shah VM, Mintz GS, Apple S, Weissman NJ. Background incidence of late malapposition after bare-metal stent implantation. *Circulation* 2002;106:1753-1755.

15. Finn AV, Joner M, Nakazawa G, Kolodgie F, Newell J, John MC, Gold HK, Virmani R. Pathological correlates of late drug-eluting stent

thrombosis: strut coverage as a marker of endothelialization. *Circulation* 2007;115:2435-2441.

16. Gonzalo N, Serruys PW, Okamura T, van Beusekom HM, Garcia-Garcia HM, van SG, van der GW, Regar E. Optical coherence tomography patterns of stent restenosis. *Am Heart J* 2009;158:284-293.

17. Guagliumi G, Sirbu V, Costa MA, Musumeci A, Trivisonno A, Matiashvili A, Lortkipanidze N, Mihalcsik L, Valsecchi O, Bezerra HG, Suzuki N, Coletta JE, Mintz G, Maehara A, Parise H, Lansky A, Christea E, Mehran R, Stone G. Long-term strut coverage of paclitaxel eluting stents compared with bare-metal stents implanted during primary PCI in acute myocardial infarction: a prospective, randomized, controlled study performed with optical coherence tomography. HORIZONS-OCT (abstr). *Circulation* 2008;118:2315.

18. Xu C, Schmitt JM, Carlier SG, Virmani R. Characterization of atherosclerosis plaques by measuring both backscattering and attenuation coefficients in optical coherence tomography. *J Biomed Opt* 2008;13:034003.

19. Carlier SG, van Damme LC, Blommerde CP, Wentzel JJ, van LG, Verheye S, Kockx MM, Knaapen MW, Cheng C, Gijsen F, Duncker DJ, Stergiopulos N, Slager CJ, Serruys PW, Krams R. Augmentation of wall shear stress inhibits neointimal hyperplasia after stent implantation: inhibition through reduction of inflammation? *Circulation* 2003;107:2741-2746.

20. Takano M, Inami S, Jang IK, Yamamoto M, Murakami D, Seimiya K, Ohba T, Mizuno K. Evaluation by optical coherence tomography of neointimal coverage of sirolimus-eluting stent three months after implantation. *Am J Cardiol* 2007;99:1033-1038.

21. Matsumoto D, Shite J, Shinke T, Otake H, Tanino Y, Ogasawara D, Sawada T, Paredes OL, Hirata K, Yokoyama M. Neointimal coverage of sirolimus-eluting stents at 6-month follow-up: evaluated by optical coherence tomography. *Eur Heart J* 2007;28:961-967.

Appendix

Aspects influencing the appearance of struts on OCT and reconstruction of strut thicknesses

We would like to emphasise two aspects that may influence strut reconstruction:

(1) **The saturation artefact:** With the stent acting like a mirror, a reflection may spread along the surface and edges of the strut, causing a "glare" of light, also called the blooming effect or saturation artefact. This glare is an artefact and may falsely enlarge the dimensions of struts, complicating their demarcation for the reconstruction of strut thicknesses, evaluation of apposition and quantification of the thickness of the strut coverage. To demonstrate this, we implanted a Micro-Driver stent (Medtronic Vascular, Santa Rosa, CA, USA) *post mortem* in the left anterior descending artery of a healthy young pig (not previously published). In order to exclude the presence of blood, the coronaries were thoroughly flushed with saline directly after excision of the heart as well as before and after stent implantation. With the M2 system (LightLab Imaging Inc., Westford, MA, USA), OCT was performed a few hours later with a pullback speed of 0.5 mm/s at 15.4 frames/s to obtain the highest possible resolution in the pullback direction (frame thickness: 30 µm). Figure 1 shows four consecutive frames from this experiment where the appearance of strut reflections changes for "corresponding" struts on moving proximally. Due to the repeating design pattern of the Micro-Driver stent, in combination with an extremely short distance between the visualised cross-sections, the change in the actual width and thickness of every separate strut from one frame to the next is virtually non-existing. Thus, the change in strut appearance on OCT in Figure 1 is probably not related to an actual change in strut dimensions, but is rather due to a glare which produces signals that exceed the dynamic range of the data acquisition system.

(2) **Marginalisation of the OCT light source:** Depending on the actual strut thickness and width, together with the location of the separate strut in relation to the OCT light source (LS), the lateral width and orientation of the reflected signal may vary between struts in the same frame.

When the image wire is centralised in the vessel lumen and the strut is parallel to the vessel wall, the light beam will fall perpendicular to the endoluminal surface of each strut and to the vessel wall abluminal to it (Figure 2). In our study, we aimed at reconstructing the strut thicknesses as perpendicular to the vessel wall as possible. However, the orientation of the reconstructed trace line may be difficult to estimate when the LS is marginalised, as in tortuous segments, since the angle between the light beam and the strut surface will vary for different struts in the same frame. The result is visualisation of different parts of the strut surface which together with the saturation artefact affects the width and orientation of the reflected signal. Thus, some struts may look wider than other although this is not necessarily so. An example is the "sunflower orientation" where struts turn "toward the image wire" in stead of to the centre of the stent, as depicted in Figure 3. As a consequence, the described optical phenomena influence the choice of starting point for the reconstruction of strut thicknesses (Figure 4). This is of importance for the measurement of stent- and vessel wall areas, particularly in cases of struts with borderline apposition, where the evaluation of apposition is influenced by how this starting point is chosen. In such cases it may be helpful to examine the change in appearance of these structures in neighbouring frames. In conclusion, strut thicknesses were reconstructed perpendicular to the vessel wall by drawing a trace line for every strut from the strongest endoluminal surface reflection, a certain distance in the abluminal direction, as specified by the stent manufacturer.

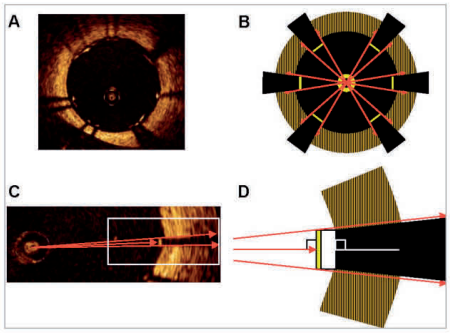

Figure 2. Appearance of stent struts and their shadows on OCT when the light source is centralised in the vessel lumen. Panel B: Schematic drawing of the OCT image in panel A. The surfaces of struts visualised by OCT are yellow, the vessel wall is black-and-yellow striped, and the lumen is black. The light source (image wire) is centralised and radiates red light beams. Panel C: Magnification of a single strut with red light beams. Panel D: Schematic drawing of panel C showing the perpendicular relation between the strut/vessel wall and the infrared light/strut shadow. The full strut thickness is depicted, including the white abluminal part that is not visualised by OCT.

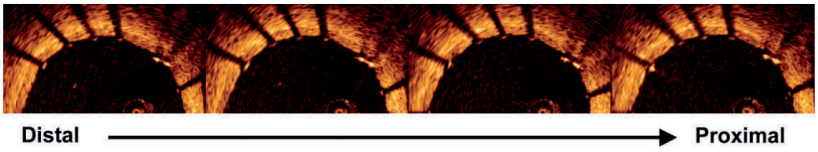

Figure 1. OCT examination of a Micro-Driver stent implanted post mortem in the left anterior descending artery of a healthy young pig. Four consecutive frames demonstrate the saturation artefact around corresponding struts on OCT.

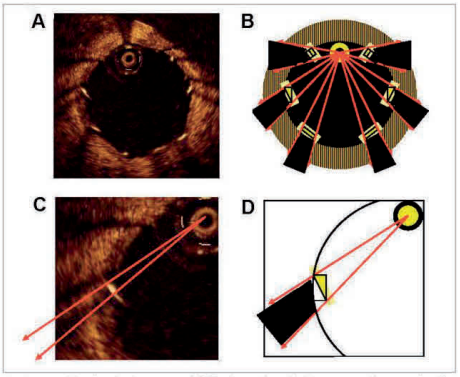

Figure 3. Appearance of stent struts and their shadows on OCT when the light source is marginalised. Panel B: Schematic drawing of the OCT image in panel A. Different parts of struts are visualised when the image wire is marginalised, causing strut reflections to "orient towards the light source". As depicted, the visualised parts of struts (yellow boxes with black borders) are probably edgy, but due to the glare artefact (light yellow boxes surrounding visualised parts of struts) in combination with a lateral resolution of 25 µm, strut borders appear smooth on OCT. The vessel wall is black-and-yellow striped, and the lumen is black. Panel C: Magnification of a single strut with red light beams drawn. Panel D: Schematic drawing of panel C showing the non-perpendicular relation between the infrared light/strut shadow and strut. The full strut thickness is depicted, including the white abluminal part that is not visualised by OCT.

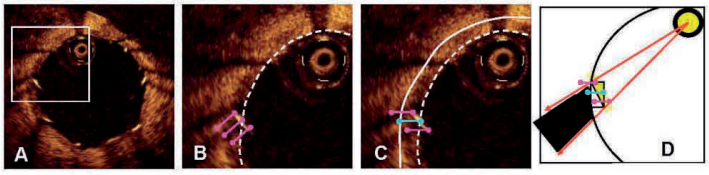

Figure 4. How marginalisation of the OCT light source influences the choice of starting point for reconstruction of struts. Panel A: OCT image with marginalised image wire. Panels B and C demonstrate that there are several possibilities of reconstructing the strut trace. In panel B, the strut trace (purple) is drawn perpendicular to the strut signal from three points in the strut surface – in the middle and at the strut edges. The dotted white line represents the border of the vessel lumen. In panel C, the strut trace is drawn perpendicular to the vessel wall from three points in the strut surface. The location of the reconstructed abluminal strut surface depends on which point along the endoluminal strut surface one chooses for strut reconstruction. Consequently, the estimation of the vessel wall area (continuous white line) is also influenced by this point. The blue trace shows how we considered the strut to be reconstructed correctly: from the strongest luminal strut reflection and perpendicular to the vessel wall. The purple traces are considered erroneous since they start either at the "glare" (lower trace), or at a surface that is probably not the luminal strut surface (upper trace), as shown schematically in panel D.

CHAPTER 2 METHODOLOGICAL CONSIDERATIONS IN THE APPLICATION OF OPTICAL COHERENCE TOMOGRAPHY FOR THE EVALUATION OF METALLIC STENTS

2.3 Optical coherence tomography at follow-up after percutaneous coronary intervention: relationship between procedural dissections, stent strut malapposition and stent healing.

Radu M, Jørgensen E, Kelbæk H, Helqvist S, Skovgaard L, Saunamäki K.

EuroIntervention. 2011;7:353-61.

Optical coherence tomography at follow-up after percutaneous coronary intervention: relationship between procedural dissections, stent strut malapposition and stent healing

Maria Radu[1]*, MD; Erik Jørgensen[1], MD; Henning Kelbæk[1], MD, DMSci; Steffen Helqvist[1], MD, DMSci; Lene Skovgaard[2], MSc; Kari Saunamäki[1], MD, DMSci

1. Department of Cardiology, The Heart Centre, Rigshospitalet, University of Copenhagen, Copenhagen, Denmark; 2. Department of Biostatistics, University of Copenhagen, Copenhagen, Denmark

KEYWORDS

- OCT
- angioplasty
- drug eluting stent
- strut apposition

Abstract

Aims: To analyse the relationship between strut apposition as visualised with optical coherence tomography (OCT) at follow-up and clinical and procedural characteristics at stent implantation, and to examine the relationship between strut apposition and stent healing.

Methods and results: Twenty-eight coronary lesions were evaluated. The lesion morphology before stent implantation was described from the baseline angiogram. Strut apposition at follow-up was divided into: (I) apposed struts, (II) struts overlying side branch ostia, (III) malapposed and (IV) protruding struts. Since malapposed and protruding struts often occurred in the same lesions, these were divided into two groups: lesions without (n=20) and lesions with (n=8) the presence of these struts. The thickness of strut coverage was used as a surrogate for stent healing. We analysed 5,159 struts. Sixteen were malapposed and 216 were protruding. Lesions with malapposed and/or protruding struts at OCT follow-up were more frequently associated with acute coronary syndrome (ACS) and procedure related dissections at stent implantation than lesions without. There was a tendency towards a less pronounced strut coverage over malapposed and protruding struts, as compared to apposed struts.

Conclusions: ACS and procedural dissections at stent implantation may be related to strut malapposition/protrusion at follow-up, which may influence the degree of strut coverage.

** Corresponding author: Department of Cardiology, The Heart Centre, Section 2013, Rigshospitalet, University of Copenhagen, Copenhagen, Blegdamsvej 9, DK-2100, Denmark. E-mail: maria_d_radu@yahoo.com.*

Introduction

Late coronary stent malapposition has been reported after bare metal stent (BMS) as well as drug-eluting stent (DES) implantation, using intravascular ultrasound (IVUS).[1,2] Although stent malapposition has been related to late stent thrombosis (LST)[3,4], the results of other studies suggest malapposition to occur in up to 10% of implanted DES without any clinical consequence at late follow-up.[5,6] The importance of late stent malapposition therefore remains controversial.

Optical coherence tomography (OCT) is an infrared light-based imaging technique that provides detailed information about the coronary vessel wall, strut apposition and tissue coverage *in vivo*.[7] With a resolution of 10 μm, OCT detects strut malapposition and strut coverage more efficiently than IVUS.[8]

We have recently suggested the following OCT based classification of strut apposition: (I) apposed struts, (II) struts overlying the ostium of a side branch, (III) malapposed struts, and (IV) pseudoapposed/protruding struts **(Figure 1)**.[9] Protruding struts were found in frames with "corrugated" lumen contours, and were characterised by finding that "pits" in the lumen contour extended beyond the stent area trace delineated from the reconstructed abluminal strut surfaces, although struts appeared to be well apposed to the vessel wall. Protruding struts were often present in frames and lesions containing malapposed struts, and were frequently surrounded by structures displaying a lower signal-intensity than the rest of the vessel wall. The nature of these structures is not known, but morphologically they resemble fibrin deposits that separate malapposed struts from the vessel wall, as seen in previously published histology images.[9,10]

The objectives of this study were (1) to analyse the relationship between the type of strut apposition at follow-up and clinical and procedural characteristics at stent implantation, and (2) to examine strut coverage as a surrogate for stent healing, in relation to strut apposition at follow-up. We hypothesised that protruding struts from a biological point of view have more similarity with malapposed struts than with apposed struts.

Methods

PATIENT POPULATION AND LESION CHARACTERISTICS AT STENT IMPLANTATION

Between September 2007 and September 2008, 35 patients were examined with OCT after stent implantation at our institution. Those with high quality OCT acquisitions, defined as an adequate visualisation of >70% of the vessel wall circumference throughout the stented area, were selected for this study. Patients with LST were excluded.

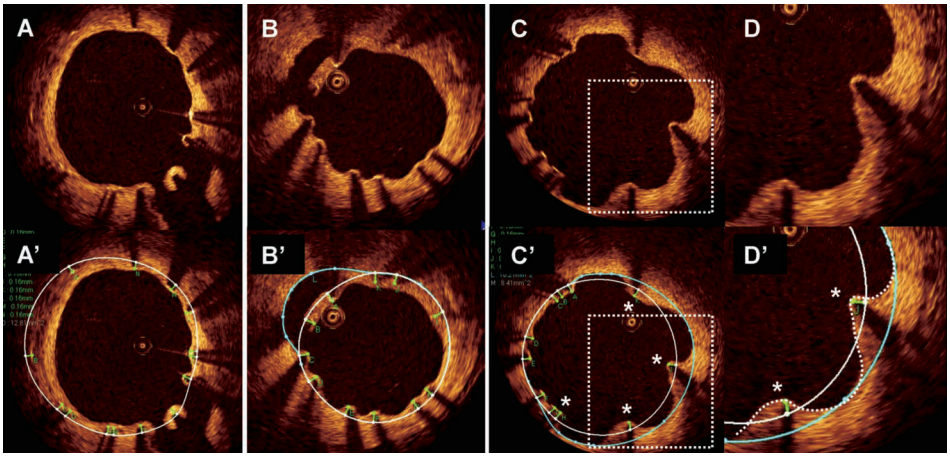

Figure 1. *Classification of strut apposition. Apposition was evaluated after reconstruction of strut thicknesses (green traces) according to manufacturers' specifications. The abluminal stent area (white line) was delineated by connecting the abluminal strut surfaces with a trace line. In case the lumen contour was located within the abluminal stent area, struts were considered apposed, unless interrupted by a side branch (panel A/A' 5 o'clock). Malapposed struts were defined as struts separated from the lumen contour (panel B). In panel B', the lumen contour behind the malapposed struts at 11 o'clock is highlighted with a blue trace. In the presence of apposed struts that protruded into the lumen (panel C/C') and where the lumen contour (dotted white line, panel D') extended beyond the abluminal stent trace (continuous white line), a help line (blue line) was drawn in extension to the abluminal stent trace, and extrapolated between the lumen contour at these points (panels C'/D'). Struts were considered protruding (asterisks, panels C'/D') only when the abluminal strut surfaces were separated from this help line, ie. when they protruded into the lumen more than the actual strut thickness.*

The morphology of each lesion at baseline was described from the coronary angiogram. Based on the hypothesis that certain lesion characteristics at baseline may influence strut apposition in the short- and/or long-term, we registered the following lesion characteristics: calcification, chronic total occlusion (>3 months), thrombus, recent total occlusion (<3 months), diffuse disease (>2 cm), excessive tortuosity and angulation >90º.[11] As minor dissections, not necessarily visible on the angiogram, occur in connection with most coronary balloon dilatations[12], we considered angiographically visible dissections as "significant"[13], and hypothesised that these could influence the healing of the vessel wall behind the stent and hence have an impact on stent strut apposition. Angiograms were analysed independently by two experienced operators who were blinded to the clinical presentation. In the case of disagreement, a consensus diagnosis was obtained by repeated readings.

OCT IMAGE ACQUISITION

OCT images were acquired with the M2 OCT system (LightLab Imaging Inc., Westford, MA, USA). Dependent on vessel anatomy, we used occlusive or non-occlusive techniques to displace blood during OCT imaging. After crossing the stent with an angioplasty wire, an over-the-wire OCT occlusion balloon catheter (Helios™) or a Renegade™ catheter (Boston Scientific, Natick, MA, USA) was advanced distally to the stented segment, and the coronary wire was exchanged with the OCT ImageWire™. For the occlusive method, the balloon catheter was retracted proximally to the stented segment and the balloon was inflated at 0.5 to 0.7 atmospheres during flush. For the non-occlusive method, the Renegade catheter was retracted into the guide catheter. During image acquisition, coronary blood was displaced by manual infusion of saline or Visipaque (Iodixanol 320; GE Health Care, Buckinghamshire, UK) for the occlusive and non-occlusive setup, respectively. Cross-sectional images were acquired at 15.4 frames/s, during automated pullback at 1 or 2 mm/s. Image acquisition was performed under haemodynamic monitoring. Although the non-occlusive technique may imply a slightly higher intracoronary pressure than the occlusive technique, the potential changes in the dimensions of the vessel wall and stent are likely to be proportional. We therefore assumed that the choice of technique would not influence strut apposition.

OCT IMAGE ANALYSIS

Cross-sections within the stented segment were analysed every 1 mm by an experienced observer, who was blinded to the clinical and angiographic characteristics. Due to an underestimation of the actual thickness of the metal strut by the OCT infrared light, all strut thicknesses were reconstructed using a method described recently[9]. Based on apposition, struts were divided into four classes: (I) apposed struts; (II) struts overlying the ostium of a side branch; (III) malapposed struts; and (IV) protruding struts, as recently described **(Figure 1)**.[9] The material covering struts was used as a surrogate for stent healing, and the minimum thickness was measured manually for every strut.

Statistical analysis

Statistical analysis was performed with the SPSS software, version 15.0 (SPSS Inc., Chicago, IL, USA). Normality of the quantitative data was assessed by visual estimation of residual plots. Continuous data are presented by their median and interquartile range (IQR), and categorical variables as percentages. Medians and frequencies were compared with the Mann-Whitney U-test and Fisher's exact test, respectively.

We planned to compare (i) the presence or absence of strut coverage, and (ii) the thickness of strut coverage (TSC), between different strut appositional classes after pooling struts in four groups and adjusting for confounders related to stent healing, namely: time from stent implantation to follow-up[14,15], clinical presentation at implantation[16-18], diabetes mellitus[19,20], stent type[21,22], lesion type[17,18], periprocedural characteristics, strut thickness and stent design.[23] Due to the complex hierarchical structure of our data (stent struts nested within frames nested within lesions), the regression analysis requires a multilevel model. However, the distribution of TSC could not be transformed to normality, and a non-parametric equivalent that can adjust for relevant covariates, is not available. Instead, median TSCs for the various strut appositional types within every separate lesion with malapposed and/or protruding struts were calculated, and the differences were compared with a Wilcoxon signed rank test, paired at the lesion level.

For the comparison of frequencies of uncovered struts between appositional types, a logistic multilevel regression analysis was not possible due to the complex data structure, combined with a relatively high number of covariates and a heterogeneous study population. However, we present the frequencies of uncovered struts per strut appositional type. Details regarding struts overlying side branch ostia are also shown, but since these are pathophysiologically different from other "non-apposed" struts (malapposed and/or protruding struts), they were excluded from the analysis.

Intra-observer reproducibility of the classification of strut apposition and frequency of uncovered struts was assessed by calculating the Kappa coefficient. A two-tailed p-value ≤ 0.05 was considered statistically significant for all analyses.

Results

STRUT APPOSITION AT FOLLOW-UP OCT IN RELATION TO CHARACTERISTICS AT STENT IMPLANTATION

Twenty-eight lesions (32 stents) from 28 patients were analysed. Eight lesions were located in the left anterior descending artery, six in the left circumflex artery, and 14 in the right coronary artery. The stents examined were both DES: Cypher (43%), Taxus Liberté (21%), Endeavor Sprint (18%), and Taxus Express; and BMS: Multilink Vision, Costar, Micro-Driver, and Palmaz-Schatz (3.6% each). A total of 507 frames containing 5,159 struts were analysed. There were 4,907 apposed struts, 20 struts overlying side branch ostia, 16 malapposed struts, and 216 protruding struts. Since malapposed and protruding struts often occurred in the same lesions, and could therefore not be analysed separately, lesions were divided into two groups: those without (group 1, n=20), and those with (group 2, n=8) the

presence of malapposed and protruding struts. All lesions from group 2 contained protruding struts, while four lesions had malapposed struts as well. The time from stent implantation to examination with OCT was similar (median (IQR): 18 (9 to 34) months and 18 (12 to 31) months for group 1 and 2, respectively, (p=0.78)).

The clinical and procedural characteristics at the time of stent implantation are shown in **Table 1**. There were no differences in patient characteristics and angiographic lesion characteristics before intervention between the two groups. None of the lesions involved bifurcations. Patients with lesions displaying malapposed and/or protruding struts at OCT follow-up, had a significantly higher frequency of acute coronary syndrome (ACS) at stent implantation, compared with patients without these types of strut apposition (75% vs. 25%, respectively, p=0.03).

Lesions with malapposed and/or protruding struts at OCT follow-up were more often associated with angiographic dissections at baseline than lesions with apposed struts only (75% vs. 20%, p=0.01). Nine of these dissections occurred after predilatation and were all angiographically sealed by stent implantation, while one; appearing during stent implantation (type A), was considered benign without necessitating additional stenting. The location of dissections induced by predilatation before stenting coincided with the location of malapposed and protruding struts by OCT at follow-up (distal/mid/proximal one third of the stent). The dissections were of the following types: group 1: type A (n=1), type B (n=2), and type D (n=1); group 2: type A (n=1), type B (n=3), and type D (n=2).

STRUT COVERAGE IN RELATION TO STRUT APPOSITION

Table 2 shows the frequencies of uncovered struts and the TSC per appositional type within the two groups of lesions. Without consideration of known confounders, non-apposed struts were more frequently uncovered, and had a tendency to have thinner strut

Table 1. Clinical and procedural characteristics.

	Lesions without malapposed and/or protruding struts n = 20 %	Lesions with malapposed and/or protruding struts n = 8 %	*p*-value
Patient characteristics			
Age (years)	65 (60 to 73)*	64 (57 to 74)*	0.78
Male gender	75	50	0.37
Hypertension	75	63	0.65
Statin therapy	100	100	–
Diabetes mellitus	35	25	1.00
Smoker (current/former)	85	63	0.31
Family history of IHD	40	25	0.67
Clinical presentation			
Patients with ACS	25	75	0.03
Angiographic lesion characteristics			
Calcification	15	25	0.60
Chronic total occlusion (>3 months)	10	13	1.00
Thrombus	10	25	0.56
Recent total occlusion (<3 months)	15	25	0.60
Diffuse disease (>20 mm)	30	25	1.00
Excessive tortuosity/angulation >90°	5	0	1.00
Procedural and stent characteristics			
Predilatation	85	100	0.54
Angiographic dissection	20	75	0.01
Implantation of DES	85	100	0.54
Stent struts >110 µm	65	75	1.00
Stent length (mm)	19 (12-31)*	22 (16-31)*	0.67
Stent overlap	10	0	1.00
Postdilatation	40	38	1.00
Maximal balloon diameter (mm)	3.0 (2.5-3.0)*	3.0 (3.0-3.5)*	0.20
Maximal balloon inflation pressure (atm)	16 (15-18)*	15 (14-17)*	0.50

* Median (IQR); IHD: ischaemic heart disease; ACS: acute coronary syndrome; PCI: percutaneous coronary intervention; DES: drug-eluting stent

Table 2. Frequencies of uncovered struts and the thickness of strut coverage per strut type for lesions without- as compared to lesions with -malapposed and/or protruding struts.

	Lesions without malapposed and/or protruding struts n=20			Lesions with malapposed and/or protruding struts n=8		
	N total struts	N (%) uncovered struts	TSC	N total struts	N (%) uncovered struts	TSC, µm
Strut apposition						
Apposed struts	3,442	16 (0.5)	160 (80-310)	1,465	98 (6.7)	110 (40-180)
SB struts	15	1 (6.7)	50 (20-90)	5	4 (80.0)	–
Malapposed struts	–			16	2 (12.5)	35 (15-50)
Protruding struts	–			216	54 (25.0)	20 (5-30)
TSC: thickness of strut coverage (median [IQR]); SB struts: struts overlying side branch ostia						

coverage, compared to apposed struts. By paired analysis, considering the lesion from which different struts originate, there was a significant difference in the TSC of apposed compared to protruding struts (median difference (IQR): 50 (13 to 88) µm, p=0.018). A corresponding comparison between apposed and malapposed struts was not possible due to a small number of malapposed struts. Comparison of the TSC over different strut appositional types within individual lesions of group 2 shows a similar trend towards thinner strut coverage over malapposed and protruding struts **(Table 3)**.

The intra-observer agreement was very good for the classification of strut apposition (Kappa coefficient [95% CI] = 0.94 [0.91 to 0.96]), and good for the identification of strut coverage (Kappa coefficient [95% CI] = 0.78 [0.75 to 0.81].

CLINICAL OUTCOMES

Immediately after the follow-up OCT examination, two of the assessed lesions were treated for restenosis and one for malapposed struts. Additionally, six patients were treated for another lesion. LST did not occur in any patient by a median (IQR) follow-up time of 26 (24-27) months after OCT examination. During this time period, 20 of 27 patients (one patient died from a non-cardiac cause four months after OCT examination) received double antiplatelet therapy and one patient received clopidogrel therapy alone. The indications for use of clopidogrel were: OCT follow-up <12 months after DES implantation (n=3), new interventions (n=14), myocardial infarction without stent implantation (n=1), malapposed- and uncovered struts (n=1), previous LST (n=1), and aspirin intolerance (n=1).

Discussion

The main findings of the present study are: (a) Malapposed and protruding struts at OCT follow-up were more frequently associated with ACS and angiographically visible dissections at stent implantation, than lesions without these strut types. Further, (b) malapposed and protruding struts seemed more often uncovered, and tended to have thinner strut coverage than apposed struts, suggesting that strut apposition may be related to stent healing. These results support the hypothesis that protruding struts resemble malapposed struts more than apposed struts. We therefore find it relevant to identify protruding struts on OCT, in order to further investigate their clinical importance.

EVALUATION AND IMPORTANCE OF STRUT APPOSITION FOR STENT HEALING

One of the aims of coronary stent imaging with OCT is to study stent healing *in vivo* in order to evaluate the risk of LST. A histopathological study has previously shown that a lack of endothelial

Table 3. Number of struts per strut type, and the thickness of the strut coverage (TSC) in lesions containing malapposed and/or protruding struts.

Lesion	N_{app}	TSC_{app}	N_{mal}	TSC_{mal}	N_{protr}	TSC_{protr}	*p*-value for Mann-Whitney U-test		
							App vs. mal	App vs. protr	Mal vs. protr
6[1,2]	91	210 (140-260)	1	50	1	20			
7[1]	132	105 (45-170)			2	25 (20-30)		0.08	
11[1,3]	86	30 (20-50)	7	50 (20-60)	81	20 (0-30)	0.28	0.06	0.04
12[1,3]	190	70 (40-110)			17	10 (0-20)		<0.001	
13[1,3]	208	35 (20-80)	1	10	44	20 (10-30)		<0.001	
24[3]	141	10 (0-30)	7	30 (0-40)	48	10 (0-20)	1.00	0.24	0.43
25[1,3]	205	170 (70-270)			6	75 (20-130)		0.03	
27[2,3]	412	160 (130-200)			17	120 (100-130)		<0.001	

N_{app}: number of apposed struts; app: well-apposed struts; mal: malapposed struts; protr: protruding struts; [1] denotes the presence of acute coronary syndrome; [2] denotes that the patient was diabetic; [3] denotes the occurrence of an angiographically visible dissection. The multiple comparison Mann-Whitney U-test was performed with a Bonferroni correction. The TSC shown is the median (IQR). In lesions where there was only one single strut per appositional type, this was excluded from the pair-wise analysis, because one single strut was not considered representative for a whole appositional group within the respective lesion. The type of stent and time point from implantation was: Lesion 6: Endeavor Sprint, 12 months; Lesion 7: Taxus Express, 51 months; Lesion 11: Cypher Select, 12 months; Lesion 12: Endeavor Sprint, 3 months; Lesion 13: Cypher Select, 20 months; Lesion 24: Cypher Select, 15 months; Lesion 25: Taxus Liberté, 21 months; Lesion 27: Cypher, 41 months.

coverage over stent struts was a typical finding in cases of LST.[10] The resolution of OCT is, however, insufficient to detect endothelial cells, which have a thickness of <10 μm. The histological study further suggested that a high ratio of uncovered struts per cross-section may be a morphometric predictor of LST.

As defined histologically, "uncovered" struts are struts that lack coverage of neointimal tissue components (extracellular matrix, smooth muscle cells and endothelial cells). Struts covered with fibrin (per definition not "tissue") are thus "uncovered".[24] Although strut coverage can have various appearances by OCT, it is not fully known whether OCT can actually distinguish a neointimal layer from fibrin, although recent findings suggest that this might be possible with a new optical frequency domain imaging system.[25] The true ratio of uncovered struts per cross-section might therefore be underestimated with OCT. Further, it should be noted that the histological ratio of uncovered struts per section, as used to estimate an odds ratio for LST, was based on an average of five cross-sections per stent.[10] Factors that may influence the size of the ratio of uncovered struts per cross-section, and thus the determination of a cut-off value indicating the risk of LST, include: (1) the number of struts per cross-section, which depends on the stent design (in our study ranging from four to 23, median 10 struts/cross-section); (2) the average number of cross-sections included in the analysis (OCT can provide up to several hundreds of cross-sections per stent); and (3) the method of selection of cross-sections (in our study, selected cross-sections were equally spaced every 1 mm of the stent up to 33 cross-sections per stent, whereas by histopathology, typically 3-5 cross-sections per stent are selected from the proximal, mid, and distal segment). Quantitative analysis of strut coverage with OCT should therefore be interpreted with caution.

The present study showed a tendency towards less pronounced strut coverage over malapposed and protruding struts, as compared to apposed struts. Although OCT and histology has been used to evaluate apposition and coverage of intracoronary stents in several studies, a specific analysis of the degree of strut coverage in relation to apposition does not seem to have been performed previously.[4,17,18,26-33] As described by pathology, stent healing follows a distinct pattern, beginning with the deposition of fibrin around struts. The fibrin is infiltrated by inflammatory cells, which subsequently attract smooth muscle cells from the media. These produce a proteoglycan and collagen-rich matrix, which constitutes the main component of the neointima.[14] When struts are separated from the vessel wall, smooth muscle cells may not be able to "reach out" to them, which might explain why non-apposed struts, in the present study, were more frequently uncovered and had thinner coverage than apposed struts. Together with the antiproliferative effects of DES, the lack of apposition to the vessel wall may retain these struts in an early healing phase.

CLINICAL AND ANGIOGRAPHIC LESION CHARACTERISTICS AT STENT IMPLANTATION

Our present findings suggest that ACS and major dissections may predispose to malapposed and protruding struts at follow-up. Several reports have already proposed a link between late stent malapposition and ACS[17,18,34,35], however, this has not previously been shown for protruding struts. Since baseline OCT examinations were not available in our study, it is not possible to evaluate whether malapposed and protruding struts were acquired or persistent. In the context of ACS, possible mechanisms could be: (a) for persistent malapposition: inappropriate apposition of struts to the vessel wall due to the presence of thrombi or necrotic cores in lipid plaques; (b) for (acquired) protrusion: inappropriate apposition and baseline with subsequent fibrin deposition between struts and the vessel wall due to blood turbulence or as part of the initiation phase of the healing process **(Figure 2A)**; or (c) for acquired malapposition: dissolution of thrombus after stent implantation.[2]

Despite the higher frequency of ACS at stent implantation in patients with malapposed and protruding struts at OCT examination, it was not accompanied by a difference in the angiographic presence of thrombus. This may be explained by the fact that smaller thrombi may be difficult to detect angiographically, or concealed in total occlusions.

In the context of procedural dissections as predisposing factors for malapposed and protruding struts, possible mechanisms could involve: (a) incomplete apposition of the stent to the vessel wall in areas of dissections (for persistent malapposition); (b) as (a) but followed by fibrin deposition between struts and the vessel wall (for acquired protruding struts); or (c) for acquired malapposed struts: a positive vessel remodelling due to inflammation caused by a deeper penetration of the drug into the vessel wall as a consequence of the dissection, causing the vessel wall to retract from the stent with time, with a simultaneous thinning of the coverage **(Figure 2B)**. Protruding struts may in the latter case represent a "transition phase" of apposed struts during the vessel remodelling before they become malapposed. Ultrasonic reports have previously suggested expansive remodelling as a cause of late stent malapposition[2,5,36,37]. However, the resolution of IVUS is probably insufficient to display protruding struts, because the distance between the average abluminal strut surface and the help line between the pits in the lumen contour is approximately 100 μm[9], which is the resolution of IVUS.

THE FREQUENCY OF MALAPPOSITION COMPARED TO PREVIOUS STUDIES

The frequency of OCT-detected malapposed struts varies considerably in previous reports, reflecting the heterogeneity of different studies. Out of eight recent OCT studie, only four reported the number of stents with malapposed struts.[17,18,26-30,33] Takano and colleagues found that all 31 Cypher stents evaluated exhibited at least one malapposed strut at three months after implantation. At a median of nine months following implantation, Gonzalo et al describe that 75% of lesions in patients with ST-elevation myocardial infarction and 25% of lesions in patients with unstable (UAP) or stable angina (SAP) had at least one malapposed strut after implantation of four different DES. Similarly, Kubo et al found by serial examination of 55 patients (24 UAP/31 SAP) immediately after implantation of Cypher stents

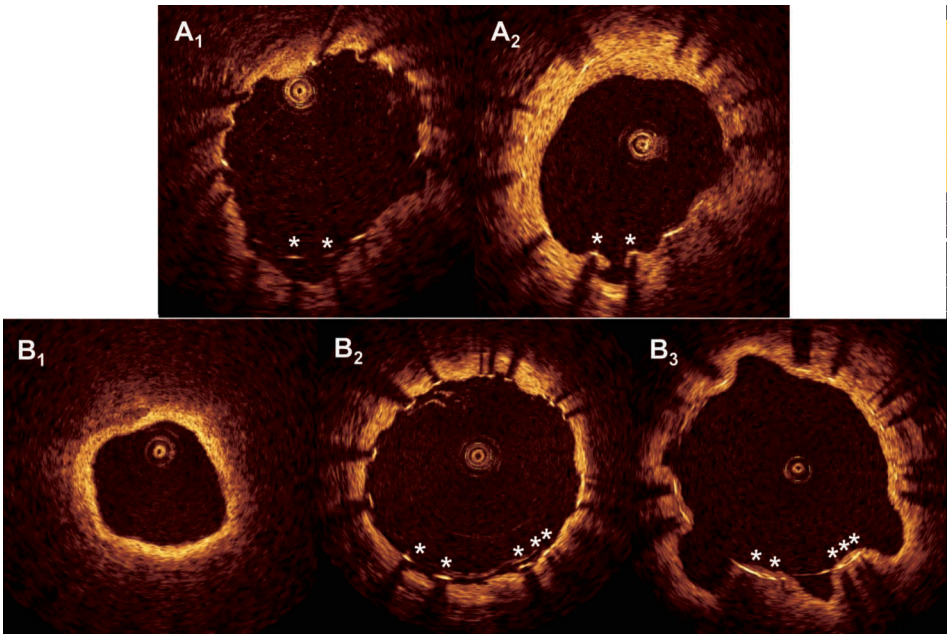

Figure 2. *Evolution of protruding struts. The cross-sections come from two patients (A and B) with protruding struts at follow-up (A2 and B3) where a baseline evaluation was available. Panels A1 and B2 show the matched cross-sections immediately after stent implantation. The protruding struts (asterisks) in A2 were malapposed at baseline (panel A1), possibly with subsequent fibrin deposition and/or neointimal healing. As opposed to this, the protruding struts in panel B3 were apposed to a regular lumen contour (panel B2) after implantation, without any evidence of thrombus in the examination before stent implantation (panel B1). The lumen contour thus seemed to have undergone positive remodelling at follow-up. Stent areas were similar at abseline and follow-up.*

and at nine months follow-up, that malapposed struts were more frequent in the UAP compared to SAP group. In addition, the rate of lesions with at least one malapposed strut decreased from baseline to follow-up (67% vs. 32%, and 33% vs. 4% for UAP and SAP, respectively). In the present study, 14% of lesions displayed malapposed struts and 29% of lesions malapposed and/or protruding struts at a median of 18 months follow-up, which is in line with the findings of Kubo et al. In a recent report, Guagliumi et al described a type of "protruding" struts, which were more frequent in DES compared to BMS.[33] These struts differ, however, methodologically from the ones described here, as we only included in this category struts that protruded into the lumen more than the actual strut thickness. Using a similar definition, emerging data from the SIRTAX-LATE trial suggest that 38% of lesions with first-generation DES display these struts at 5-year follow-up.[38] Nevertheless, the rate of malapposed/protruding struts for different stent types, in different clinical settings and at different time points, needs further clarification in larger studies.

CLINICAL IMPORTANCE OF MALAPPOSED AND PROTRUDING STRUTS

We observed no occurrence of stent thrombosis at late follow-up after OCT examination. However, 74% of our patients were prescribed dual antiplatelet therapy during this time. In a recent meta-analysis, late stent malapposition evaluated by IVUS was associated with LST.[39] Cook et al found stent malapposition in 77% of patients with LST, as opposed to 12% of patients routinely examined at eight months following stent implantation without this complication at two years.[3] Out of the 13 patients with LST, only one was treated with both aspirin and clopidogrel at the time of the event (no report of the clopidogrel use in the control group). Several case reports describe the occurrence of LST after discontinuation of antiplatelet therapy, with or without angiographic or ultrasonic signs of malapposition. Due to the insufficient resolution of IVUS, the extent of strut coverage in relation to stent apposition has not been possible to evaluate adequately in these studies. It remains to be settled whether OCT-detected strut malapposition and protrusion together with evaluation of the degree of strut coverage, may be of additional value for predicting LST.

LIMITATIONS

Limitations of this study include the lack of a reference OCT examination at the time of the index procedure, and thereby the inability to differentiate between persistent and acquired malapposition. Moreover, the patient population was small and heterogeneous: stent implantation included both BMS and DES, and OCT follow-up was performed at different time points. Further, it cannot be excluded that strut apposition might have changed during the extended follow-up, and that this, together with the prolonged clopidogrel therapy could have influenced the natural clinical course of the studied stents.

Conclusion

Clinical characteristics at stent implantation such as ACS and major periprocedural dissections seem to influence strut apposition, which in turn may play a role in stent healing. The present study supports the concept that protruding struts may have more in common with malapposed than with well apposed struts. The incidence, as well as the pathophysiology and clinical importance of protruding struts, remains to be settled.

Conflict of interest statement

The authors have no conflict of interest to declare.

References

1. Serruys PW, Degertekin M, Tanabe K, Abizaid A, Sousa JE, Colombo A, Guagliumi G, Wijns W, Lindeboom WK, Ligthart J, de Feyter PJ, Morice MC. Intravascular ultrasound findings in the multicenter, randomized, double-blind RAVEL (RAndomized study with the sirolimus-eluting VElocity balloon-expandable stent in the treatment of patients with de novo native coronary artery Lesions) trial. *Circulation* 2002;106:798-803.

2. Shah VM, Mintz GS, Apple S, Weissman NJ. Background incidence of late malapposition after bare-metal stent implantation. *Circulation* 2002;106:1753-1755.

3. Cook S, Wenaweser P, Togni M, Billinger M, Morger C, Seiler C, Vogel R, Hess O, Meier B, Windecker S. Incomplete stent apposition and very late stent thrombosis after drug-eluting stent implantation. *Circulation* 2007;115:2426-2434.

4. Joner M, Finn AV, Farb A, Mont EK, Kolodgie FD, Ladich E, Kutys R, Skorija K, Gold HK, Virmani R. Pathology of drug-eluting stents in humans: delayed healing and late thrombotic risk. *J Am Coll Cardiol* 2006;48:193-202.

5. Ako J, Morino Y, Honda Y, Hassan A, Sonoda S, Yock PG, Leon MB, Moses JW, Bonneau HN, Fitzgerald PJ. Late incomplete stent apposition after sirolimus-eluting stent implantation: a serial intravascular ultrasound analysis. *J Am Coll Cardiol* 2005;46: 1002-1005.

6. Hoffmann R, Morice MC, Moses JW, Fitzgerald PJ, Mauri L, Breithart G, Schofer J, Serruys PW, Stoll HP, Leon MB. Impact of late incomplete stent apposition after sirolimus-eluting stent implantation on 4-year clinical events: intravascular ultrasound analysis deom the multicentre, randomised, RAVEL, E-SIRIUS and SIRIUS trials. *Heart* 2008;94:322-328.

7. Regar E, Schaar JA, Mont E, Virmani R, Serruys PW. Optical coherence tomography. *Cardiovasc Radiat Med* 2003;4:198-204.

8. Suzuki Y, Ikeno F, Koizumi T, Tio F, Yeung AC, Yock PG, Fitzgerald PJ, Fearon WF. In vivo comparison between optical coherence tomography and intravascular ultrasound for detecting small degrees of in-stent neointima after stent implantation. *JACC Cardiovasc Interv* 2008;1:168-173.

9. Radu M, Jorgensen E, Kelbaek H, Helqvist S, Skovgaard L, Saunamaki K. Strut apposition after coronary stent implantation visualised with optical coherence tomography. *EuroIntervention* 2010;6:86-93.

10. Finn AV, Joner M, Nakazawa G, Kolodgie F, Newell J, John MC, Gold HK, Virmani R. Pathological correlates of late drug-eluting stent thrombosis: strut coverage as a marker of endothelialization. *Circulation* 2007;115:2435-2441.

11. Krone RJ, Laskey WK, Johnson C, Kimmel SE, Klein LW, Weiner BH, Cosentino JJ, Johnson SA, Babb JD. A simplified lesion classification for predicting success and complications of coronary angioplasty. Registry Committee of the Society for Cardiac Angiography and Intervention. *Am J Cardiol* 2000;85: 1179-1184.

12. Gonzalo N, Serruys PW, Okamura T, Shen ZJ, Onuma Y, Garcia-Garcia HM, Sarno G, Schultz C, van Geuns RJ, Ligthart J, Regar E. Optical coherence tomography assessment of the acute effects of stent implantation on the vessel wall: a systematic quantitative approach. *Heart* 2009;95:1913-1919.

13. Huber MS, Mooney JF, Madison J, Mooney MR. Use of a morphologic classification to predict clinical outcome after dissection from coronary angioplasty. *Am J Cardiol* 1991;68:467-471.

14. Virmani R, Kolodgie FD, Farb A, Lafont A. Drug eluting stents: are human and animal studies comparable? *Heart* 2003;89: 133-138.

15. Prati F, Zimarino M, Stabile E, Pizzicannella G, Fouad T, Rabozzi R, Filippini A, Pizzicannella J, Cera M, De Caterina R. Does optical coherence tomography identify arterial healing after stenting? An in vivo comparison with histology, in a rabbit carotid model. *Heart* 2008;94:217-221.

16. Nakazawa G, Finn AV, Joner M, Ladich E, Kutys R, Mont EK, Gold HK, Burke AP, Kolodgie FD, Virmani R. Delayed arterial healing and increased late stent thrombosis at culprit sites after drug-eluting stent placement for acute myocardial infarction patients: an autopsy study. *Circulation* 2008;118:1138-1145.

17. Kubo T, Imanishi T, Kitabata H, Kuroi A, Ueno S, Yamano T, Tanimoto T, Matsuo Y, Masho T, Takarada S, Tanaka A, Nakamura N, Mizukoshi M, Tomobuchi Y, Akasaka T. Comparison of vascular response after sirolimus-eluting stent implantation between patients with unstable and stable angina pectoris: a serial optical coherence tomography study. *JACC Cardiovasc Imaging* 2008;1:475-484.

18. Gonzalo N, Barlis P, Serruys PW, Garcia-Garcia HM, Onuma Y, Ligthart J, Regar E. Incomplete stent apposition and delayed tissue coverage are more frequent in drug-eluting stents implanted during primary percutaneous coronary intervention for ST-segment elevation myocardial infarction than in drug-eluting stents implanted for stable/unstable angina: insights from optical coherence tomography. *JACC Cardiovasc Interv* 2009;2:445-452.

19. Stone GW, Ellis SG, Cox DA, Hermiller J, O'Shaughnessy C, Mann JT, Turco M, Caputo R, Bergin P, Greenberg J, Popma JJ, Russell ME. A polymer-based, paclitaxel-eluting stent in patients with coronary artery disease. *N Engl J Med* 2004;350:221-231.

20. Serruys PW, Ong AT, Morice MC, De Bruyne B, Colombo A, Macaya C, Richardt G, Fajadet J, Hamm C, Dawkins K, O'Malley AJ, Bressers M, Donohoe D. Arterial Revascularisation Therapies Study Part II - Sirolimus-eluting stents for the treatment of patients with multivessel de novo coronary artery lesions. *EuroIntervention* 2005;1:147-156.

21. Morice MC, Serruys PW, Sousa JE, Fajadet J, Ban Hayashi E, Perin M, Colombo A, Schuler G, Barragan P, Guagliumi G, Molnar F, Falotico R. A randomized comparison of a sirolimus-eluting stent with a standard stent for coronary revascularization. *N Engl J Med* 2002;346:1773-1780.

22. Morice MC, Colombo A, Meier B, Serruys P, Tamburino C, Guagliumi G, Sousa E, Stoll HP. Sirolimus- vs paclitaxel-eluting stents in de novo coronary artery lesions: the REALITY trial: a randomized controlled trial. *JAMA* 2006;295:895-904.

23. Tanigawa J, Barlis P, Dimopoulos K, Dalby M, Moore P, Di Mario C. The influence of strut thickness and cell design on immediate apposition of drug-eluting stents assessed by optical coherence tomography. *Int J Cardiol* 2009;134:180-188.

24. Finn AV, Nakazawa G, Joner M, Kolodgie FD, Mont EK, Gold HK, Virmani R. Vascular responses to drug eluting stents: importance of delayed healing. *Arterioscler Thromb Vasc Biol* 2007;27: 1500-1510.

25. Templin C, Meyer M, Muller MF, Djonov V, Hlushchuk R, Dimova I, Flueckiger S, Kronen P, Sidler M, Klein K, Nicholls F, Ghadri JR, Weber K, Paunovic D, Corti R, Hoerstrup SP, Luscher TF, Landmesser U. Coronary optical frequency domain imaging (OFDI) for in vivo evaluation of stent healing: comparison with light and electron microscopy. *Eur Heart J* 2010;31:1792-1801.

26. Matsumoto D, Shite J, Shinke T, Otake H, Tanino Y, Ogasawara D, Sawada T, Paredes OL, Hirata K, Yokoyama M. Neointimal coverage of sirolimus-eluting stents at 6-month follow-up: evaluated by optical coherence tomography. *Eur Heart J* 2007;28:961-967.

27. Takano M, Inami S, Jang IK, Yamamoto M, Murakami D, Seimiya K, Ohba T, Mizuno K. Evaluation by optical coherence tomography of neointimal coverage of sirolimus-eluting stent three months after implantation. *Am J Cardiol* 2007;99:1033-1038.

28. Moore P, Barlis P, Spiro J, Ghimire G, Roughton M, Di Mario C, Wallis W, Ilsley C, Mitchell A, Mason M, Kharbanda R, Vincent P, Sherwin S, Dalby M. A randomized optical coherence tomography study of coronary stent strut coverage and luminal protrusion with rapamycin-eluting stents. *JACC Cardiovasc Interv* 2009;2: 437-444.

29. Chen BX, Ma FY, Luo W, Ruan JH, Xie WL, Zhao XZ, Sun SH, Guo XM, Wang F, Tian T, Chu XW. Neointimal coverage of bare-metal and sirolimus-eluting stents evaluated with optical coherence tomography. *Heart* 2008;94:566-570.

30. Kim JS, Jang IK, Kim TH, Takano M, Kume T, Hur NW, Ko YG, Choi D, Hong MK, Jang Y. Optical coherence tomography evaluation of zotarolimus-eluting stents at 9-month follow-up: comparison with sirolimus-eluting stents. *Heart* 2009;95:1907-1912.

31. Ozaki Y, Okumura M, Ismail TF, Naruse H, Hattori K, Kan S, Ishikawa M, Kawai T, Takagi Y, Ishii J, Prati F, Serruys PW. The fate of incomplete stent apposition with drug-eluting stents: an optical coherence tomography-based natural history study. *Eur Heart J;* 2010;31:1470-1476.

32. Barlis P, Regar E, Serruys PW, Dimopoulos K, van der Giessen WJ, van Geuns RJ, Ferrante G, Wandel S, Windecker S, van Es GA, Eerdmans P, Juni P, di Mario C. An optical coherence tomography study of a biodegradable vs. durable polymer-coated limus-eluting stent: a LEADERS trial sub-study. *Eur Heart J* 2010;31:165-176.

33. Guagliumi G, Costa MA, Sirbu V, Musumeci G, Bezerra HG, Suzuki N, Matiashvili A, Lortkipanidze N, Mihalcsik L, Trivisonno A, Valsecchi O, Mintz GS, Dressler O, Parise H, Maehara A, Cristea E, Lansky AJ, Mehran R, Stone GW. Strut coverage and late malapposition with paclitaxel-eluting stents compared with bare metal stents in acute myocardial infarction. Optical coherence tomography substudy of the Harmonizing outcomes with revascularization and stents in acute myocardial infarction (HORIZONS-AMI) trial. *Circulation* 2011;123:274-281.

34. Hong MK, Mintz GS, Lee CW, Kim YH, Lee SW, Song JM, Han KH, Kang DH, Song JK, Kim JJ, Park SW, Park SJ. Incidence, mechanism, predictors, and long-term prognosis of late stent malapposition after bare-metal stent implantation. *Circulation* 2004;109:881-886.

35. Hong MK, Mintz GS, Lee CW, Park DW, Park KM, Lee BK, Kim YH, Song JM, Han KH, Kang DH, Cheong SS, Song JK, Kim JJ, Park SW, Park SJ. Late stent malapposition after drug-eluting stent implantation: an intravascular ultrasound analysis with long-term follow-up. *Circulation* 2006;113:414-419.

36. Mintz GS, Shah VM, Weissman NJ. Regional remodeling as the cause of late stent malapposition. *Circulation* 2003;107:2660-2663.

37. Tanabe K, Serruys PW, Degertekin M, Grube E, Guagliumi G, Urbaszek W, Bonnier J, Lablanche JM, Siminiak T, Nordrehaug J, Figulla H, Drzewiecki J, Banning A, Hauptmann K, Dudek D, Bruining N, Hamers R, Hoye A, Ligthart JM, Disco C, Koglin J, Russell ME, Colombo A. Incomplete stent apposition after implantation of paclitaxel-eluting stents or bare metal stents: insights from the randomized TAXUS II trial. *Circulation* 2005;111:900-905.

38. Räber L, Baumgartner S, Garcia-Garcia HM, Kalesan B, Justiz J, Pilgrim T, Moschovitis A, Meier B, Serruys PW, Jüni P, Windecker S. Vascular healing response five years after implantation of first generation DES. The SIRTAX-LATE optical coherence tomography study. EuroPCR 2011, Late breaking science session, 19th May 2011.

39. Hassan AK, Bergheanu SC, Stijnen T, van der Hoeven BL, Snoep JD, Plevier JW, Schalij MJ, Wouter Jukema J. Late stent malapposition risk is higher after drug-eluting stent compared with bare-metal stent implantation and associates with late stent thrombosis. *Eur Heart J* 2009;31:1172-1180.

CHAPTER 3 THE APPLICATION OF OPTICAL COHERENCE TOMOGRAPHY IN THE CLINICAL EVALUATION OF THE ACUTE EFFECTS AND VASCULAR REACTIONS TO METALLIC STENT IMPLANTATION

3.1 Coronary evaginations are associated with positive vessel remodelling and are nearly absent following implantation of newer-generation drug-eluting stents: An optical coherence tomography and intravascular ultrasound study.

Radu MD*, Räber L*, Kalesan B, Muramatsu T, Kelbæk H, Heo J, Jørgensen E, Helqvist S, Farooq V, Brugaletta S, Garcia-Garcia HM, Jüni P, Saunamäki K, Windecker W, Serruys PW.

European Heart Journal. 2014;35:795-807.

Coronary evaginations are associated with positive vessel remodelling and are nearly absent following implantation of newer-generation drug-eluting stents: an optical coherence tomography and intravascular ultrasound study

Maria D. Radu[1,2†], Lorenz Räber[1,3†], Bindu Kalesan[4], Takashi Muramatsu[1], Henning Kelbæk[2], Jungho Heo[1], Erik Jørgensen[2], Steffen Helqvist[2], Vasim Farooq[1], Salvatore Brugaletta[1], Hector M. Garcia-Garcia[5], Peter Jüni[4], Kari Saunamäki[2], Stephan Windecker[3], and Patrick W. Serruys[1]*

[1]Thoraxcenter, Erasmus University Medical Centre, Ba583a, 's-Gravendijkwal 230, 3015 CE Rotterdam, Netherlands; [2]Rigshospitalet, Copenhagen University Hospital, Copenhagen, Denmark; [3]Department of Cardiology, Bern University Hospital, Bern, Switzerland; [4]Institute of Social and Preventive Medicine, Bern University, Bern, Switzerland; and [5]Cardialysis BV, Rotterdam, Netherlands

Received 16 August 2012; revised 11 June 2013; accepted 6 August 2013

Objectives	The purpose of this study was to assess the occurrence, predictors, and mechanisms of optical coherence tomography (OCT)-detected coronary evaginations following drug-eluting stent (DES) implantation.
Background	Angiographic ectasias and aneurysms in stented segments have been associated with a risk of late stent thrombosis. Using OCT, some stented segments show coronary evaginations reminiscent of ectasias.
Methods	Evaginations were defined as outward bulges in the luminal contour between struts. They were considered major evaginations (MEs) when extending $\geq$3 mm along the vessel length, with a depth $\geq$10% of the stent diameter. A total of 228 patients who had sirolimus (SES)-, paclitaxel-, biolimus-, everolimus (EES)-, or zotarolimus (ZES)-eluting stents implanted in 254 lesions, were analysed after 1, 2, or 5 years; and serial assessment using OCT and intravascular ultrasound (IVUS) was performed post-intervention and after 1 year in 42 patients.
Results	Major evaginations occurred frequently at all time points in SES ($\sim$26%) and were rarely seen in EES (3%) and ZES (2%, $P = 0.003$). Sirolimus-eluting stent implantation was the strongest independent predictor of ME [adjusted OR (95% CI) 9.1 (1.1–77.4), $P = 0.008$]. Malapposed and uncovered struts were more common in lesions with vs. without ME (77 vs. 25%, $P < 0.001$ and 95 vs. 20%, $P < 0.001$, respectively) as was thrombus [49 vs. 14%, OR 7.3 (95% CI: 1.7–31.2), $P = 0.007$]. Post-intervention intra-stent dissection and protrusion of the vessel wall into the lumen were associated with an increased risk of evagination at follow-up [OR (95% CI): 2.9 (1.8–4.9), $P < 0.001$ and 3.3 (1.6–6.9), $P = 0.001$, respectively]. In paired IVUS analyses, lesions with ME showed a larger increase in the external elastic membrane area (20% area change) compared with lesions without ME (5% area change, $P < 0.001$).
Conclusion	Optical coherence tomography-detected MEs are a specific morphological footprint of early-generation SES and are nearly absent in newer-generation ZES and EES. Evaginations appear to be related to vessel injury at baseline; are associated with positive vessel remodelling; and correlate with uncoverage, malapposition, and thrombus at follow-up.

Keywords Optical coherence tomography • Intravascular ultrasound • Coronary evaginations • Early-generation drug-eluting stents • Newer-generation drug-eluting stents • Positive remodelling • Malapposition • Uncovered stent struts

† M.D.R. and L.R. contributed equally to this work.

*Corresponding author. Tel: +31 104635260, Fax: +31 104369154, Email: p.w.j.c.serruys@erasmusmc.nl

Introduction

Early-generation drug-eluting stents (DESs) have been associated with an increased risk of very late stent thrombosis (ST) due to delayed arterial healing with evidence of prolonged inflammation, resulting in incomplete endothelialization and acquired malapposition.[1,2] Owing to an ultrahigh resolution (10 μm), optical coherence tomography (OCT) allows an *in vivo* histology-like evaluation of coronary arteries and implanted devices, including the identification of uncovered and malapposed struts.[3,4] Using OCT, it has been observed that some stented segments show outward vessel bulging—'coronary evaginations'—of the luminal contour between struts during the follow-up.[5,6] Three-dimensional (3D) visualization of these segments suggests an ectatic appearance of the vessel wall reminiscent of that seen in angiographic ectasias and aneurysms, which were previously shown to be associated with cardiovascular adverse events.[7,8] Although both drugs and polymers of DES have been suspected as culprits for these changes, the specific mechanisms of the luminal enlargement remain unknown and can only be determined with serial invasive assessment. At present, there are no data on the occurrence, predictors, and mechanisms of OCT-detected coronary evaginations following implantation of early- and newer-generation DES. The objectives of the present study were therefore to assess evaginations using OCT at follow-up in a large cohort of patients; and to investigate the underlying mechanism by serial investigations with OCT and intravascular ultrasound (IVUS) in a subset of patients.

Methods

Study population

The pooled analysis included OCT acquisitions from the LEADERS-, RESOLUTE-, and SIRTAX-LATE OCT substudies, and from the Copenhagen OCT registry, employing the following stents: Cypher Select® (Cordis, Johnson and Johnson, Warren, NJ, USA); Taxus Express® (Boston Scientific, Natick, MA, USA); Endeavor Resolute® (Medtronic, Inc., Santa Rosa, CA, USA); Xience V® (Abbott Vascular, Santa Clara, CA, USA); and Biomatrix® (Biosensors, Inc., Newport Beach, CA, USA). The design and eligibility criteria for LEADERS-, RESOLUTE-, and SIRTAX-LATE OCT substudies are described in detail elsewhere.[6,9,10] The Copenhagen OCT registry was a single-centre prospective non-randomized evaluation of strut coverage and apposition at 12-month follow-up in relation to apposition at baseline, using the Cypher Select®, Taxus Express®, and Endeavor Resolute® stents. Patients were eligible if they had ≥1 lesion with >50% diameter stenosis in a native coronary artery, with a reference vessel diameter between 2.25 and 4.0 mm. Exclusion criteria were ST-segment elevation myocardial infarction (MI), left ventricular ejection fraction <30%, renal insufficiency (creatinine >133 μmol/L), and lesion location in the left main stem or bypass graft. Optical coherence tomography and IVUS were performed after a satisfactory angiographic result, defined as a residual diameter stenosis <20% and thrombus in MI flow grade 3, and imaging with both modalities was repeated at 1-year follow-up. A total of 56 consecutive patients were included at baseline out of which eight withdrew consent for follow-up, and two were excluded due to system failure or insufficient quality for analysis. *Figure 1* shows an overview of the number of patients, lesions, and stent types included in each cohort, and the time point of OCT acquisition.

Out of the 46 patients with 48 lesions from the Copenhagen OCT registry, 43 patients with 45 lesions were available with complete serial OCT assessment at baseline and follow-up. Out of these, 40 patients with 42 lesions had a serial IVUS assessment. All studies were conducted in accordance with the Declaration of Helsinki and approved by the ethical committees of the involved centres. All patients provided written informed consent prior to the enrolment.

Optical coherence tomography and intravascular ultrasound acquisitions

Optical coherence tomography-images were acquired with commercially available time-domain M2 and M3 systems; and the frequency-domain C7 system from LightLab/St Jude (Westford, MA, USA) at a frame rate of 15.6, 20, and 100 frames/s; and a pullback speed of 1, 3, and 10 mm/s; with the M2, M3, and C7, respectively. Acquisition with occlusive (M2) and non-occlusive (M3 and C7) techniques was described previously.[11] Intravascular ultrasound images were acquired with the Atlantis SR Pro 40 MHz catheter and iLab system (Boston Scientific, Natick, MA, USA) at a frame rate of 30 frames/s and pullback speed of 0.5 mm/s, according

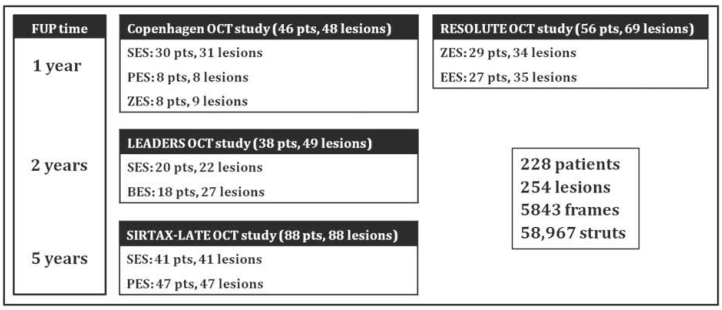

Figure 1 Overview of the optical coherence tomography data used for the pooled analysis. FUP, follow-up; SES, sirolimus-eluting stent; PES, paclitaxel-eluting stent; ZES, zotarolimus-eluting stent; EES, everolimus-eluting stent; BES, biolimus-eluting stent.

to accepted standards. As for serial investigations, the same imaging systems were used at baseline and follow-up.

Optical coherence tomography image analysis

The region of interest included the stented segments which were analysed systematically at 1 mm intervals according to corelab standards (Cardialysis, BV, Rotterdam, The Netherlands). The methodology is shown in *Figure 2A*. The lumen- and stent area were assessed as previously reported.[12] *Malapposition* was considered to be present when the distance from the endoluminal strut border to the lumen contour was larger than the sum of strut metal + polymer thickness, resulting in cut-offs of ≥160 μm for Cypher, ≥160 μm for Taxus Express, ≥100 μm for Endeavor Resolute, ≥90 μm for Xience V, and ≥130 μm for the Biomatrix stent.[10,12,13] In case of malapposition, the incomplete

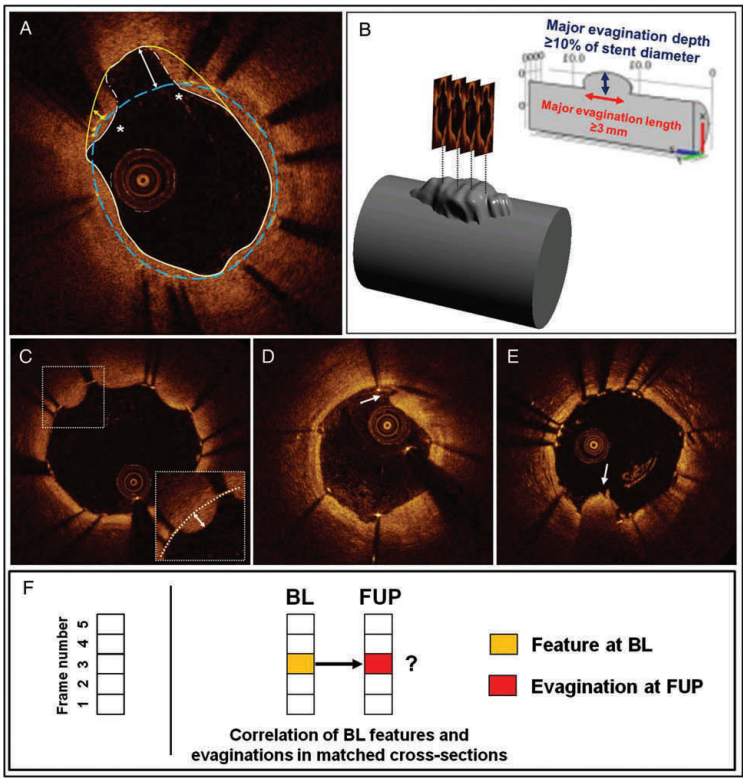

Figure 2 Overview of optical coherence tomography image analysis. (*A*) Frame-level analysis included the assessment of the stent area (blue-broken trace) and lumen area (white trace). Evaginations were defined as bulges in the luminal contour between struts with a maximum depth (white double-headed arrow) exceeding the actual strut thickness. Evagination areas were delineated by the stent contour towards the centre of the lumen and the lumen contour in the opposite direction (broken trace along the luminal contour at 11 o'clock). Struts projecting into the lumen without separation from the vessel wall were defined as protruding when the distance (yellow double-headed arrow) from the stent area trace to a 'lumen help line' (yellow trace extrapolated between deepest point of evaginations and lumen contour) exceeded the actual strut thickness. (*B*) A three-dimensional reconstruction of an evagination. Evaginations were considered major when extending ≥3 mm longitudinally, with a depth ≥10% of the stent diameter. Prolapse (*C*) was defined as convex-shaped tissue projecting into the lumen between struts without disruption of the luminal continuity, and registered only when the distance from the stent area trace (white-dotted line) to the maximum point of prolapse was ≥150 μm. Intra-stent dissections (*D*) were defined as disruptions of the luminal vessel contour within the stented segment, whereas tissue protrusion (*E*) was defined as a mass with an irregular surface attached to the vessel wall or struts and protruding into the lumen. Various features at baseline (i.e. prolapse, intra-stent dissection, tissue protrusion, and malapposed struts) were cross-correlated with the presence of evaginations in matched cross-sections at follow-up (*F*).

stent apposition (ISA) area was measured. Struts projecting into the lumen without obvious separation from the vessel wall were labelled *protruding* when the distance from the strut marker to a 'lumen help line' exceeded that of the actual strut thickness, using the same cut-offs as for malapposition.[5,6] The 'lumen help line' was drawn by extrapolating a trace line between the deepest points in evagination/s and the luminal vessel contour laterally. Struts within overlapped segments and those overlying side branch ostia were excluded from the analysis. Struts were considered *uncovered* if any part of the strut was visibly exposed to the lumen, and covered if a layer of tissue was identified above the struts.[3]

A *coronary evagination* (*Figure 2A*) was defined as the presence of an outward bulge in the luminal vessel contour between apposed struts with a maximum *depth* of the bulge exceeding that of the actual strut thickness, as measured semi-automatically from the deepest point in the bulge to the stent area trace using the thickness-ruler function.[6] The same cut-offs as for malapposition were used. For each evagination, we assessed the *evagination area* defined as the area limited by the stent contour towards the centre of the lumen and the lumen contour in the opposite direction. Imaging of evaginations with both time- and Fourier-domain OCT systems was performed in a few cases, excluding any influence of OCT system on the appearance of evaginations.

Evaginations may extend over several consecutive cross-sections, giving the vessel an ectatic appearance by 3D reconstruction (*Figure 2B*). Thus, evaginations can be characterized both at the 2D cross-sectional level, and along the length of the stented segment. We assessed the presence of *major evagination* (ME), defined as the occurrence of cross-sectional evagination in $\geq$3 adjacent frames (i.e. minimum 3 mm of length) with a minimal evagination depth of 10% of the nominal stent diameter. Evagination areas of the various cross-sections belonging to a ME were assumed to be constant 0.5 mm proximal and distal to the analysed cross-section in order to calculate evagination volumes for each 1 mm segment. If evaginations were present in adjacent cross-sections, they were assumed to be in a continuum, and their volumes were summed up to calculate the total *evagination volume*. In addition, we assessed the presence of thrombus defined as a mass $\geq$100 μm in diameter with an irregular surface attached to the vessel wall or struts and protruding into the lumen.

Table 1 Baseline demographics and baseline patient and lesion level predictors of major evaginations adjusted for time to follow-up

Characteristics	Entire cohort	Major evagination at follow-up		Crude OR (95% CI)	*P*-value	Adj OR (95% CI)	*P*-value
	n (%)	Yes, *n* (%)	No, *n* (%)				
No. of patients	228	31	197				
Age	60.0 ± 10.4	59.2 ± 11.0	60.2 ± 10.3	1.00 (0.96–1.04)	1.00	1.00 (0.96–1.05)	0.89
Male gender	179 (78.5)	24 (77.2)	155 (78.7)	0.88 (0.35–2.26)	0.78	0.89 (0.33–2.41)	0.82
Hypertension	127 (55.7)	15 (48.4)	112 (56.9)	0.77 (0.35–1.69)	0.52		
Hyperlipidaemia	153 (67.1)	20 (64.5)	133 (67.5)	0.87 (0.38–2.00)	0.74		
Diabetes mellitus	44 (19.3)	4 (12.9)	40 (20.3)	0.58 (0.19–1.80)	0.35		
Current/previous smoker	87 (38.2)	11 (35.5)	76 (38.6)	0.75 (0.33–1.71)	0.49		
Previous MI	58 (25.7)	6 (19.4)	52 (26.7)	0.68 (0.26–1.82)	0.45		
LVEF $\leq$50	42 (18.4)	12 (38.7)	30 (15.2)	3.20 (1.32–7.72)	0.01	2.71 (1.03–7.16)	0.044
STEMI	48 (21.1)	9 (29.0)	39 (19.8)	1.89 (0.74–4.82)	0.19	1.48 (0.49–4.44)	0.48
Stent type					0.0055		0.0084
EES (reference)	27 (11.8)	1 (3.2)	26 (13.2)	Reference		Reference	
PES	55 (24.1)	4 (12.9)	51 (25.9)	2.06 (0.19–22.48)		1.96 (0.17–22.53)	
BES	18 (7.9)	2 (6.5)	16 (8.1)	3.26 (0.27–39.38)		3.80 (0.31–46.61)	
ZES	37 (16.2)	1 (3.2)	36 (18.3)	0.72 (0.04–12.08)		0.83 (0.05–14.01)	
SES	91 (40.0)	23 (74.2)	68 (34.5)	8.84 (1.07–72.97)		9.05 (1.06–77.35)	
Multivessel disease	23 (13.4)	3 (10.3)	20 (14.0)	0.61 (0.15–2.57)	0.51		
No. of lesions	254	33	221				
Target vessel					0.15		
Left main (reference)	3 (1.2)	1 (3.1)	2 (0.9)	Reference			
LAD	101 (40.0)	7 (21.9)	94 (43.1)	0.16 (0.01–2.45)	0.19		
Circumflex	57 (22.8)	7 (21.9)	50 (22.9)	0.20 (0.01–3.26)	0.26		
RCA	88 (35.2)	17 (53.1)	71 (32.6)	0.47 (0.03–6.93)	0.58		
Graft	1 (0.4)	0 (0)	1 (0.5)	0.16 (0.01–2.45)	0.19		
Stent diameter[a]	3.0 ± 0.4	3.1 ± 0.4	3.0 ± 0.4	7.05 (0.42–119.3)	0.18		
Total stented length[a]	21.6 ± 13.9	22.6 ± 10.4	21.4 ± 14.3	1.00 (0.91–1.11)	0.96		
Stents per lesion[a]	1.4 ± 0.7	1.4 ± 0.8	1.4 ± 0.7	0.91 (0.07–11.12)	0.94		

[a]Expressed as means ± SD.

The Copenhagen OCT registry included OCT examinations at baseline and 1-year follow-up. Cross-sections at baseline and follow-up were matched on the basis of distance from stent borders and the presence of anatomical landmarks such as side branches. This allowed the following serial assessments at the cross-sectional level (*Figure 2C–E*):

At baseline, we assessed the presence of tissue prolapse, intra-stent dissection and tissue protrusion. *Tissue prolapse* was defined as convex-shaped tissue with a regular surface protruding into the lumen between adjacent struts without disruption of the continuity of the luminal vessel surface.[14] The tissue was considered prolapsing only when the distance from the stent area trace to the maximum point of prolapse was $\geq$150 μm, chosen arbitrarily since some degree of prolapse can be seen in most cross-sections. *Intra-stent dissections* were defined as disruptions of the luminal vessel contour within the stented segment, whereas *tissue protrusion* was defined as a mass with an irregular surface attached to the vessel wall or struts and protruding into the lumen. These features as well as the presence of $\geq$1 malapposed strut were then correlated with the presence of evagination at the time of serial follow-up, in matched cross-sections (*Figure 2F*).

Intravascular ultrasound image analysis

Intravascular ultrasound pullbacks were analysed off-line using the QCU-CMS software (Medis, Leiden, The Netherlands) at standard 1 mm intervals, in the same region of interest as for OCT, following the international consensus.[15] Accordingly, we measured the lumen-, stent-, and external elastic membrane area, the latter referred to as vessel area. The plaque and media (P&M) area was calculated as (vessel area – stent area – lumen area outside the stent), and the plaque burden as (P&M area/vessel area) × 100. Positive vessel remodelling was defined as an increase in the vessel area from baseline to follow-up.

Statistical analysis

We used Bayesian hierarchical random-effects model based on Markov chain Monte–Carlo simulation methods[16] with non-informative priors, to compare OCT features such as strut malapposition, protrusion, and coverage between lesions with ME and lesions without. The model included random-effects at the level of cross-sections and lesions, accounting for the correlation of characteristics of cross-sections within lesions, and assigning analytical weights to each lesion depending on the number of struts or cross-sections observed per lesion. Continuous characteristics of lesions such as lumen area and stent area were compared between lesions with vs. without ME using frequentist mixed maximum-likelihood regression models with study cohort, type of stent, patient, and/or lesion as random intercepts. Means and standard deviations were estimated from predicted values. To determine the association of characteristics of lesions and patients at baseline with the presence or absence of ME at follow-up, we used mixed maximum logistic regression models adjusted for time to follow-up (1, 2, or 5 years) with study cohort, type of stent and lesion specified as random intercepts. The same model was used to analyse stent and lumen area over time as assessed with OCT and IVUS in the Copenhagen OCT registry. Mixed maximum logistic regression models with type of stent, patient, and lesion as random intercepts were used to assess the association of the baseline cross-sectional OCT features intra-stent dissection, strut malapposition, tissue protrusion, and prolapse with cross-sectional evagination at follow-up, with univariable and multivariable mutual adjustments for all four features. Statistical analyses were performed using WinBUGS version 1.4.3 (Imperial College and MRC, UK) and Stata, version 11.0 (StataCorp, College Station, TX, USA).

Results

Incidence and extent of evaginations

A total of 228 patients with 254 lesions containing 5843 frames with 58 967 struts were included in the analysis (*Figure 1*). Overall, 75.8% of patients were male and 19.3% had diabetes (*Table 1*). The clinical setting at stent implantation was STEMI in 21.1% of cases, and 40.0% of patients received a SES. Overall, a median (IQR) of 19 (15–26) cross-sections and 183 (140–273) struts were analysed per lesion. Out of 254 lesions, 152 (59.8%) had at least one cross-section with evagination, and 33 (13.0%) lesions contained at least one ME. Out of the 33 lesions with ME, 23 had a SES implanted, four a PES, four a BES, one a ZES, and one an EES. The frequency of cross-sectional and ME according to stent type and time point of implantation are shown in *Table 2*. Both 'any' cross-sectional and ME were more frequent in the SES group when compared with the PES-, ZES-, and EES-groups. The frequency of ME was low for lesions treated with ZES and EES at 1 year, and PES at 5 years.

Table 3 shows the mean evagination- and ISA volumes per lesion in lesions with any cross-sectional evagination and lesions with ME according to stent type and time since implantation. Evagination volumes were consistently larger for the SES group when compared with the other stents. Incomplete stent apposition volumes were similarly larger in SES at 2 and 5 years. Evaluating SES alone, there was a trend for an increase in ISA volumes from 1 to 2 to 5 years (all lesions: $P = 0.024$; lesions with any cross-sectional evagination:

Table 2 Occurrence of cross-sectional and major evaginations stratified by stent type and time to follow-up

Lesions	SES	PES	BES	ZES	EES	*P*-value
No. of lesions with any evagination/total no. of lesions (%)						
Year 1	22 /31 (71)	4 /8 (50)		25 /43 (58)	13 /35 (37)	0.045
Year 2	16/22 (73)		15 /27 (56)			0.25
Year 5	29 /41 (71)	28/47 (60)				0.37
No. of lesions with major evagination/total no. of lesions (%)						
Year 1	8/31 (26)	1 /8 (13)		1 /43 (2)	1 /35 (3)	0.003
Year 2	4/22 (18)		4 /27 (15)			1.00
Year 5	11/41 (27)	3/47 (6)				0.02

Table 3 **Evagination and incomplete stent apposition volumes at the lesion level in lesion with any and major evaginations by stent type and time to follow-up**

	SES	PES	BES	ZES	EES	*P*-value
At Year 1						
Lesions with any evagination						
EV	2.24 ± 1.68 (22)	0.50 ± 0.72 (4)		0.38 ± 1.79 (25)	0.42 ± 1.29 (13)	0.002
ISAV	0.20 ± 2.12 (22)	3.00 ± 0.90 (4)		0.76 ± 2.25 (25)	2.20 ± 1.63 (13)	0.30
Lesions with ME						
EV	24.20 ± 1.77 (8)	5.31 ± 0.59 (1)		4.42 ± 0.59 (1)	10.28 ± 0.59 (1)	0.39
ISAV	0.54 ± 1.64 (8)	12.10 ± 0.58 (1)		0.26 ± 0.58 (1)	6.23 ± 0.58 (1)	<0.001
All lesions						
ISAV	0.14 ± 1.80 (31)	1.51 ± 0.92 (8)		0.57 ± 2.12 (43)	0.92 ± 1.92 (35)	0.17
At Year 2						
Lesions with any evagination						
EV	2.47 ± 2.52 (16)		0.57 ± 2.44 (15)			0.03
ISAV	1.54 ± 3.32 (16)		0.19 ± 3.21 (15)			0.24
Lesions with ME						
EV	30.40 ± 1.30 (4)		4.08 ± 1.19 (4)			0.01
ISAV	5.22 ± 5.15 (4)		0.79 ± 5.15 (4)			0.21
All lesions						
ISAV	1.34 ± 2.69 (22)		0.12 ± 2.98 (27)			0.12
At Year 5						
Lesions with any evagination						
EV	2.54 ± 1.58 (29)	0.72 ± 1.55 (28)				<0.001
ISAV	3.81 ± 6.69 (29)	1.42 ± 6.57 (28)				0.10
Lesions with ME						
EV	11.80 ± 0.59 (11)	4.40 ± 0.25 (3)				0.008
ISAV	7.47 ± 13.52 (11)	1.91 ± 7.06 (3)				0.41
All lesions						
ISAV	2.72 ± 5.49 (41)	1.04 ± 5.88 (47)				0.09

ME, major evagination; EV, evagination volume; ISAV, incomplete stent apposition volume. Volumes are expressed as means ± SD (no. of lesions) mm^3 and predicted from maximum-likelihood models.

$P = 0.016$; lesions with ME: $P = 0.14$). The average depths and lengths of cross-sectional and ME are presented in the appendix.

Predictors of major evaginations

Table 1 presents patient and lesion characteristics and their association with ME. The indication for stent implantation was STEMI in 29.0% of patients with and 19.8% of patients without ME ($P = 0.19$). Left ventricular ejection fraction ≤50% was more frequent in patients with compared with those without ME, and the use of SES emerged as an independent predictor for the presence of ME.

Pooled optical coherence tomography analysis

The quantitative results of the OCT analysis at the time of follow-up are shown in *Table 4*. Minimal and average lumen and stent areas were larger in lesions with when compared with those without ME. Malapposed, protruding, and uncovered struts were more common in lesions with than without ME, and found in 77.2 vs. 24.9% ($P < 0.001$), 97.0 vs. 82.1% ($P < 0.001$), and 94.6 vs. 20.1% ($P < 0.001$) lesions, respectively. Similarly, the proportion of lesions with ≥10% malapposed and uncovered struts was significantly larger in the ME group. The average (means ± SD) thickness of strut coverage was smaller in lesions with MEs compared with those without this feature [0.11 ± 0.29 vs. 0.14 ± 0.23 mm; difference (95% CI): −0.03 (−0.06 to −0.004) mm, $P = 0.022$]. At follow-up, thrombus was more frequent in lesions with 'any' evagination [28.0 vs. 5.9%, OR (95% CI): 6.1 (2.0–17.1), $P = 0.001$] as well as ME [48.5 vs. 14.0%, OR (95% CI): 7.3 (1.7–31.5), $P = 0.007$].

Serial optical coherence tomography and intravascular ultrasound analyses

Quantitative serial OCT results are shown in *Table 5*. All lesions with ME were implanted with SES. The stent and lumen areas were larger

Table 4 **Results of follow-up optical coherence tomography analysis**

	Major evagination at follow-up		Difference (95% CI)	*P*-value
	Yes	No		
Lesions analysed, *n*	33	221		
Frames analysed, *n*	804	5039		
Struts analysed, *n*	8385	50,582		
Lumen area, mm^{2a}	8.34 ± 5.90	6.44 ± 2.50	1.90 (1.08–2.72)	<0.001
Minimal lumen area, mm^{2a}	5.99 ± 5.60	4.88 ± 2.20	1.12 (0.34–1.89)	0.005
Stent area, mm^{2a}	8.50 ± 6.10	7.37 ± 3.00	1.13 (0.33–1.93)	0.006
Minimal stent area, mm^{2a}	6.71 ± 6.40	5.88 ± 3.70	0.83 (0.03–1.62)	0.04
Strut type, % (95% CrI)				
Malapposed struts[b]				
Malapposed struts per lesion	1.07 (0.41–2.62)	0.11 (0.06–0.17)	0.96 (0.31–2.52)	<0.001
Lesions with ≥1	77.20 (52.80–92.80)	24.9 (15.40–34.90)	51.80 (25.40–72.60)	<0.001
Lesions with ≥10%	5.53 (0.86–19.30)	0.18 (0.02–1.19)	5.24 (0.70–18.90)	0.001
Protruding struts[b]				
Protruding struts per lesion	3.04 (1.52–5.87)	0.11 (0.06–0.17)	2.92 (1.42–5.77)	<0.001
Lesions with ≥1	97.00 (86.70–99.60)	82.1 (72.30–89.60)	14.30 (4.04–23.80)	0.01
Lesions with ≥10%	9.34 (2.03–27.10)	4.93 (1.93–10.80)	4.09 (-3.42–21.20)	0.37
Uncovered struts[b]				
Uncovered struts per lesion	3.82 (2.12–6.82)	1.39 (1.06–1.79)	2.43 (0.70–5.46)	0.002
Lesions with ≥1	94.60 (81.00–99.10)	20.10 (11.40–30.00)	74.00 (56.00–85.80)	<0.001
Lesions with ≥10%	5.59 (0.85–19.30)	<0.01 (<0.01–0.16)	5.57 (0.84–19.30)	<0.001

Lumen and stent areas are expressed as means ± SD.
CrI, credibility interval.
[a]Using traditional mixed maximum-likelihood model.
[b]Using Bayesian hierarchical 2-level logistic regression model.

Table 5 **Quantitative serial optical coherence tomography results of the stented segment**

	Major evagination at follow-up		Difference (95% CI)	*P*-value
	Yes	No		
Patients analysed, *n*	8	35		
Lesions analysed, *n*	8	37		
Frames analysed, *n*	154	705		
SA BL, mm^2	8.60 ± 1.42	7.14 ± 1.22	1.84 (0.32–3.37)	0.02
SA FUP, mm^2	9.21 ± 1.59	7.33 ± 1.36	2.28 (0.57–3.98)	0.009
SA change, mm^2	0.61 ± 0.29	0.20 ± 0.24	0.43 (-0.02–0.88)	0.06
LA BL, mm^2	8.85 ± 1.11	7.30 ± 0.92	1.89 (0.45–3.33)	0.01
LA FUP, mm^2	9.03 ± 1.22	6.29 ± 1.01	2.89 (1.27–4.52)	<0.001
LA change, mm^2	0.17 ± 0.66	−1.00 ± 0.59	0.99 (0.29–1.69)	0.006

Areas are presented as means ± SD.
SA, stent area; LA, lumen area; BL, baseline; FUP, follow-up.

in lesions with when compared with those without ME at both baseline and follow-up, with a significant change in the lumen area at follow-up in both groups [increase in the lumen area in lesions with ME ($P = 0.01$), and decrease in the lumen area in lesions without ME ($P < 0.001$)]. The change in the stent area from baseline to follow-up within the ME group was not significant ($P = 0.15$).

Table 6 shows the association of OCT characteristics recorded at baseline with cross-sectional evagination at follow-up in matched

Table 6 Assessment of the correlation of baseline optical coherence tomography features and evaginations, in matched cross-sections

	Evagination at follow-up		Crude OR (95% CI)	*P*-value	Multivariable OR (95% CI)	*P*-value
	Yes	No				
No. of frames at follow-up	128	713				
Characteristics of cross-section at baseline						
Intra-stent dissection, *n* (%)	60 (46.9)	159 (21.8)	3.01 (1.81–5.00)	<0.001	2.93 (1.75–4.89)	<0.001
Malapposed strut, *n* (%)	12 (9.4)	35 (4.8)	1.76 (0.77–4.03)	0.18	1.69 (0.72–3.99)	0.23
Tissue protrusions, *n* (%)	27 (21.1)	73 (10.0)	3.27 (1.59–6.70)	0.001	3.34 (1.61–6.93)	0.001
Prolapse, *n* (%)	26 (20.3)	162 (22.2)	1.04 (0.57–1.90)	0.90	1.06 (0.57–1.99)	0.85

Using mixed logistic regression with stent type, patient, and lesion as random intercept.

cross-sections. In both uni- and multivariable analyses, intra-stent dissections, and tissue protrusions at baseline were associated with cross-sectional evagination at follow-up: the odds of evagination at follow-up were increased by about three in the presence of either dissection or tissue protrusion at baseline.

The corresponding serial IVUS analyses are summarized in *Table 7*. At baseline, the vessel area was larger among lesions with ME. Serial IVUS analysis showed a larger increase in the vessel area and positive remodelling in lesions with ME when compared with those without (21.1 vs. 4.6%, $P < 0.001$), mainly driven by an increase in the P&M area and accompanied by an increase in the lumen area. Again, the stent area appeared to increase between baseline and follow-up in lesions with ME ($P = 0.84$), but not in lesions without [difference in change between groups (95% CI): 0.43 (0.01–0.85) mm^2, $P = 0.04$].

Discussion

The present study shows that OCT-detected MEs are specifically related to early-generation SES, and much smaller and in general less frequent in newer-generation DES. The mechanism underlying the pathogenesis of ME was suggestively a positive remodelling. Signs of injury documented immediately after stent implantation were associated with an increased risk of evagination at follow-up.

Positive remodelling as a cause of coronary evagination

Coronary artery ectasias and aneurysms following DES implantation have generated great interest owing to their association with ST.[7,8,17] These vessel distensions have often been accompanied by ISA, suggesting positive remodelling as the underlying pathomechanism, since regional vessel remodelling was previously identified as a cause of late acquired stent malapposition (LASM).[7,17,18] In the present study, we took advantage of information obtained by OCT on depth, cross-sectional area, and longitudinal extent, to assess evaginations in three dimensions. The association between positive remodelling and ME suggests that positive remodelling is the mechanism underlying the pathogenesis of evaginations.

We observed that ME in general occurred more frequently and appeared to be larger in SES, suggesting these to be a specific morphological footprint of these early-generation DES. Conversely, MEs were less frequent in PES compared with SES at 5 years—a difference which is confirmatory of the SIRTAX-LATE OCT study. At 1 year, MEs were less frequent in PES compared with SES but were almost absent in newer-generation ZES and EES. No difference, however, was observed between SES and BES at 2 years—something that needs to be interpreted in light of a relatively low sample size of only 18 SES and 18 BES patients at 2 years of follow-up. (Accordingly, it cannot be excluded that this finding could be due to chance. Nevertheless, assessment of evagination volumes showed that these were significantly larger for SES compared with BES, thus being in line with the findings in the other subgroups, particularly the SES vs. ZES and EES, where the sample size was also relatively low.) In a meta-analysis, Hassan *et al.*[19] reported similar findings in terms of IVUS-detected LASM, which were also accompanied by positive vessel remodelling, with the highest incidence in SES followed by PES, and newer-generation ZES and EES. These similarities, together with the observed association of ME with malapposed, protruding, and uncovered struts, suggest that these features may be part of the same disease entity.

Pre-clinical and human autopsy studies previously demonstrated that the inflammatory response following DES implantation strongly relates to the type of stent: SES typically induces granulomatous inflammation with macrophages, giant cells, lymphocytes, and eosinophils; PES exhibits extensive fibrin deposition and medial smooth muscle cell necrosis; ZES and EES show only low levels of inflammation and fibrin deposition.[1,20–22] In addition, SES has been associated with marked adventitial inflammation and fibrosis—findings associated with positive remodelling.[20,23] These results are in line with observations of aneurysmal vessel dilation, stent malapposition, and generalized eosinophilic vasculitis in a case of late ST in a patient with SES.[24] Similarly, the extent of vascular remodelling predominantly after SES implantation correlated with the number of eosinophils harvested from thrombus aspirates in patients with very late ST,[25] supporting the notion that OCT-detected ME represent a pathological vascular reaction particularly related to this stent.

If evaginations and protruding struts are precursors of ISA, a stretch in the P&M may occur during the vessel expansion before complete detachment from the stent. Interestingly, we observed a trend towards a decrease in the size of ME from 1 and 2 to 5-year

Table 7 Quantitative serial intravascular ultrasound results of the stented segment

	Major evagination at follow-up		Diff (95% CI)	*P*-value
	Yes	No		
SA BL, mm^2	8.67 ± 1.94	7.61 ± 1.62	1.31 (−0.43 to 3.05)	0.14
SA FUP, mm^2	9.18 ± 2.03	7.67 ± 1.68	1.76 (−0.09 to 3.60)	0.06
SA change, mm^2	0.50 ± 0.31	0.06 ± 0.24	0.43 (0.01 to 0.85)	0.04
LA BL, mm^2	8.67 ± 1.92	7.59 ± 1.61	1.33 (−0.39 to 3.06)	0.13
LA FUP, mm^2	9.28 ± 2.00	7.37 ± 1.63	2.10 (0.24 to 3.97)	0.03
LA change, mm^2	0.59 ± 0.40	−0.22 ± 0.33	0.75 (0.22 to 1.28)	0.006
VA BL, mm^2	16.53 ± 2.63	13.78 ± 1.99	3.44 (0.62 to 6.25)	0.02
VA FUP, mm^2	20.06 ± 3.44	14.41 ± 2.76	6.29 (3.00 to 9.59)	<0.001
VA change, mm^2	3.51 ± 1.19	0.63 ± 1.00	2.84 (1.71 to 3.98)	<0.001
P&M area BL, mm^2	7.86 ± 1.79	6.14 ± 1.56	2.11 (0.52 to 3.70)	0.009
P&M area FUP, mm^2	10.78 ± 2.36	7.02 ± 2.06	4.17 (2.08 to 6.27)	<0.001
P&M area change, mm^2	2.89 ± 0.92	0.87 ± 0.76	2.06 (1.11 to 3.00)	<0.001
PB BL, %	46.82 ± 4.02	44.36 ± 2.95	3.02 (−2.65 to 8.70)	0.30
PB FUP, %	52.78 ± 4.36	48.46 ± 3.15	5.26 (−0.93 to 11.46)	0.10
PB change, %	5.90 ± 1.98	3.95 ± 1.72	2.21 (−0.08 to 4.49)	0.06

Areas are presented as means ± SD.
SA, stent area; LA, lumen area; VA, vessel area; P&M, plaque and media; PB, plaque burden; BL, baseline; FUP, follow-up.

follow-up among SES-stented segments, while there was a trend towards an increase in ISA volume, suggesting that evaginations may transition into ISA. Regarding the large ISA volumes at 1 year in the two cases of PES and ZES with ME; the ISA in the PES represented persistent malapposition, whereas the ISA in ZES was located in the proximity of a large bifurcation and thus likely present at baseline.

The unexpected finding of a larger stent area only in lesions with ME, which was consistent across the pooled analysis as well as the serial independent evaluation with OCT and IVUS, may either be related to the vessel expansion before detachment or due to chance. It is unlikely that a more intense use of nitroglycerine or potentially higher flush rate during OCT acquisition at follow-up when compared with baseline could have induced these findings only in lesions with ME.

Mechanisms of vessel remodelling

The SES-specific remodelling pattern may be triggered by the polymer rather than the drug. Evidence in favour of this hypothesis is the presence of a focal giant cell reaction surrounding polymer remnants separated from the stent struts,[24] together with observations that durable-polymer SES when compared with polymer-free SES and bare-metal stents are associated with a larger external elastic membrane area.[23] Considering that 80% of sirolimus is released from durable-polymer SES within the first 4 weeks, it seems unlikely that sirolimus itself induces long-term alterations of the vessel wall such as the ME detected up to 5 years in the present study.

The specific mechanisms by which polymers may induce positive remodelling in cases of coronary aneurysms and LASM remain speculative. In relation to SES, it is known that methacrylate may exert a toxic effect on endothelial cells and leucocytes, and can modulate pro-coagulant activities of monocytes.[26] Exposure to the poly-*n*-butyl-methacrylate polymer can furthermore cause delayed (type IV) hypersensitivity reactions mediated at least in part by accumulated CD4 T-helper cells secreting interleukin (IL)-4 and IL-13.[24] Of note, IL-13 was associated with increased smooth muscle cell contractility in asthma,[27] and can induce alveolar remodelling and emphysema in mice via induction of matrix metalloproteinase (MMP)-9 and MMP-12.[28] Both these MMPs were identified as important factors in the development of abdominal aortic aneurysms in humans by degradation of elastin.[29] At the same time, MMP-12 has been found to be a mediator of the accumulation of macrophages and eosinophils.[28] Similar pathways may be responsible for the remodelling and eosinophilia observed in SES-treated coronary arteries. However, then remains the question why not all patients develop this finding.

To further address this, we compared OCT findings following stent implantation with the presence of evaginations at follow-up in corresponding cross-sections. Accordingly, our study demonstrated that cross-sections exhibiting intra-stent dissections and tissue protrusions at baseline—both representing markers of injury—were associated with an increased risk of evagination at the time of OCT follow-up. (Of note, tissue protrusions were defined as tissue projections with irregular lumen contour and thereby suggestive of either thrombus or tissue disruptions other than intra-stent dissections, whereas tissue prolapses were characterized by an intact lumen contour, suggestive of prolapsing plaque.) This relationship is supported by previous observations relating OCT-detected evaginations and coronary artery aneurysms with vessel wall dissections and deep arterial injury caused by oversized balloons, stents, and atherectomy.[5,30,31] Nevertheless, considering that intra-stent

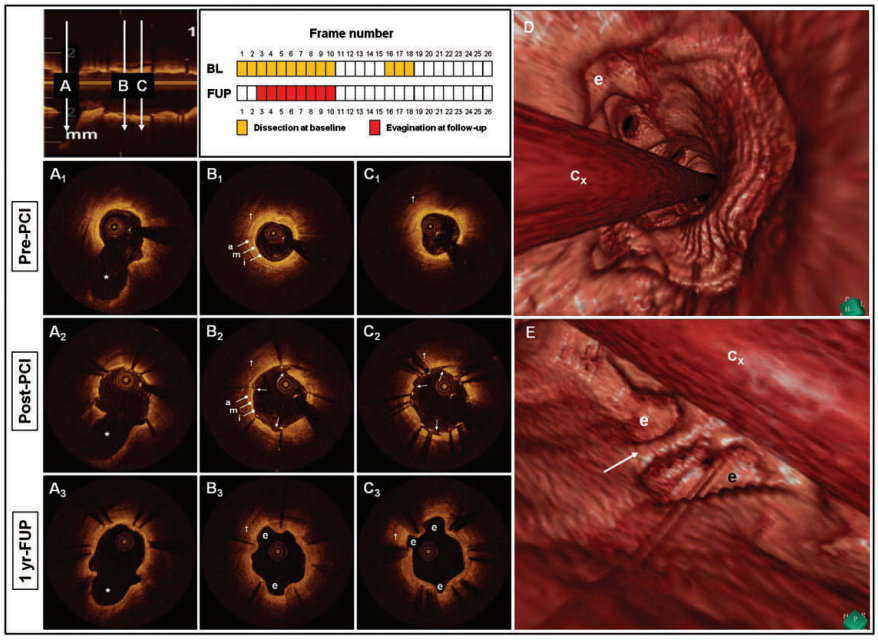

Figure 3 Co-location of intra-stent dissections post-PCI and evaginations at follow-up. (*A*–*C*) Three cross-sections obtained at corresponding sites before (A_1–C_1), immediately after (A_2–C_2), and at 1 year (A_3–C_3) following stent implantation. The large side-branch (*) in (A_1)–(A_3) confirms a good matching, as does the pericardial space (†) and evidence of trilaminar vessel structure (i, intima; m, media; a, adventitia) in (B_1)–(B_3) and (C_1)–(C_3). In (B_2) and (C_2), a large intra-stent dissection extends from 10 to 1 o'clock (white arrows), exposing the underlying adventitia, and a small dissection is seen at 6 o'clock (white arrow). Of note, evaginations (e) are clearly seen at the corresponding sites at follow-up in (B_3) and (C_3). The upper middle panel shows a schematic overview of the location of intra-stent dissection at baseline and evagination at follow-up within matched frames. (*D*) An endoscopic three-dimensional view of the vessel in question, where evaginations (e) create an irregular luminal surface. The optical coherence tomography-catheter (Cx) is located to the left of the 'point of view'. (*E*) A perpendicular view of the evagination in (B_3) and (C_3) at 10 o'clock (white e in (*E*)), which in the three-dimensional reconstruction is separated from another evagination (black e in (*E*)) along the vessel segment by a strut (white arrow). The evagination at 12 o'clock in (C_3) is hidden behind the optical coherence tomography-catheter (Cx) in (*E*).

dissections were present in 27%, 15%, and 31% of cross-sections in SES, PES and ZES, respectively, it may be argued that the influence of stent type, as compared to that of vessel injury, is relatively greater on the development of ME, which in the serially studied lesions were all present in segments implanted with SES. Although the depth of intra-stent dissections could not be systematically assessed due to the limited tissue penetration of OCT, we did observe 12 cases of evaginations following intra-stent dissections extending into the media and adventitia (*Figure 3*).

Potential clinical relevance of coronary evaginations

Features associated with very late ST include uncovered struts, late malapposition, positive remodelling, chronic inflammation as well as ectasias and aneurysms.[1,2,7,8,17,25,32] We found nearly all these features to be more common in lesions with ME, suggesting that ME may be part of the same pathophysiological entity commonly recognized as inappropriate healing following DES implantation, proposing a possible link with late ST. Moreover, our finding of a greater frequency of thrombus in lesions with 'any' and MEs may be an expression of a potential thrombogenicity of these lesions compared with those without evaginations. Although our pooled study sample included one of the largest OCT cohorts to date, it was too small for a meaningful evaluation of such a relationship, however, two of the patients with ME from the SIRTAX-LATE cohort experienced very late ST at 5 and 12 months following 5-year OCT follow-up. Both of these occurred in SES which had some of the most extensive evagination- and ISA volumes in the entire cohort.[6] Along the same line, Alfonso *et al.*[7] described that among patients with angiographic

coronary artery aneurysms, subsequent ST correlated with a larger vessel and lumen volume by IVUS at the time of imaging. Similarly, Imai *et al.*[8] observed an increased risk of ST and target lesion revascularization in SES with ectasias measuring $\geq$ 20% of the stent diameter and extending longitudinally at least the length of the stent diameter, corresponding to an ectasia depth and length of 0.6 mm and 3 mm in a 3 mm stent, respectively—a similar length but twice the depth of the ME definition used in our study. These data suggest that the extent of evagination matters and that clarification of the natural history of evaginations as well as the relationship between the degree of evagination and clinical events merits consideration.

Although first-generation SES are no longer manufactured, they have been implanted in a considerable number of patients worldwide. Recent data from a registry of >12 000 patients, and a meta-analysis including 49 trials, suggest that treatment with newer-generation EES is associated with a lower risk of very late ST when compared with early-generation SES and PES,[33,34] which are additionally associated with a continued risk of very late ST when compared with EES. In this context, it is interesting that the occurrence of evaginations, malapposition, and uncoverage by OCT in the present study, as well as the incidence of IVUS-detected LASM in previous studies,[19] follow a similar pattern. Our findings therefore suggest that evaginations detected with high-resolution OCT may be predictors of late ST particularly in SES, and alongside malapposition and uncoverage provide a possible explanation for differences in late adverse ischaemic events in early- compared with newer-generation DES. Conversely, PES when compared with SES showed fewer ME and only a modest increase when compared with newer-generation DES. Although clinical rates of ST have been comparable between SES and PES, the trigger leading to thrombosis appears to differ[21] in view of substantial differences in the frequency of evaginations. Studies assessing clinical outcomes with OCT and IVUS—particularly with serial imaging—are demanding to perform due to the relatively complex and costly set-ups and the large number of patients required. In view of this, the present study, although relatively small with the 254 imaged lesions, provides important new insights into the utility of OCT for assessing vascular reactions following stent implantation, and suggests that this technology can identify features specific for different stents, which may be useful for improving the prediction of events in the future.

Limitations

The following shortcomings must be considered when interpreting the results of the present study. First, we pooled data from four separate cohorts with different time to follow-up, out of which one came from a non-randomized registry. Efforts were made to adjust for these issues by using frequentist and Bayesian mixed models accounting for the clustered nature of data. Secondly, we did not assess the type of malapposition at follow-up primarily as our focus was on evaginations, and since the relationship between acquired malapposition and positive remodelling has already been shown.[18] Considering that positive remodelling is a common denominator of evaginations and LASM, it seems reasonable to assume that the majority of malapposed struts at follow-up within lesions with ME were late acquired, particularly since there was no correlation between malapposed struts at baseline and ME at follow-up. Thirdly, we extrapolated cross-sectional evagination areas 0.5 mm proximal and distal to the frame of interest to estimate the volume of ME, which may both over- and underestimate the size. Separate evaluation of cross-sectional and ME does however not affect the results of the relative occurrence and predictors of evaginations. Whether this is also true for the mechanisms is unknown since serial IVUS was only available for one of the cohorts. In this regard, it cannot be discarded that evaginations at 2 and 5 years may be caused by mechanisms other than remodelling as observed at 1 year. Furthermore, OCT cross-sections were analysed at 1 mm intervals, although the highest sampling density with commercially available new-generation OCT is 0.2 mm. This could potentially give inaccurate estimates of the occurrence and size of cross-sectional and ME. Considering that gold-standard histology typically evaluates entire lesions based on three to five cross-sections—remarkably lower compared with the average 19 cross-sections per lesion assessed in our study—we chose to accept this level of accuracy, as well as the potential imprecision in the selection of corresponding cross-sections at baseline and follow-up, which is inevitably present whenever serial evaluations are performed. Also, although care was taken to obtain as accurate measurements of evagination- and ISA-volumes as possible, the inherent risk of multiplication of small measurement errors cannot be excluded. Finally, even though this study is one of the largest OCT studies to date, the small number of lesions with MEs, especially in the ZES and EES groups at 1 year, nonetheless limits the power of the study.

Conclusion

Optical coherence tomography-detected MEs are a specific morphological footprint of early-generation SES and are nearly absent in newer-generation ZES and EES. Optical coherence tomography detected intra-stent dissections and tissue protrusions at baseline are associated with an increased risk of evaginations at follow-up. The mechanism underlying the pathogenesis of ME is suggestively a positive remodelling.

Acknowledgements

We are grateful to Marcel Zwahlen and Thomas Gsponer at the Institute for Social and Preventive Medicine at the University of Bern, Switzerland, for advice on statistical modelling.

Funding

This work was supported by the following funding: M.D.R has received research grants from The Heart Centre Rigshospitalet Research Foundation and Copenhagen University. Part of the analysis was funded by intramural grants provided by CTU Bern, Bern University Hospital, the Institute of Social and Preventive Medicine, University of Bern, and a grant to S.W., P.J., L.R. (SPUM) from the Swiss National Science Foundation (Grant 33CM30-124112).

Conflict of interest: Dr. S.W. has received consulting and lecture fees from Abbott, Boston Scientific, Biosensors, Cordis, and Medtronic.

Appendix

Addendum to the methodology and results

Optical coherence tomography and intravascular ultrasound image analysis

The *lumen area* (*LA*) was measured using the automatic area trace function. *Stent struts* were defined as signal-intense spots with dorsal shadowing and a marker was placed at the endoluminal leading edge of the strut, in the mid-point of its axis. The *stent area* (*SA*) was measured by connecting the strut markers with a trace line. *Strut apposition* was assessed for each strut by measuring the distance from the strut marker to the lumen contour semi-automatically using the thickness-ruler function.

For the LEADERS and RESOLUTE trials, lumen and stent area measurements, strut apposition, and strut coverage were assessed by corelab analysts (Cardialysis) blinded to stent type and clinical outcomes. The OCT analyses of the SIRTAX-LATE OCT substudy, the Copenhagen OCT registry, and the assessment of evaginations and protruding struts in all studies were performed by two observers. In case of disagreement, a referee was consulted to a final decision. The time-consuming assessment of evaginations in the LEADERS, RESOLUTE, and Copenhagen cohorts were performed un-blinded, as blinding would have implied a detailed assessment of evaginations using the cut-off of the thinnest stent (Xience, 90 μm or Resolute, 100 μm), and thus the assessment of a large number of bulges in the thicker stents which would, following un-blinding, not fulfil the definition of evagination. Assessments of OCT cross-sections at baseline and follow-up were performed independently, without knowledge of the characteristics of matched cross-sections. The same methodology was used throughout all four OCT studies.

Intravascular ultrasound analyses were performed by two observers, and in case of disagreement a referee was consulted to reach a final decision. Baseline IVUS assessment was performed independently of the follow-up evaluation, and without knowledge of the results of the OCT analysis.

Details of the Bayesian approach

The proportions of malapposed, protruding, and uncovered struts per lesion were analysed using a model with Bernoulli distribution, while the proportions of lesions with $\geq$1 and $\geq$10% malapposed, protruding, and uncovered struts were analysed using Bayesian hierarchical random-effects model with logit distribution. Estimates were derived from the median of the posterior distribution of the 50 001 to 150 000 iteration, with the initial 50 000 iterations discarded as 'burn-in'. We derived 95% credibility intervals (95% CrI) from the 2.5th and 97.5th percentiles of the posterior distribution, also calculating two-sided *P*-values from the posterior distribution. 95% CrI and *P*-values from posterior distributions can be interpreted similarly to conventional 95% confidence intervals and *P*-values.

Additional details on the evagination size

The average depths and lengths of cross-sectional and ME are presented in the appendix table 1 and 2.

Appendix table 1 Specification of the volume, depth and number of cross-sections spanned for "any" cross-sectional evaginations, by stent type and time to FUP

	SES	PES	BES	ZES	EES	p
At Year 1						
Lesions with any evagination N	*22*	*4*		*25*	*13*	
EV	2.24 ± 1.68	0.50 ± 0.72		0.38 ± 1.79	0.42 ± 1.29	0.002
Max depth	0.36 ± 0.45	0.33 ± 0.19		0.23 ± 0.48	0.25 ± 0.34	0.005
N CS/lesion*	4.02 (2.90–6.68)	2.56 (2.09–3.67)		3.01 (2.34–4.16)	2.26 (1.94–2.88)	0.46
At Year 2						
Lesions with any evagination N	*16*		*15*			
EV	2.47 ± 2.52		0.57 ± 2.44			0.03
Max depth	0.32 ± 0.63		0.26 ± 0.61			0.15
N CS/lesion*	4.41 (3.57–10.96)		2.32 (1.74–8.49)			0.13
At Year 5						
Lesions with any evagination N	*29*	*28*				
EV	2.54 ± 1.58	0.72 ± 1.55				<0.001
Max depth	0.36 ± 0.80	0.30 ± 0.56				0.13
N CS/lesion*	4.44 (3.99–5.92)	2.25 (1.96–2.73)				<0.001

N CS/lesions refers to the number of CSs per lesion with any evagination. Values are presented as means ± SD unless otherwise specified.
EV, evagination volume; CS, cross-section.
*Expressed as median (IQR). Volumes are expressed in mm^3, and depths in mm.

Appendix table 2 Specification of the volume, depth and number of cross-sections spanned for major evaginations, by stent type and time to FUP

	SES	PES	BES	ZES	EES	p
At Year 1						
Lesions with ME N	*8*	*1*		*1*	*1*	
EV	24.20 ± 1.77	5.31 ± 0.59		4.42 ± 0.59	10.28 ± 0.59	0.39
Max depth	0.57 ± 0.50	0.58 ± 0.17		0.75 ± 0.17	0.69 ± 0.17	0.90
N CS/lesion*	9.00 (7.00–11.00)	6.00 (6.00–6.00)		13.00 (13.00–13.00)	11.00 (11.00–11.00)	0.39
At Year 2						
Lesions with ME N	*4*		*4*			
EV	30.40 ± 1.30		4.08 ± 1.19			0.01
Max depth	0.49 ± 0.59		0.43 ± 0.54			0.54
N CS/lesion*	19.00 (12.00–28.50)		7.50 (5.50–11.50)			0.02
At Year 5						
Lesions with ME N	*11*	*3*				
EV	11.80 ± 0.59	4.40 ± 0.25				0.009
Max depth	0.58 ± 0.55	0.40 ± 0.23				0.18
N CS/lesion*	7.00 (6.00–12.00)	4.00 (2.00–7.00)				0.06

N CS/lesions refers to the number of CSs per lesion with any evagination. Values are presented as means ± SD unless otherwise specified.
ME, major evagination; CS, cross-section.
*Expressed as median (IQR). Volumes are expressed in mm^3, and depths in mm.

References

1. Joner M, Finn AV, Farb A, Mont EK, Kolodgie FD, Ladich E, Kutys R, Skorija K, Gold HK, Virmani R. Pathology of drug-eluting stents in humans: delayed healing and late thrombotic risk. *J Am Coll Cardiol* 2006;**48**:193–202.
2. Finn AV, Joner M, Nakazawa G, Kolodgie F, Newell J, John MC, Gold HK, Virmani R. Pathological correlates of late drug-eluting stent thrombosis: strut coverage as a marker of endothelialization. *Circulation* 2007;**115**:2435–2441.
3. Tearney GJ, Regar E, Akasaka T, Adriaenssens T, Barlis P, Bezerra HG, Bouma B, Bruining N, Cho JM, Chowdhary S, Costa MA, de Silva R, Dijkstra J, Di Mario C, Dudeck D, Falk E, Feldman MD, Fitzgerald P, Garcia H, Gonzalo N, Granada JF, Guagliumi G, Holm NR, Honda Y, Ikeno F, Kawasaki M, Kochman J, Koltowski L, Kubo T, Kume T, Kyono H, Lam CC, Lamouche G, Lee DP, Leon MB, Maehara A, Manfrini O, Mintz GS, Mizuno K, Morel MA, Nadkarni S, Okura H, Otake H, Pietrasik A, Prati F, Raber L, Radu MD, Rieber J, Riga M, Rollins A, Rosenberg M, Sirbu V, Serruys PW, Shimada K, Shinke T, Shite J, Siegel E, Sonada S, Suter M, Takarada S, Tanaka A, Terashima M, Troels T, Uemura S, Ughi GJ, van Beusekom HM, van der Steen AF, van Es GA, van Soest G, Virmani R, Waxman S, Weissman NJ, Weisz G. Consensus standards for acquisition, measurement, and reporting of intravascular optical coherence tomography studies: a report from the international working group for intravascular optical coherence tomography standardization and validation. *J Am Coll Cardiol* 2012;**59**:1058–1072.
4. Nakano M, Vorpahl M, Otsuka F, Taniwaki M, Yazdani SK, Finn AV, Ladich ER, Kolodgie FD, Virmani R. Ex vivo assessment of vascular response to coronary stents by optical frequency domain imaging. *JACC Cardiovasc Imaging* 2012;**5**:71–82.
5. Radu M, Jorgensen E, Kelbaek H, Helqvist S, Skovgaard L, Saunamaki K. Optical coherence tomography at follow-up after percutaneous coronary intervention: relationship between procedural dissections, stent strut malapposition and stent healing. *EuroIntervention* 2011;**7**:353–361.
6. Räber L, Baumgartner S, Garcia-Garcia H, Kalesan B, Justiz J, Pilgrim T, Moschovitis A, Meier B, Serruys P, Jüni P, Windecker S. Vascular healing response five years after implantation of first-generation DES. The SIRTAX-LATE optical coherence tomography study. *JACC Cardiovasc Interv*. 2012;**5**:946–57.
7. Alfonso F, Perez-Vizcayno MJ, Ruiz M, Suarez A, Cazares M, Hernandez R, Escaned J, Banuelos C, Jimenez-Quevedo P, Macaya C. Coronary aneurysms after drug-eluting stent implantation: clinical, angiographic, and intravascular ultrasound findings. *J Am Coll Cardiol* 2009;**53**:2053–2060.
8. Imai M, Kadota K, Goto T, Fujii S, Yamamoto H, Fuku Y, Hosogi S, Hirono A, Tanaka H, Tada T, Morimoto T, Shiomi H, Kozuma K, Inoue K, Suzuki N, Kimura T, Mitsudo K. Incidence, risk factors, and clinical sequelae of angiographic peri-stent contrast staining after sirolimus-eluting stent implantation. *Circulation* 2011;**123**:2382–2391.
9. Barlis P, Regar E, Serruys PW, Dimopoulos K, van der Giessen WJ, van Geuns RJ, Ferrante G, Wandel S, Windecker S, van Es GA, Eerdmans P, Juni P, di Mario C. An optical coherence tomography study of a biodegradable vs. durable polymer-coated limus-eluting stent: a LEADERS trial sub-study. *Eur Heart J* 2010;**31**:165–176.
10. Gutierrez-Chico JL, van Geuns RJ, Regar E, van der Giessen WJ, Kelbaek H, Saunamaki K, Escaned J, Gonzalo N, di Mario C, Borgia F, Nuesch E, Garcia-Garcia HM, Silber S, Windecker S, Serruys PW. Tissue coverage of a hydrophilic polymer-coated zotarolimus-eluting stent vs. a fluoropolymer-coated everolimus-eluting stent at 13-month follow-up: an optical coherence tomography substudy from the RESOLUTE All Comers trial. *Eur Heart J* 2011;**32**:2454–2463.
11. Prati F, Cera M, Ramazzotti V, Imola F, Giudice R, Albertucci M. Safety and feasibility of a new non-occlusive technique for facilitated intracoronary optical coherence tomography (OCT) acquisition in various clinical and anatomical scenarios. *EuroIntervention* 2007;**3**:365–370.
12. Gonzalo N, Garcia-Garcia HM, Serruys PW, Commissaris KH, Bezerra H, Gobbens P, Costa M, Regar E. Reproducibility of quantitative optical coherence tomography for stent analysis. *EuroIntervention* 2009;**5**:224–232.
13. Barlis P, Tanigawa J, Di Mario C. Coronary bioabsorbable magnesium stent: 15-month intravascular ultrasound and optical coherence tomography findings. *Eur Heart J* 2007;**28**:2319.
14. Gonzalo N, Serruys PW, Okamura T, Shen ZJ, Onuma Y, Garcia-Garcia HM, Sarno G, Schultz C, van Geuns RJ, Ligthart J, Regar E. Optical coherence tomography assessment of the acute effects of stent implantation on the vessel wall: a systematic quantitative approach. *Heart* 2009;**95**:1913–1919.
15. Mintz GS, Nissen SE, Anderson WD, Bailey SR, Erbel R, Fitzgerald PJ, Pinto FJ, Rosenfield K, Siegel RJ, Tuzcu EM, Yock PG. American College of Cardiology Clinical Expert Consensus Document on Standards for Acquisition, Measurement and Reporting of Intravascular Ultrasound Studies (IVUS). A report of the American College of Cardiology Task Force on Clinical Expert Consensus Documents. J Am Coll Cardiol 2001;**37**:1478–1492.
16. Spiegelhalter DJ, Myles JP. *Bayesian Approaches to Clinical Trials and Health Care Evaluation*. Chicester: John Wiley & Sons; 2004.
17. Cook S, Wenaweser P, Togni M, Billinger M, Morger C, Seiler C, Vogel R, Hess O, Meier B, Windecker S. Incomplete stent apposition and very late stent thrombosis after drug-eluting stent implantation. *Circulation* 2007;**115**:2426–2434.
18. Mintz GS, Shah VM, Weissman NJ. Regional remodeling as the cause of late stent malapposition. *Circulation* 2003;**107**:2660–2663.
19. Hassan AK, Bergheanu SC, Stijnen T, van der Hoeven BL, Snoep JD, Plevier JW, Schalij MJ, Wouter Jukema J. Late stent malapposition risk is higher after drug-eluting stent compared with bare-metal stent implantation and associates with late stent thrombosis. *Eur Heart J* 2009;**31**:1172–1180.

20. Wilson GJ, Nakazawa G, Schwartz RS, Huibregtse B, Poff B, Herbst TJ, Baim DS, Virmani R. Comparison of inflammatory response after implantation of sirolimus- and paclitaxel-eluting stents in porcine coronary arteries. *Circulation* 2009;**120**: 141–149. 141–142.
21. Nakazawa G, Finn AV, Vorpahl M, Ladich ER, Kolodgie FD, Virmani R. Coronary responses and differential mechanisms of late stent thrombosis attributed to first-generation sirolimus- and paclitaxel-eluting stents. *J Am Coll Cardiol* 2011;**57**: 390–398.
22. Otsuka F, Nakano M, Vorpahl M, Yazdani SK, Ladich E, Kolodgie F, Finn AV, Virmani R. Pathology of second- versus first-generation drug-eluting stents in humans: does safety issue still exist?. *Eur Heart J* 2011;**32**(Abstract supplement):82.
23. John MC, Wessely R, Kastrati A, Schomig A, Joner M, Uchihashi M, Crimins J, Lajoie S, Kolodgie FD, Gold HK, Virmani R, Finn AV. Differential healing responses in polymer- and nonpolymer-based sirolimus-eluting stents. *JACC Cardiovasc Interv* 2008;**1**:535–544.
24. Virmani R, Guagliumi G, Farb A, Musumeci G, Grieco N, Motta T, Mihalcsik L, Tespili M, Valsecchi O, Kolodgie FD. Localized hypersensitivity and late coronary thrombosis secondary to a sirolimus-eluting stent: should we be cautious?. *Circulation* 2004;**109**:701–705.
25. Cook S, Ladich E, Nakazawa G, Eshtehardi P, Neidhart M, Vogel R, Togni M, Wenaweser P, Billinger M, Seiler C, Gay S, Meier B, Pichler WJ, Juni P, Virmani R, Windecker S. Correlation of intravascular ultrasound findings with histopathological analysis of thrombus aspirates in patients with very late drug-eluting stent thrombosis. *Circulation* 2009;**120**:391–399.
26. Dahl OE, Westvik AB, Kierulf P, Lyberg T. Effect of monomethylmethacrylate on procoagulant activities of human monocytes and umbilical vein endothelial cells *in vitro*. *Thromb Res* 1994;**74**:377–387.
27. Risse PA, Jo T, Suarez F, Hirota N, Tolloczko B, Ferraro P, Grutter P, Martin JG. Interleukin-13 inhibits proliferation and enhances contractility of human airway smooth muscle cells without change in contractile phenotype. *Am J Physiol Lung Cell Mol Physiol* 2011;**300**:L958–L966.
28. Lanone S, Zheng T, Zhu Z, Liu W, Lee CG, Ma B, Chen Q, Homer RJ, Wang J, Rabach LA, Rabach ME, Shipley JM, Shapiro SD, Senior RM, Elias JA. Overlapping and enzyme-specific contributions of matrix metalloproteinases-9 and -12 in IL-13-induced inflammation and remodeling. *J Clin Invest* 2002;**110**:463–474.
29. Curci JA, Liao S, Huffman MD, Shapiro SD, Thompson RW. Expression and localization of macrophage elastase (matrix metalloproteinase-12) in abdominal aortic aneurysms. *J Clin Invest* 1998;**102**:1900–1910.
30. Bell MR, Garratt KN, Bresnahan JF, Edwards WD, Holmes DR Jr. Relation of deep arterial resection and coronary artery aneurysms after directional coronary atherectomy. *J Am Coll Cardiol* 1992;**20**:1474–1481.
31. Slota PA, Fischman DL, Savage MP, Rake R, Goldberg S. Frequency and outcome of development of coronary artery aneurysm after intracoronary stent placement and angioplasty. STRESS Trial Investigators. *Am J Cardiol* 1997;**79**:1104–1106.
32. Guagliumi G, Sirbu V, Musumeci G, Gerber R, Biondi-Zoccai G, Ikejima H, Ladich E, Lortkipanidze N, Matiashvili A, Valsecchi O, Virmani R, Stone GW. Examination of the *in vivo* mechanisms of late drug-eluting stent thrombosis: findings from optical coherence tomography and intravascular ultrasound imaging. *JACC Cardiovasc Interv* 2012;**5**:12–20.
33. Räber L, Magro M, Stefanini GG, Kalesan B, van Domburg RT, Onuma Y, Wenaweser P, Daemen J, Meier B, Juni P, Serruys PW, Windecker S. Very late coronary stent thrombosis of a newer-generation everolimus-eluting stent compared with early-generation drug-eluting stents: a prospective cohort study. *Circulation* 2012;**125**:1110–1121.
34. Palmerini T, Biondi-Zoccai G, Della Riva D, Stettler C, Sangiorgi D, D'Ascenzo F, Kimura T, Briguori C, Sabate M, Kim HS, De Waha A, Kedhi E, Smits PC, Kaiser C, Sardella G, Marullo A, Kirtane AJ, Leon MB, Stone GW. Stent thrombosis with drug-eluting and bare-metal stents: evidence from a comprehensive network meta-analysis. *Lancet* 2012;**379**:1393–1402.

CHAPTER 3 THE APPLICATION OF OPTICAL COHERENCE TOMOGRAPHY IN THE CLINICAL EVALUATION OF THE ACUTE EFFECTS AND VASCULAR REACTIONS TO METALLIC STENT IMPLANTATION

3.2 Flow disturbances in stent-related coronary evaginations – A computational fluid-dynamic simulation study.

Radu MD*, Pfenniger A*, Räber L*, De Marchi SF, Obrist D, Kelbæk H, Windecker S, Serruys PW, Vogel R.

EuroIntervention. 2014;10:113-23.

Flow disturbances in stent-related coronary evaginations: a computational fluid-dynamic simulation study

Maria D. Radu[1,2], MD; Aloïs Pfenniger[3,4], PhD; Lorenz Räber[2,5], MD; Stefano F. de Marchi[5], MD; Dominik Obrist[6], PhD; Henning Kelbæk[1], MD, DMSci; Stephan Windecker[5], MD; Patrick W. Serruys[2]*, MD, PhD; Rolf Vogel[3,7], MD, PhD

M.D. Radu, A. Pfenniger and L. Räber contributed equally to this work.

1. The Heart Centre, Rigshospitalet, Copenhagen University Hospital, Copenhagen, Denmark; 2. Thoraxcenter, Erasmus University Medical Centre, Rotterdam, The Netherlands; 3. ARTORG Cardiovascular Engineering, University of Bern, Bern, Switzerland; 4. Graduate School for Cellular and Biomedical Sciences, University of Bern, Bern, Switzerland; 5. Department of Cardiology, Swiss Cardiovascular Center, Bern, Switzerland; 6. Institute of Fluid Dynamics, ETH Zurich, Zurich, Switzerland; 7. Department of Cardiology, Bürgerspital, Solothurn, Switzerland

GUEST EDITOR: Rafael Beyar, MD, DSc, MPH; *Department of Cardiology, Rambam Medical Centre and Technion-Israel Institute of Technology, Haifa, Israel*

This paper also includes accompanying supplementary data published online at: http://www.pcronline.com/eurointervention/72nd_issue/18

KEYWORDS

- computational fluid-dynamic simulation
- coronary evaginations
- flow disturbance
- optical coherence tomography

Abstract

Aims: Angiographic ectasias and aneurysms in stented segments have been associated with late stent thrombosis. Using optical coherence tomography (OCT), some stented segments show coronary evaginations reminiscent of ectasias. The purpose of this study was to explore, using computational fluid-dynamic (CFD) simulations, whether OCT-detected coronary evaginations can induce local changes in blood flow.

Methods and results: OCT-detected evaginations are defined as outward bulges in the luminal vessel contour between struts, with the depth of the bulge exceeding the actual strut thickness. Evaginations can be characterised cross-sectionally by depth and along the stented segment by total length. Assuming an ellipsoid shape, we modelled 3-D evaginations with different sizes by varying the depth from 0.2-1.0 mm, and the length from 1-9 mm. For the flow simulation we used average flow velocity data from non-diseased coronary arteries. The change in flow with varying evagination sizes was assessed using a particle tracing test where the particle transit time within the segment with evagination was compared with that of a control vessel. The presence of the evagination caused a delayed particle transit time which increased with the evagination size. The change in flow consisted locally of recirculation within the evagination, as well as flow deceleration due to a larger lumen – seen as a deflection of flow towards the evagination.

Conclusions: CFD simulation of 3-D evaginations and blood flow suggests that evaginations affect flow locally, with a flow disturbance that increases with increasing evagination size.

**Corresponding author: Erasmus University Medical Centre, Thoraxcenter, Ba583a, 's-Gravendijkwal 230, 3015 CE Rotterdam, The Netherlands. E-mail: p.w.j.c.serruys@erasmusmc.nl*

Introduction

Drug-eluting stent (DES) implantation has revolutionised the treatment of coronary artery disease by dramatically reducing the rates of target lesion revascularisation, as compared to bare metal stent implantation. However, shortly after the introduction of DES, late stent thrombosis (LST) emerged as a major concern related to their use. Subsequent autopsy reports and *in vivo* imaging studies have suggested a number of mechanisms, including incomplete endothelialisation/uncovered struts, chronic inflammation, and stent malapposition, possibly triggered by the antiproliferative drugs and durable polymers[1-4]. Although newer-generation DES have significantly reduced the rate of LST, concern still exists for the patients who received a first-generation DES, not least as emerging data indicate a continued risk of LST over time with these devices[5,6]. Identification of reliable predictors that can be assessed with an accurate imaging technology is therefore needed.

Intravascular optical coherence tomography (OCT) has an ultra-high resolution of 10 µm allowing an *in vivo* histology-like evaluation of intracoronary stents including strut coverage and apposition, as previously validated[7]. Although the presence of uncovered and malapposed struts has been associated with LST[8], OCT relatively often demonstrates the presence of these features even in lesions from asymptomatic patients at up to very long-term follow-up[9]. This suggests that additional mechanisms may be involved in causing these adverse events and, indeed, neoatherosclerosis was recently proposed as an additional potential cause of LST[10,11]. Using OCT in DES at follow-up after implantation, we have observed that some stented segments show outward bulging – "coronary evaginations" – of the luminal contour between struts **(Figure 1A)**[9,12]. Previous *in vivo* and computer-simulated haemodynamic studies have demonstrated that severe arterial dilations, such as aneurysms of the aorta, cerebral vessels and coronary arteries, are accompanied by changes in blood flow and shear stresses[13-15]. It has also been proposed that these features may be responsible for adverse events related hereto, namely ischaemia due to thrombosis and/or dissection[14,15]. Although the evaginations observed by OCT in DES are smaller than the aneurysms encountered in, e.g., Kawasaki's coronary vasculitis with luminal diameters up to 28 mm[13], it may be hypothesised that these evaginations – analogous to other vessel dilations – may cause disturbances in coronary haemodynamics, which may in turn promote local thrombogenicity. The purpose of this study was therefore to explore, using computational fluid-dynamic (CFD) simulations, whether OCT-detected coronary evaginations can induce local changes in blood flow and, if so, whether this varies for different evagination sizes.

Methods

The study was set up in two steps beginning with the CFD simulation of a three-dimensional (3-D) reconstructed evagination obtained *in vivo* from a patient (referred to as "actual" evagination), yielding results which motivated additional flow simulations in modelled evaginations of varying sizes.

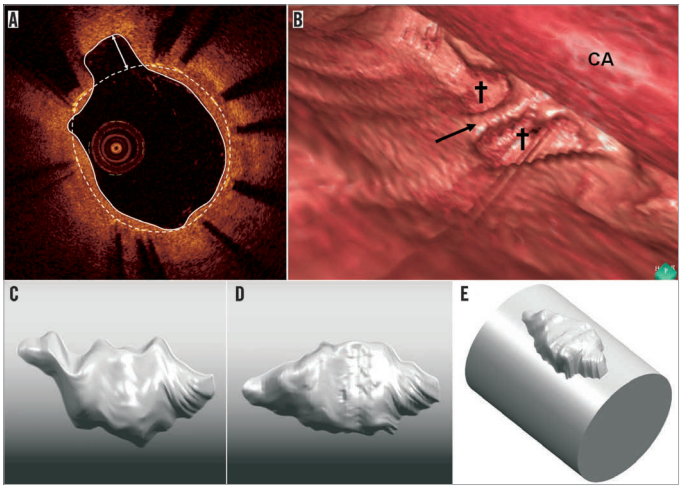

Figure 1. *OCT-detected evagination. A) shows a cross-section of a stent where struts are visualised as bright spots with dorsal shadowing. The stent area is demarcated by the white dashed line connecting the endoluminal surfaces of struts. At 11 o'clock, the luminal contour (white trace line) creates an outward bulge in the vessel wall between struts. Since the maximum depth of the bulge (white double-headed arrow) is greater than the actual strut thickness, it is termed a coronary evagination. B) shows a 3-D reconstruction of a vessel segment with two evaginations (crosses) separated by a strut (black arrow). CA: OCT catheter. C and D show a 3-D reconstructed evagination before (C) and after (D) compensation for catheter rotation. In E, the evagination in D has been merged with a cylindrical vessel.*

DEFINITION AND 3-D RECONSTRUCTION OF AN ACTUAL EVAGINATION

OCT-detected evaginations are defined in the cross-sectional view as outward bulges in the luminal vessel contour between struts, where the maximum depth of the bulge exceeds the actual thickness of the strut **(Figure 1A)**. Accordingly, evaginations can be characterised quantitatively by a depth and an area. Evaluation of entire OCT pullbacks shows that evaginations are often present over several consecutive frames – something appearing as focal outward bulges on 3-D reconstructions **(Figure 1B)**. In order to define how to computer-model evaginations, we selected an actual evagination representing a typical geometry as observed in ~300 previously studied evaginations, and reconstructed the 3-D geometry from a set of consecutive OCT slices. Each slice was expressed in a cylindrical coordinate system taking the centre of the stent as origin. The luminal vessel contour including the luminal evagination contour was given coordinates derived from a series of radii measured at one degree increments along the circumference of the vessel. The rotation of the vessel relative to the OCT catheter during pullback, mainly related to cardiac motion, was compensated for by first determining in each slice the vector pointing from the lumen centre to the evagination centroid, and, secondly, aligning the vectors throughout the slices using MATLAB® (MathWorks, Natick, MA, USA). In this way, we obtained a surface of the evagination, which was converted into a volume using Geomagic Studio® (Geomagic Solutions, Morrisville, NC, USA) and finally merged in Unigraphics NX (Siemens PLM Software, Plano, TX, USA) with a cylindrical vessel 3.55 mm in diameter according to the size of the original vessel. **Figure 1C** and **Figure 1D** show this 3-D reconstruction before and after compensation for catheter rotation, and **Figure 1E** shows the final result after merging with the cylindrical vessel.

COMPUTER MODELLING OF EVAGINATIONS

From this 3-D reconstruction and for simplicity, it is reasonable to assume an ellipsoid 3-D shape for the subsequent assessment of local flow changes in evaginations of varying sizes. These ellipsoids were modelled to protrude with no offset from a straight cylindrical vessel, meaning that the distance between the centreline of the vessel and the horizontal centreline of the evagination equals the vessel radius. The ellipsoid evaginations were inserted right at the inlet of the cylindrical vessel using SolidWorks (Dassault Systèmes SolidWorks Corporation, Waltham, MA, USA) **(Figure 2A)**, and the obtained geometries were imported into COMSOL Multiphysics (COMSOL® Inc., Stockholm, Sweden) for the CFD simulations. For all simulations, the length of the vessel segment was 10 mm and the diameter 3 mm. For the evaluation of the effect of different evagination sizes on blood flow, we varied for each simulation the principal axes of the ellipsoids as follows: the depth was varied at 0.1 mm increments beginning from 0.2 mm up to 1 mm, with the width always equalling twice the depth of the evagination **(Figure 2B)**. The length of the evagination was varied from 1 mm up to 9 mm, at 1 mm increments. The rationale for using these values and increments was based on the range of depths and lengths of ~300 studied evaginations **(Figure 3)**. In order to compensate for the sharp edge between the cylinder and the ellipsoid which does not occur *in vivo* and which may lead to unwanted artefacts in CFD, we introduced a smoothing fillet with an

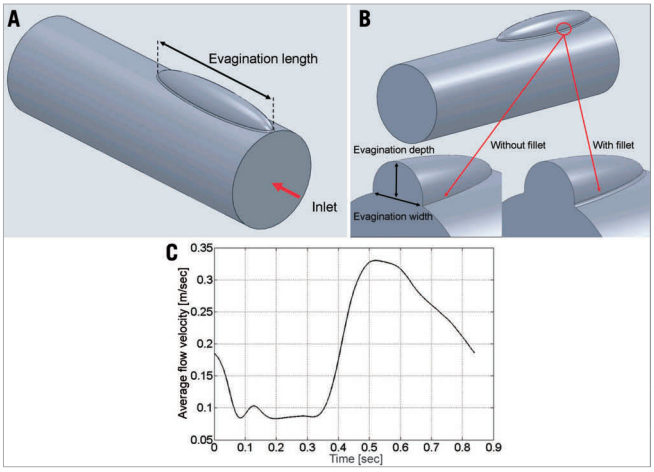

Figure 2. *Modelling of evaginations and flow velocity. A) and B) show an example of a modelled elliptic evagination used in the simulations. The geometry is characterised by a length (A), a depth and a width (B). The sharp edge between the ellipsoid and the cylindrical vessel was compensated for by the insertion of a smoothing fillet (B). C) shows the flow velocity curve used in the simulations.*

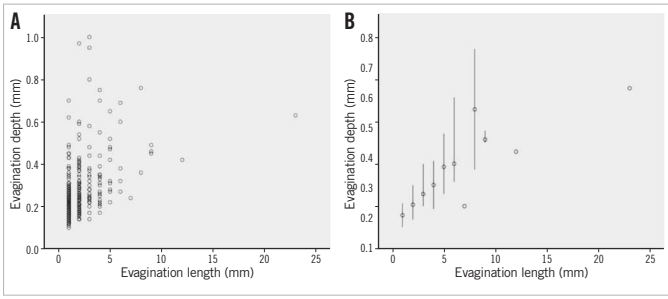

C

Evagination length (mm)	N	Evagination depth (mm)
1	202	0.21 (0.17-0.25)
2	80	0.25 (0.20-0.31)
3	25	0.28 (0.24-0.38)
4	19	0.31 (0.23-0.39)
5	10	0.37 (0.28-0.48)
6	5	0.38 (0.32-0.60)
7	1	0.24 (0.24-0.24)
8	2	0.56 (0.36-0.76)
9	3	0.46 (0.45-0.49)
12	1	0.42 (0.42-0.42)
13	1	0.63 (0.63-0.63)

Figure 3. *We previously studied 254 lesions implanted with DES at a follow-up time of 1 year (117 lesions), 2 years (49 lesions) and 5 years (88 lesions). The maximum length of consecutive cross-sections containing evaginations was calculated and the maximum depth within that specific "cluster" of cross-sections with evaginations was analysed. A) shows the depth and length of each studied evagination; B) shows the median depth (and range) of evaginations of a certain length whereas the table in C specifically shows the number and depth of evaginations of a certain length.*

arbitrary radius amounting to 10% of the evagination depth **(Figure 2B)**. Considering the symmetry of the evagination and vessel, the simulation was performed for half of the geometry only.

Assessment of haemodynamics in evaginations

MODELLING OF BLOOD FLOW

We used an average flow velocity curve **(Figure 2C)** attained by superimposition of coronary flow data from 23 patients assessed at steady state (without adenosine infusion) in non-diseased left anterior descending arteries. The flow velocity curves included the entire cardiac cycle with an average duration of 0.84 sec, corresponding to a heart rate ~71 beats/min. The average peak flow velocity amounted to 33 cm/sec. Doppler signals were measured using ComboWire® guidewires (Volcano Corp., San Diego, CA, USA) equipped with a miniaturised Doppler probe located at the tip and connected to a ComboMap® interface (Volcano Corp.) able to visualise and route incoming Doppler signals. The Doppler-derived instantaneous peak velocity signals were digitised at a sample frequency of 500 Hz using a NI cDAQ-9172 system equipped with a NI 9206 A/D-converter module (National Instruments, Austin, TX, USA). Signal averaging was performed using MATLAB (MathWorks). All recordings were obtained in the setting of another study, and were previously approved by the local ethics committee.

COMPUTATIONAL FLUID-DYNAMIC SIMULATION CONDITIONS

In the actual evagination, the Reynolds number at peak forward flow did not exceed 355 (Reynolds number based on blood density=1,060 kg/m^3; blood viscosity=3.5 mPa·s; vessel diameter=3.55 mm; peak flow velocity=33 cm/sec), and therefore the flow was treated as laminar and computed using the Navier-Stokes equations for incompressible flow. The frequency spectrum of the flow curve shown in **Figure 2C** exhibits a strong peak at the fundamental frequency of the heartbeat, i.e., 1.19 Hz, and two other peaks of negligible amplitude at the second and third harmonic frequency. Using the Womersley theory[16], we concluded that viscous effects dominate and that a Poiseuille flow can safely be assumed at the inlet of the vessel. A fully developed parabolic velocity profile was therefore set as inlet boundary condition. A zero-pressure zero-viscous-stress boundary condition was defined at the outlet. No-slip and slip boundary conditions were imposed at the vessel wall and the symmetry plane, respectively. The geometry was discretised with an automatically generated tetrahedral mesh comprising two boundary layers at the vessel wall (sweeping of a cross-sectional mesh along the vessel was not possible due to the presence of the evagination). A smooth initialisation of the time-dependent simulation was achieved by computing initial values for the flow in the vessel for a stationary situation with an inlet velocity of 18.5 cm/sec (**Figure 2C**, time=0 sec). Both the stationary and time-dependent computations used a PARDISO direct solver.

PARTICLE TRACING

Since the change in flow (pattern and velocity) with varying evagination dimensions cannot be quantified numerically using computational models, we performed a "particle tracing" test. This test model consists of simulating the release of a certain number of passive tracer particles (zero mass) at the inlet of the vessel and subsequently collecting them at the outlet. The passage of each particle can be characterised by the transit time, defined as the time elapsed from the moment a particle is released at the inlet until the particle has reached the outlet. Subsequently, one can derive the number and percentage of "delayed particles", i.e., the number of particles that have a longer transit time as compared to a certain reference. As reference, we used the transit time of the slowest released particle in a control vessel without evagination. Accordingly, the transit time for each particle was determined and

used as surrogate for the change in flow pattern and velocity in relation to the increase in evagination size by assessing the percentage of delayed particles.

Based on the results from the actual evagination, we concluded that particles located closer to the luminal centre are not affected by the evagination. We therefore released particles in six layers parallel to the vessel surface where the first layer was placed at an offset of 20 µm from the vessel wall and the remaining ones at 100 µm increments **(Figure 4A)**. The percentage of delayed particles was determined for each layer separately. Accordingly, a certain particle in a layer was considered delayed when its transit time was longer than the transit time of the slowest particle in the corresponding layer of the control vessel. To eliminate the arbitrariness in selecting the radial position of the different layers, we combined the results from each layer to one single value, namely delayed particles *(DP)*:

$$DP_{l,d} = \sum_{n=1}^{6} DP_{l,d,n}\, 2\pi r_n dr$$

where n denotes the index of the layer and r_n its radius, and l and d denote the length and the depth of the simulated evagination, respectively. This can be understood as integrating the orange area in **Figure 4B** over one complete revolution around the vessel centreline. Finally, we normalised $DP_{l,d}$ with the maximum $DP_{l,d}$ of all tested configurations:

$$DP_{norm} = \frac{DP}{\max(DP)}$$

The particle tracing simulation was performed with the COMSOL Multiphysics software using the described flow velocity data. The total simulation time was set to four seconds, encompassing almost five cardiac cycles. The first cycle was used as a run-in period, after which sets of particles were released 100 times at a constant rate during the second cardiac cycle. The total simulation time of four seconds was chosen to allow sufficient time for all the released particles to reach the outlet in the control vessel. Time stepping in the time-dependent simulation was a critical issue since we had to deal with particles sticking to the wall due to numerical inaccuracy. By enforcing a maximal time step of five milliseconds, we ensured that the number of sticking particles did not exceed 0.5% for any layer. Sticking particles were excluded from the analysis.

Results

ASSESSMENT OF HAEMODYNAMICS IN THE ACTUAL EVAGINATION

The actual evagination measured (length×width×depth) 3.2 mm×1.5 mm×0.65 mm. Computational modelling of blood flow in terms of the particle tracing test revealed a local affection of flow through the vessel with evagination as compared to a control vessel without **(Moving image 1)**. The flow closer to the luminal centre of the vessel appeared not to be affected by the evagination **(Moving image 1)**. The change in flow consisted mainly of recirculation within the evagination, which occurred during the period in the cardiac cycle encompassing maximum speed and maximum flow deceleration

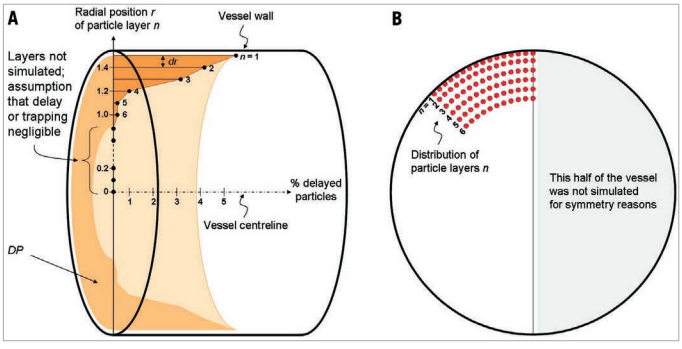

Figure 4. *Set-up for the particle tracing test. The cylinder in panel A represents a modelled vessel (evagination omitted for simplicity) in which the vessel centreline is added as an x-axis. Along the y-axis, representing the vessel radius (1.5 mm), the distance from the centreline and the radial position (r) of various particle layers (n) is indicated. Accordingly, the layer closest to the vessel wall (n=1) is positioned 1.48 mm from the centreline, i.e., 20 µm from the vessel wall, with subsequent layers placed at 100 µm increments from the vessel wall towards the centreline (dr denotes the distance between two adjacent layers). Since particles closer to the centre of the vessel were not affected by the actual evagination, we included only layers 1-6 in the simulation of flow in modelled evaginations (B). To eliminate the arbitrariness in selecting the radial position of the different layers, we combined the results from each layer (% delayed particles) to one single value, namely delayed particles, DP (light orange volume), represented by the integration of the dark orange area over one revolution around the vessel centreline. The DP of each evagination size was then normalised to the maximum DP in the entire sample.*

(Figure 2C, Figure 5). The testing of a modelled evagination with dimensions comparable with the actual evagination (3.0 mm×-1.2 mm×0.6 mm), but in a 3 mm vessel, showed qualitatively a similar flow behaviour with regard to the occurrence of recirculation **(Figure 5)**, confirming that the model assumptions of vessels with evaginations were appropriate. Taken together, these findings motivated the further exploration of the impact of varying evagination size on local flow behaviour.

ASSESSMENT OF HAEMODYNAMICS IN MODELLED EVAGINATIONS

A total of 81 vessels with modelled evaginations of different sizes were assessed. The particle tracing test showed that the number of particles being delayed on their passage through the vessel segment with evagination as compared to the control segment – expressed as the normalised *DP* – increased with increasing evagination size **(Figure 6A)**. In addition, there was a tendency towards depth playing a greater role in local affection of flow in certain shorter evaginations compared to some longer evaginations, as evidenced by the asymmetrical change in *DP* **(Figure 6A)**. To evaluate this more closely, we selected the simulated depth where this effect was most pronounced, namely 1 mm, and plotted the magnitude of normalised *DP* against the evagination length (**Figure 6B**, solid line). This showed more clearly the slight increase in the number of delayed particles in shorter evaginations at this depth followed by a small decrease and then an almost linear increase with increasing evagination length. By inspection of the animated particle trajectories of the individual particle tracing tests, we observed that recirculation prevailed in shorter evaginations (1-3 mm), whereas the flow deceleration and deflection increased with evagination length and depth **(Moving image 2)**. Based on these qualitative findings, the course of the solid curve in **Figure 6B** may be explained by two components, namely deceleration due to larger lumen, which increases the

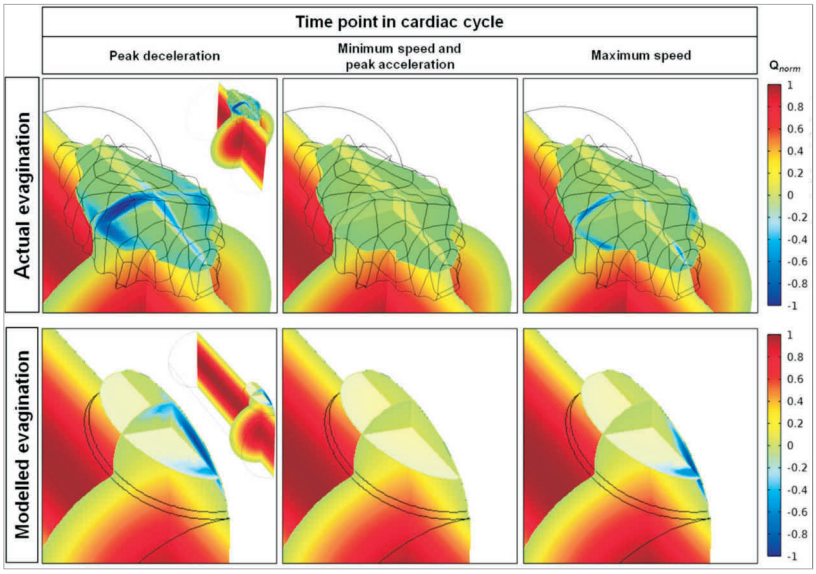

Figure 5. *Change in flow induced by the actual and corresponding modelled evagination. The normalised flow velocity (Qnorm) is expressed in colour where red represents the maximum velocity of forward flow; green, flow stagnation (velocity=0); and dark blue, maximum velocity of backward flow. The vessel with an actual evagination is shown in the upper panels and the corresponding vessel with modelled evagination is shown in the lower panels, at different times in the cardiac cycle (in* **Figure 2C***: peak deceleration=0.048 sec; minimum speed=0.198 sec; peak acceleration=0.41 sec; maximum speed=0.52 sec). The inlet is located closest to the viewer. For orientation purposes, zoomed-out images of the respective vessels are shown in the right corners of the upper and lower left panels. The flow velocity is shown in three dimensions by transsection of the evagination longitudinally (along the length of the vessel axis), cross-sectionally, and horizontally (at half the depth of the evagination). Accordingly, flow velocity is highest at the centre of the vessel and zero close to the vessel wall. Backward flow and thus recirculation is evident close to the luminal surface at the proximal half of both evaginations. As seen by the black mesh, the actual evagination displays an irregular surface.*

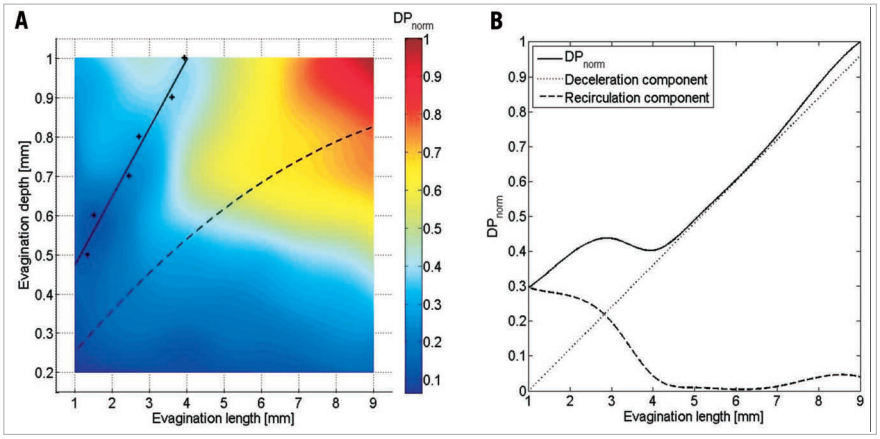

Figure 6. *Results of the particle tracing test. A) shows the normalised number of delayed particles (DPnorm) in modelled vessels with evaginations of varying sizes as compared to a control vessel without evagination. The increase in DPnorm generally increases with increasing evagination size; however, there is a tendency towards a relatively greater increase for deep evaginations (0.7-1.0 mm) even at smaller lengths (2-4 mm). This is most pronounced at 1 mm depth. B) shows the result after plotting DPnorm for depth 1 mm against the evagination length (solid line) showing more clearly the increase in DP followed by a decrease and then again an increase. According to particle trajectory lines* **(Moving image 2)***, the initial increase is represented by recirculation, whereas the subsequent increase is more related to the flow deceleration due to the larger lumen at the evagination, seen as a deflection of flow towards the evagination. The solid line can thus be decomposed into a deceleration (dotted line) and a recirculation component (dashed line). Determination of the point where the recirculation component becomes irrelevant for various evagination sizes (crosses in A) yields the linear solid curve in A, whereas the asymptotic dashed curve represents the cut-off for evagination sizes above which recirculation can be observed for at least one particle at least once in the cardiac cycle (dashed curve determined by inspection of the animated particle trajectories).*

transit time linearly with evagination length and depth, and recirculation, which is most pronounced at lengths below 4 mm. The solid curve in **Figure 6B** can thus be decomposed into two curves: a flow deceleration curve (dotted line), obtained by setting the intercept at zero and adjusting the slope to obtain a tangential contact to the more linear part of the original normalised *DP* curve, and a recirculation curve (dashed line), obtained by subtracting the deceleration curve from the original normalised *DP* curve. By comparison of **Figure 6A** and **Figure 6B** we observed that the dip in *DP* in the colour plot is the point where recirculation becomes irrelevant based on the graph in **Figure 6B** (at evagination length 4 mm, where the decrease in overall *DP* [solid line] has stagnated and where the *DP* caused by recirculation [dashed line] approximates 0). This specific point was determined for various evagination depths, as shown by the crosses in **Figure 6A**, which could be more or less approximated by a straight line. Accordingly, for evaginations located to the left of this line, recirculation is the predominant mechanism to explain the increase in number of delayed particles, whereas the asymptotic dashed curve represents the cut-off for evagination sizes above which recirculation can be observed for at least one particle once during one cardiac cycle.

Discussion

In the present study, we assessed the potential influence of coronary evaginations on blood flow with the following main findings. 1) Computational modelling of flow in a 3-D reconstructed vessel with an actual evagination showed that the presence of the evagination affects flow locally by inducing both a general flow deceleration due to a larger lumen, seen as a deflection of flow towards the evagination, as well as recirculation of flow within the evagination. 2) The use of a modelled ellipsoid evagination of similar dimension to an actual evagination demonstrated similar changes in flow. 3) The affection of flow as measured by the number of "delayed simulated particles" appeared to increase with increasing evagination size.

THE EFFECT OF EVAGINATIONS ON BIOMECHANICAL CONDITIONS

It is generally accepted that biomechanical conditions play an important role in the genesis and development of vascular disease[17-19]. As expressed by the triad of Virchow, disturbances in blood flow may lead to stasis and thereby thrombosis[20]. This is the first computational flow study to describe the magnitude of stasis

by particle tracing within the newly described morphological finding of coronary evaginations. Compared to previous reports on haemodynamic investigations of vascular aneurysms[13,21,22], we observed similar flow disturbances in the region of evaginations in terms of stagnation and flow reversal, suggesting that, although relatively small compared to true aneurysms, coronary evaginations have the potential to affect blood flow and may thus be of clinical relevance. As compared to the study of haemodynamics in aortic aneurysms, which is typically performed in selected individual cases[15,21], we estimated more broadly how the magnitude of flow disturbance varies with incremental changes in evagination lengths and depths, based on data obtained from an *in vivo* study employing OCT. The flow disturbance appeared to increase with increasing evagination sizes. Specifically, we observed a non-linearity in flow alteration with a transient relatively larger increase for short evaginations at greater depths as compared to longer evaginations **(Figure 6)**, apparently due to an inconsistent variation in the magnitude of flow reversal and deceleration at different evagination sizes. The cause of this non-linearity can only be speculated, and one possibility may relate to the geometrical shape of the evaginations. The gradual increase in depth in short evaginations is relatively larger in relation to the length as compared to longer evaginations. Thus, the former acquire a somewhat "saccular" shape sooner than the latter, which remain "fusiform" until the depth is increased relatively more. Although a specific relationship between the severity of flow disturbance and ectasia size and shape had not been established previously, haemodynamic simulations of individual aortic aneurysms suggest that saccular aneurysms generally affect flow relatively more than those that are fusiform[21]. However, there is a suggestion that the magnitude of flow disturbance depends not only on the maximum cross-sectional area of the aneurysm but also on the total size of the recirculation zone, which can be considerable in fusiform vessel dilations[21].

POTENTIAL CLINICAL IMPLICATIONS

In the setting of vascular aneurysms, the main purpose of fluid-dynamic simulations is to assess the risk of rupture in order to initiate timely intervention[23]. In this regard, focus has mainly been on wall shear stresses and oscillatory shear indices with data indicating that high oscillations in shear stresses during the cardiac cycle correlate with a risk of rupture[22]. As compared to large aneurysms of native vessels, it may be postulated that rupture of coronary evaginations is rather unlikely due to an assumedly stabilising effect of the stent. Instead, there may be a risk of thrombosis considering the presence of stasis and recirculation. Based on this, our aim was to study flow behaviour within lesions with evaginations, and therefore analysis of wall shear stress was omitted. We previously reported the occurrence of very late thrombosis in stented segments exhibiting evaginations[9]. Although the mechanisms leading to thrombosis in lesions with evaginations are unclear, above all two particular possibilities are attractive. Firstly, evaginations may induce thrombosis directly by promoting the convection of platelets towards the vessel wall where stasis and recirculation contribute to their aggregation. Secondly, thrombosis may occur following a co-action of evaginations with other risk factors to increase the risk for thrombosis. In a recent study of 254 lesions treated with DES and imaged with OCT at one to five years, we found a significantly higher frequency of malapposed and uncovered struts in lesions with evaginations as compared to those without[24], both features associated with stent thrombosis[1,3]. In addition, non-occlusive (subclinical) thrombus was more common in lesions with evaginations. On further analysis, IVUS suggested positive remodelling to be the mechanism of evaginations. It is conceivable that, with continuing outward remodelling of the vessel, it may at some point detach from the rigid stent exposing not only tissue factor but also stent struts which consequently become malapposed. These features in combination with the flow disturbances caused by evaginations fulfil all the criteria of the triad of Virchow **(Figure 7A)**, suggesting a high propensity of thrombosis. Accordingly, in the presence of evaginations, malapposed and uncovered struts may be more prone to serve as a nidus for thrombus formation **(Figure 7B)**.

Assuming the proposed coaction of various risk factors, it seems logical that the clinically relevant threshold of evagination depth and length would also depend on the relative extent of the other risk factors and vice versa. Nevertheless, it is tempting to speculate on a threshold above which evaginations may induce clinically relevant flow disturbances. Imai and colleagues previously assessed the clinical importance of peri-stent contrast staining (PSS) – an angiographic phenomenon observed in previously stented segments, suggested to be due to vessel ectasias at these sites[25]. In lesions with PSS, per definition extending >20% and >100% of the stent diameter, in the depth and length, respectively (e.g., in a 3 mm stent this would mean a cut-off for ectasia/evagination depth >0.6 mm and length >3 mm), they found an increased risk of target lesion revascularisation and stent thrombosis as compared to lesions without PSS. Since evaginations and PSS reflect the same phenomenon **(Figure 7B)**, it is interesting that PSS dimensions above the defined cut-off occur in **Figure 6A** in the region with increased flow disturbance, suggesting that this cut-off might be clinically relevant. Considering the above, it is possible that the pattern of flow disturbance (flow recirculation vs. deceleration) at the site of evagination is less important than the size of evagination. Although it is unknown whether increasing evagination size with/without other risk factors indeed translates into clinical events, the findings of the present study will hopefully stimulate further investigations to assess the impact of evaginations on clinical outcomes.

Limitations

For simplicity, we omitted the modelling of the stent, which might alter haemodynamics, as this would have required consideration of different stent designs and strut thicknesses, yielding an unsurpassably large number of combinations to test. The tested regular ellipsoid shape of our modelled evaginations in conjunction with a "healthy" straight cylindrical vessel of only one size may not reflect *in vivo* evaginations correctly, with their complex luminal configurations. Furthermore, the tested vessel segment assumed

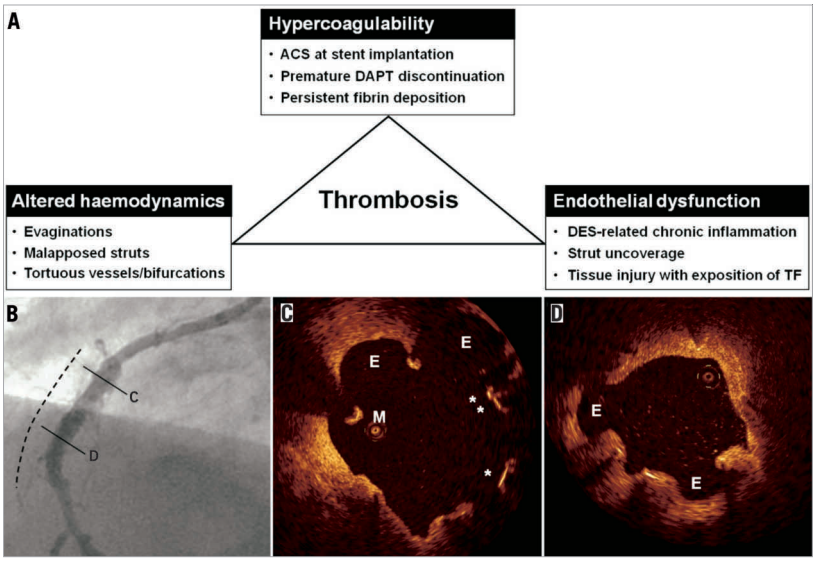

Figure 7. *Factors associated with late stent thrombosis. A) shows a number of factors associated with late stent thrombosis and classified according to the triad of Virchow. B) and C) show the angiographic and OCT findings in a case of late stent thrombosis. This 54-year-old male had a sirolimus-eluting stent implanted in the right coronary artery in the setting of a STEMI. Seventeen months later, clopidogrel was discontinued and, 27 months following stent implantation, the patient presented with an inferior STEMI. One week following thrombolysis, angiography showed peri-stent contrast staining in the previously stented segment (dashed line). OCT demonstrated evaginations (E), malapposed (M), and uncovered (*) struts, as shown in C and D. Please note that OCT was performed without a guidewire, which is a differential diagnosis for the malapposed strut in C. ACS: acute coronary syndrome; DAPT: dual antiplatelet therapy; DES: drug-eluting stent; TF: tissue factor*

only one single evagination per cross-section, and thus the assessment of interplay in case of several evaginations was omitted. Additionally, a side effect of the compensation of vessel rotation around the catheter may be an excessive straightening of the shape of the evagination that may further affect haemodynamics. With respect to the fluid-dynamic simulation conditions, our simulation model used massless particles, which together with the particle layer approach may not precisely reflect the *in vivo* blood flow. Furthermore, due to the lack of published data relating the exposure time to stagnating and recirculating flow with the rate of thrombocyte adhesion, we could not use the derived metric *DP* to predict thrombus formation in an evagination. The results were therefore normalised.

Conclusion

OCT-detected coronary evaginations in stented segments represent an outward bulging of the luminal contour between struts. Following computational modelling of 3-D evaginations and blood flow, we found that evaginations affect flow locally, and that the flow disturbance increases with increasing evagination size. The clinical implications of these findings need to be evaluated further.

Guest Editor

This paper was Guest Edited by Rafael Beyar, MD, DSc, MPH; Rambam Health Care Campus (RHCC), & Technion, Haifa, Israel.

Funding

This work was supported by the following funding: M. Radu has received research grants from The Heart Centre Rigshospitalet Research Foundation and Copenhagen University. L. Räber and S. Windecker have received grants from the Swiss National Science Foundation (Grant 33CM30-124112).

Conflict of interest statement

The authors have no conflicts of interest to declare. The Guest Editor has no conflicts of interest to declare.

References

1. Finn AV, Joner M, Nakazawa G, Kolodgie F, Newell J, John MC, Gold HK, Virmani R. Pathological correlates of late drug-eluting stent thrombosis: strut coverage as a marker of endothelialization. *Circulation*. 2007;115:2435-41.

2. Joner M, Finn AV, Farb A, Mont EK, Kolodgie FD, Ladich E, Kutys R, Skorija K, Gold HK, Virmani R. Pathology of drug-eluting stents in humans: delayed healing and late thrombotic risk. *J Am Coll Cardiol.* 2006;48:193-202.

3. Cook S, Wenaweser P, Togni M, Billinger M, Morger C, Seiler C, Vogel R, Hess O, Meier B, Windecker S. Incomplete stent apposition and very late stent thrombosis after drug-eluting stent implantation. *Circulation*. 2007;115:2426-34.

4. Cook S, Ladich E, Nakazawa G, Eshtehardi P, Neidhart M, Vogel R, Togni M, Wenaweser P, Billinger M, Seiler C, Gay S, Meier B, Pichler WJ, Juni P, Virmani R, Windecker S. Correlation of intravascular ultrasound findings with histopathological analysis of thrombus aspirates in patients with very late drug-eluting stent thrombosis. *Circulation*. 2009;120:391-9.

5. Wenaweser P, Daemen J, Zwahlen M, van Domburg R, Juni P, Vaina S, Hellige G, Tsuchida K, Morger C, Boersma E, Kukreja N, Meier B, Serruys PW, Windecker S. Incidence and correlates of drug-eluting stent thrombosis in routine clinical practice. 4-year results from a large 2-institutional cohort study. *J Am Coll Cardiol.* 2008;52:1134-40.

6. Räber L, Magro M, Stefanini GG, Kalesan B, van Domburg RT, Onuma Y, Wenaweser P, Daemen J, Meier B, Juni P, Serruys PW, Windecker S. Very late coronary stent thrombosis of a newer generation everolimus-eluting stent compared with early generation drug-eluting stents: a prospective cohort study. *Circulation*. 2012;125:1110-21.

7. Nakano M, Vorpahl M, Otsuka F, Taniwaki M, Yazdani SK, Finn AV, Ladich ER, Kolodgie FD, Virmani R. Ex vivo assessment of vascular response to coronary stents by optical frequency domain imaging. *JACC Cardiovasc Imaging.* 2012;5:71-82.

8. Guagliumi G, Sirbu V, Musumeci G, Gerber R, Biondi-Zoccai G, Ikejima H, Ladich E, Lortkipanidze N, Matiashvili A, Valsecchi O, Virmani R, Stone GW. Examination of the in vivo mechanisms of late drug-eluting stent thrombosis: findings from optical coherence tomography and intravascular ultrasound imaging. *JACC Cardiovasc Interv.* 2012;5:12-20.

9. Räber L, Baumgartner S, Garcia HM, Kalesan B, Justiz J, Pilgrim T, Moschovitis A, Khattab AA, Buellesfeld L, Wenaweser P, Meier B, Serruys PW, Juni P, Windecker S. Long-term vascular healing in response to sirolimus- and paclitaxel-eluting stents: an optical coherence tomography study. *JACC Cardiovasc Interv.* 2012;5:946-57.

10. Nakazawa G, Otsuka F, Nakano M, Vorpahl M, Yazdani SK, Ladich E, Kolodgie FD, Finn AV, Virmani R. The pathology of neoatherosclerosis in human coronary implants bare-metal and drug-eluting stents. *J Am Coll Cardiol.* 2011;57:1314-22.

11. Kang SJ, Mintz GS, Akasaka T, Park DW, Lee JY, Kim WJ, Lee SW, Kim YH, Whan Lee C, Park SW, Park SJ. Optical coherence tomographic analysis of in-stent neoatherosclerosis after drug-eluting stent implantation. *Circulation*. 2011;123:2954-63.

12. Radu M, Jorgensen E, Kelbaek H, Helqvist S, Skovgaard L, Saunamaki K. Optical coherence tomography at follow-up after percutaneous coronary intervention: relationship between procedural dissections, stent strut malapposition and stent healing. *EuroIntervention.* 2011;7:353-61.

13. Kuramochi Y, Ohkubo T, Takechi N, Fukumi D, Uchikoba Y, Ogawa S. Hemodynamic factors of thrombus formation in coronary aneurysms associated with Kawasaki disease. *Pediatr Int.* 2000;42:470-5.

14. Bluestein D, Dumont K, De Beule M, Ricotta J, Impellizzeri P, Verhegghe B, Verdonck P. Intraluminal thrombus and risk of rupture in patient specific abdominal aortic aneurysm - FSI modelling. *Comput Methods Biomech Biomed Engin.* 2009;12:73-81.

15. Biasetti J, Hussain F, Gasser TC. Blood flow and coherent vortices in the normal and aneurysmatic aortas: a fluid dynamical approach to intra-luminal thrombus formation. *J R Soc Interface.* 2011;8:1449-61.

16. Womersley JR. Method for the calculation of velocity, rate of flow and viscous drag in arteries when the pressure gradient is known. *J Physiol.* 1955;127:553-63.

17. Gijsen F, Mortier P, De Beule M, Wentzel JJ, Segers P. Fundamentals of coronary biomechanics. In: Eeckhout E, Serruys PW, Wijns W, Vahanian A, Van Sambeek M, De Palma R, eds. The PCR-EAPCI Textbook. Vol 1, Part II. Toulouse: PCR Publishing; 2012.

18. Wentzel JJ, Krams R, Schuurbiers JC, Oomen JA, Kloet J, van Der Giessen WJ, Serruys PW, Slager CJ. Relationship between neointimal thickness and shear stress after Wallstent implantation in human coronary arteries. *Circulation*. 2001;103:1740-5.

19. Roach MR, Smith NB. Does high shear stress induced by blood flow lead to atherosclerosis? *Perspect Biol Med.* 1983;26:287-303.

20. Virchow R. Thrombose und Embolie. Gefässentzündung und septische Infektion. Gesammelte Abhandlungen zur wissenschaftligen Medizin. Frankfurt am Main: Von Meidinger und Sohn; 1856.

21. Biasetti J, Gasser TC, Auer M, Hedin U, Labruto F. Hemodynamics of the normal aorta compared to fusiform and saccular abdominal aortic aneurysms with emphasis on a potential thrombus formation mechanism. *Ann Biomed Eng.* 2010;38:380-90.

22. Kawaguchi T, Nishimura S, Kanamori M, Takazawa H, Omodaka S, Sato K, Maeda N, Yokoyama Y, Midorikawa H, Sasaki T, Nishijima M. Distinctive flow pattern of wall shear stress and oscillatory shear index: similarity and dissimilarity in ruptured and unruptured cerebral aneurysm blebs. *J Neurosurg.* 2012;117:774-80.

23. Humphrey JD, Holzapfel GA. Mechanics, mechanobiology, and modeling of human abdominal aorta and aneurysms. *J Biomech.* 2012;45:805-14.

24. Radu MD, Räber L, Kalesan B, Muramatsu T, Kelbæk H, Heo J, Jørgensen E, Helqvist S, Farooq V, Brugaletta S, Garcia-Garcia HM, Jüni P, Saunamäki K, Windecker S, Serruys PW. Coronary evaginations are associated with positive vessel remodelling and are nearly absent following implantation of newer-generation drug-eluting stents: an optical coherence tomography and intravascular ultrasound study. *Eur Heart J.* 2014;35:795-807.

25. Imai M, Kadota K, Goto T, Fujii S, Yamamoto H, Fuku Y, Hosogi S, Hirono A, Tanaka H, Tada T, Morimoto T, Shiomi H, Kozuma K, Inoue K, Suzuki N, Kimura T, Mitsudo K. Incidence, risk factors, and clinical sequelae of angiographic peri-stent contrast staining after sirolimus-eluting stent implantation. *Circulation*. 2011;123:2382-91.

Online data supplement

Moving image 1. Panels A and B show the particle trajectories during the particle tracing test of the 3-D reconstructed actual evagination. In panel A, the particles are released in a random fashion, where it is evident that particles located closer to the lumen were not affected by the evagination, whereas particles closer to the vessel wall were both deflected towards the evagination and recirculating within the evagination. For reasons of simplicity, the simulation was therefore performed with 6 layers of particles, as shown in panels B and C, the latter showing the results within a control vessel without evagination. The particle colour indicates the release time (blue=first set of particles; red=last set of particles).

Moving image 2. This image shows the results of the particle tracing test in a control vessel and in modelled vessels with evaginations of varying depths (ED) and lengths (EL). Recirculation is most prominent in shorter evaginations, whereas the overall flow deceleration due to the larger lumen at the evagination, seen as a deflection of flow towards the evagination, increased steadily with increasing evagination length. The particle colour indicates the release time (blue=first set of particles; red=last set of particles).

CHAPTER 3 THE APPLICATION OF OPTICAL COHERENCE TOMOGRAPHY IN THE CLINICAL EVALUATION OF THE ACUTE EFFECTS AND VASCULAR REACTIONS TO METALLIC STENT IMPLANTATION

3.3 Natural history of optical coherence tomography-detected non-flow-limiting edge dissections following drug-eluting stent implantation.

Radu MD, Räber L, Heo JH, Jørgensen E, Kelbæk H, Muramatsu T, Helqvist S, Gogas BD, Farooq V, Garcia-Garcia HM, Windecker S, Saunamäki K, Serruys PW.

EuroIntervention. 2014;9:1085-94.

Natural history of optical coherence tomography-detected non-flow-limiting edge dissections following drug-eluting stent implantation

Maria D. Radu[1,2], MD; Lorenz Räber[2,3], MD; Jungho Heo[2], MD; Bill D. Gogas[2], MD; Erik Jørgensen[1], MD; Henning Kelbæk[1], MD, DMSci; Takashi Muramatsu[2], MD; Vasim Farooq[2], MBChB, MRCP; Steffen Helqvist[1], MD, DMSci; Hector M. Garcia-Garcia[4], MD, PhD; Stephan Windecker[3], MD; Kari Saunamäki[1], MD, DMSci; Patrick W. Serruys[2]* , MD, PhD

1. Rigshospitalet, Copenhagen University Hospital, Copenhagen, Denmark; 2. Thoraxcenter, Erasmus University Medical Centre, Rotterdam, The Netherlands; 3. Bern University Hospital, Bern, Switzerland; 4. Cardialysis BV, Rotterdam, The Netherlands

GUEST EDITOR: *Michael Joner, MD; Facharzt für Innere Medizin und Kardiologie, Deutsches Herzzentrum München, Technische Universität, Munich, Germany*

KEYWORDS

- dissection
- intravascular ultrasound
- optical coherence tomography
- stent implantation

Abstract

Aims: Angiographic evidence of edge dissections has been associated with a risk of early stent thrombosis. Optical coherence tomography (OCT) is a high-resolution technology detecting a greater number of edge dissections – particularly non-flow-limiting – compared to angiography. Their natural history and clinical implications remain unclear. The objectives of the present study were to assess the morphology, healing response, and clinical outcomes of OCT-detected edge dissections using serial OCT imaging at baseline and at one year following drug-eluting stent (DES) implantation.

Methods and results: Edge dissections were defined as disruptions of the luminal surface in the 5 mm segments proximal and distal to the stent, and categorised as flaps, cavities, double-lumen dissections or fissures. Qualitative and quantitative OCT analyses were performed every 0.5 mm at baseline and one year, and clinical outcomes were assessed. Sixty-three lesions (57 patients) were studied with OCT at baseline and one-year follow-up. Twenty-two non-flow-limiting edge dissections in 21 lesions (20 patients) were identified by OCT; only two (9%) were angiographically visible. Flaps were found in 96% of cases. The median longitudinal dissection length was 2.9 mm (interquartile range [IQR] 1.6-4.2 mm), whereas the circumferential and axial extensions amounted to 1.2 mm (IQR: 0.9-1.7 mm) and 0.6 mm (IQR: 0.4-0.7 mm), respectively. Dissections extended into the media and adventitia in seven (33%) and four (20%) cases, respectively. Eighteen (82%) OCT-detected edge dissections were also evaluated with intravascular ultrasound which identified nine (50%) of these OCT-detected dissections. No stent thrombosis or target lesion revascularisation occurred up to one year. At follow-up, 20 (90%) edge dissections were completely healed on OCT. The two cases exhibiting persistent dissection had the longest flaps (2.81 mm and 2.42 mm) at baseline.

Conclusions: OCT-detected edge dissections which are angiographically silent in the majority of cases are not associated with acute stent thrombosis or restenosis up to one-year follow-up.

**Corresponding author: Erasmus MC, Thoraxcenter, Ba583a, 's-Gravendijkwal 230, 3015 CE Rotterdam, The Netherlands. E-mail: p.w.j.c.serruys@erasmusmc.nl*

Introduction

Stent implantation is the preferred treatment for coronary artery stenosis. As a consequence of vessel trauma during stent implantation, edge dissections occasionally occur and may lead to abrupt or threatened vessel closure due to obstruction from prolapsing tissue or thrombosis. Previous reports have suggested an association between angiographic as well as intravascular ultrasound (IVUS)-detected edge dissections and early stent thrombosis (ST)[1-5]. At the same time, other studies evaluating the outcomes following stent implantation have shown that only a minority of patients with edge dissections experience clinical adverse events[6-8]. The impact of these findings and their management has therefore been debated.

Optical coherence tomography (OCT) is a high-resolution technology allowing a detailed assessment of the coronary vessel wall and implanted devices[9]. Consequently, OCT detects a higher number of edge dissections as compared to angiography and IVUS[9,10]. The often dramatic appearance of these vessel disruptions, even when angiographically silent, may generate concern for further complications and trigger additional stent implantation[11,12]. The question whether this is justifiable at a time where OCT is increasingly used during interventions has thus resurfaced. At present, the natural history and clinical implications of these findings in the short and long term remain insufficiently described. The objectives of the present study were to assess the morphology, healing response, and clinical outcomes of OCT-detected edge dissections using serial OCT imaging at baseline and at one year following drug-eluting stent (DES) implantation.

Methods

STUDY POPULATION

The study included serial data from the Copenhagen OCT registry and from the OCT substudy of the RESOLUTE all-comers trial[13]. The Copenhagen OCT registry was a single-centre prospective non-randomised evaluation of strut coverage and apposition at 12-month (average) follow-up in relation to apposition at baseline, using the following DES: CYPHER SELECT® Plus (Cordis, Johnson & Johnson, Warren, NJ, USA), TAXUS® Express™ (Boston Scientific, Natick, MA, USA), and Resolute® (Medtronic Inc., Santa Rosa, CA, USA). Patients were included between June 2008 and November 2010, and were eligible if they had ≥1 lesion with >50% diameter stenosis in a native coronary artery, with a reference vessel diameter between 2.25 and 4.0 mm. Exclusion criteria were ST-segment elevation myocardial infarction (MI), left ventricular ejection fraction <30%, renal insufficiency (creatinine >133 µmol/L), and lesion location in the left main stem or bypass graft. OCT as well as IVUS were performed after a satisfactory angiographic result, defined as a residual diameter stenosis <20% and Thrombolysis In Myocardial Infarction (TIMI) flow grade 3. It was prespecified that angiographically visible edge dissections occurring during the procedure would only be treated in case they were obstructive and flow-limiting (defined as dissections at least type C with a residual diameter stenosis >50% and a TIMI flow ≤2). Specifically, treatment of edge dissections visible by OCT was not permitted unless they fulfilled the angiographic criteria. Administration of glycoprotein (GP) IIb/IIIa inhibitors was left to the discretion of the operator. Whether this was a consequence of the dissection or not was noted. Imaging with both OCT and IVUS was repeated at 12-month (average) follow-up. Of note, six patients (out of a total 49 patients) imaged at baseline in the Copenhagen cohort were excluded due to withdrawal of consent for follow-up.

The RESOLUTE trial was a randomised multicentre all-comers non-inferiority trial comparing the Resolute and XIENCE V® (Abbott Vascular, Santa Rosa, CA, USA) stents[14]. Inclusion criteria were broad, including patients with chronic stable angina as well as acute coronary syndromes, having ≥1 lesion with >50% diameter stenosis with a reference vessel diameter between 2.25 and 4.0 mm. Exclusion criteria were known intolerance to any of the stent components, and planned surgery within six months of the index procedure. Administration of GP IIb/IIIa inhibitors was left to the discretion of the operator. The OCT substudy included patients randomly selected for angiographic follow-up at 13 months from centres where OCT was available. The principal endpoint was strut coverage at follow-up[13]. A limited number of patients, included between May and November 2008, also had a baseline evaluation. There were no per protocol prespecified instructions regarding the management of edge dissections; however, for the purpose of this study, the occurrence of angiographic edge dissections after stent implantation was noted and, if present, also whether these were treated with additional stent implantation.

From the serial data available, we included lesions exhibiting edge dissections as assessed by OCT after stent implantation. Both studies were approved by the local ethics committees and written informed consent was obtained from all patients prior to enrolment.

OCT AND IVUS ACQUISITIONS

OCT acquisitions were performed with commercially available systems (time-domain M2 and M3 systems; frequency-domain C7 system) from LightLab/St. Jude (Westford, MA, USA). OCT images were acquired at a frame rate of 15.6, 20, and 100 frames/s at a pullback speed of 1, 3 and 10 mm/s with the M2, M3 and C7, respectively. Acquisition with occlusive (M2) and non-occlusive (M3 and C7) techniques has been described previously[15]. IVUS images were acquired with the Atlantis SR Pro 40 MHz catheter and iLab system (Boston Scientific, Natick, MA, USA) at a frame rate of 30 frames/s and pullback speed of 0.5 mm/s, according to accepted standards[16].

ANGIOGRAPHIC ANALYSIS

All angiograms were assessed by three independent cardiologists with regard to the presence of edge dissections. In case of disagreement, a consensus diagnosis was obtained. If present, the dissection was graded according to the National Heart, Lung, and Blood Institute classification[17].

OCT IMAGE ANALYSIS

OCT pullbacks were analysed off-line using proprietary software from LightLab/St. Jude. The region of interest included reference vessel segments (RVS) 5 mm proximal and distal to the stent, which were analysed systematically at 0.5 mm intervals. Edge dissections

were defined as disruptions in the luminal vessel surface in the RVS, with or without involvement of the stented segment.

Dissections were classified as flaps, cavities, double-lumen dissections or fissures **(Figure 1A-Figure 1D)**, and their longitudinal extensions along the stented segment were measured. For flaps, the flap root thickness was assessed semi-automatically from the joint point with the vessel wall to the luminal surface along a line projected through the gravitational centre of the lumen. The flap length was measured from the joint point with the vessel wall to the tip of the flap. The flap area was measured as the area bounded by the flap root thickness trace and the luminal contours of the flap. For cavities, the cavity depth was measured along a line projected through the gravitational centre of the lumen, from the deepest point in the cavity to a virtual line extrapolated between the luminal vessel contours on each side of the cavity. The cavity width was quantified at its widest point as parallel to the virtual line as possible, and the cavity area was assessed as the area bounded by the luminal contour of the cavity and the help line extrapolated between the luminal vessel contour on each side of the cavity. Double-lumen dissections were those having a false lumen separated from the true lumen by a cap. The cap thickness was quantified semi-automatically from the joint point with the vessel wall to the luminal vessel contour along a line projected through the gravitational centre of the lumen, and the largest of the two cap thicknesses was used. The cap length was measured as the distance between the two joint points connected by a straight line, while the cap area was defined as the area bounded luminally by the vessel surface to the sides by the cap thickness traces, and in the depth by the false lumen. Fissures were present when a split was visible delineating a flap-like structure not lifted from the vessel wall, which otherwise displayed an uninterrupted luminal contour. Due to a poor demarcation of the root of the flap-like structure, no measurements were performed on the fissures at the cross-sectional level; however, they were included in the assessment of longitudinal extension as it was hypothesised that they were consistent with injury. The circumferential extension of the dissection was expressed as the number of quadrants involved. The axial injury of the dissection was described as intimal involvement when only the intima was affected and media was still intact, as medial involvement when the dissection extended into the media without disruption of the entire medial layer, and as adventitial involvement when the media was dissected throughout its thickness **(Figure 1E-Figure 1G)**. In case the media was not discernible, the dissection was classified as involving only the intima. The lumen area was assessed in each selected frame of the RVS as the area bounded by the luminal vessel contour. The kappa value for inter-observer reproducibility of the classification of edge dissections at the lesion level was 1.0.

We also assessed the underlying tissue at the site of the dissections (at the lesion level) with respect to plaque type, which was classified as fibrous (>500 µm thick in at least one quadrant), fibrocalcific, or thin-cap (TCFA) fibroatheroma according to the international consensus (the two latter plaque types considered to be present when the calcified or lipid regions extended >1 quadrant)[18]. We also noted whether the extension was eccentric or concentric.

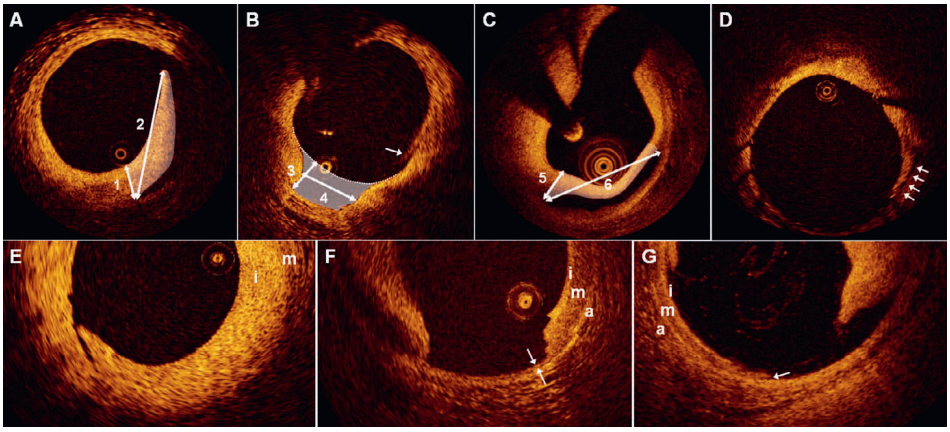

Figure 1. *Classification of edge dissections. A) shows a dissection flap with indication of the flap root thickness (1), flap length (2), and flap area (white shading). B) shows a dissection cavity with the cavity depth (3), cavity width (4) and cavity area (white shading) displayed. The white arrow points to an artefact caused by non-uniform rotational distortion, and should not be misinterpreted as a dissection. The diagnosis was made by inspecting adjacent frames (not shown). C) shows a double-lumen dissection with indication of the largest cap thickness (5), cap width (6), and cap area (white shading). D) the arrows point to a fissure. Panels E-G show dissections involving only the intima (i) (E), the media (m) (F), and the adventitia (a) (G). F) the double arrows demarcate the only intact portion of the disrupted media. G) the arrow indicates the point where the media is lifted from the adventitia.*

IVUS IMAGE ANALYSIS

IVUS pullbacks were analysed off-line using the QCU-CMS software (Medis, Leiden, The Netherlands) at standard 1 mm intervals in the described region of interest. Dissections were defined as tears in the intima-media with visualisation of blood speckle behind a flap or within a cavity or double lumen. The presence of dissections was assessed at the lesion level. The lumen area was measured in the RVS as the area bounded by the luminal vessel contour, whereas the external elastic membrane (EEM) area encompassed the area bounded by the interface between the intima-media layer and the adventitia. The plaque and media area was calculated as the EEM area minus the lumen area. The kappa value for inter-observer reproducibility of the presence or not of edge dissection by IVUS was 1.0.

CLINICAL OUTCOMES

Clinical outcomes in terms of death, MI, target lesion revascularisation (TLR) and target vessel revascularisation (TVR) were assessed for the Copenhagen OCT registry by two independent observers blinded to the imaging results, and for the RESOLUTE trial by a clinical events adjudication committee. The overall rate of stent thrombosis at one year was assessed according to the Academic Research Consortium definitions[19].

STATISTICAL ANALYSIS

Continuous data were presented as means±standard deviations or median and interquartile ranges (IQR), depending on their distribution, which was assessed using the Kolmogorov-Smirnov test. Categorical data were presented as frequencies and percentages. The morphometric data at baseline and follow-up were compared using a paired t-test, and a two-sided $p \leq 0.05$ was considered statistically significant.

Results

CLINICAL AND PROCEDURAL CHARACTERISTICS

Out of a total of 57 patients with 63 lesions, 20 patients with 21 lesions and 22 OCT-defined edge dissections were included in the final analysis **(Figure 2)**. **Table 1** shows the baseline demographics. The average age was 63 years, 15 (75%) patients were males, and 14 (70%) patients presented with acute coronary syndrome. All lesions had a final TIMI 3 flow. Out of the 22 OCT-defined edge dissections, two (9%) were angiographically visible as type A haziness, and both were located within the same vessel (distal lesion with proximal dissection and proximal lesion with distal dissection), separated by only 2 mm. Of note, none of the 63 lesions was treated with additional stents, whereas five (25%) of 20 patients received treatment with GP IIb/IIIa inhibitors directly as a consequence of the OCT findings.

Results of OCT analysis

Out of the 62 assessable lesions with 58 distal and 30 proximal visible edges, 21 (34%) lesions with 16 (28%) distal and six (30%) proximal edges showed dissections, respectively. One of these lesions had both a proximal and distal dissection. **Table 2** shows the characteristics of these dissections at baseline. Six (27%) dissections also involved the stented segments. None of the six patients from the Copenhagen cohort who withdrew consent for follow-up exhibited dissections at baseline examination.

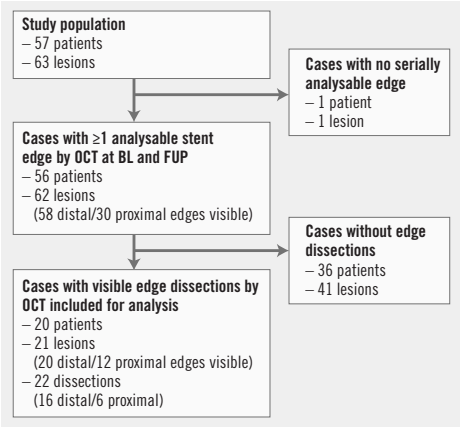

Figure 2. *Flow chart.*

Twenty (90%) out of 22 dissections were completely healed at follow-up **(Figure 3)**. The two dissections that did not heal **(Figure 4)** exhibited the longest circumferential extension (2.81 and 2.42 mm), and in one case the longest longitudinal extension (6.0 mm) at baseline, and both were combinations of flaps and double-lumen dissections.

The morphometric results are presented in **Table 3**. Luminal dimensions in the reference vessel segment remained stable at follow-up.

The plaque type at the site of dissection was: an eccentric fibrous plaque in 17 (77.3%) lesions; concentric fibrous plaque in one (4.5%) lesion; eccentric fibrocalcific plaque in four (18.2%) lesions; and an eccentric TCFA in one (4.5%) lesion. In all cases of eccentric plaque, the point of dissection was at the transition site between the normal intima/thinnest point of plaque and the point where the plaque increases in thickness (**Figure 2** and **Figure 3**). The two cases exhibiting signs of incomplete healing at follow-up had both underlying eccentric fibrous plaques.

RESULTS OF IVUS ANALYSIS

IVUS imaging at baseline was available for 18 (82%) lesions, of which nine (50%) exhibited edge dissections. The results of serial morphometric analyses from 17 (77%) lesions are presented in **Table 3**. The lumen and EEM areas of the RVS increased slightly at follow-up; however, the plaque and media area remained stable.

CLINICAL OUTCOMES

All patients but one received dual antiplatelet therapy with aspirin and clopidogrel during the entire one-year follow-up period. One patient received clopidogrel alone. There were no deaths, MIs,

Table 1. Baseline demographics.

Patient characteristics, N=20		N (%)
Age, years*		63.0 (56.5-67.5)
Male gender		15 (75.0)
Hypertension		11 (55.0)
Hyperlipidaemia		16 (80.0)
Diabetes mellitus		5 (25.0)
Current/previous smoker		4 (20.0)
Family history		14 (82.4)
Previous MI		3 (15.0)
LVEF		60 (55-60)
Clinical presentation	ACS	14 (70.0)
	SAP	6 (30.0)
Multivessel disease		9 (45.9)
Lesion and procedural characteristics, N=21		
Target vessel	LAD	6 (28.6)
	LCX	4 (19.0)
	RCA	11 (52.4)
Target segment	Proximal	9 (42.9)
	Mid	8 (38.1)
	Distal	4 (19.0)
Stent type	CYPHER Select Plus	9 (42.9)
	Resolute	5 (23.8)
	XIENCE V	4 (19.9)
	TAXUS Express	3 (14.3)
Stent diameter, mm*		3.0 (3.0-3.5)
Total stented length, mm*		23 (18-28)
Stents per lesion, n*		1.0 (1.0-2.0)
Overlap		5 (23.8)
TIMI pre	<3	5 (23.8)
	3	16 (76.2)
TIMI post	3	21 (100.0)
Predilatation		15 (71.4)
Post-dilatation		10 (47.6)
Maximum implantation/dilation diameter, mm*		3.0 (3.0-3.5)
Maximum implantation/dilation pressure, atm*		16 (14-20)
GP IIb/IIIa use		5 (25)¶

*Values are median (interquartile range). ACS: acute coronary syndrome; atm: atmospheres; LAD: left anterior descending artery; LCX: left circumflex artery; LVEF: left ventricular ejection fraction; MI: myocardial infarction; N: number; RCA: right coronary artery; SAP: stable angina pectoris; TIMI: Thrombolysis In Myocardial Infarction. ¶denominator equals n=20 patients.

Table 2. Dissection characteristics.

Dissection characteristics, N=22		N (%)
Exhibited features within dissections	Flap	21 (95.5)
	Cavity	8 (36.4)
	Double lumen cap	7 (31.8)
	Fissure	3 (13.6)
Predominant dissection type within dissections	Flap	21 (95.5)
	Cavity	1 (4.5)
	Double lumen cap	0
	Fissure	0
Total longitudinal dissection length, mm*		2.90 (1.60-4.20)
Maximal circumferential extension¶, mm*		1.20 (0.86-1.67)
Maximal axial extension‡, mm		0.61 (0.38-0.70)
Maximal dissection area, mm^2*		0.58 (0.27-0.76)
Dissection volume, mm^3*		0.65 (0.19-1.06)
Maximal circumferential extent	1 quadrant	18 (81.8)
	2 quadrants	4 (18.2)
Maximal vessel injury	Intimal involvement	11 (50.0)
	Medial involvement	7 (33.3)
	Percent frames with medial involvement*#	52.8 (33.3-80.0)
	Adventitial involvement	4 (19.5)
	Percent frames with medial involvement*#	60.4 (22.2-89.2)

Values are median (interquartile range); N: number; *values are median (interquartile range); ¶circumferential extension refers to the flap length, cavity width and cap length; ‡axial extension refers to flap root thickness, cavity depth and cap thickness; #in the respective lesions

TLRs or stent thromboses during the entire follow-up for any of the patients. However, at the one-year imaging procedure one patient had a clinically driven TVR. The two patients with lesions exhibiting signs of persistent edge dissections at one-year follow-up were free of any major adverse cardiac events up to three years after the index procedure. None of the six patients from the Copenhagen cohort who had withdrawn consent for a follow-up OCT examination experienced any events at follow-up.

Discussion

Percutaneous coronary interventions are inevitably associated with vascular injury, including intimal tears and medial disruption[20,21]. Using a systematic classification and quantification of the extent of injury in three dimensions, we studied the natural history of OCT-detected non-flow-limiting edge dissections and found the following: 1) edge dissections were in principle constituted by dissection flaps, although cavity, double lumen and fissure formation were also seen; 2) the majority of OCT-detected edge dissections healed uneventfully without excessive tissue formation; and 3) OCT-detected edge dissections, most of which were angiographically silent, were in this series of patients associated with favourable procedural outcomes and mid-term prognosis.

INCIDENCE OF EDGE DISSECTIONS AND MECHANISM OF HEALING

The incidence of edge dissections following stent implantation ranges from 1.7-6.4%[1,2] by angiography, increasing to 7.8-19.3% by IVUS[7,8,22], and 26.3%[10] up to 34% seen by OCT in the present study. This not only reflects differences in resolution, but also indicates that the use of intracoronary imaging tools more often requires a decision regarding management of apparently "imperfect" results.

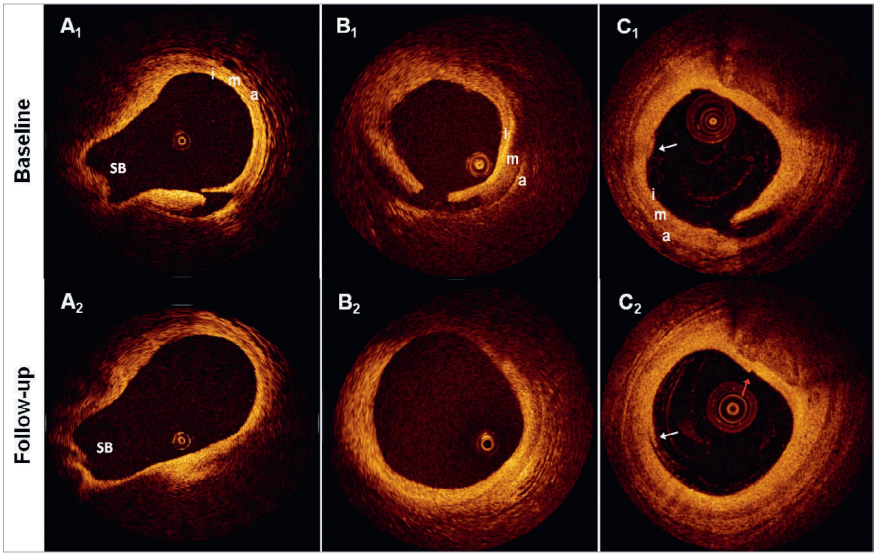

Figure 3. *Examples of healed dissections. The figure shows three dissection sites (A-C) at baseline and follow-up. Of note, there were no changes in signal intensity from baseline to follow-up at any of the dissection sites in the study. SB: side branch; i: intima; m: media; a: adventitia; white arrows in C1 and C2 point to residual blood in the vessel lumen, which should not be mistaken for dissections (diagnosis made by inspecting adjacent frames (not shown)); red arrow in C2 points to a seam line artefact, which should not be mistaken for a dissection.*

Published evidence, as well as the notable (25%) dissection-triggered use of GP IIb/IIIa inhibitors in the present study, confirm that OCT-detected edge dissections may cause concern for further events[11,12], although their sequelae up until now have not been sufficiently explored. Our data show that the majority of edge dissections healed completely during follow-up with only two out of 22 lesions showing residual signs of injury at one year. As indirectly suggested by the absence of an increase in plaque area by IVUS, the mechanism of healing was previously proposed to be a "layering" or "tacking down" rather than filling in of the gap with plaque material[7] – something which OCT in our study provided direct evidence for. It may be hypothesised that this is the consequence of the normal physiological response to injury, where fibrin deposition at the disrupted surfaces of exposed tissues contributes to "gluing" the dissected layers together following the approximation of fluttering tissue flaps against the vessel wall by the flowing blood. It therefore

Table 3. Morphometric results by OCT and IVUS.

Parameter	Baseline	Follow-up	Absolute change	Relative change	*p*-value
Optical coherence tomography, N=22 – Reference vessel segment					
Lumen area, mm^2	5.35±1.73	5.58±1.72	0.21±0.81	6.7±18.4%	0.203
Lumen diameter, mm	2.58±0.42	2.64±0.38	0.06±0.20	3.1±8.8%	0.174
Intravascular ultrasound, N=17 – Reference vessel segment					
Lumen area, mm^2	5.95±2.29	6.84±1.98	0.89±1.51	22.6±34.6%	0.027
Lumen diameter, mm	2.70±0.50	2.92±0.39	0.22±0.35	9.9±15.1%	0.021
EEM area, mm^2	11.20±2.38	12.40±2.58	1.21±1.92	12.9±20.3%	0.020
EEM diameter, mm	3.75±0.40	3.95±0.39	0.20±0.32	5.9±9.4%	0.020
P&M area, mm^2	5.25±1.27	5.56±1.61	0.32±1.09	6.5±20.1%	0.251
Values are mean±standard deviation.					

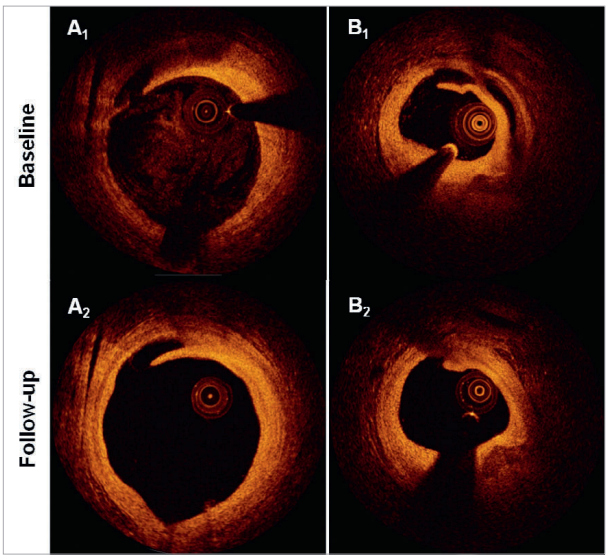

Figure 4. *Incompletely healed dissections. The figure shows the serial appearance of the two incompletely healed edge dissections (A-B). Of note is that the flap length in both cases was reduced at follow-up, although the dissection in panel A extended slightly longer longitudinally.*

seems reasonable to assume that large flaps, in particular in the circumferential direction, are more mobile than smaller ones, and may not only increase the risk of obstruction and thrombosis, but also predispose to delayed vessel healing if continuously being separated from the vessel wall by blood, somewhat analogous to observations from wound healing[23]. In fact, the two edge dissections which healed incompletely at follow-up in the present study exhibited the largest flap length (2.81 and 2.42 mm) at baseline and thus the longest circumferential extension in the entire cohort. Due to the low incidence of incomplete healing, we can only speculate that the maximum flap length may be more important for predicting healing than the extension in the axial and longitudinal direction, since the former is perpendicular to the blood flow. However, the combination with a double-lumen formation, kept open by the blood stream, may also play a role and could possibly have been the cause of the slight progression in longitudinal length in one of these cases at follow-up (from 1.8-2.0 mm). Although the sample size was relatively low, as were the frequencies of TCFA and fibrocalcific plaques at the stent edges, there seemed to be no particular association between the underlying plaque type and propensity of healing.

In terms of healing of edge dissections, our data are in line with a recent report by Kume et al[24] who observed, in a total of 36 patients (39 lesions) with 12 edge dissections, that all but one were fully healed at follow-up. However, the following differences should be noted: data in the present study were collected prospectively (vs. retrospectively); with prespecified instructions on the interventional strategy in 45/63 (71%) lesions (vs. strategy left to the discretion of the operator); with similar follow-up time in all patients (vs. median (range) follow-up of 188 (98-461) days); solely with the use of DES (vs. DES+bare metal stents [BMS]); with a methodology comprising all types of edge dissections including cavities and double-lumen dissections which occurred in 13.6% to 36.4% of cases (vs. flaps alone). Although the number of non-healed dissections at one year was very low, the present study provides details on the characteristics that may have contributed to the lack of complete healing, and which may be regarded as hypothesis-generating for the further understanding of factors of importance for vessel healing.

CLINICAL IMPORTANCE OF EDGE DISSECTIONS

The absence of early events in our study is in line with previous IVUS reports and the OCT report by Kume et al, indicating that there appears to be no increased risk of early stent thrombosis in lesions with residual edge dissections as compared to those without[8,24-26]. In the present study, this may be attributed to several factors: 1) the small injury defect; 2) an early "tacking down" limiting the risk of obstruction and thrombosis; and 3) a potent antithrombotic and antiplatelet therapy. However, the fact that the vast majority of dissections were angiographically silent and half were unidentified by IVUS indicates that they were relatively smaller in comparison to those previously associated with early stent thrombosis, including angiographic type B-F dissections[1-3]. Most importantly, however,

these and other studies unanimously showed that, in addition to edge dissections, other "abnormal findings" were concurrently present by angiography and IVUS, most consistently a low final minimal lumen diameter/area and poor stent expansion, but also a reduced final TIMI flow <3[4,5,27,28], suggesting that stent edge dissections may not *per se* cause acute events.

EDGE DISSECTIONS AND RESTENOSIS

In the long term, our morphometric analysis showed an absence of restenosis at the site of previous dissection despite the presence in several cases of deep vessel injury involving the media and/or adventitia, something otherwise known to be associated with a hyperproliferative response[29]. Our results confirm previous findings by Sheris et al who similarly observed that the plaque and media area in the RVS by IVUS remained stable over a period of six months, even in the presence of submedial dissections[7]. It could be speculated that the antiproliferative drug from the DES in our study could have had a beneficial effect in preventing restenosis even in the RVS. However, considering that Sheris et al found the same in patients with BMS, together with other data showing that non-occlusive type A-D dissections following balloon angioplasty were associated with a reduced risk of restenosis compared to lesions without dissections[6], it is likely that the process of "tacking down" by the flowing blood was more important, as it is well known that wounds with separated edges often heal with extensive scar formation, compared with wounds with approximated edges which heal with hairline scars[23].

As it relates to the differences in lumen areas between the various imaging techniques used, it is well known that areas as measured by IVUS tend to be larger than by OCT[30-32] (with the old as well as the new OCT systems), and our measurements are fully in line with this. The differences have occasionally been shown to be very large (25-72% difference)[31]. This can be caused by the use of an occlusion balloon; however, another possible cause is the relatively greater degree of cardiac motion by IVUS due to a very slow pullback (0.5 mm/s) as compared to OCT (1-20 mm/s), resulting in a relatively larger "imprecise" matching between baseline and follow-up. In addition, with the resolution of OCT being 10-20 μm, and that of IVUS 100-150 μm, "inaccuracies" within the resolution window are relatively larger by IVUS (±100-150 μm) than by OCT (±10-20 μm) which may result in significant differences[32].

MANAGEMENT OF OCT-DETECTED RESIDUAL EDGE DISSECTIONS

Due to the absence of adverse events in the present cohort, we cannot provide any quantitative directives on which dissections will cause events and which will not. However, longitudinal extensions up to an average of 7.8 mm in previous IVUS studies[25], and a circumferential extension up to 2.81 mm by OCT as seen in our study, were both associated with an uneventful mid-term clinical course. The additional mechanical treatment of OCT-detected residual edge dissections being mainly angiographically silent should therefore be carefully evaluated, not least when considering that additional IVUS-guided stent implantation for residual edge dissections has not been shown to entail any benefits in terms of reducing the rate of restenosis and stent thrombosis when compared to an angiographically guided group without treatment of these injuries[24], but was rather associated with complications in terms of TLR[8]. Considering that GP IIb/IIIa inhibitors seem to exert a protective effect against early stent thrombosis[3,33], these may be a reasonable alternative to stent implantation in the presence of large non-flow-limiting OCT-detected edge dissections.

Limitations

The number of patients in this observational study was relatively small, mainly related to the requirement of serial assessment with OCT and IVUS. Furthermore, the inability of OCT to image proximally/ostially located regions, due to the need for blood clearance during acquisition, precluded visualisation of all proximal reference vessel segments. Together with a certain selection of patients, the dissection incidence of 34% may not reflect that in the real world, although it may be assumed that they are fairly representative for OCT-detected edge dissections which are for the most part angiographically silent. The low number of patients further limited our ability to detect rare adverse events and thus to provide recommendations on when a residual dissection imposes an increased risk of, e.g., acute stent thrombosis. Finally, we did not assess the predictors of edge dissections as our focus was on their natural history, and as predictors had previously been evaluated[8]. Furthermore, considering that the majority of these dissections underwent complete healing, this may seem redundant.

Conclusion

OCT-detected edge dissections, which are angiographically silent in the majority of cases, constitute a relatively frequent and benign finding after DES implantation, and are not associated with acute stent thrombosis or restenosis up to one-year follow-up.

Guest Editor

This paper was Guest Edited by Michael Joner, MD; Facharzt für Innere Medizin und Kardiologie, Deutsches Herzzentrum München, Technische Universität, Munich, Germany.

Acknowledgments

M. Radu has received research grants from The Heart Centre Rigshospitalet Research Foundation and Copenhagen University. L. Räber is the recipient of a research fellowship (SPUM) funded by the Swiss National Science Foundation (Grant 33CM30-124112).

Conflict of interest statement

S. Windecker has received consulting and lecture fees from Abbott, Boston Scientific, Biosensors, Cordis, and Medtronic. The other authors have no conflicts of interest to declare. The Guest Editor has no conflict of interest to declare.

References

1. Cutlip DE, Baim DS, Ho KK, Popma JJ, Lansky AJ, Cohen DJ, Carrozza JP Jr, Chauhan MS, Rodriguez O, Kuntz RE. Stent throm-

bosis in the modern era: a pooled analysis of multicenter coronary stent clinical trials. *Circulation.* 2001;103:1967-71.

2. Biondi-Zoccai GG, Agostoni P, Sangiorgi GM, Airoldi F, Cosgrave J, Chieffo A, Barbagallo R, Tamburino C, Vittori G, Falchetti E, Margheri M, Briguori C, Remigi E, Iakovou I, Colombo A. Incidence, predictors, and outcomes of coronary dissections left untreated after drug-eluting stent implantation. *Eur Heart J.* 2006;27:540-6.

3. van Werkum JW, Heestermans AA, Zomer AC, Kelder JC, Suttorp MJ, Rensing BJ, Koolen JJ, Brueren BR, Dambrink JH, Hautvast RW, Verheugt FW, ten Berg JM. Predictors of coronary stent thrombosis: the Dutch Stent Thrombosis Registry. *J Am Coll Cardiol.* 2009;53:1399-409.

4. Cheneau E, Leborgne L, Mintz GS, Kotani J, Pichard AD, Satler LF, Canos D, Castagna M, Weissman NJ, Waksman R. Predictors of subacute stent thrombosis: results of a systematic intravascular ultrasound study. *Circulation.* 2003;108:43-7.

5. Alfonso F, Suarez A, Angiolillo DJ, Sabate M, Escaned J, Moreno R, Hernandez R, Banuelos C, Macaya C. Findings of intravascular ultrasound during acute stent thrombosis. *Heart.* 2004;90:1455-9.

6. Hermans WR, Rensing BJ, Foley DP, Deckers JW, Rutsch W, Emanuelsson H, Danchin N, Wijns W, Chappuis F, Serruys PW. Therapeutic dissection after successful coronary balloon angioplasty: no influence on restenosis or on clinical outcome in 693 patients. The MERCATOR Study Group (Multicenter European Research Trial with Cilazapril after Angioplasty to prevent Transluminal Coronary Obstruction and Restenosis). *J Am Coll Cardiol.* 1992;20:767-80.

7. Sheris SJ, Canos MR, Weissman NJ. Natural history of intravascular ultrasound-detected edge dissections from coronary stent deployment. *Am Heart J.* 2000;139:59-63.

8. Liu X, Tsujita K, Maehara A, Mintz GS, Weisz G, Dangas GD, Lansky AJ, Kreps EM, Rabbani LE, Collins M, Stone GW, Moses JW, Mehran R, Leon MB. Intravascular ultrasound assessment of the incidence and predictors of edge dissections after drug-eluting stent implantation. *JACC Cardiovasc Interv.* 2009;2:997-1004.

9. Bouma BE, Tearney GJ, Yabushita H, Shishkov M, Kauffman CR, DeJoseph Gauthier D, MacNeill BD, Houser SL, Aretz HT, Halpern EF, Jang IK. Evaluation of intracoronary stenting by intravascular optical coherence tomography. *Heart.* 2003;89:317-20.

10. Gonzalo N, Serruys PW, Okamura T, Shen ZJ, Garcia-Garcia HM, Onuma Y, van Geuns RJ, Ligthart J, Regar E. Relation between plaque type and dissections at the edges after stent implantation: an optical coherence tomography study. *Int J Cardiol.* 2011;150:151-5.

11. Imola F, Mallus MT, Ramazzotti V, Manzoli A, Pappalardo A, Di Giorgio A, Albertucci M, Prati F. Safety and feasibility of frequency domain optical coherence tomography to guide decision making in percutaneous coronary intervention. *EuroIntervention.* 2010;6:575-81.

12. Motreff P, Souteyrand G. Optical coherence tomography to diagnose under-expansion of a drug-eluting stent. *JACC Cardiovasc Imaging.* 2009;2:245-6; author reply 246.

13. Gutierrez-Chico JL, van Geuns RJ, Regar E, van der Giessen WJ, Kelbaek H, Saunamaki K, Escaned J, Gonzalo N, di Mario C, Borgia F, Nuesch E, Garcia-Garcia HM, Silber S, Windecker S, Serruys PW. Tissue coverage of a hydrophilic polymer-coated zotarolimus-eluting stent vs. a fluoropolymer-coated everolimus-eluting stent at 13-month follow-up: an optical coherence tomography substudy from the RESOLUTE All Comers trial. *Eur Heart J.* 2011;32:2454-63.

14. Serruys PW, Silber S, Garg S, van Geuns RJ, Richardt G, Buszman PE, Kelbaek H, van Boven AJ, Hofma SH, Linke A, Klauss V, Wijns W, Macaya C, Garot P, DiMario C, Manoharan G, Kornowski R, Ischinger T, Bartorelli A, Ronden J, Bressers M, Gobbens P, Negoita M, van Leeuwen F, Windecker S. Comparison of zotarolimus-eluting and everolimus-eluting coronary stents. *N Engl J Med.* 2010;363:136-46.

15. Prati F, Regar E, Mintz GS, Arbustini E, Di Mario C, Jang IK, Akasaka T, Costa M, Guagliumi G, Grube E, Ozaki Y, Pinto F, Serruys PW. Expert review document on methodology, terminology, and clinical applications of optical coherence tomography: physical principles, methodology of image acquisition, and clinical application for assessment of coronary arteries and atherosclerosis. *Eur Heart J.* 2009;31:401-15.

16. Mintz GS, Nissen SE, Anderson WD, Bailey SR, Erbel R, Fitzgerald PJ, Pinto FJ, Rosenfield K, Siegel RJ, Tuzcu EM, Yock PG. American College of Cardiology Clinical Expert Consensus Document on Standards for Acquisition, Measurement and Reporting of Intravascular Ultrasound Studies (IVUS). A report of the American College of Cardiology Task Force on Clinical Expert Consensus Documents. *J Am Coll Cardiol.* 2001;37:1478-92.

17. Huber MS, Mooney JF, Madison J, Mooney MR. Use of a morphologic classification to predict clinical outcome after dissection from coronary angioplasty. *Am J Cardiol.* 1991;68:467-71.

18. Tearney GJ, Regar E, Akasaka T, Adriaenssens T, Barlis P, Bezerra HG, Bouma B, Bruining N, Cho JM, Chowdhary S, Costa MA, de Silva R, Dijkstra J, Di Mario C, Dudeck D, Falk E, Feldman MD, Fitzgerald P, Garcia H, Gonzalo N, Granada JF, Guagliumi G, Holm NR, Honda Y, Ikeno F, Kawasaki M, Kochman J, Koltowski L, Kubo T, Kume T, Kyono H, Lam CC, Lamouche G, Lee DP, Leon MB, Maehara A, Manfrini O, Mintz GS, Mizuno K, Morel MA, Nadkarni S, Okura H, Otake H, Pietrasik A, Prati F, Raber L, Radu MD, Rieber J, Riga M, Rollins A, Rosenberg M, Sirbu V, Serruys PW, Shimada K, Shinke T, Shite J, Siegel E, Sonada S, Suter M, Takarada S, Tanaka A, Terashima M, Troels T, Uemura S, Ughi GJ, van Beusekom HM, van der Steen AF, van Es GA, van Soest G, Virmani R, Waxman S, Weissman NJ, Weisz G. Consensus standards for acquisition, measurement, and reporting of intravascular optical coherence tomography studies: a report from the international working group for intravascular optical coherence tomography standardization and validation. *J Am Coll Cardiol.* 2012;59:1058-72.

19. Cutlip DE, Windecker S, Mehran R, Boam A, Cohen DJ, van Es GA, Steg PG, Morel MA, Mauri L, Vranckx P, McFadden E, Lansky A, Hamon M, Krucoff MW, Serruys PW. Clinical end points in coronary stent trials: a case for standardized definitions. *Circulation.* 2007;115:2344-51.

20. Potkin BN, Roberts WC. Effects of percutaneous transluminal coronary angioplasty on atherosclerotic plaques and relation of plaque composition and arterial size to outcome. *Am J Cardiol.* 1988;62:41-50.

21. Farb A, Virmani R, Atkinson JB, Kolodgie FD. Plaque morphology and pathologic changes in arteries from patients dying after coronary balloon angioplasty. *J Am Coll Cardiol.* 1990;16:1421-9.

22. Hong MK, Park SW, Lee NH, Nah DY, Lee CW, Kang DH, Song JK, Kim JJ, Park SJ. Long-term outcomes of minor dissection at the edge of stents detected with intravascular ultrasound. *Am J Cardiol.* 2000;86:791-5, A799.

23. Harvey C. Wound healing. *Orthop Nurs.* 2005;24:143-57; quiz 158-9.

24. Kume T, Okura H, Miyamoto Y, Yamada R, Saito K, Tamada T, Koyama T, Neishi Y, Hayashida A, Kawamoto T, Yoshida K. Natural history of stent edge dissection, tissue protrusion and incomplete stent apposition detectable only on optical coherence tomography after stent implantation. *Circ J.* 2012;76:698-703.

25. Russo RJ, Silva PD, Teirstein PS, Attubato MJ, Davidson CJ, DeFranco AC, Fitzgerald PJ, Goldberg SL, Hermiller JB, Leon MB, Ling FS, Lucisano JE, Schatz RA, Wong SC, Weissman NJ, Zientek DM. A randomized controlled trial of angiography versus intravascular ultrasound-directed bare-metal coronary stent placement (the AVID Trial). *Circ Cardiovasc Interv.* 2009;2:113-23.

26. Nishida T, Colombo A, Briguori C, Stankovic G, Albiero R, Corvaja N, Finci L, Di Mario C, Tobis JM. Outcome of nonobstructive residual dissections detected by intravascular ultrasound following percutaneous coronary intervention. *Am J Cardiol.* 2002;89:1257-62.

27. Okabe T, Mintz GS, Buch AN, Roy P, Hong YJ, Smith KA, Torguson R, Gevorkian N, Xue Z, Satler LF, Kent KM, Pichard AD, Weissman NJ, Waksman R. Intravascular ultrasound parameters associated with stent thrombosis after drug-eluting stent deployment. *Am J Cardiol.* 2007;100:615-20.

28. Uren NG, Schwarzacher SP, Metz JA, Lee DP, Honda Y, Yeung AC, Fitzgerald PJ, Yock PG. Predictors and outcomes of stent thrombosis: an intravascular ultrasound registry. *Eur Heart J.* 2002;23:124-32.

29. Schwartz RS, Huber KC, Murphy JG, Edwards WD, Camrud AR, Vlietstra RE, Holmes DR. Restenosis and the proportional neointimal response to coronary artery injury: results in a porcine model. *J Am Coll Cardiol.* 1992;19:267-74.

30. Suzuki Y, Ikeno F, Koizumi T, Tio F, Yeung AC, Yock PG, Fitzgerald PJ, Fearon WF. In vivo comparison between optical coherence tomography and intravascular ultrasound for detecting small degrees of in-stent neointima after stent implantation. *JACC Cardiovasc Interv.* 2008;1:168-73.

31. Gonzalo N, Serruys PW, Garcia-Garcia HM, van Soest G, Okamura T, Ligthart J, Knaapen M, Verheye S, Bruining N, Regar E. Quantitative ex vivo and in vivo comparison of lumen dimensions measured by optical coherence tomography and intravascular ultrasound in human coronary arteries. *Rev Esp Cardiol.* 2009;62:615-24.

32. Nakano M, Vorpahl M, Otsuka F, Taniwaki M, Yazdani SK, Finn AV, Ladich ER, Kolodgie FD, Virmani R. Ex vivo assessment of vascular response to coronary stents by optical frequency domain imaging. *JACC Cardiovasc Imaging.* 2012;5:71-82.

33. Dangas G, Aymong ED, Mehran R, Tcheng JE, Grines CL, Cox DA, Garcia E, Griffin JJ, Guagliumi G, Stuckey T, Lansky AJ, Stone GW. Predictors of and outcomes of early thrombosis following balloon angioplasty versus primary stenting in acute myocardial infarction and usefulness of abciximab (the CADILLAC trial). *Am J Cardiol.* 2004;94:983-8.

CHAPTER 4 METHODOLOGICAL CONSIDERATIONS IN THE APPLICATION OF OPTICAL COHERENCE TOMOGRAPHY FOR THE EVALUATION OF BIORESORBABLE SCAFFOLDS

4.1

Farooq V, Onuma Y, **Radu M**, Okamura T, Gomez-Lara J, Brugaletta S, Gogas BD, van Geuns RJ, Regar E, Schultz C, Windecker S, Lefèvre T, Brueren BR, Powers J, Perkins LL, Rapoza RJ, Virmani R, García-García HM, Serruys PW.

Optical coherence tomography (OCT) of overlapping bioresorbable scaffolds: from benchwork to clinical application.

EuroIntervention. 2011;7:386-99.

Optical coherence tomography (OCT) of overlapping bioresorbable scaffolds: from bench-work to clinical application

Vasim Farooq[1], MBChB, MRCP; Yoshinobu Onuma[1], MD; Maria Radu[1], MD; Takayuki Okamura[1], MD, PhD; Josep Gomez-Lara[1], MD; Salvatore Brugaletta[1], MD; Bill D. Gogas[1], MD; Robert-Jan van Geuns[1], MD, PhD; Evelyn Regar[1], MD, PhD; Carl Schultz[1], MD, PhD; Stephan Windecker[2], MD; Thierry Lefèvre[3], MD, FESC; B.R. Guus Brueren[4], MD, PhD; Jennifer Powers[5], BS; Laura L. Perkins[5], DVM, PhD, DACVP; Richard J. Rapoza[5], PhD; Renu Virmani[6], MD; Hector M. García-García[1], MD, MSc, PhD; Patrick W. Serruys[1]*, MD, PhD

1. Thoraxcenter, Erasmus University Medical Centre, Rotterdam, The Netherlands; 2. Inselspital Bern, Bern, Switzerland; 3. Institut Jacques Cartier, Paris, France; 4. Catharina Ziekenhuis, Eindhoven, The Netherlands; 5. Abbott Vascular, Santa Clara, CA, USA; 6. CVPath Institute, Gaithersburg, MD, USA

J. Powers, L.L Perkins and R.J. Rapoza are employees of Abbott Vascular. R. Virmani has received research support from Medtronic AVE, Abbott Vascular, Atrium Medical, OrbusNeich Medical, Terumo Corporation, Cordis Corporation, BioSensors International; and is a consultant for Medtronic AVE, Abbott Vascular, W.L. Gore, Atrium Medical, Arsenal Medical, and Lutonix. The remaining authors have no conflict of interest to declare.
This paper also includes accompanying supplementary data published at the following website: www.eurointervention.org

Introduction

Fully bioresorbable everolimus-eluting vascular scaffolds (BVS; Abbott Vascular, Santa Clara, CA, USA) are a novel approach to treating coronary lesions. The ABSORB cohort A and cohort B trials investigated the implantation of 3 mm BVS, up to a maximum length of 18 mm, in simple lesions only.[1,2] The implantation of overlapping BVS in longer lesions has not previously been reported. Although the initial results in ABSORB cohort A were very promising, it was found that the main limitation of the BVS (BVS 1.0) was a premature reduction in radial strength.[3-7] Through several design modifications, primarily aimed at maintaining the structural integrity of the BVS for longer, excellent results were obtained in ABSORB cohort B at six months.[8-10] This second generation BVS (BVS 1.1) is now the subject of a large, international, multicentre, ABSORB EXTEND Single Arm Study with the aim of recruiting over 1,000 patients from over 50 centres worldwide. As part of this study, a 50 patient sub-study will be conducted to assess the outcomes of overlapping BVS in the treatment of long lesions, with the use of optical coherence tomography (OCT) at both baseline and follow-up.

Firstly, we report our initial experiences of the different types of overlap achievable with the BVS through implantation in an *in vitro* phantom model followed by 2-dimensional (2D) and 3-dimensional (3D) OCT imaging (frequency domain OCT [FD-OCT]). Secondly, we report our experiences of some of these overlap methodologies in a healthy porcine coronary artery model at 28 and 90 days to assess the neointimal response and strut coverage. Thirdly, we report our initial findings in humans from four of the first five patients to have had implantation of overlapping BVS from the ABSORB EXTEND Single Arm Study. Baseline angiographic, intravascular ultrasound (IVUS), 2D and 3D FD-OCT reconstructions of the varying types of overlapping BVS will be demonstrated. Lastly we report our revised OCT methodology protocol for the assessment of the overlapping BVS at baseline and subsequent angiographic and OCT follow-up, in order to assess the coverage of the overlapping BVS. Since the overlapping BVS segment area is highly complex, the standard OCT assessment of the BVS, which has previously been performed in the ABSORB cohort A and B trials,[3,7,10] is not possible and a new methodology is therefore required.

** Corresponding author: Erasmus MC, 's-Gravendijkwal 230, 3015 CE Rotterdam, The Netherlands*
E-mail: p.w.j.c.serruys@erasmusmc.nl

BVS

The BVS revision 1.1 (Figure 1) is a balloon expandable device consisting of a polymer backbone of Poly-L (racemic)-lactide (PLLA) coated with a thin layer of a 1:1 mixture of an amorphous matrix of Poly-D, L (racemic)-lactide (PDLLA) polymer, and 100 micrograms/cm^2 of the anti-proliferative drug everolimus. The PDLLA allows for the controlled release of everolimus, 80% of which is eluted within the first 30-days. The elution rate, tissue concentration and dose density of everolimus are similar for both the BVS and the XIENCE V everolimus eluting stent (EES). Both PLLA and PDLLA are fully bioresorbable. The polymer is degraded via hydrolysis of the ester bonds in the backbone. The resulting poly-lactide low molecular weight oligomers eventually leave the polymer matrix and are hydrolysed and metabolised through the pyruvate and Kreb energy cycles in the surrounding tissues and blood. Small particles, less than 2 µm in diameter, are phagocytosed by macrophages. According to preclinical studies, the time for complete bioresorption of the polymer backbone is approximately two years.[9]

Two platinum markers (Figure 1) located at each BVS edge allows for the accurate visualisation of the radiolucent BVS during coronary angiography and OCT. The cell area in the pattern of the BVS was reduced in size during the design modification from BVS 1.0 to 1.1 in order to give maximum and more uniform support to the vessel wall (Figure 1)[8].

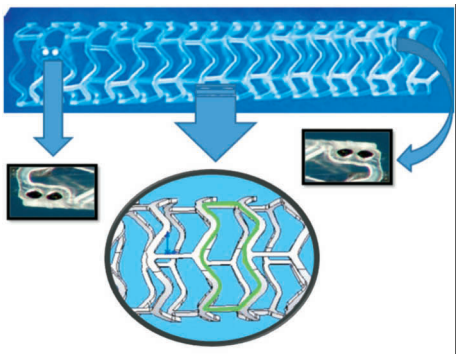

Figure 1. The BVS 1.1 device. Two platinum markers can be seen clearly on the left side, the corresponding platinum markers on the other side of the BVS 1.1 are located posteriorly. The green zone represents the cell area which was reduced in size during the design modification from BVS 1.0 to 1.1.

Bench testing (*in vitro* phantom model) and implantation in a porcine model

Bench testing

A commercially available OCT M2 system (ImageWire™ ; LightLab Imaging Inc., Westford, MA, USA) was used for imaging. The OCT probe was stripped down with the removal of the fibreoptic imaging core (150 microns in diameter) from the OCT probe. The fibreoptic imaging core was subsequently directly inserted into the guidewire lumen of the BVS deployment catheter. This helped to maintain the near perfect central position of the imaging core within the phantom model, with the consequential benefits of avoiding potential imaging artefacts.

A perspex (Plexiglas®) tube with an internal diameter of 3.5 mm and filled with contrast, kept at a temperature of 37 degrees Celsius to approximate human body conditions, was used as the phantom model to bench test the overlapping BVS. The transparent nature of the phantom model allowed us to directly visualise the longitudinal position of the imaging core of the OCT probe relative to the overlap of the BVS struts, thereby allowing the acquisition of cross-sectional 2D OCT images of the entire overlap region (Online moving image). The cross-sectional images of the overlapping BVS struts were acquired at 15.4 frames/sec, with the fibreoptic imaging core being pulled back at a speed of 0.1 mm/sec.

Overlapping 3.0 mm diameter BVS, 18 mm in length, were implanted in the phantom model in three different overlapping configurations (described below) to best replicate the types of overlap that could potentially be achieved in human implantation.

"Interdigitating or adjacent positioning struts without overlap" of two adjacent BVS (Figures 2a-2d): this involved the near perfect positioning of the two BVS devices adjacent to each other, through very careful positioning of the platinum markers so that they were sited side by side, with each BVS virtually "slotting" into the other. As illustrated, 2D and 3D OCT imaging showed the uniform distribution of struts without gap or "stacking" of struts.

"Complete overlap with multiple numbers of stacked struts" of two adjacent BVS (Figures 2e-2h): OCT imaging shows struts clearly overlapped and completely superimposed on each other ("stacked struts") thereby forming a total strut thickness of at least 300 microns in these stacked strut regions. In the phantom model, this kind of overlap was achieved through the overlapping of the platinum markers as demonstrated (Figures 2e and 2g).

"Complete overlap with reduced numbers of stacked struts" of two adjacent BVS (Figures 2i-2l): this was a standard overlap with rotation of the BVS platinum markers so that they were positioned 90 degrees to each other. This allowed an overlap, but reduced the number of stacked struts, as many of the would-be overlapping struts in one BVS tended to slot into the cell space between the strut of the other BVS. Using this approach, most of the BVS strut thicknesses at the overlap were maintained at 150 microns, with fewer areas with stacked struts. In the phantom model, this kind of overlap was achieved through the positioning of each of the BVS markers at right angles to each other.

Implantation in an animal model

From the bench-work experimentations, we elected to test in a non-diseased porcine coronary artery model the two types of complete overlap achievable that best represented single or stacked strut appearances.

Overlapping BVS were implanted in the coronary arteries of healthy swine. After 28 and 90, days the segments implanted with overlapped BVS were harvested and scanning electron microscopy undertaken. Results indicated that in the complete overlap with

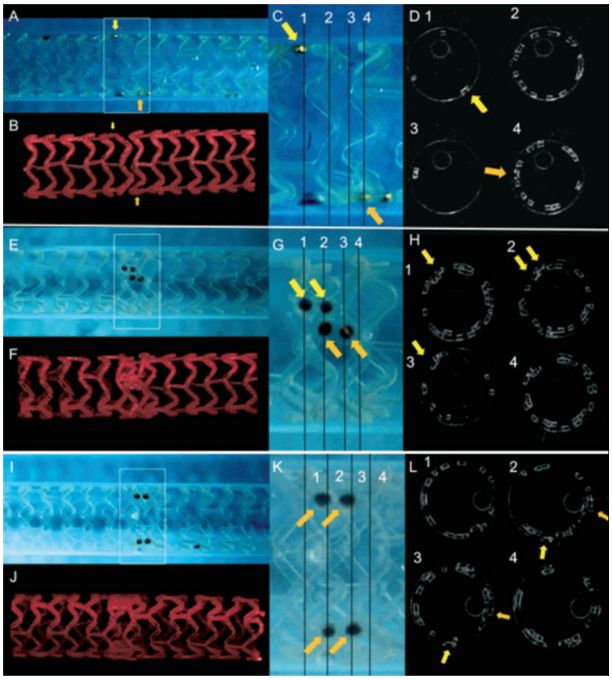

Figure 2. Outer appearances of the overlapping BVS in a phantom model (A, E and I), 3D reconstruction of OCT (B, F, J), magnified image of outer appearances (C, G and K) and corresponding cross-sectional OCT images (D, H and L) are presented. Yellow arrows indicate platinum marker positions. The upper panel represents "inter-digitating" or "adjacent positioning" of the BVS without overlap. The middle and lower panels represent the two differing forms of "complete overlap" that can be achieved. Note in the lower panel, there are a reduced number of stacked struts as compared to the middle panel – this is because in the lower panel, the platinum markers are positioned at 90 degrees to each other, this causes the majority of the overlapped struts to be positioned in the cell area between the struts rather than being stacked on top of each other.

multiple stacked struts, each with a thickness of at least 300 microns, (Figure 3a) there was a somewhat delayed endothelialisation at 28 days. Conversely, in the complete overlap with reduced number of stacked struts, thereby minimising the thickness of struts with a thickness of 300 microns with most struts having a thickness of 150 microns, endothelialisation appeared to be almost complete at 28 days (Figure 3b). At 90 days however, all forms of the overlap tested in the porcine model were fully covered and endothelialised (Figure 3c).

Replicating the forms of bench-tested overlapping BVS in humans

Trying to intentionally achieve any of the three overlapping BVS we have bench-tested during conventional percutaneous coronary intervention (PCI) is highly difficult and is more likely to occur by chance. With the "interdigitating" or adjacent positioning of BVS during conventional PCI, the main risk is leaving a gap ("geographical miss")[11] between the BVS with the consequential risk of restenosis. With the other two techniques, either type of complete overlap will occur only by chance as the markers need to be positioned at 90 degrees to each other in order to reduce the number of stacked struts, something that would be practically unachievable during conventional PCI.

Implantation in humans - case examples from the ABSORB EXTEND Single Arm Study

Case 1: "complete overlap with multiple number of stacked struts" (Figure 4)

A 66-year-old gentleman presented with stable angina (Canadian Cardiovascular Society angina Class II), he was an ex-smoker and had no other comorbidities. Coronary angiography demonstrated a significant long lesion, of at least 24 mm in length, in the proximal LAD, with quantitative coronary angiography (QCA) revealing an interpolated reference vessel diameter (RVD) at the minimal lumen diameter (MLD) of 2.33 mm. Proximal and distal Dmax of the intended implantation site were 2.50 mm each, which made this vessel suitable for implantation with two overlapping 3×18 mm BVS devices.[12] Pre-dilatation was undertaken with a 2.5 mm balloon and

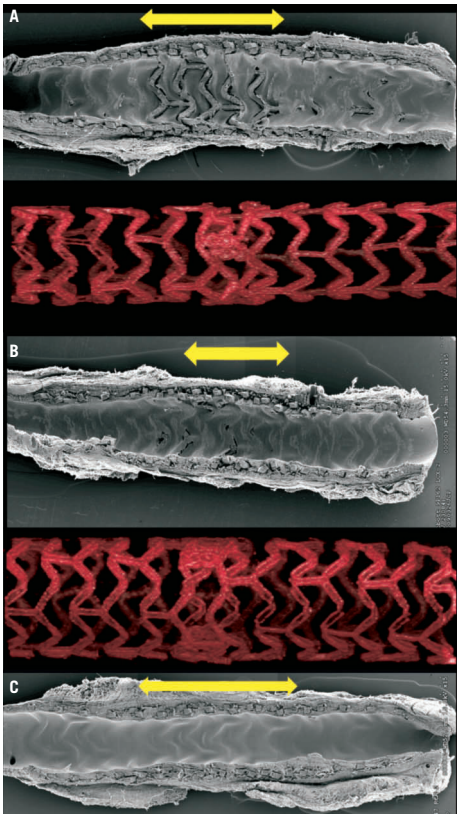

Figure 3. Scanning electron microscopic images acquired from healthy porcine coronary models representing the two forms of complete overlap of BVS. Delayed endothelialisation at 28 days is seen with multiple numbers of stacked struts at the overlap (corresponds to Figure 2e-2h) (a). Almost complete endothelialisation at 28 days is seen with reduced numbers of stacked struts at the overlap (corresponds to figure 2i-2l) (b). However at 90 days complete endothelialisation was seen with both overlapping types (c). Yellow arrows indicate overlapped segments.

two overlapping 3×18 mm BVS were implanted with at least 4 mm of overlap. Mild under-deployment of the BVS at the overlap was noted (Dmin 2.35 mm of deploying balloon) which required post-dilatation with the BVS deploying balloon to higher pressures. Post-implantation, IVUS and OCT imaging were carried out. Off-line 3D reconstruction and volume rendering of the OCT images were undertaken (INTAGE Realia; KGT, Tokyo, Japan), the methodology of which has previously been described.[13] As illustrated, the IVUS and OCT imaging clearly shows the complete overlap with multiple stacked struts as previously demonstrated in the bench and animal model.

A further example of complete overlap with multiple stacked struts is illustrated online (Online Appendix).

Case 2: "Combination of interdigitating and complete overlap" (Figure 5)

A 78-year-old male presented with stable angina (Canadian Cardiovascular Society angina Class III). He was an ex-smoker with no other risk factors. Coronary angiography demonstrated a single lesion in the obtuse marginal vessel, 14 mm in length with a 90% diameter stenosis (RVD 2.5 mm). Predilatation with a 2×15 mm balloon was performed without complication and a 3.0×18 mm BVS was deployed. Because of incomplete lesion coverage after initial BVS deployment, a second 3.0×18 mm BVS was deployed more distally overlapping with the first. No post-dilatation was performed and the patient made an uneventful recovery.

The area of overlap was calculated to be 2.7 mm by 2D OCT and when visualised on 3D OCT, the upper portion of the overlap appeared to be "interdigitating" and the lower part appeared to be completely overlapping with the struts of one BVS positioned within the cells of the other BVS (Figure 5b), thereby reducing the number of stacked struts.

Case 3: "Adjacent positioning of the BVS with minimal overlap" (Figure 6)

A 74-year-old female, with a history of hypertension and a previous myocardial infarction four months previously, presented with unstable angina (Braunwald Classification Class II). Coronary angiography identified a single lesion in the proximal RCA, 27 mm in length with a maximum of 90% diameter stenosis (RVD 2.8 mm) and TIMI 1 flow. Pre-dilatation was successfully performed with a 2×20 mm balloon and two overlapping BVS (3.0×18 mm) were subsequently deployed in the proximal RCA (maximum pressure 14 atm). No post-dilatation was performed.

2D and 3D OCT appeared to show an example of adjacent positioning of both BVS with a very minimal (0.5 mm) overlap between the two adjacent BVS in the proximal RCA.

2D OCT assessment of the overlap in humans

The 2D assessment of the non-overlapping BVS at baseline and follow-up has previously been conducted in the ABSORB cohort A and B studies.[3,7,10] As part of the OCT substudy in the ABSORB EXTEND Single Arm Study, OCT assessment of the overlapping BVS will be performed by an independent core laboratory. However, given the complexities of the overlapping struts as shown in the case examples, with the varying and unique patterns of strut distribution and stacking seen from frame to frame (Figure 7), the standard OCT methodology for assessing simple lesions cannot be applied to the overlap. It is therefore necessary to include all the frames in the overlap to allow for the accurate baseline and follow up assessment. This is in contrast to the assessment of non-overlapping segments from the ABSORB cohort A and B trials, where frames occurring every 1 mm were routinely analysed. Dependent on the length of the overlap, this will proportionately increase or decrease the number of frames for analysis.

The nomenclature and principles of analysis of OCT frames, previously applied to the shorter lesions in ABSORB cohort A and B, will be maintained for the overlap frames at both baseline and follow

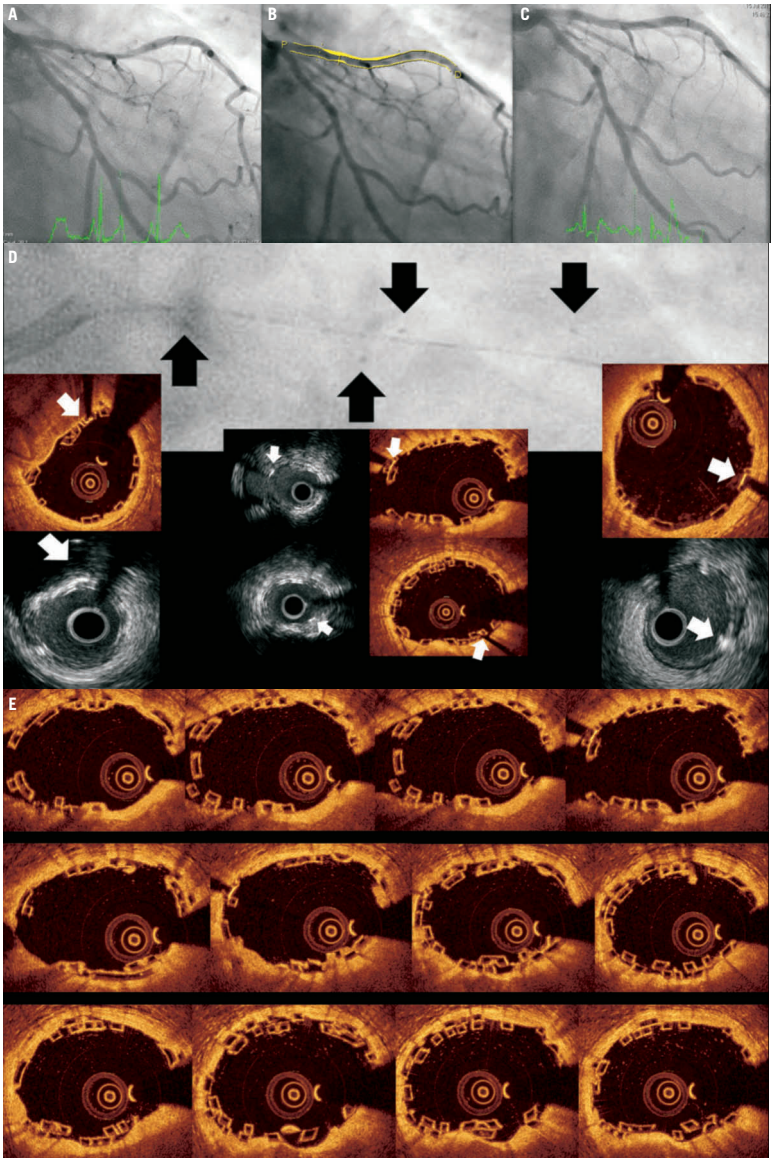

Figure 4. Case 1: "Complete overlap with multiple stacked struts" Coronary angiography revealed a long lesion in the proximal-mid LAD (A), interpolated RVD at MLD of 2.3 mm (B) and the final angiographic result post overlapping BVS implantation (C). OCT and IVUS identified the proximal, overlapping and distal platinum markers (D) - black arrows indicate the position of the markers seen on coronary angiography and white arrows the position of the markers seen on OCT and IVUS imaging. Consecutive OCT images across the overlap (pullback speed 20 mm/sec) (E) reveals multiple configurations of struts with numerous stacked struts seen.

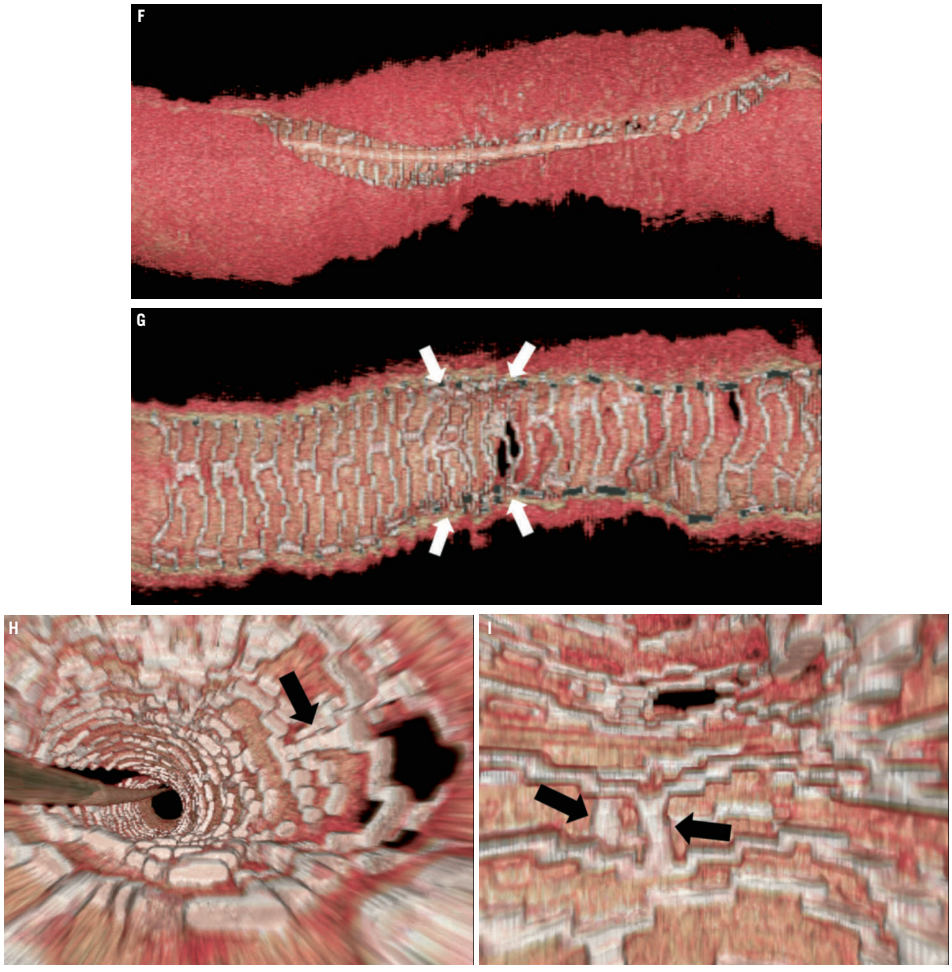

Figure 4 (cont). Three-dimensional volume rendered images of OCT images of the vessel, with guide-wire shadow (F), internal longitudinal view of the vessel showing the 4 mm overlap (G), a fly-through view (proximal-distal) of the vessel at the overlap (H) and a close up view of the vessel wall at the area of overlap (I). White arrows (G) represents the edge of each respective overlapping BVS, note the side-branch (septal branch) which marks the location of one end of the overlap in all views. Black arrows (H, I) represents the overlap in the fly-through view.

up (Table 1). However, in most cases, the methodology will vary slightly to reflect the complexities in strut distribution seen at the overlap. The study investigators will be aware that the frames analysed are from the overlap and that these frames will be investigated separately, as compared to the non-overlapped segments.

The following OCT parameters, with a brief description of the methodology, will be analysed for the overlap.

1. Lumen area (Figure 8)

This is calculated in the conventional way as with a simple, non-overlapping lesion. The internal vessel contour is drawn around with multiple correction points using the OCT software which then, through a process of "splining," automatically draws in the lumen which the operator can adjust so that it corresponds to the lumen contour. Of note is that the lumen contour on baseline OCT images will always be drawn behind (i.e., abluminally) the struts, even if they are embedded

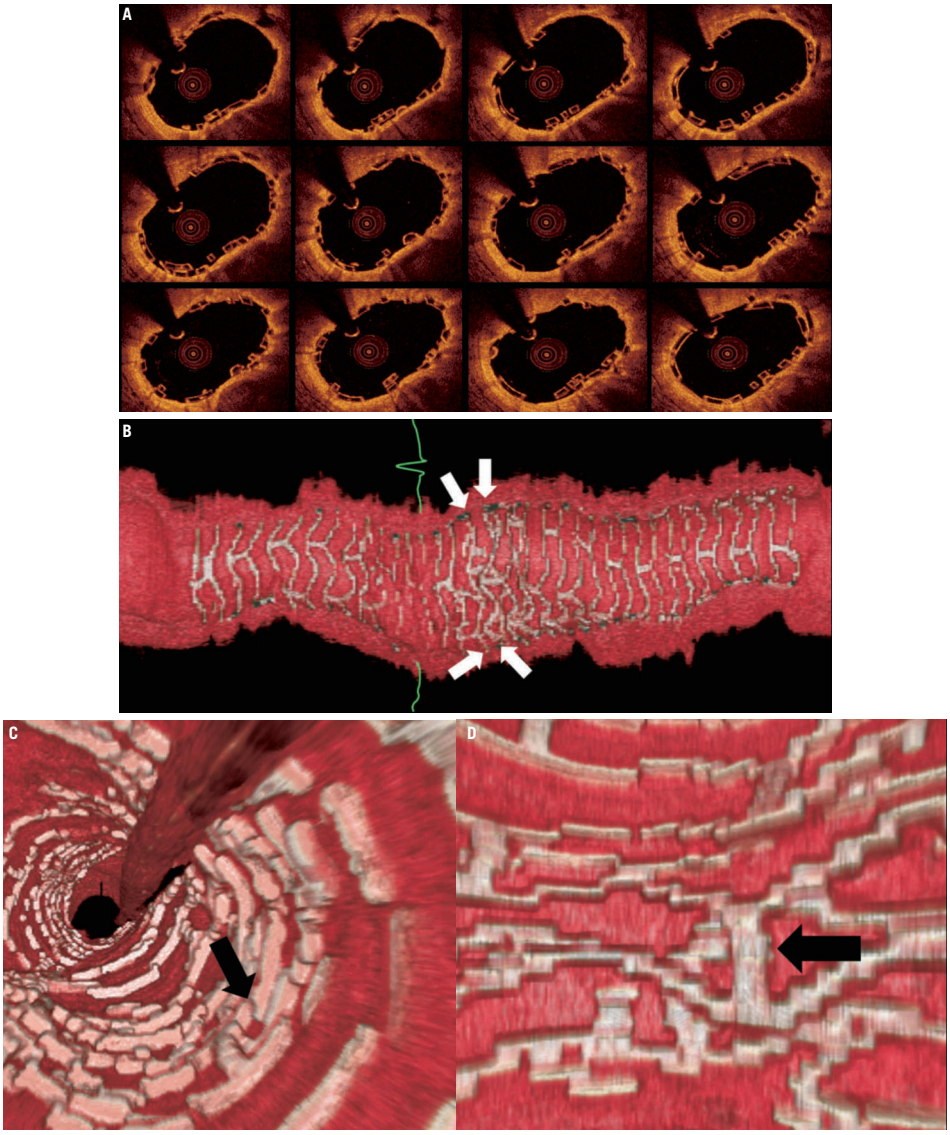

Figure 5. Case 2: Combination of "complete overlap" and "interdigitating struts without overlap." Consecutive OCT images across the overlap (pullback speed 20 mm/sec) (A) showing overlapping BVS struts with a small number of stacked struts. Longitudinal view of the vessel in 3D OCT (B). White arrows show the edge of each BVS with "interdigitating struts" at the upper margin and "complete overlap" at the lower end with the struts positioned in the cell area of the other BVS thereby reducing the number of stacked struts. Virtual fly-through view (proximal-distal) (C) with black arrow indicating overlapped segment and a close up view of the overlap (D) with black arrow indicating same position of overlap. The guidewire can clearly be seen (B). Note the "drop out" in the strut resolution to the left of the overlap (B) – this is an artefact due to a premature cardiac beat, this is a potential problem when slower pullback speeds of the FD-OCT probe are used.

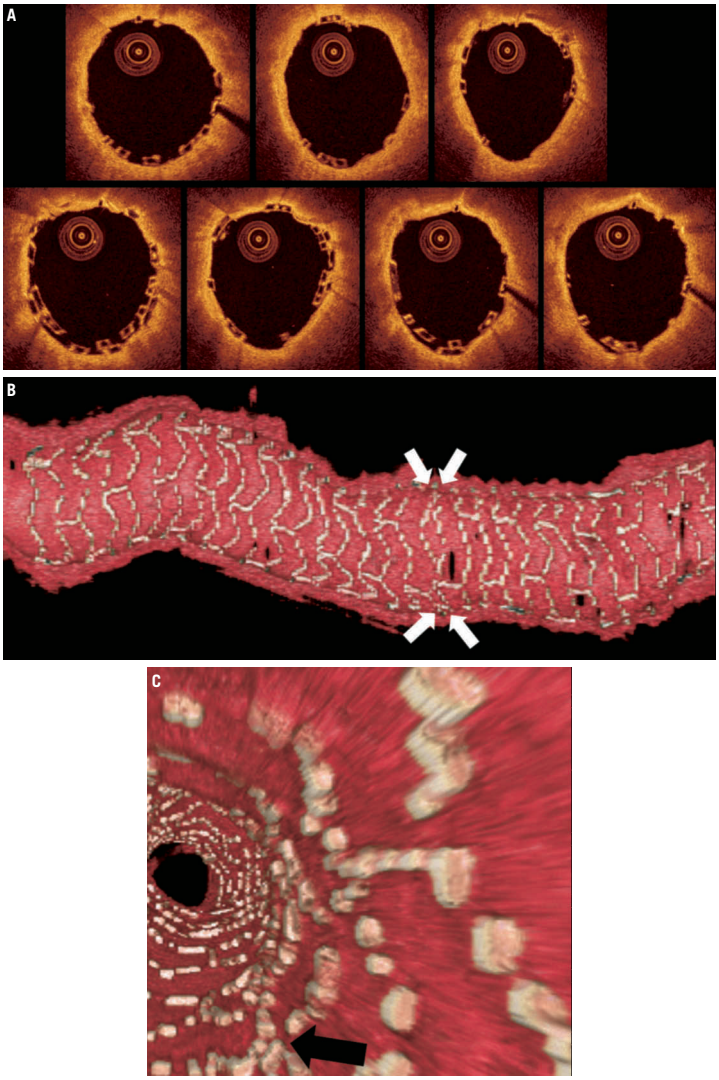

Figure 6. Case 3: BVS with minimal (0.5 mm) overlap. Consecutive OCT images across the overlap (pullback speed 20 mm/sec) (A). The OCT images show a few stacked struts in 4-5 OCT frames only. Longitudinal section of the vessel (B), white arrows show the edge of each BVS positioned with approximately 0.5 mm of overlap. Fly-through view (proximal-distal) (C) with black arrow indicating the minimal overlapped segments.

(Figure 8b – see struts in 12 o'clock position) on follow-up OCT, the lumen contour will be drawn behind the struts if they are uncovered only.

2. Scaffold area (Figure 11)

The scaffold area, as the name suggests, is the area contained within the BVS frame and in non-overlapping lesions, is usually a circular area drawn around all the abluminal sides ("back side") of the BVS struts. The scaffold area is an important concept for bioresorbable scaffolds, as changes can signal losses in material radial strength or structural integrity. Unfortunately drawing the scaffold area at the overlap can potentially be difficult, given that

Table 1. OCT parameters for measurement at the overlap.

OCT Parameters to be measured at the overlap
Lumen area
Scaffold area
Black core area
Flow area
Thickness of struts to assess strut coverage – thickness of single strut, thickness of single strut at side branch – thickness of stacked struts, thickness of stacked struts at the side branch
Incomplete scaffold apposition (ISA)
Black core ISA
Thickness ISA

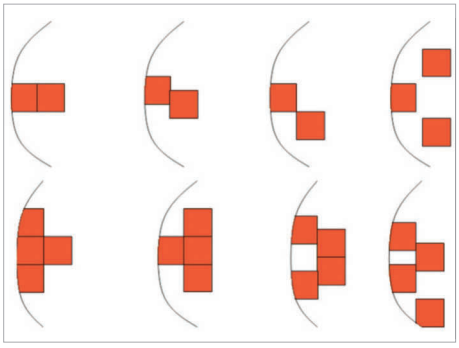

Figure 7. Illustration to demonstrate the varying appearances of the stacked BVS struts seen on OCT analysis. Stacked struts and stacked strut clusters (collections of struts all apposed to each other) are shown.

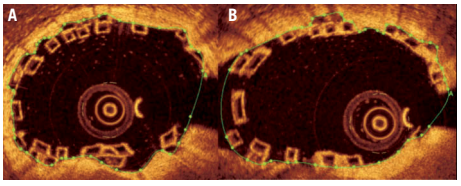

Figure 8. Lumen area in an overlapping BVS segment. The lumen area is drawn in the conventional way by following the contours of the lumen in non-bifurcating (A) and bifurcating (B) vessels.

there are multiple stacked struts clusters (collections of struts all apposed to each other) and the operator potentially not knowing around which struts to draw the scaffold area.

The OCT image of a BVS 1.1 strut consists of a "black core" area surrounded by a "white frame" (Figure 9). The white frame is interpreted to comprise an area of backscatter from the surfaces of the BVS strut, whereas the black core is interpreted as representing the completely radiolucent bulk material. The BVS strut thickness is approximately 150 microns. When the strut becomes covered at follow-up (Figure 9), the black core area

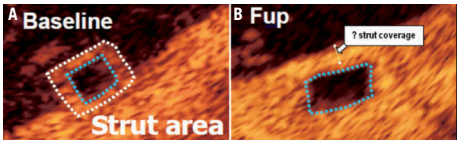

Figure 9. Characteristics of BVS 1.1 strut at baseline and six month follow-up (case example form ABSORB Cohort B). At baseline, each strut consists of a black core surrounded by a white frame (A). At six month follow-up (b) the black core remains intact, however when the strut becomes covered, trying to identify the white frame is not possible with reliability as demonstrated (B).

remains translucent. However, trying to identify the white frame with reliability is difficult and subjective. In the overlap situation, where the struts are either apposing each other or even embedded in the vessel wall, trying to again identify the white frame with reliability is also difficult (see case examples). Conversely, long-term animal studies have shown that the black core area seen on OCT, although replaced by proteoglycans upon bioresorption of the polymer, retains its shape and translucency on OCT at up to two years follow-up;[9] the black core area is therefore a constant point of reference to measure from.

We therefore recommend that the scaffold area be measured from the abluminal side of the black core area. Wherever the struts (either single strut of part of a stacked strut cluster) appose the vessel wall, the contour line of the scaffold area is drawn around the abluminal side of the black core for those particular struts, with a correction point marked at the halfway position of the abluminal black core border (Figure 10). The computer software can then use these correction points to create the scaffold area through the splining process as previously described. The rationale being that the BVS delivers its radial strength through areas of the scaffold in apposition to the vessel wall, and any overlapping struts not apposing the vessel wall will deliver their radial strength to the vessel wall through their apposition to struts which already appose the vessel wall.

In situations where a strut or strut cluster is seen to be not apposing the vessel wall, the scaffold area is drawn around the abluminal side of the black core of the struts that are the nearest to the vessel wall (Figure 11). Struts not apposing the vessel wall at the overlap do not necessarily imply incomplete scaffold apposition (ISA); this is more likely to be related to either the strut being located at a side branch, or it being part of a stacked strut cluster that typically is apposing the wall on the next few OCT frames.

It should be noted that only one correction point per strut is required for the computer software to create, through the process of splining, the scaffold area when performing the OCT analysis of the overlap. (Figure 11). Whilst placing two correction points per strut may make the scaffold area more agreeable to the eye, i.e., it being more circular, we have found that the actual differences in terms of the scaffold area appears to be insignificant as illustrated (Figure 12).

3. Black core area (Figure 13)

The black core area for each frame is calculated as illustrated. This is used for calculating the "flow area" as described below.

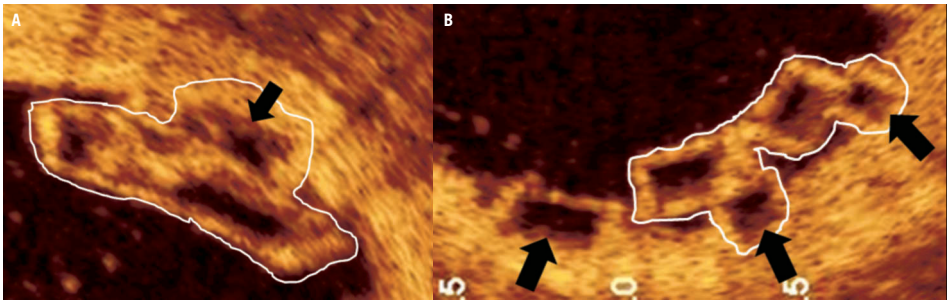

Figure 10. Methodology of drawing the scaffold area around the single strut, the stacked struts and stacked strut clusters of the BVS. The scaffold area is drawn around the abluminal side of the black core area in a single strut. In a stacked strut cluster (A), the scaffold area is drawn around the abluminal side of the black core area (black arrow) at each strut that apposes the vessel endothelium (A, B), as these are points of scaffolding to the vessel. White boundaries indicate a stacked strut cluster.

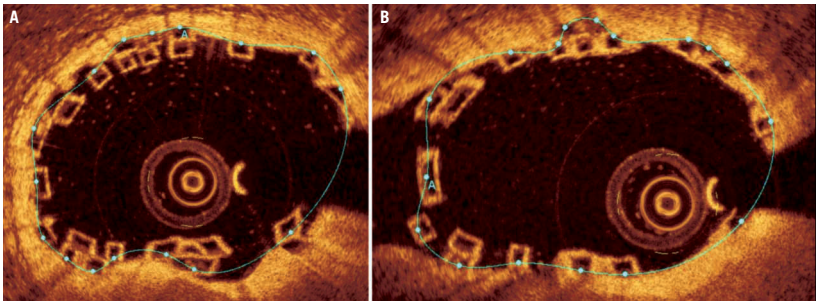

Figure 11. Scaffold area in the overlapping BVS in the main-branch (A) and side-branch (B). (A) This is drawn from the "backside" (i.e., abluminal side) of the black core area of the outermost strut or stacked strut cluster (at the point of all the struts apposing the vessel endothelium) apposing the vessel wall. Where there does not appear to be any apposition of a single strut or stacked strut cluster to the vessel endothelium, the contour of the scaffold area continues to follow the outermost (most abluminal) scaffold strut or stacked strut cluster.

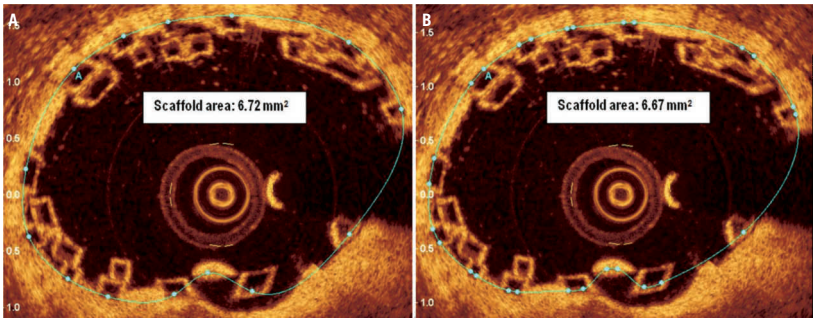

Figure 12. Scaffold area requires one correction point per black-core area to allow the computer software to create the scaffold area through a process of "splining." One (A) or two correction points (B) can be placed for each black-core area. Although a more smoother and visual appealing scaffold area is seen with two markers per black core area – the actual difference in terms of scaffold area is not significant.

4. Flow area (Figure 14)

Effectively the flow area is the area of the vessel where blood flows through. This is calculated as the lumen area minus the black core area. Theoretically, the area occupied by the white frame of the BVS strut should also be subtracted from the flow area; however, because of the unreliability of measuring the white frame area as previously described, this has been omitted from the flow area calculation. As the flow area will be calculated at baseline and follow up, the white

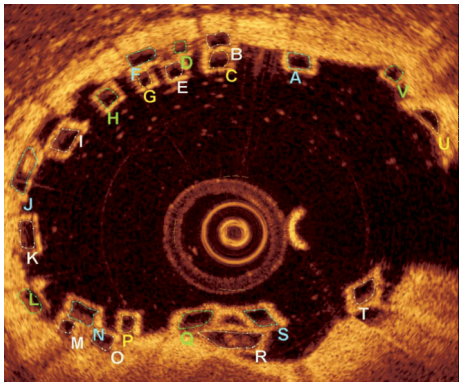

Figure 13. Black core area. Each single strut or stacked strut cluster has its individual black core area measured to calculate the strut area for each OCT image at the overlap.

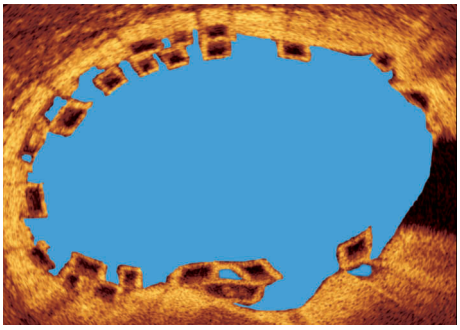

Figure 14. Flow area. As illustrated – this is the lumen area minus the strut area.

frame area in both the baseline and follow up flow areas will effectively cancel each other out when the difference in flow area is calculated. At follow up, if all the struts are covered, the flow area will equal the lumen area. If, however, all the struts are not covered, the flow area will equal lumen area minus uncovered black core/white frame areas.

5. Thickness of single struts and thickness of stacked struts to assess strut coverage (Figure 15)

The thickness of struts is taken from the midpoint of the endoluminal side of the black core area in single struts to the lumen area boundary (thickness of single strut), from the midpoint of the most endoluminal strut in stacked strut clusters to the lumen area boundary (thickness of stacked struts) and also from the endoluminal side of a stacked strut cluster to the lumen area boundary, when more than 50% of the more abluminal strut is not covered by the more endoluminal strut.

In side branches this principle is maintained for both single struts (thickness of single strut at side branch) and stacked strut clusters (thickness of stacked struts at side branch) with the thickness measured to the presumed lumen area boundary.

At follow-up OCT, the thickness of the covered single or stacked struts will have a positive value in covered struts, whilst uncovered struts will continue to have a negative value as was seen at baseline.

6. Black core ISA and thickness ISA (Figure 16)

Incomplete scaffold apposition (ISA) is measured both at baseline and follow-up to assess for procedural or late acquired ISA. As the black core area is constant, all ISA measurements will be made from here. The "thickness ISA" is measured from the abluminal side of the white frame zone to the lumen area boundary. The black core ISA is measured from the abluminal side of the black core area, where the margin is very clear (Figure 16), to the lumen area boundary as illustrated.

Discussion

Based on the bench-work and subsequent data from the animal model, it would appear that either the "interdigitating position" or complete overlap with reduced number of stacked struts would be

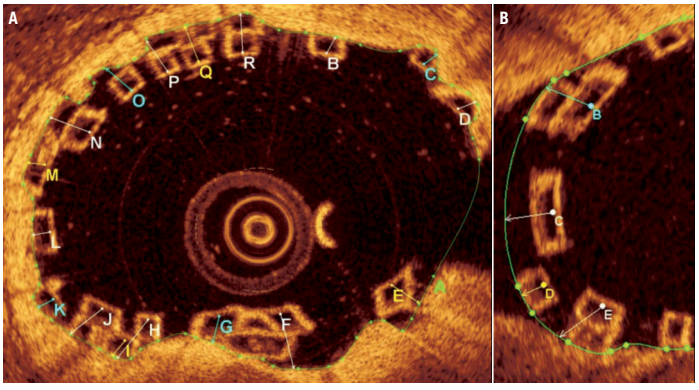

Figure 15. Thickness of single struts and thickness of stacked struts in a non-bifurcating (A) and bifurcating (B) vessel. Green area represents the lumen area boundary.

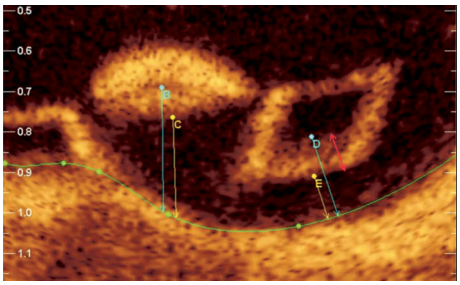

Figure 16. Black core ISA and thickness ISA. The "black core ISA" (B, D) and the "thickness ISA" (C, E) are clearly demonstrated. Note the black core ISA is taken from the abluminal side of black core ISA where the border is very clear – the red arrow indicates a zone from the abluminal white frame to the black core area where the margin of the black core cannot be clearly be defined. The black core area should therefore not be measured from within this zone.

the ideal solutions in order to ensure more rapid endothelialisation at the overlap. By using these methods, the number of stacked struts would be minimised, remembering that each stacked strut has a minimum thickness of 300 microns as opposed to a single strut thickness of 150 microns, and that the evidence from the animal model suggests that these stacked struts would potentially be at risk of delayed endothelialisation. However, both of these overlapping techniques cannot be performed angiographically with reliability, and are more likely to occur by chance rather than by procedural technique as previously described.

The occurrences of reduced endothelialisation at the overlap has previously been described with overlapping metallic drug eluting stents (DES).[14,15] Finn et al 2005[14] showed in a rabbit iliac artery model that both overlapping sirolimus (SES) and paclitaxel (PES) eluting stents demonstrated evidence of a persistent inflammatory response, fibrin deposition and delayed endothelialisation. With overlapping metallic DES, damage or cracking of the polymer[16,17] can potentially occur at the overlap with the consequent risk being persistent foreign body inflammation. In clinical practice however, the evidence for a lack of endothelialisation at the overlap with metallic DES is more controversial. Some studies have suggested an association between higher number of uncovered struts and adverse events[18,19] and other studies have failed to make this association[20,21] or even suggested differences in coverage pattern (but not in the number of uncovered struts) dependent on the type of DES implanted.[21]

With the BVS 1.1, the polymer is both bioresorbable and biocompatible, thereby the scaffold will gradually bioresorb from six months to 24 months and the inflammatory response to the polymer should be minimal.[9] Thus the polymer and scaffold substrates are removed, theoretically eliminating the risk of late stent ("scaffold") thrombosis. Based on the results of the bench-work and animal models, perhaps the more practical and pragmatic solution in implanting overlapping BVS is positioning each BVS very close to each other and ensuring only a small territory of overlap occurs between each BVS i.e., minimal overlap as shown in case 3. This would potentially minimise the numbers of stacked struts, limit the risk of a gap occurring between the BVS and theoretically increase the rate towards complete endothelialisation. The outcomes from the OCT substudy in the ABSORB EXTEND Single Arm Study investigating the overlap are therefore awaited with interest.

Acknowledgements

The first author wishes to acknowledge the support of The Dickinson Trust Travelling Scholarship Fund, Manchester Royal Infirmary, Manchester, England, UK.

References

1. Ormiston JA, Serruys PW, Regar E, Dudek D, Thuesen L, Webster MW, Onuma Y, Garcia-Garcia HM, McGreevy R, Veldhof S. A bioabsorbable everolimus-eluting coronary stent system for patients with single de-novo coronary artery lesions (ABSORB): a prospective open-label trial. *Lancet* 2008;371:899-907.

2. Waksman R. Biodegradable stents: they do their job and disappear. *J Invasive Cardiol* 2006;18:70-74.

3. Serruys PW, Ormiston JA, Onuma Y, Regar E, Gonzalo N, Garcia-Garcia HM, Nieman K, Bruining N, Dorange C, Miquel-Hebert K, Veldhof S, Webster M, Thuesen L, Dudek D. A bioabsorbable everolimus-eluting coronary stent system (ABSORB): 2-year outcomes and results from multiple imaging methods. *Lancet* 2009;373:897-910.

4. Onuma Y, Serruys PW, Ormiston JA, Regar E, Webster M, Thuesen L, Dudek D, Veldhof S, Rapoza RJ. Three-year results of clinical follow-up after a bioresorbable everolimus-eluting scaffold in patients with de novo coronary artery disease: the ABSORB trial. *EuroIntervention* 2010; in press.

5. Tanimoto S, Serruys PW, Thuesen L, Dudek D, de Bruyne B, Chevalier B, Ormiston JA. Comparison of in vivo acute stent recoil between the bioabsorbable everolimus-eluting coronary stent and the everolimus-eluting cobalt chromium coronary stent: insights from the ABSORB and SPIRIT trials. *Catheter Cardiovasc Interv* 2007;70:515-523.

6. Tanimoto S, Bruining N, van Domburg RT, Rotger D, Radeva P, Ligthart JM, Serruys PW. Late stent recoil of the bioabsorbable everolimus-eluting coronary stent and its relationship with plaque morphology. *J Am Coll Cardiol* 2008;52:1616-1620.

7. Ormiston J, Webster M. Absorbable coronary stents. *Lancet* 2007;369:1839-1840.

8. Okamura T, Garg S, Gutierrez-Chico JL, Shin ES, Onuma Y, Garcia-Garcia HM, Rapoza RJ, Sudhir K, Regar E, Serruys PW. In vivo evaluation of stent strut distribution patterns in the bioabsorbable everolimus-eluting device: an OCT ad hoc analysis of the revision 1.0 and revision 1.1 stent design in the ABSORB clinical trial. *EuroIntervention* 2010;5:932-938.

9. Onuma Y, Serruys PW, Perkins L, Okamura T, Gonzalo N, Garcia-Garcia HM, Regar E, Kamberi M, Powers J, Rapoza RJ, van Beusekom H, van der Giessen W, Virmani R. Intracoronary optical coherence tomography (OCT) and histology at 1 month, at 2, 3 and 4 years after implantation of everolimus-eluting bioresorbable vascular scaffolds in a porcine coronary artery model: An attempt to decipher the human OCT images in the ABSORB trial. *Circulation* 2010;122:2288-300.

10. Serruys PW, Onuma Y, Ormiston JA, de Bruyne B, Regar E, Dudek D, Thuesen L, Smits PC, Chevalier B, McClean D, Koolen J, Windecker S, Whitbourn R, Meredith I, Dorange C, Veldhof S, Miquel-Hebert K, Rapoza R, García-García HM. Evaluation of the second generation of a bioresorbable everolimus drug-eluting vascular scaffold for

treatment of de novo coronary artery stenosis: six-month clinical and imaging outcomes. *Circulation* 2010;122:2301-12.

11. Costa MA, Angiolillo DJ, Tannenbaum M, Driesman M, Chu A, Patterson J, Kuehl W, Battaglia J, Dabbons S, Shamoon F, Flieshman B, Niederman A, Bass TA. Impact of stent deployment procedural factors on long-term effectiveness and safety of sirolimus-eluting stents (final results of the multicenter prospective STLLR trial). *Am J Cardiol* 2008;101:1704-1711.

12. Gomez-Lara J, Brugaletta S, Onuma Y, Farooq V, Thuesen L, McClean D, Koolen J, Ormiston JA, Windecker S, Whitbourn R, Dudek D, Dorange C, Veldhof S, Rapoza R, Regar E, Garcia-Garcia HM, Serruys PW. Angiographic maximal luminal diameter and appropriate deployment of the everolimus-eluting Bioresorbable Vascular Scaffold as assessed by optical coherence tomography. *EuroIntervention* in press.

13. Okamura T, Onuma Y, Garcia-Garcia HM, Regar E, Wykrzykowska JJ, Koolen J, Thuesen L, Windecker S, Whitbourn R, McClean DR, Ormiston JA, Serruys PW. 3-Dimensional optical coherence tomography assessment of jailed side branches by bioresorbable vascular scaffolds: a proposal for classification. *JACC Cardiovasc Interv* 2010;3:836-844.

14. Finn AV, Kolodgie FD, Harnek J, Guerrero LJ, Acampado E, Tefera K, Skorija K, Weber DK, Gold HK, Virmani R. Differential response of delayed healing and persistent inflammation at sites of overlapping sirolimus- or paclitaxel-eluting stents. *Circulation* 2005;112:270-278.

15. Lim SY, Jeong MH, Hong SJ, Lim do S, Moon JY, Hong YJ, Kim JH, Ahn Y, Kang JC. Inflammation and delayed endothelization with overlapping drug-eluting stents in a porcine model of in-stent restenosis. *Circ J* 2008;72:463-468.

16. Otsuka Y, Chronos NA, Apkarian RP, Robinson KA. Scanning electron microscopic analysis of defects in polymer coatings of three commercially available stents: comparison of BiodivYsio, Taxus and Cypher stents. *J Invasive Cardiol* 2007;19:71-76.

17. Basalus MW, Ankone MJ, van Houwelingen GK, de Man FH, von Birgelen C. Coating irregularities of durable polymer-based drug-eluting stents as assessed by scanning electron microscopy. *EuroIntervention* 2009;5:157-165.

18. Tahara S, Bezerra HG, Sirbu V, Kyono H, Musumeci G, Rosenthal N, Guagliumi G, Costa MA. Angiographic, IVUS and OCT evaluation of the long-term impact of coronary disease severity at the site of overlapping drug-eluting and bare metal stents: a substudy of the ODESSA trial. *Heart* 2010;96:1574-1578.

19. Costa JR, Jr., Sousa A, Moreira AC, Costa RA, Cano M, Maldonado G, Campos C, Carballo M, Pavanello R, Sousa JE. Incidence and predictors of very late (>or=4 years) major cardiac adverse events in the DESIRE (Drug-Eluting Stents in the Real World)-Late registry. *JACC Cardiovasc Interv* 2010;3:12-18.

20. Aoki J, Mintz GS, Weissman NJ, Mann JT, Cannon L, Greenberg J, Grube E, Masud AR, Koglin J, Mandinov L, Stone GW. Chronic arterial responses to overlapping paclitaxel-eluting stents: insights from serial intravascular ultrasound analyses in the TAXUS-V and -VI trials. *JACC Cardiovasc Interv* 2008;1:161-167.

21. Guagliumi G, Musumeci G, Sirbu V, Bezerra HG, Suzuki N, Fiocca L, Matiashvili A, Lortkipanidze N, Trivisonno A, Valsecchi O, Biondi-Zoccai G, Costa MA. Optical coherence tomography assessment of in vivo vascular response after implantation of overlapping bare-metal and drug-eluting stents. *JACC Cardiovasc Interv* 2010;3:531-539.

Online data supplement

Moving image. Demonstration of the phantom model used to assess the overlapping BVS. The recording on the right shows the pullback of the OCT fibreoptic imaging core and the recording on the left demonstrates the corresponding OCT images obtained during the pullback.

Figure M. 3D OCT demonstrating a virtual fly-through (proximal-distal) of the vessel (pullback speed of FD-OCT probe 10 mm/sec). The treated lesion was 28 mm in length with a maximum of 60% diameter stenosis (RVD 2.5 mm) and TIMI 3 flow; two overlapping BVS (3.0×18 mm) were successfully deployed (maximum pressure 14 atm). No post-dilatation was performed. The overlap in the mid RCA can clearly be visualised (6 mm) with multiple stacked struts.

CHAPTER 4 METHODOLOGICAL CONSIDERATIONS IN THE APPLICATION OF OPTICAL COHERENCE TOMOGRAPHY FOR THE EVALUATION OF BIORESORBABLE SCAFFOLDS

4.2 Spatial distribution and temporal evolution of optical coherence tomography "white dots" in the poly-L-lactide backbone of an intracoronary bioresorbable scaffold: association to polymer crazes during crimping of the device.

Gutierrez-Chico JL, **Radu MD**, Diletti R, Sheehy A, Glauser T, Harrington J, Rapoza R, Onuma Y, Serruys PW.

Circulation Journal. 2012;76:342-50.

Spatial Distribution and Temporal Evolution of Scattering Centers by Optical Coherence Tomography in the Poly(L-Lactide) Backbone of a Bioresorbable Vascular Scaffold

Juan Luis Gutiérrez-Chico, MD, PhD; Maria D. Radu, MD; Roberto Diletti, MD; Alexander Sheehy, PhD; Mary Beth Kossuth, PhD; James P. Oberhauser, PhD; Thierry Glauser, PhD; Joel Harrington, PhD; Richard J. Rapoza, PhD; Yoshinobu Onuma, MD; Patrick W. Serruys, MD, PhD

Background: Scattering centers (SC) are often observed with optical coherence tomography (OCT) in some struts of bioresorbable vascular scaffolds (BVS). These SC might be caused by crazes in the polymer during crimp-deployment (more frequent at inflection points) or by other processes, such as physiological loading or hydrolysis (eventually increasing with time). The spatial distribution and temporal evolution of SC in BVS might help to understand their meaning.

Methods and Results: Three patients were randomly selected from 12 imaged with Fourier-domain OCT at both baseline and 6 months in the ABSORB cohort B study (NCT00856856). Frame-by-frame analysis of the SC distribution was performed using spread-out vessel charts, and the results from baseline and 6 months were compared. A total of 4,328 struts were analyzed. At baseline and follow-up all SC appeared at inflection points. No significant difference was observed between baseline and 6 months in the number of SC struts (14.9 vs. 14.5%, P=0.754) or in the distribution of SC. The proportion and distribution of SC did not vary substantially among the patients analyzed.

Conclusions: The SC observed in OCT imaging of the BVS are located exclusively at inflection points and do not increase with time. These findings strongly suggest that SC are caused by crazes in the polymer during crimp-deployment, ruling out any major role of hydrolysis or other time-dependent processes.

Key Words: Coronary stenosis; Drug-eluting stents; Optical coherence; Poly(lactide); Tomography

The Abbott Vascular bioresorbable vascular scaffold (BVS) (Santa Clara, CA, USA) consists of a semi-crystalline poly(L-lactide) (PLLA) backbone and conformal coating of amorphous poly(D,L-lactide) (PDLLA) and the antiproliferative agent, everolimus. The molecular weight of the BVS polymers is degraded primarily through hydrolysis of the ester bonds present in each monomer subunit. Crystalline residues with a characteristic dimension less than 2 μm are phagocytosed by macrophages. Ultimately, PLLA and PDLLA degrade to lactate, which is metabolised via the Krebs' cycle and other metabolic pathways,[1] similarly to other biodegradable polymers.[2] Complete polymer resorption occurs approximately 2 years after implantation.[3,4] The BVS is laser-cut from a single piece of polymer tubing and then crimped onto a balloon. The structural design of the BVS consists of 19 W-shaped rings connected longitudinally by straight links (**Figure 1**). The BVS has delivered acceptable and durable clinical and angiographic results up to 2 years post-procedure when the scaffold has been completely resorbed.[5,6]

Unlike metallic stents,[2,7–11] the translucency of the processed polylactide used in the Abbott Vascular BVS makes it particularly suitable for optical coherence tomography (OCT) imaging. The optical radiation can penetrate the translucent polymer, with significant backscattering occurring only at the borders of struts where the refractive index of the medium changes. Alternatively, the strut core has been characterized as a "black box",[3,5,6] signifying the absence of refractive index changes within the material (**Figure 2**). However, some OCT images show a focal hyperintense signal in the strut core without apparent contact with either the axial or transversal strut

Received July 19, 2011; revised manuscript received September 17, 2011; accepted October 7, 2011; released online November 19, 2011
Time for primary review: 38 days

Erasmus Medical Centre, Thoraxcentre, Interventional Cardiology Department, Rotterdam, The Netherlands (J.L.G.-C., M.D.R., R.D., Y.O., P.W.S.) and Abbott Vascular, Santa Clara, California, USA (A.S., M.B.K., J.P.O., T.G., J.H., R.J.R.)

Clinical trial registration: NCT00856856; URL: http://clinicaltrials.gov

Mailing address: Patrick W. Serruys, MD, PhD, FESC, FACC, Professor, Head of Interventional Cardiology, Erasmus MC, Thoraxcenter, Ba583a. 's-Gravendijkwal 230, 3015 CE Rotterdam, The Netherlands. E-mail: p.w.j.c.serruys@erasmusmc.nl

ISSN-1346-9843 doi:10.1253/circj.CJ-11-0726

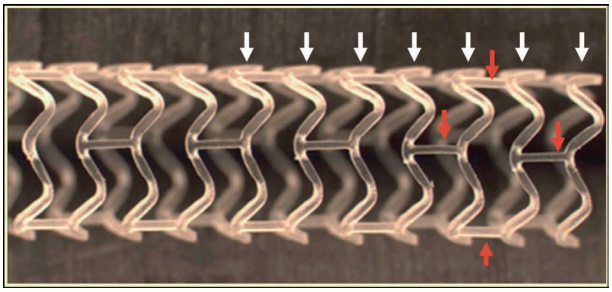

Figure 1. Structure of the Abbott Vascular bioresorbable vascular scaffold revision 1.1. An 18-mm length scaffold consists of 19 W-shaped rings (white arrows), connected with the adjacent rings by 3 straight longitudinal units (red arrows).

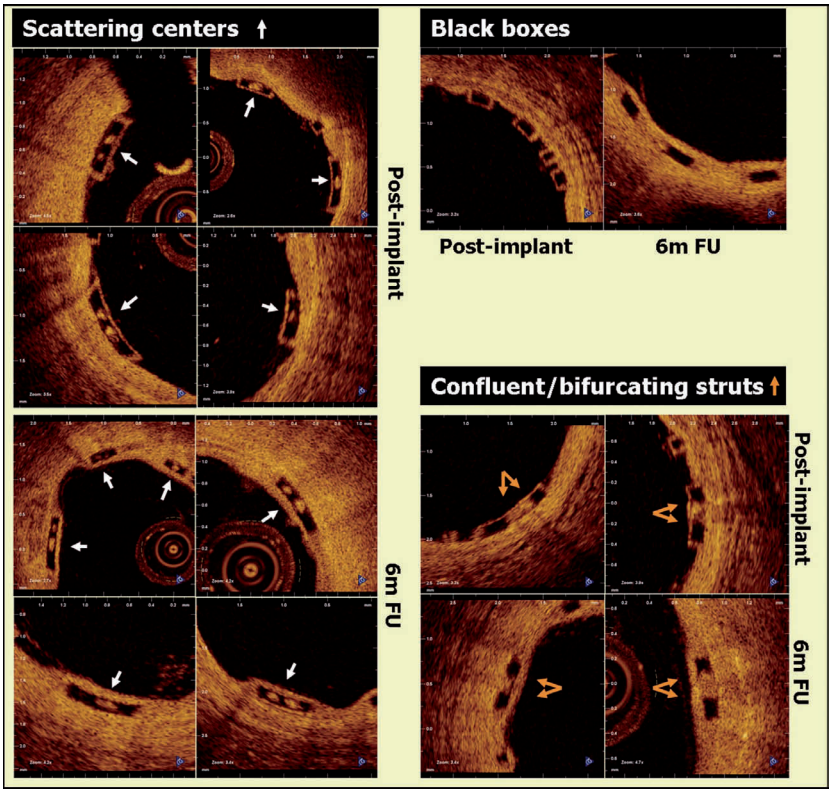

Figure 2. Definition of scattering centers (SC). The struts classified as having SC present a focal hyperintense backscattering signal in the core of the strut, which typically does not reach either the axial or the transversal strut edges, thus taking the appearance of a "dot" inside a box (**Left**). Notice the difference with the typical "black box" appearance of the BVS struts (**Right upper**). It is important to differentiate between SC from the optical appearance of confluent or bifurcating struts, where there is also a hyperintense signal in the core of the strut; however, in this case, it reaches its axial edges (**Right lower**).

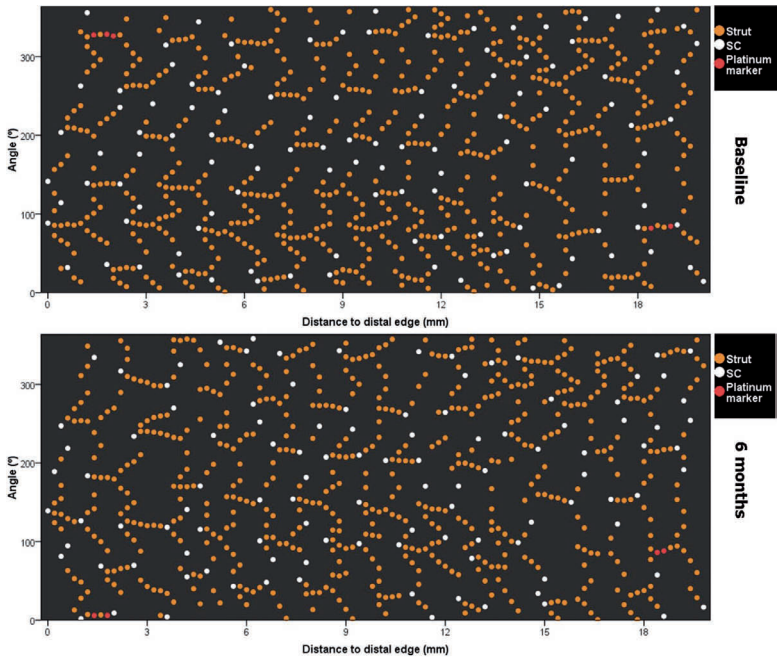

Figure 3. Patient 3: spread-out vessel chart showing the spatial distribution of the struts with scattering centers in the scaffolded vessel immediately post-implantation (baseline) and at the 6-month follow-up. The x-axis represents the distance from the distal edge of the stent to the strut; the y-axis represents the angle where the strut is located in the circular cross-section respect to the center of gravity of the vessel, taking as reference 0° the position at 3 o'clock. The result is a graphic representation of the spatial distribution of the struts along the scaffolded vessel as if it had been cut along the reference angle (0°) and spread out on a flat surface.

edges (**Figure 2**). The cause of this backscattering signal remains to be elucidated: it might reflect a change in the polymer's optical properties induced by the hydrolysis process or it might correspond to deformation-induced crazes in the backbone of the PLLA polymer, the latter preferentially located at hinge points of the BVS structure. The existence of regions with accelerated hydrolysis in humans or the presence of polymer crazes, eventually growing under continuous physiologic load, could both jeopardize the structural integrity of the BVS required to be functional.

This study explored the hypothesis that scattering centers (SC) observed in strut cores at baseline OCT imaging are derived from polymer crazing caused by the mechanical deformation of scaffold crimping and deployment, analyzing whether the spatial distribution of the SC at baseline is consistent with that hypothesis. The temporal evolution of these SC at 6 months permits assessment of the eventual influence of physiological loading, polymer degradation, or tissue integration in the genesis of the SC.

Methods

Study Sample

The ABSORB Cohort B registry (NCT00856856) design has been published elsewhere.[3] The study enrolled patients older than 18 years, with diagnosis of stable or unstable angina pectoris or silent ischemia, and de novo lesions in native coronary arteries amenable for percutaneous treatment with the BVS (percent diameter stenosis ≥50% by visual estimation, reference vessel diameter 2.5–3.5 mm). Exclusion criteria included: acute myocardial infarction, unstable arrhythmias, left ventricular ejection fraction ≤30%, restenotic lesions, lesions located in the left main coronary artery or in bifurcations involving a side branch >2 mm, a second clinically or hemodynamically significant lesion in the target vessel, documentation of intracoronary thrombus, or initial TIMI 0 flow. For invasive follow-up purposes, the cohort was subdivided into 2 groups: cohort B1, undergoing multimodality invasive imaging (QCA, intravascular ultrasound, virtual histology, palpography, and OCT) at 6 and 24 months; and cohort B2, with an identical imaging follow-up protocol scheduled at 12 and 36 months. All of the study lesions were treated with the BVS Revision 1.1 design

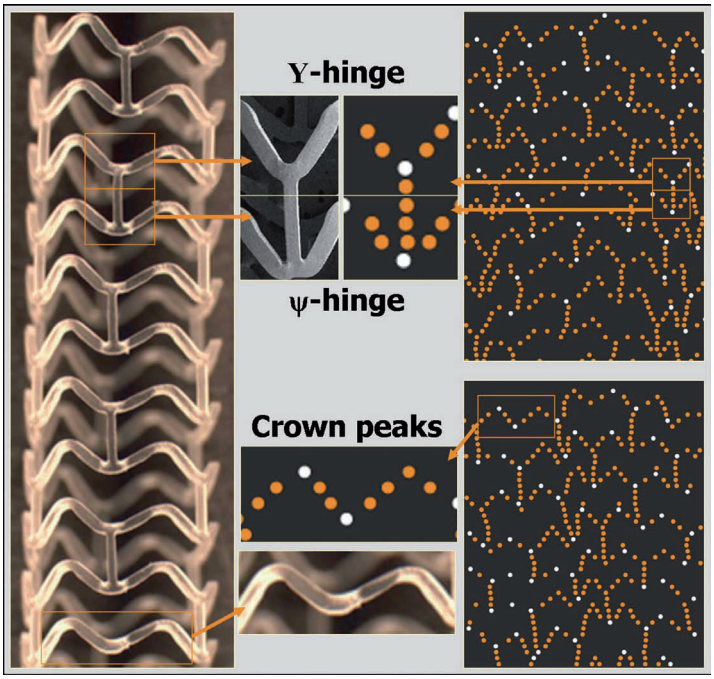

Figure 4. Schematic representation of the 3 types of hinges in the scaffold structure and their locations in the spread-out vessel diagram. The longitudinal connectors between the rings define inflection points that include ψ- and Y-hinges (see schematic). Angulations in the zig-zag ring at a point where there is no longitudinal connector are denominated "crown peaks". The scaffold has 19 rings; each ring contains 3 ψ-hinges, 3 Y-hinges and 6 crown peaks, except the most distal ring (3 ψ-hinges and 9 crown peaks) and the most proximal ring (3 Y-hinges and 9 crown peaks).

3.0×18 mm (**Figure 1**). The registry was approved by the ethics committee at each participating institution, and each patient gave written informed consent before inclusion.

For the present pilot study, a random sample of 3 patients in cohort B1 was selected among those patients who had undergone OCT imaging with a Fourier-domain C7 system (Lightlab Imaging, Westford, MA, USA) at baseline and at the 6-month follow-up.

OCT Study

OCT pullbacks were obtained at baseline and follow-up with a Fourier-domain C7 system using a Dragonfly catheter (Lightlab Imaging) at a rotation speed of 100 frames/s with a non-occlusive technique.[12] After infusion of intracoronary nitroglycerine, the imaging wire was withdrawn by a motorized pullback at a constant speed of 20 mm/s, while Iodixanol 320 contrast (Visipaque™, GE Health Care, Cork, Ireland) was infused through the guiding catheter at a continuous rate of 2–6 ml/min.

Two independent operators analyzed the selected OCT pullbacks offline using proprietary software (Lightlab Imaging). The region of interest was defined as that between the most distal and most proximal frames in which struts could be detected by OCT. In this region of interest, a frame-by-frame analysis (0.2-mm longitudinal intervals) was performed. In every cross-section the lumen contour was drawn and a marker set at the mid-point of the adluminal leading edge of each strut. The markers defined the circumferential position of the strut with respect to the center of gravity of the vessel as an angle, taking the position at 3 o'clock as the 0° reference.

Struts were labeled as containing SC if one or more focal hyperintense regions could be seen in the core of the strut, separated from the axial and transverse strut border interfaces. Struts with hyperintense central regions extending to the lumen border were considered to be related to the optical appearance of bifurcating/confluent struts but not classified as SC. In some of these cases, an indentation between the 2 bifurcating/confluent struts could be identified (**Figure 2**). Two investigators classified the struts independently, and the discrepancies were resolved by consensus.

Spread-Out Vessel Charts

The spatial distribution of the struts along the scaffolded vessel was analyzed through spread-out vessel charts. These

graphics were obtained by correlating the longitudinal distance of each strut from the distal edge of the scaffold (abscises) with the angle defining its circumferential position with respect to the center of gravity of the vessel (ordinates) in each OCT pullback.[13,14] The resulting charts represent the scaffolded vessel as if it had been cut longitudinally along the reference angle 0° and spread out on a flat surface (**Figure 3**).

Inflection Points (Hinges) Analysis

The results displayed on the spread-out vessel charts permit visual identification of the different inflection points[15] in the scaffold structure. The inflection points were classified into 3 types (**Figure 4**): (1) ψ-hinges (psi-hinges) at the distal part of a longitudinal connector, where the angle between the connector and the W-shaped ring is acute; (2) Υ-hinges (ipsilon-hinges) at the proximal part of a longitudinal connector, where the angle between the connector and the W-shaped ring is obtuse; (3) crown peaks: hinges in the W-shaped rings at inflection points with no longitudinal connector. A 3.0×18 mm BVS consists of 19 W-shaped rings, 54 longitudinal connectors and 120 crown peaks. In each BVS ring 3 ψ-hinges, 3 Υ-hinges, and 6 crown peaks can be identified, except in the most distal (3 ψ-hinges and 9 crown peaks) and the most proximal (3 Υ-hinges and 9 crown peaks).

At least 4 points are required to define the shape of ψ or Υ, whereas 3 points are sufficient to define the shape of a crown peak. A hinge was considered associated with SC if SC appeared in any of the struts minimally required to define the hinge shape around the inflection point.

Individual tracking of the temporal evolution of each hinge was performed by matching the hinges in the spread-out vessel charts at baseline and 6-month follow-up.

Bench Analysis

Devices with the same design as the BVS in cohort B were used for a bench evaluation. Scaffolds were analyzed under light microscopy for the presence of enhanced opacity caused by scattering. Three uncrimped and 3 deployed devices were examined with optical microscopy (Keyence VHX-600) with incident light to maximize scattering within the bulk of the polymer and minimize surface reflection. SC were defined as areas of whitening greater than 20 μm in diameter (**Figure 5**). The spatial distribution of SC along the scaffolded vessel was recorded using the spread-out vessel charts.

Statistical Analysis

The fraction of struts and hinge points with SC was calculated and the results compared with Pearson's chi-square test. The ability of OCT to track SC hinges between the baseline and follow-up pullbacks of the same patient was tested with a weighted κ coefficient for the number count of white-dotted hinges per ring. Interobserver variability for the count of struts and of struts containing SC was calculated per cross-section by Kendall's tau-b and Spearman correlations. All the analyses and graphics were performed with the PASW 17.0.2 statistical package (SPSS Inc, Chicago, IL, USA).

Results

The 24 patients in the ABSORB cohort B1 underwent OCT at baseline and at 6-month follow-up; in 12 of these cases, the images were acquired with a Fourier-domain C7 system. No case was excluded from the analysis because of image quality issues. From these 12 cases, 3 were randomly selected for the spatial and temporal analysis of the SC. In all cases but one (patient 1, baseline OCT), the operator removed the guidewire before starting the OCT pullback to improve the image quality.

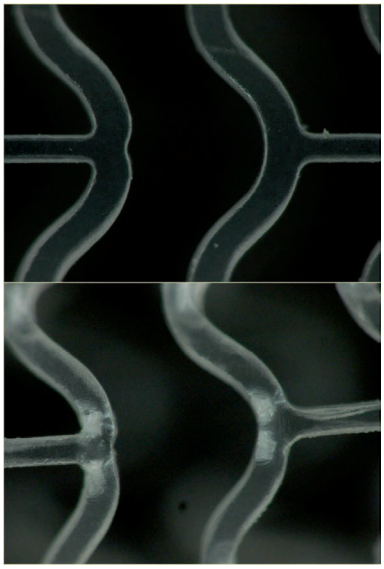

Figure 5. Representative images from the bench analysis of pre-crimp (**Upper**) and post-deployment (**Lower**), showing the stress-whitening at hinge points. Before crimp/deployment, scaffolds appeared transparent under optical microscopy. After deployment, scattering evidenced by increased opacity was observed at all hinge regions of the device.

A total of 4,328 struts were analyzed: 1,502 in patient 1 (718 at baseline, 784 at 6 months), 1,403 in patient 2 (700 at baseline, 703 at 6 months) and 1,423 in patient 3 (728 at baseline, 695 at 6 months). The interobserver agreement was excellent for the count of struts per cross-section (Kendall's tau-b=0.872, Spearman rho=0.932 at baseline, P<0.001; Kendall's tau-b=0.851, Spearman rho=0.912 at follow-up, P<0.001), and for the count of struts containing SC (Kendall's tau-b=0.936, Spearman rho=0.959 at baseline, P<0.001; Kendall's tau-b=0.954, Spearman rho=0.971 at follow-up, P<0.001). Analyst 1 tended to count on average 0.18 struts more per cross-section than analyst 2 at baseline (P=0.014), and 0.22 struts more at follow-up (P=0.04). No significant interobserver bias was detected in the count of struts with SC.

Analysis of the proportion of SC with respect to the total number of struts showed no significant difference between baseline and follow-up in any of the patients (**Table 1**). No significant difference was found between patients for the proportion of SC at any time point.

Figures 4, **S1** and **S2** present the spread-out vessel charts at baseline and 6-month follow-up of the 3 patients. All of the SC were located around hinges; no SC were detected in straight segments. Some hinges were sliced in different cross-sections because of the coincidence with systolic cardiac motion; in those cases it can be seen that the SC are located in the inner curvature of the bending (acute angle), without corresponding

Table 1. Proportion of Struts With Scattering Centers Immediately Post-Implantation and at the 6-Month Follow-up

	Post-implant	6 months	P value
Patient 1			
No. of struts	718	784	0.919
SC	91 (12.7%)	98 (12.5%)	
Patient 2			
No. of struts	700	703	0.586
SC	116 (16.6%)	109 (15.5%)	
Patient 3			
No. of struts	728	695	0.818
SC	112 (15.4%)	110 (15.8%)	
Total			
No. of struts	2,146	2,182	0.754
SC	319 (14.9%)	317 (14.5%)	
Patient 1 vs. Patient 2 (P value)	0.106	0.130	

SC, scattering centers. Data are n (%)

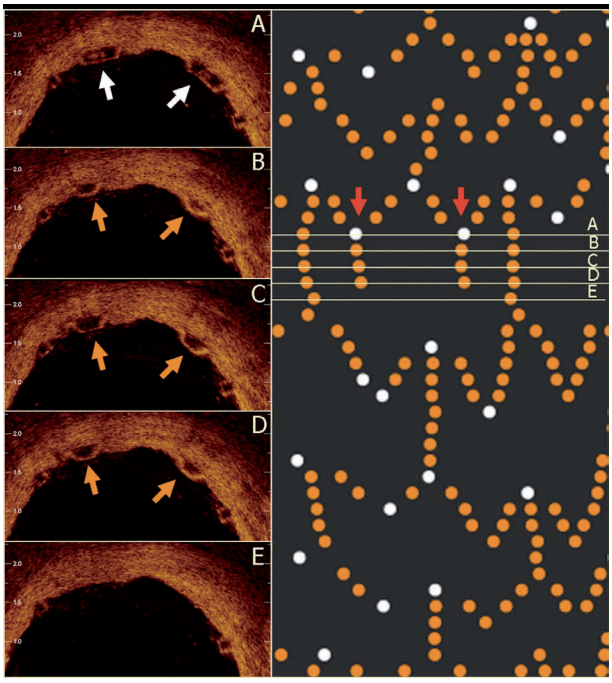

Figure 6. Hinges sliced in different cross-sections because of the coincidence with systolic cardiac motion (vessel and catheter moving in the same direction). The image shows 2 crown peaks with scattering centers and illustrates how the scattering is located in the inner curvature of the hinge (right side, red arrows; **A**), with no scattering in the slices corresponding to the outer curvature (**B**–**E**).

SC in the outer curvature (obtuse angle) (**Figure 6**).

A comparison of the proportion of SC hinges did not show any significant difference between baseline and follow-up or between patients (**Table 2**).

Visual analysis of **Figures 4**–**6** highlights the difficulty of tracking specific SC between baseline and the 6-month follow-up. The spatial distribution of the SC did not match exactly, suggesting that different features are revealed with any given pullback. To assess the ability to match the SC location at the 2 time points, the agreement in the number count of white-dotted hinges per ring between baseline and follow-up was tested with a weighted κ, which showed very poor agreement between the different hinges: best agreement for ψ-hinges (weighted κ range 0.23–0.62), for the rest of hinges,

Table 2. Number and Percentage of Struts Characterized by the Presence of Scattering Centers Immediately Post-Implantation and at the 6-Month Follow-up

	Post-implant	6 months	P value
Patient 1*			
ψ-hinges (n=54)	27 (54.0%)	33 (61.1%)	0.463
Y-hinges (n=54)	25 (49.0%)	27 (50.0%)	0.920
Crown peaks (n=120)	36 (31.6%)	37 (30.8%)	0.902
All inflection points (n=228)	88 (40.9%)	97 (42.5%)	0.731
Patient 2			
ψ-hinges (n=54)	34 (63.0%)	36 (66.7%)	0.687
Y-hinges (n=54)	25 (46.3%)	25 (46.3%)	1.000
Crown peaks (n=120)	53 (44.2%)	45 (37.5%)	0.293
All hinges (n=228)	112 (49.1%)	106 (46.5%)	0.574
Patient 3			
ψ-hinges (n=54)	38 (70.4%)	41 (75.9%)	0.515
Y-hinges (n=54)	21 (38.9%)	27 (50.0%)	0.245
Crown peaks (n=120)	53 (43.3%)	42 (35.0%)	0.186
All hinges (n=228)	111 (48.7%)	110 (48.2%)	0.925
Between patients (P value)			
ψ-hinges	0.226	0.250	
Y-hinges	0.555	0.906	
Crown peaks	0.091	0.547	
All hinges	0.154	0.457	

Data are n (%)
*In patient 1 only 50 ψ-hinges, 51 Y-hinges and 114 crown peaks were analyzable at baseline, because of the presence of a guidewire in the pullback (Table presents corrected %).

weighted κ<0.34 (**Table S1**).

In the bench study, a total of 684 hinge regions in each group of uncrimped and deployed devices were evaluated by optical microscopy. Analysis revealed the complete absence of SC in all regions of the uncrimped devices. In contrast, after deployment there were SC in all hinge regions (**Figure 3**).

Discussion

In this study we used a novel methodology for analyzing morphological changes in the polymeric scaffold of a BVS using OCT. Spread-out vessel charts have been previously described in trials comparing the performance of intracoronary devices using OCT per strut analysis.[13,14,16] They are simple and intuitive graphic representations of the spatial distribution and clustering of the studied phenomenon, in this case of the SC along the BVS, providing insight into how the scaffold material may be changing over time post-implantation. This study is the first to use spread-out vessel charts as the primary tool for detailed spatial analysis, and the results presented here prove its potential and motivate future development of the technique. This methodology may complement 3D-rendering technologies, which are appealing imaging tools but limited in analytical capability.

The spread-out vessel charts presented here also illustrate another unanticipated phenomenon, namely, the effect of cardiac motion on the images obtained during the OCT pullback. One can see the elongation of the segments imaged in systole (when the vessel moves in the same direction as the pullback catheter) and the compression of the segments imaged in diastole (when vessel and pullback move in opposite directions).

Visual analysis of the struts displayed in the spread-out vessel charts showed that all of the SC were located at hinge points. OCT relies upon changes in refractive index on a length scale greater than that of the wavelength of light used in the instrument to create signal intensity.[17,18] Thus, the presence of SC within the strut core is suggestive of the creation of new interfaces in the polymeric material, leading to microscopic changes in the refractive index. In vivo, mechanical deformation, polymer molecular weight degradation, and tissue integration are all potential causes of refractive index changes. The exclusive location of the SC at hinge points strongly suggests that they represent micro-crazes in the polymer. Deformation-induced crazing has long been demonstrated in both amorphous and semicrystalline polymers.[19] In semicrystalline polymers, crazes are typically microvoids traversed by fibrils in the direction of the applied stress, a combination that preserves the strength of the material while creating a discontinuity in the index of refraction.[19–21] The BVS undergoes varying magnitudes of mechanical deformation during crimping and deployment, depending on the location on the scaffold, but the highest strain (and stress) is experienced at the hinge points, the points about which the scaffold collapses and expands during crimping and deployment, respectively. Optically, this deformation manifests in the deployed device as stress-whitening at the hinge points (**Figure 3**), which is also evidence of crazing. The spatial distribution of the SC in OCT parallels that of the crazing observed in optical microscopy, clustering around the hinge points and leaving the scaffold areas that experience little or no mechanical deformation as unblemished "black boxes".

Though hydrolysis is a natural part of PLLA degradation, the presence of SC immediately post-implantation in a proportion comparable to that at the 6-month follow-up, likely rules out the involvement of hydrolysis in the genesis of these images during the first 6 months. Likewise, the similar proportion of SC at baseline and at the 6-month follow-up suggests that other processes, such as physiological loading, induce minimal crazing of the polymer after deployment. Therefore, the structural integrity of the scaffold is not jeopardized by hydrolysis or

crazing up to 6 months. The preservation of structural integrity, especially in the first 3 months after implantation (the so-called "revascularization phase") is of the utmost importance to counteract vessel recoil and adverse remodeling, hence maintaining the initial luminal gain.[1] Our finding is consistent with the excellent clinical outcomes reported for the BVS to date.[3,5,6]

Previous studies from our group unsuccessfully attempted to track the individual SC between baseline and follow-up using 3D-rendering technologies (unpublished data). The current approach offers a clearer and more visual representation of the spatial location of the SC, but still fails to track them individually between 2 time points. Furthermore, the poor agreement between baseline and follow-up regarding the SC count per ring discourages any further attempt of matching. At a rotation speed of 100 Hz and a pullback speed of 20 mm/s, any feature smaller than 200 μm will be difficult to capture in multiple pullbacks, and the OCT study should be rather considered a random sampling of the study phenomenon. This might explain the failure to match individual SC, and also why OCT detected SC in only 43–49% of the hinges, even though light microscopy had shown stress-whitening in 100%. Consistent with this, OCT had the highest sensitivity for SC detection in the largest hinges (ψ-hinges: 61–76%) and the lowest sensitivity in the smallest hinges (crown peaks: 31–44%).

Study Limitations

The OCT longitudinal image co-registration is limited in this study because of the pullback and rotation speeds used in the acquisition, which are the standard for clinical applications with a Fourier-domain C7 system. This study is a retrospective analysis from patients included in a clinical study, aimed at interpreting intriguing imaging observations; therefore, the pullback speed could not be altered to examine the factors that may govern longitudinal co-registration. For in vitro, preclinical, or prospective designs, a slower pullback speed (eg, 10 mm/s) would improve the ability to reproducibly observe features smaller than 200 μm and improve co-registration accuracy.

The presence of a guidewire in one of the pullbacks might affect the comparability of these OCT studies, because the projected shadow hides a random sector of the cross-section. We minimized this problem by analyzing the proportion of SC with respect to the number of visible struts/hinges in the pullback.

The similarity between anomalous SC and the images generated by confluent or bifurcating struts might have affected the results. Although the defined analysis methodology attempted to differentiate between these essentially different images and showed excellent reproducibility, classification imprecision cannot be totally excluded.

The compression of the images during diastole made the reconstruction of the BVS structure difficult in some segments. Although the reconstruction was possible in all cases, following the pattern of the device, the accuracy of the analysis is hampered in those segments.

Conclusions

The SC observed in the Abbott Vascular BVS are located exclusively at hinge points and present at baseline and 6-month follow-up in similar proportions, suggesting that these images may represent polymer crazing caused by mechanical deformation during the crimping and deployment processes, likely ruling out any role of hydrolysis in their genesis. The consistent number and location of the SC between baseline and the 6-month follow-up suggests that physiological loading is not inducing further crazing on length scales greater than the spatial resolution capability of OCT.

Disclosures

This study analyzes data from a registry sponsored by ABBOTT Vascular, Santa Clara, CA, USA. A. Sheehy, M.B. Kossuth, J.P. Oberhauser, T. Glauser, J. Harrington and R.J. Rapoza are employees of Abbott Vascular.

References

1. Oberhauser JP, Hossainy S, Rapoza RJ. Design principles and performance of bioresorbable polymeric vascular scaffolds. *EuroIntervention Suppl* 2009; **5**(Suppl)**:** F15–F22.
2. Kozuki A, Shite J, Shinke T, Miyoshi N, Sawada T, Hellig F, et al. STELLIUM 1: First-in-man follow-up evaluation of bioabsorbable polymer-coated paclitaxel-eluting stent. *Circ J* 2010; **74:** 2089–2096.
3. Serruys PW, Onuma Y, Ormiston JA, De Bruyne B, Regar E, Dudek D, et al. Evaluation of the second generation of a bioresorbable everolimus drug-eluting vascular scaffold for treatment of de novo coronary artery stenosis: 6-month clinical and imaging outcomes. *Circulation* 2010; **122:** 2301–2312.
4. Onuma Y, Serruys PW, Perkins LE, Okamura T, Gonzalo N, Garcia-Garcia HM, et al. Intracoronary optical coherence tomography and histology at 1 month and 2, 3, and 4 years after implantation of everolimus-eluting bioresorbable vascular scaffolds in a porcine coronary artery model: An attempt to decipher the human optical coherence tomography images in the ABSORB Trial. *Circulation* 2010; **122:** 2288–2300.
5. Ormiston JA, Serruys PW, Regar E, Dudek D, Thuesen L, Webster MW, et al. A bioabsorbable everolimus-eluting coronary stent system for patients with single de-novo coronary artery lesions (ABSORB): A prospective open-label trial. *Lancet* 2008; **371:** 899–907.
6. Serruys PW, Ormiston JA, Onuma Y, Regar E, Gonzalo N, Garcia-Garcia HM, et al. A bioabsorbable everolimus-eluting coronary stent system (ABSORB): 2-year outcomes and results from multiple imaging methods. *Lancet* 2009; **373:** 897–910.
7. Teramoto T, Ikeno F, Otake H, Lyons JK, van Beusekom HM, Fearon WF, et al. Intriguing peri-strut low-intensity area detected by optical coherence tomography after coronary stent deployment. *Circ J* 2010; **74:** 1257–1259.
8. Kim JS, Kim JS, Kim TH, Fan C, Lee JM, Kim W, et al. Comparison of neointimal coverage of sirolimus-eluting stents and paclitaxel-eluting stents using optical coherence tomography at 9 months after implantation. *Circ J* 2010; **74:** 320–326.
9. Miyoshi N, Shite J, Shinke T, Otake H, Tanino Y, Ogasawara D, et al. Comparison by optical coherence tomography of paclitaxel-eluting stents with sirolimus-eluting stents implanted in one coronary artery in one procedure: 6-month follow-up. *Circ J* 2010; **74:** 903–908.
10. Liu Y, Imanishi T, Kubo T, Tanaka A, Kitabata H, Tanimoto T, et al. Assessment by optical coherence tomography of stent struts across side branch: Comparison of bare-metal stents and drug-elution stents. *Circ J* 2010; **75:** 106–112.
11. Goto I, Itoh T, Kimura T, Fusazaki T, Matsui H, Sugawara S, et al. Morphological and quantitative analysis of vascular wall and neointimal hyperplasia after coronary stenting: Comparison of bare-metal and sirolimus-eluting stents using optical coherence tomography. *Circ J* 2011; **75:** 1633–1640.
12. Prati F, Cera M, Ramazzotti V, Imola F, Giudice R, Giudice M, et al. From bench to bedside: A novel technique of acquiring OCT images. *Circ J* 2008; **72:** 839–843.
13. Gutierrez-Chico JL, van Geuns RJ, Regar E, van der Giessen WJ, Kelbaek H, Saunamaki K, et al. Tissue coverage of a hydrophilic polymer-coated zotarolimus-eluting stent vs. a fluoropolymer-coated everolimus-eluting stent at 13-month follow-up: An optical coherence tomography substudy from the RESOLUTE All Comers trial. *Eur Heart J* 2011; **32:** 2454–2463.
14. Gutiérrez-Chico J, van Geuns RJ, Koch K, Koolen J, Duckers HJ, Regar E, et al. Paclitaxel-coated balloon in combination with bare metal stent for treatment of de novo coronary lesions: An optical coherence tomography first-in-human randomized trial balloon-first vs. stent first. *EuroIntervention* 2011; **7:** 711–722.
15. Sangiorgi G, Melzi G, Agostoni P, Cola C, Clementi F, Romitelli P, et al. Engineering aspects of stents design and their translation into clinical practice. *Ann Ist Super Sanita* 2007; **43:** 89–100.
16. Gutiérrez-Chico J, Jüni P, García-García HM, Regar E, Nüesch E, Borgia F, et al. Long term tissue coverage of a biodegradable polylactide polymer-coated biolimus-eluting stent: Comparative sequential

assessment with optical coherence tomography until complete resorption of the polymer. *Am Heart J* 2011 (in press).
17. Schmitt JM. Optical coherence tomography (OCT): A Review. *IEEE J Sel Top Quantum Electron* 1999; **5:** 1205–1215.
18. Fujimoto J, Drexler W. Introduction to optical coherence tomography. *In*: Greenbaum E, editor. Biological and medical physics, biomedical engineering. Berlin: Springer, 2008; 1–45.
19. Olf HG, Peterlin A. Crazing and fracture in crystalline, isotactic polypropylene and the effect of morphology, gaseous environments, and temperature. *J Polym Sci Polym Phys Ed* 1974; **12:** 2209–2251.
20. Kojima M. Stress whitening in crystalline propylene-ethylene block copolymers. *J Macromol Sci B Physics* 1981; **19:** 523–541.
21. Liu Y, Kennard CHL, Truss RW, Calos NJ. Characterization of stress-whitening of tensile yielded isotactic polypropylene. *Polymer* 1997; **38:** 2797–2805.

Supplemental Files

Supplemental File 1

Figure S1. Patient 1: spread-out vessel chart showing the spatial distribution of the struts with scattering centers in the scaffolded vessel immediately post-implantation (baseline) and at the 6-month follow-up.

Figure S2. Patient 2: spread-out vessel chart showing the spatial distribution of the struts with scattering centers in the scaffolded vessel immediately post-implantation (baseline) and at the 6-month follow-up.

Table S1. Agreement on the Number of White-Dotted Hinge Points per Scaffold Ring Between Baseline and the 6-Month Follow-up

Please find supplemental file(s);
http://dx.doi.org/10.1253/circj.CJ-11-0726

CHAPTER 4 METHODOLOGICAL CONSIDERATIONS IN THE APPLICATION OF OPTICAL COHERENCE TOMOGRAPHY FOR THE EVALUATION OF BIORESORBABLE SCAFFOLDS

4.3 Evaluation with in vivo optical coherence tomography and histology of the vascular effects of the everolimus-eluting bioresorbable vascular scaffold at two years following implantation in a healthy porcine coronary artery model: implications of pilot results for future pre-clinical studies.

Gogas BD*, **Radu M***, Onuma Y, Perkins L, Powers JC, Gomez-Lara J, Farooq V, Garcia-Garcia HM, Diletti R, Rapoza R, Virmani R, Serruys PW.

International Journal of Cardiovascular Imaging. 2012;28:499-511.

Evaluation with in vivo optical coherence tomography and histology of the vascular effects of the everolimus-eluting bioresorbable vascular scaffold at two years following implantation in a healthy porcine coronary artery model: implications of pilot results for future pre-clinical studies

Bill D. Gogas · Maria Radu · Yoshinobu Onuma · Laura Perkins · Jennifer C. Powers · Josep Gomez-Lara · Vasim Farooq · Hector M. Garcia-Garcia · Roberto Diletti · Richard Rapoza · Renu Virmani · Patrick W. Serruys

Received: 16 December 2010 / Accepted: 29 March 2011

Abstract To quantify with in vivo OCT and histology, the device/vessel interaction after implantation of the bioresorbable vascular scaffold (BVS). We evaluated the area and thickness of the strut voids previously occupied by the polymeric struts, and the neointimal hyperplasia (NIH) area covering the endoluminal surface of the strut voids (NIH_{EV}), as well as the NIH area occupying the space between the strut voids (NIH_{BV}), in healthy porcine coronary arteries at 2, 3 and 4 years after implantation of the device. Twenty-two polymeric BVS were implanted in the coronary arteries of 11 healthy Yucatan minipigs that underwent OCT at 2, 3 and 4 years after implantation, immediately followed by euthanasia. The areas and thicknesses of 60 corresponding strut voids previously occupied by the polymeric struts and the size of 60 corresponding NIH_{EV} and 49 NIH_{BV} were evaluated with both OCT and histology by 2 independent observers, using a single quantitative analysis software for both techniques. At 3 and 4 years after implantation, the strut voids were no longer detectable by OCT or histology due to complete polymer resorption. However, analysis performed at 2 years still provided clear delineation of these structures, by both techniques. The median [ranges] areas of these strut voids were 0.04 [0.03–0.16] and 0.02 [0.01–0.07] mm^2 by histology and OCT, respectively. The mean (±SD) thickness by histology and OCT was 220 ± 40 and 120 ± 20 μm, respectively. The median [ranges] NIH_{EV} by histology and OCT was 0.07 [0.04–0.20] and 0.03 [0.01–0.08] mm^2, while the mean (±SD) NIH_{BV} by histology and OCT was 0.13 ± 0.07 and 0.10 ± 0.06 mm^2. Our study indicates that in vivo OCT of the BVS provides correlated measurements of the same order of magnitude as histomorphometry, and is reproducible for the evaluation of certain vascular and device-related characteristics. However, histology systematically gives larger values for all the measured structures compared to OCT, at 2 years post implantation.

Bill D. Gogas and Maria Radu contributed equally to this manuscript.

B. D. Gogas · M. Radu · Y. Onuma · J. Gomez-Lara · V. Farooq · H. M. Garcia-Garcia · R. Diletti · P. W. Serruys (✉)
Thoraxcenter, Erasmus University Medical Centre, 's Gravendijkwaal 230, 3015 Rotterdam, The Netherlands
e-mail: p.w.j.c.serruys@erasmusmc.nl

L. Perkins · J. C. Powers · R. Rapoza
Abbott Vascular, Santa Clara, CA, USA

R. Virmani
CVPath, Gaithersburg, MA, USA

Keywords Bioresorbable vascular scaffold · Vascular healing · Optical coherence tomography · Histology

Introduction

Bioresorbable coronary scaffolds are a novel approach to the percutaneous treatment of coronary artery disease. Recently, the everolimus-eluting bioresorbable vascular scaffold (BVS) (Abbott Vascular, Santa Clara, Santa Clara, USA) has been studied in the first-in-man ABSORB cohort A trial, which demonstrated the feasibility and safety of this device, with a rate of major adverse cardiac events of 3.4% up to 3 years [1–3]. The BVS is composed of a backbone of poly-L-lactide (PLLA), covered with the polymer poly-D, L-lactide (PDLLA), containing and controlling the release of the drug, everolimus (Novartis, Basel, Switzerland). PLLA and PDLLA degrade to lactic acid which is metabolized via the Krebs' cycle during the bioresorption process. The radiolucent device is visualized on angiography by radio-opaque platinum markers located at each end [4]. The introduction of these new devices prompts us to refine our methods of evaluation, using state-of-the-art imaging modalities, such as optical coherence tomography (OCT). This imaging technique has a near-histological resolution ($\sim$15 μm), which makes it ideal for studying the device/vessel interaction in detail [5]. As the polymeric struts are translucent, light-based imaging modalities are particularly suitable for this purpose. Up to now, histological morphometry has been crucial in the evaluation of the performance of new devices [6]. As histology is limited to animal and human post-mortem studies, in vivo assessment using OCT is highly desirable. This porcine study was set up in 2006 with the goal to evaluate the device/vessel interaction after implantation of the BVS at 2, 3 and 4 years, using OCT and histology. The qualitative strut-related characteristics with regards to the process of biodegradation were published recently [7]. In this part of the study, we sought to evaluate whether mimicking the histological morphometric approach using OCT is feasible and reproducible for the evaluation of the vascular healing following implantation with the BVS.

Specifically, we sought to compare a number of quantitative parameters assessed by ex vivo/"post processed" histology and in vivo/"non-processed" OCT, in order to assess the agreement between these techniques. These parameters include: the number and size of the structures resembling struts, and quantification of the tissue growth covering the endoluminal surface and the tissue growth between these structures.

Methods

Study sample and OCT imaging

Twenty two polymeric devices, BVS revision 1.0 (3×12 mm) were implanted in 11 healthy Yucatan minipig coronary arteries, with a balloon: artery ratio of 1.2:1. The BVS revision 1.0 has three main components: the polymeric backbone, the polymeric drug reservoir, and the antiproliferative drug, everolimus. The polymeric scaffold is balloon-expandable, and is composed of a high molecular weight PLLA with serpentine rings interconnected by links. The scaffold body design is coated with a matrix of PDLLA and everolimus in a 1:1 ratio. The device is laser cut from an extruded tube and has two radio-opaque platinum markers at both ends [8]. Since OCT at 3 and 4 years following implantation displayed no signal at the site where struts were expected to have been previously implanted, we evaluated only the devices available at 2 years follow-up. At this time point, the PLLA backbone is almost completely resorbed, as evidenced by gel permeation chromatography, and histology shows accumulations of proteoglycans (stained positively with Alcian blue) at corresponding sites. By OCT, however, these "strut voids" appear as well delineated hyporeflective foci. Since it is known that by OCT, immediately after implantation, BVS polymeric struts appear as black boxes with bright borders [1], these findings indicate that OCT does not distinguish between the BVS strut polymeric material and the provisional matrix that replaces the strut after full bioresorption [7]. Throughout the entire length of this manuscript, we will use the term "strut void" to describe these strut-like structures, previously occupied by the polymeric material.

OCT was performed in vivo using the M2 CV imaging system (LightLab Imaging, Westford, MA, USA). In brief, the low-pressure Helios^{TM} occlusion

balloon catheter was advanced distally to the region of interest over a conventional 0.014 inch angioplasty wire, which was then exchanged with the OCT ImageWire^{TM}. After calibration of the image wire by correction of the Z-offset [9], the occlusion balloon catheter was withdrawn proximally to the region of interest, and inflated to 0.5–0.7 atmospheres. During image acquisition, blood clearance was achieved by manual continuous flushing with lactated Ringer's solution. Cross-sectional images were acquired at 15.6 frames/s, with an automatic pullback speed of 1 mm/s. Images were stored digitally for off-line analysis.

Processing for histology and selection of corresponding OCT and histology images

Animal sacrifice was performed immediately after OCT imaging by intravenous sodium pentobarbital infusion. The heart was explanted from the thoracic cavity, the aorta clamped, and the coronary arteries were pressure perfused at 100–120 mm Hg: first with 0.9% saline, followed by 10% neutral buffered formalin for approximately 30 min. Hearts were then immersed in formalin for complete fixation. Following this, arteries were carefully dissected off the heart. The location of the scaffolds was confirmed by high-contrast film-based radiographs (Faxitron X-ray Corp., Lincolnshire, IL, USA) and the specimens were dehydrated in a graded series of ethanol. The scaffolded segments were then embedded in methyl methacrylate (MMA) for polymerization [4]. The MMA block was sawed into three 4 mm segments, and three cross-sections were cut using a rotary microtome with a tungsten carbide blade: one at the proximal scaffold segment, 2 mm distal to the proximal metallic marker; one at the middle segment, 6 mm distal to the proximal marker; and one at the distal scaffold segment, 2 mm proximal to the distal marker. Finally, the samples were mounted and stained with hematoxylin and eosin (HE) and/or elastic Van Gieson (EVG).

Corresponding OCT cross-sections were selected by one observer (YO), using the distances from the platinum markers and anatomical landmarks, such as side branches, as references. Two observers (BG, MR) identified the corresponding structures of interest. The quantitative analysis was performed with the observers blinded to each other's results, as well as to the correspondence between the OCT and histology images. We assumed that the sharp boundary of the strut voids by histology corresponded to the sharply delineated bright borders of the "black boxes" by OCT.

Quantitative analysis of OCT and histology images

OCT and histology images were analyzed with the QCU-CMS software version 4.64 (Laboratory of Clinical and Experimental Image processing, Leiden, The Netherlands), which has previously been shown to provide correlated quantitative measurements as compared to the LightLab software [20]. Once images were uploaded, calibration was performed: for OCT, the diameter (0.36 mm) of the image wire was used, whilst histology images were calibrated using the scale bar provided by the pathologist. After calibration of the images, the following parameters were quantified: (1) the number of strut voids previously occupied by the polymeric struts (2) the lumen area and the area encompassing the abluminal surfaces of these strut voids; (3) the area and thickness of these strut voids and (4) the neointimal hyperplasia (NIH) area covering the endoluminal surface (NIH_{EV}) and the NIH area between the strut voids (NIH_{BV}) (Fig. 1). To be more specific, the measurements were performed in the following way (Figs. 1 and 2): 1. "Scaffold" area: after manual localization of the strut voids by setting a green circle at the mid point of their abluminal surfaces, these points were connected automatically by a trace line placed by the software. In addition, the center of gravity of the scaffold area was determined automatically by the software. 2. Lumen area: the lumen contour was automatically traced by the software; 3. The area of the strut void: this was manually demarcated by following the contour of these structures; 4. NIH_{BV}: in order to demarcate the NIH areas laterally, we used the angle tool of the software, which takes the center of gravity of the scaffold as reference.

The rays of the angle tool were placed as help lines, at the edges of every strut void creating an area between these which was limited axially by the scaffold line and the lumen contour and laterally by the help lines (Fig. 1 and 2); 5. NIH_{EV}: was defined as the area limited by the "help lines" placed at the edges of the strut voids, their endoluminal surfaces,

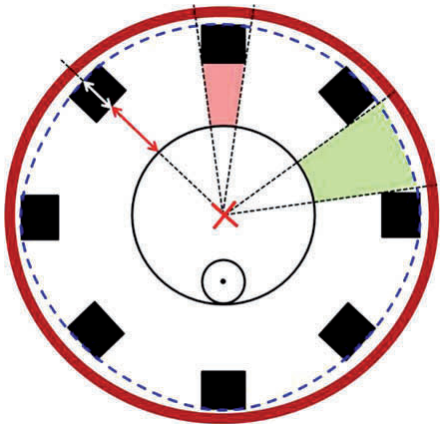

Fig. 1 Schematic representation of the quantitative analysis. Panel **a** The *thick red line* represents the vessel wall; the *black continuous line*, the lumen contour; *black squares* strut voids previously occupied by the polymeric struts; and the *blue dotted line* the abluminal "scaffold" area. The *red cross* indicates the center of gravity of the remnants of the scaffold, which was provided automatically by the software after manual indication of the mid point of the abluminal surfaces of the strut-like structures. The center of gravity point was used to place "the help lines" (*black dotted lines*) for the measurement of the neointimal hyperplasia area covering the endoluminal surface of these structures (*red area*), and the neointimal hyperplasia area between these structures (*green area*). The neointimal thickness (*red arrow*) was measured from the endoluminal surface of the strut voids to the lumen contour, along a line projected through the center of gravity of the scaffold and the mid point of the abluminal surface of these structures. The strut void thickness (*white arrow*) was measured in a similar way

and the lumen area contour; 6. Neointimal thickness: this was measured from the mid point of the endoluminal surface of the strut voids to the lumen contour, along a line projected through the center of gravity of the scaffold; 7: Strut void thickness: this was assessed by measuring the distance between the mid points of the endoluminal and abluminal surfaces of the strut voids.

Statistical analysis

Statistical analyses were performed with SPSS, version 16 (SPSS Inc.,Chicago, IL, USA). Discrete variables are presented as counts and percentages, and continuous variables as mean ± standard deviations, or medians and interquartile ranges or ranges (minimum–maximum). The Pearson's correlation coefficient (r^2) was computed to compare OCT and histological measurements. Bland–Altman plots, displaying the systematic (mean absolute difference) and random (95% limits of agreement) errors, and the interclass correlation coefficient for absolute agreement (ICCa) and consistency (ICCc) were used to assess the agreement between techniques. Inter-observer variability was assessed using the correlation coefficient (r^2). A two-sided p-value ≤ 0.05 was considered significant.

Results

A total of six corresponding cross-sections were available for the purpose of this study (Fig. 3). Histology displayed 75 strut voids previously occupied by the polymeric struts whilst OCT showed only 60. Fifteen of these strut voids by histology could not be identified in the OCT images due to non-uniform rotational distortion, marginalization of the image wire into a side branch and a long distance to the image wire, together with a low light incidence angle resulting in a high light attenuation (Fig. 4). Thus, a total of 60 corresponding strut voids were included in the analysis. In only 1 of 6 frames were all corresponding strut remnants visualised by both OCT and histology with the consequence that the lumen and scaffold area was only accurately assessed in this frame (OCT: 2.78 and 5.14 mm^2; histology: 1.02 and 4.40 mm^2, for lumen and scaffold area, respectively). The ratio between the lumen area and stent area for the OCT was 0.54 while for histology was 0.23 and the % area obstruction of the scaffold for OCT was 45% while for histology 76%. Apart from the strut voids that were not adequately visualized, all images were successfully analysed using the histomorphometrical methodology with the dedicated off-line software. Table 1 and Fig. 5 show the descriptive statistics and Bland–Altman plots for the different parameters measured with OCT and histology. The average difference and 95% limits of agreement were: for the strut area: 0.03 [0.07; −0.01], for the strut thickness: 0.10 [0.18; 0.02], for the NIHEV: 0.04 [0.10; −0.02] and for the NIHBV: 0.03 [0.21; 0.15]. In general, histomorphometry provided larger values for all parameters compared

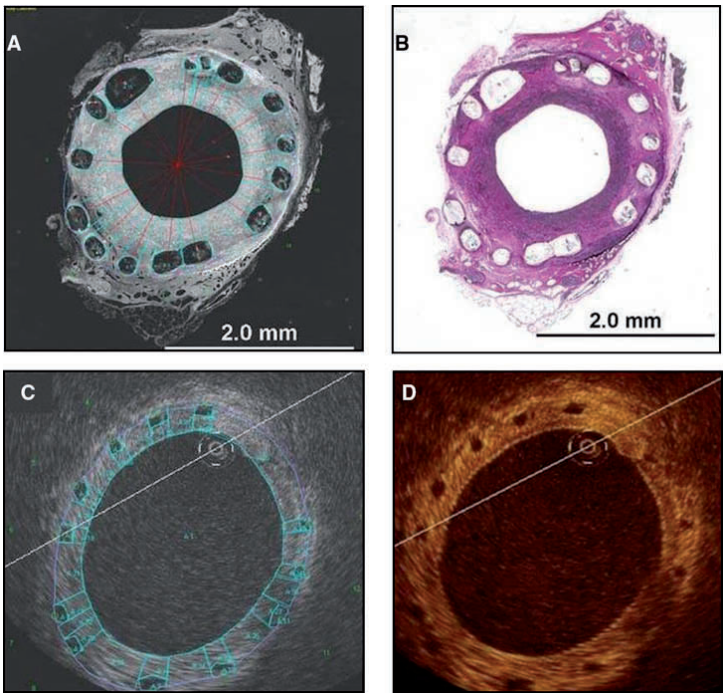

Fig. 2 Demonstration of quantitative measurements by histology and OCT. Panels **A** and **B** show the *inverted grey scale* and color histology images, respectively, with superimposed quantitative measurements (*green lines* in **A**), and panels **C** and **D**, the corresponding grey scale and sepia OCT, with the respective measurements (only **C**). The *red lines* are provided by the software, and are projected from the center of gravity of the scaffold through the mid points of the abluminal surfaces of the struts

to OCT. Interobserver variability was evaluated for all variables assessed with histology and OCT (Fig. 6). The mean (SD) differences between observers were negligible for the parameters measured in the histological sections (area and thickness of strut voids 0.00 (0.00) mm^2 and 0 (30) μm, repcetively; NIH_{EV} 0.00 (0.00) mm^2, and NIH_{BV} 0.00 (0.01) mm^2), as well as for those assessed in the OCT cross-sections (for area and thickness of strut voids: 0.00 (0.00) mm^2 and 0 [10] μm, respectively; for NIH_{EV} 0.00 (0.01) mm^2, and NIH_{BV} −0.03 (0.01) mm^2).

The Lin's correlation coefficient interpreted by the ICCc and ICCa for the area of strut voids were: 0.34 [95% confidence interval (CI): 0.10–0.55], $P < 0.004$ and 0.18 [95% CI: −0.08 to 0.43], $P < 0.004$; for the thickness of these structures: 0.08 [95% CI: −0.18 to 0.33], $P = 0.271$ and 0.01 [95% CI: −0.03 to 0.07], $P = 0.271$; for NIH_{EV}: 0.39 [95% CI: 0.15–0.59], $P < 0.001$ and 0.19 [95% CI: −0.09 to 0.46], $P < 0.001$; and for NIH_{BS}: −0.03 [95% CI: −0.29 to 0.29], $P = 0.50$ and −0.03 [95% CI: −0.27 to 0.28], $P = 0.50$.

The Pearson's correlation coefficient (r^2) for the interobserver variability for the histology assessment was: for the thickness and area of the strut voids thickness: $r^2 = 0.89$ and $r^2 = 0.78$, respectively; for NIH_{EV}: $r^2 = 0.87$; and for NIH_{BV}: $r^2 = 0.86$ ($P < 0.001$ for all analyses). Corresponding results for the OCT measurements were: for thickness and area of strut voids: $r^2 = 0.70$ and $r^2 = 0.57$, respectively; for NIH_{EV}: $r^2 = 0.67$; and for NIH_{BV}: $r^2 = 0.66$ ($P < 0.001$ for all analyses).

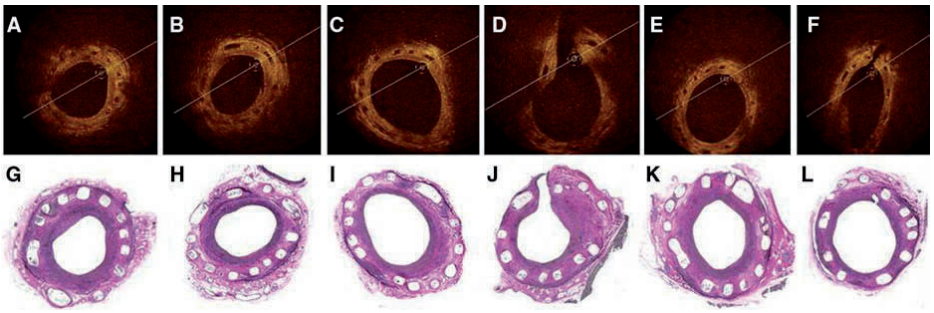

Fig. 3 Cross-sections of corresponding OCT and histology of the left anterior descending artery (*A*/*G*, *B*/*H*, *C*/*I*), and the right coronary artery (*D*/*J*, *E*/*K*, *F*/*L*). Histology specimens are stained with elastic Van Gieson

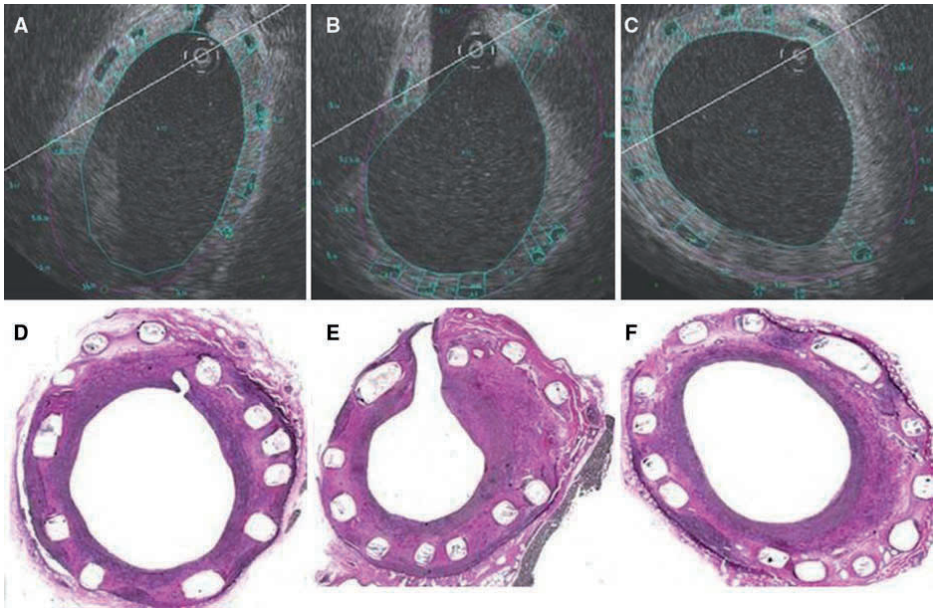

Fig. 4 Factors precluding identification of some of the strut voids in corresponding OCT and histology images. Panels **A**–**C** demonstrate how non-uniform rotational distortion (**A**), marginalisation of the image wire into a side branch (**B**), and a long distance between the image wire and *black boxes* preclude visualisation of these strut voids by OCT, as compared to corresponding histology (**D**–**F**). Due to the lack of visualization of these structures, abluminal scaffold areas could not be accurately assessed. In order to obtain reproducible measurements, it was before the analysis decided to trace the scaffold area only at the sites of *black boxes* that are visualized, with the consequence of an underestimation of the "true" OCT scaffold area

Table 1 Descriptive statistics of all parameters measured by OCT and histology

	OCT	Histology
Area of the strut voids, mm^2	0.02 (0.01–0.07)	0.04 (0.03–0.16)
Thickness of the strut voids	120 (70–180)	220 (120–350)
NIH_{BV}, mm^2	0.03 (0.01–0.08)	0.07 (0.04–0.20)
NIH_{EV}, mm^2	0.09 (0.01–0.27)	0.13 (0.01–0.31)

NIH neointimal hyperplasia, *BV* between the voids, *EV* endoluminal surfaces of the voids, values are median (range)

Discussion

In the present study, we performed a quantitative analysis of in vivo OCT images of the remnants of bioresorbable vascular scaffolds at 2 years following implantation, using a methodology similar to the morphometric approach used with histology. The main findings of this pilot study are: 1. Histology appears to systematically give larger values, when compared with OCT; 2. the approach similar to histomorphometry for quantitative analysis of OCT images is feasible and reproducible for the evaluation

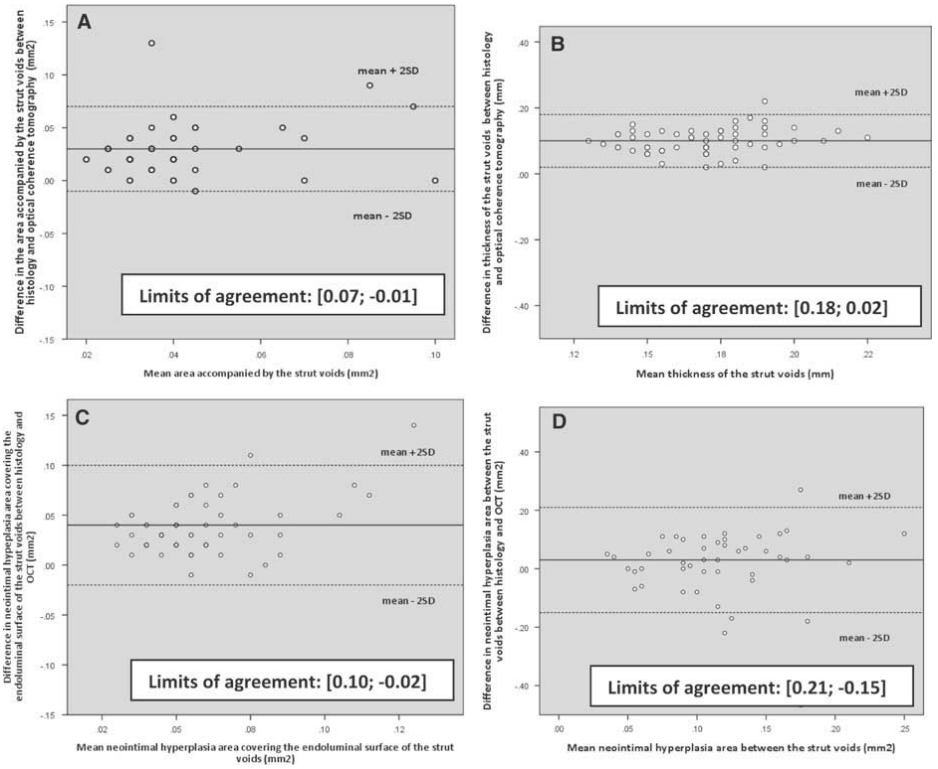

Fig. 5 Bland-Altman plots depicting the agreement between techniques for the evaluation of the area (panel **A**) and thickness (panel **B**) of the strut voids previously occupied by the polymeric struts, the neointimal hyperplasia area covering the endoluminal surface of these voids (panel **C**), and the neointimal hyperplasia area between the voids (panel **D**), with histology and OCT

at follow up after implantation of the BVS; and 3. despite the use of anatomical landmarks and intra-scaffold radiopaque markers to identify corresponding cross-sections, higher numbers of strut voids were visualized by histology than by OCT.

Differences in quantitative measurements between OCT and histology

The observation that quantitative measurements by histology and OCT may differ is not new, as previous studies have suggested that histological processing may induce a certain degree of artifacts related to formalin fixation and dehydration [10]. Surprisingly however, our study showed that all morphological characteristics analyzed were systematically larger by histology as compared to OCT. More specifically, the strut void area, strut void thickness, NIH_{EV} and NIH_{BV} were 100%, 83%, 130% and 44% larger by histology compared to OCT, respectively. Several factors may have contributed to this difference. The first involves the calibration of the OCT image wire by adjustment of the Z-offset before image acquisition, as well as calibration of the scaling of OCT and histology images before analysis, which are crucial for any quantitative measurement. In the present study, these were all performed according to current standards [9]. Secondly, differences can potentially be related to the application of different analysis softwares for different techniques. We tried to circumvent this by utilizing the same software, as well as by using semi-automatic approaches, for all analyses, which was evidenced in the good interobserver reproducibility seen. Nevertheless, the quantitative results by histology were systematically larger than by OCT, as compared to previous studies, even if these applied different softwares for the different techniques [11, 12]. Other interfering factors are therefore likely to be involved. For the NIH areas, our results resemble those reported by Murata et al. and Templin et al., who found that histology estimated the NIH areas covering metallic stents slightly higher than OCT, at 28 and 90 days, and at 10, 14 and 28 days, respectively [13, 14]. However, in our study, the overestimation by histology was greater. This may be related to the combined differences in: the mechanical constraints imparted on the tissue between the bioresorbable vascular scaffold as compared to metallic stents; in the tissue composition at time point of examination (2 years), which includes a higher proportion of collagen and smooth muscle cells as compared to time points less than 90 days [15]; and in the composition of the strut voids which, as shown by Onuma et al., are replaced by highly water-containing acid mucopolysacharides material, which stains positively with Alcian Blue, at this time point [7]. Further, previous studies have indicated that formaldehyde, which we used for tissue fixation, can cause dimensional changes that are dependent on the composition of the tissue (for example causing swelling in liver tissue and shrinkage in muscle tissue), the pH of the tissue, and the temperature and concentration of the fixative [10]. In addition to tissue fixation, dehydration with ethanol, embedding and polymerization in MMA, and subsequent deplastization likely further impacted the tissue dimensions obtained histologically. Considering the contrasting nature of the tissues at late follow-up of the BVS, namely the proteoglycan-rich tissue replacing pre-existing struts compared to the surrounding smooth muscle cell and collagen-dense tissue of the arterial wall, these tissue-specific dimensional changes are especially notable at follow-up after implantation of the BVS. This is supported by the qualitative results regarding the histological appearance of the strut-like structures at 2 and 3 years. At 2 years, the strut voids appear more spherical, having a highly water-containing proteoglycan, while they are contracted and almost completely coalesced into the arterial wall at 3 years (Fig. 6) [7]. Considering this, it is likely that the proteoglycan-based nature of strut foci at 2 years resulted in their swelling as an artifact of histological processing.

The fact that OCT was performed in vivo, when the vessel has a tonus and is naturally pressurized, may also explain some of the discrepancies, although efforts were made to pressurize vessels during histology preparation. However, the most plausible explanation involves the attempt to correspond OCT and histology cross-sections, which depends on the orientation of the OCT image wire relative to the vessel curvature and relative to the location in the vessel lumen, which in turn influence how the OCT "biotome" cross-sects the tissue and the scaffold. The difficulty finding completely corresponding cross-sections may be further affected by the

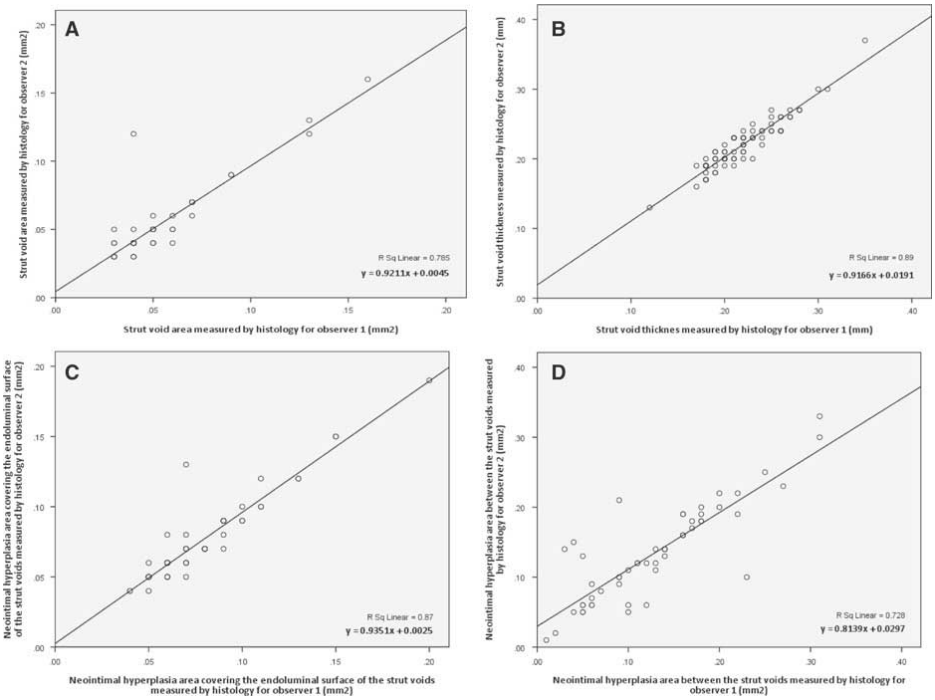

Fig. 6 Linear regression analysis plots depicting the interobserver variability for the evaluation of the area and thickness of the strut voids, the neointimal hyperplasia area covering the endoluminal surface of these voids, and the neointimal hyperplasia area between the voids, with histology (panels **A**–**D**) and OCT (panels **E**–**H**), respectively

differences in slice thicknesses of the samples provided by the different techniques. For histology, the minimum slice thickness possible to obtain, is in the range of 4–5 μm with a sampling interval of 100 μm [16], and depends on the microtome, while the minimum frame thickness available with the OCT system used in the present study is 60 μm and depends on the longitudinal sampling distance, which is in turn related to the frame rate (15.6 frames/s) and the pullback speed (1 mm/s). Nevertheless, it should be stressed that wherever possible, efforts were made to secure corresponding cross-sections by histology and OCT using the scaffold platinum markers and anatomical structures, as landmarks. Thus, our report highlights some of the difficulties that may be encountered in this type of study, which are important to acknowledge (Fig. 7).

Consideration of technical aspects with OCT imaging

Although efforts were made to obtain matched cross-sections between OCT and histology using landmarks, we found a higher density of strut voids by histology than by OCT. In addition to the factors mentioned above, we noticed that the intrinsic properties of the OCT technology related to the use of light also influenced our analysis. By marginalization of the light source, causing an acute incidence angle of the light on the vessel wall, as well as by the relatively low scan diameter of the employed time domain-OCT system (7 mm) compared to newer generation frequency domain (FD)-OCT systems (10 mm), visualisation of the strut voids along the entire 360 degree vessel circumference was hindered

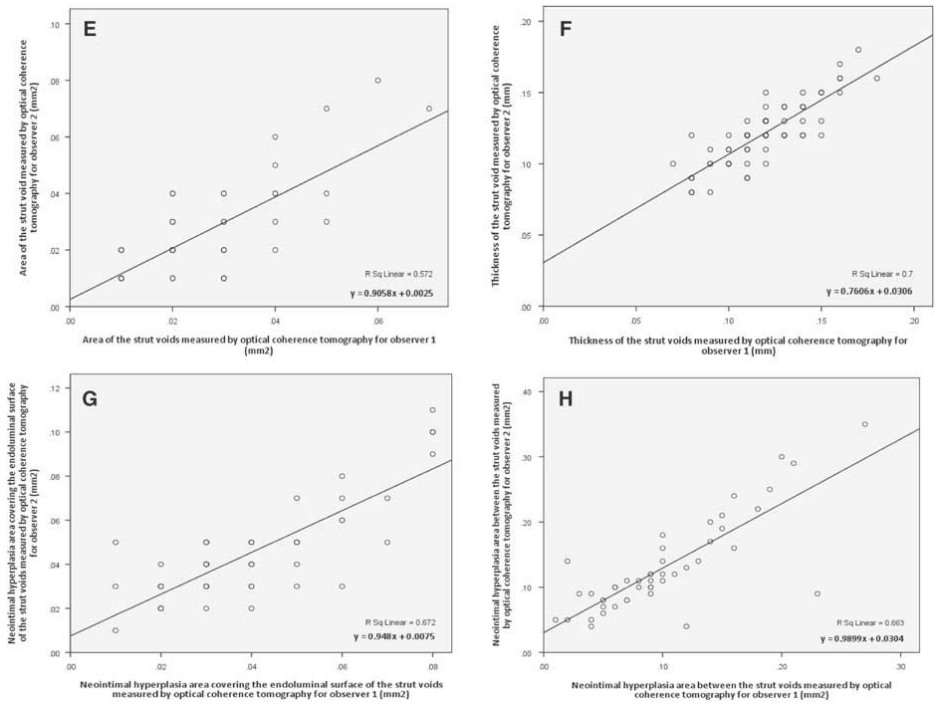

Fig. 6 continued

(Fig. 3B, C), which prevented the identification of these structures and the accurate delineation of the abluminal scaffold area, as well as delineation of the lumen area. Nevertheless, the only available accurate corresponding lumen and scaffold areas by OCT and histomorphometry showed that measurements by OCT were larger than those by histology, which is in line with previous studies [11–13]. Despite the potential advantages of in vivo "non-processed" OCT, the presence of non-uniform rotational distortion, which is related to vessel tortuosity, as well as the presence of artefacts due to heart motion in systole and diastole, further complicated the selection of perfectly corresponding frames. The new generation FD-OCT which has a much higher frame rate, allowing a higher pullback-speed without significant loss in longitudinal sampling density [14, 17, 18], promises to overcome some of these issues, together with recent advances allowing retrospective reconstruction of gated OCT acquisitions [19]. However, these technologies were not available at the time of data acquisition.

Histomorphometry-like analysis with OCT

Onuma et al. recently described a qualitative analysis of OCT images of the polymeric struts of the BVS. As opposed to that analysis, our study focused on the evaluation of the quantitative tissue response around the strut voids previously occupied by the polymeric struts in terms of neointimal hyperplasia between and on the endoluminal surface of these, which we found to be feasible and reproducible, with a good interobserver reproducibility. Despite the mentioned issues regarding comparison between OCT and histology, OCT represents at present the in vivo imaging modality with the highest resolution, which enables

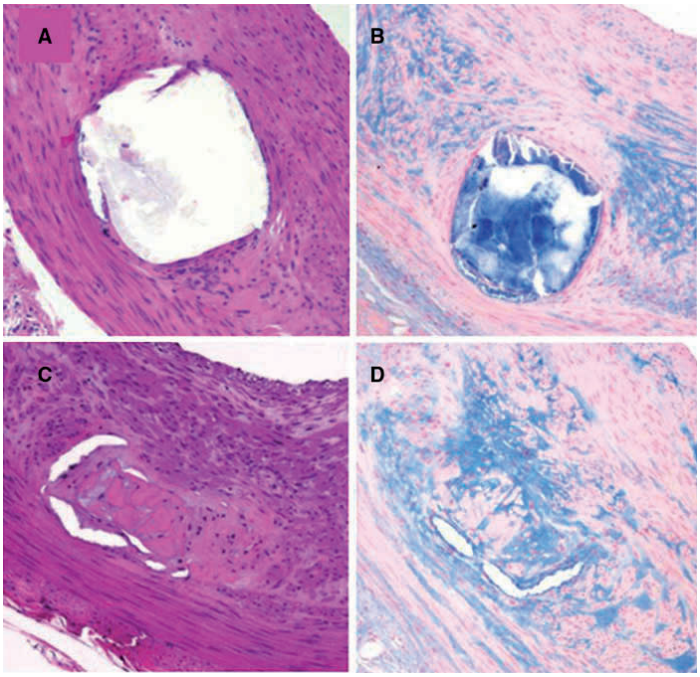

Fig. 7 Histological examples of the appearance of strut voids at 2 and 3 years following implantation of the bioresorbable vascular scaffold. Panels **A**–**D** show strut voids at 2 and 3 years follow-up, respectively. At 2 years, the proteoglycan-rich matrix appears to collapse in the middle of the void upon histological preparation, giving a spherical appearance, while the matrix at 3 years is coalesced with the neointima of the vessel wall, giving the impression that the borders of the contents of the void are better held together with the neointima. Panels **A** and **C** are stained with hematoxylin and eosin, while panels **B** and **D** are stained with Alcian blue. Reproduced from Onuma et al. Circulation 2010

us to evaluate fine details in the assessment of the device/vessel interaction.

Study limitations

Our initial goal was to assess the morphometric parameters of the remnants of the device implanted with OCT at 2, 3, and 4 years following implantation. As part of the degradation process, the number of bioresorbable struts identified by OCT decreased with time. We now know that the polymeric struts are completely resorbed and replaced by proteoglycans by 2 years. However, this respective time point could not be foreseen at the time of planning of the study. For the comparison of different measurements by OCT and histology, it was necessary to select a time point where strut-like structures (strut voids) are fully visible with OCT. Consequently, specimens at 3 and 4 years could not be included in this study, wherefore the sample size was relatively small. We cannot dismiss the possibility that the low sample size could, to some extent, explain the relatively large distribution of individual parameters. Nevertheless, we believe that the findings of this pilot study are interesting as they represent our initial quantitative experience with the novel bioresorbable technology, and may serve as a guide to the planning of future trials with corresponding OCT and histomorphometry to evaluate bioresorbable vascular scaffolds.

Conclusion

The present pilot study showed that an approach for quantitative analysis of OCT images akin to histomorphometry is feasible and reproducible for the evaluation of the vascular healing at follow up after implantation of the BVS and that corresponding OCT and histomorphometry provide results of the same order of magnitude. Despite the use of landmarks to identify corresponding cross-sections, histology systematically provided larger measurements for all studied parameters. Whether this is related to factors influencing acquisition and processing of images, or the bioresorbable nature of the device, requires further investigation, for example using the new-generation FD-OCT, and a larger sample analysed with a higher sampling density.

Acknowledgments Bill D. Gogas wishes to acknowledge the continued funding support of the Hellenic Heart Foundation (ELIKAR), Athens, Greece.

Conflicts of interest Laura Perkins, Jennifer Powers, and Richard Rapoza are employees of Abbott Vascular.

References

1. Ormiston JA, Serruys PW, Regar E, Dudek D, Thuesen L, Webster MW, Onuma Y, Garcia-Garcia HM, McGreevy R, Veldhof S (2008) A bioabsorbable everolimus-eluting coronary stent system for patients with single de novo coronary artery lesions (ABSORB): a prospective open-label trial. Lancet 371(9616):899–907
2. Serruys PW, Ormiston JA, Onuma Y, Regar E, Gonzalo N, Garcia-Garcia HM, Nieman K, Bruining N, Dorange C, Miquel-Hebert K, Veldhof S, Webster M, Thuesen L, Dudek D (2009) A bioabsorbable everolimus-eluting coronary stent system (ABSORB): 2-year outcomes and results from multiple imaging methods. Lancet 373(9667):897–910
3. Onuma Y, Serruys PW, Ormiston JA, Regar E, Webster M, Thuesen L, Dudek D, Veldhof S, Rapoza R (2010) Three-year results of clinical follow-up after a bioresorbable everolimus-eluting scaffold in patients with de novo coronary artery disease: the ABSORB trial. Euro Interven 6(4):447–453
4. Ormiston JA, Serruys PW (2009) Bioabsorbable coronary stents. Circ Cardiovasc Interv 2(3):255–260
5. Regar E, Schaar JA, Mont E, Virmani R, Serruys PW (2003) Optical coherence tomography. Cardiovasc Radiat Med 4(4):198–204
6. Virmani R, Kolodgie FD, Farb A, Lafont A (2003) Drug eluting stents: are human and animal studies comparable? Heart 89(2):133–138
7. Onuma Y, Serruys PW, Perkins LE, Okamura T, Gonzalo N, Garcia-Garcia HM, Regar E, Kamberi M, Powers JC, Rapoza R, van Beusekom H, van der Giessen W, Virmani R (2010) Intracoronary optical coherence tomography and histology at 1 month and 2, 3, and 4 years after implantation of everolimus-eluting bioresorbable vascular scaffolds in a porcine coronary artery model. An attempt to decipher the human optical coherence tomography images in the ABSORB trial. Circulation 122(22):2288–2300
8. Okamura T, Garg S, Gutierrez-Chico JL, Shin ES, Onuma Y, Garcia-Garcia HM, Rapoza RJ, Sudhir K, Regar E, Serruys PW (2010) In vivo evaluation of stent strut distribution patterns in the bioabsorbable everolimus-eluting device: an OCT ad hoc analysis of the revision 1.0 and revision 1.1 stent design in the ABSORB clinical trial. Euro Interven 5(8):932–938
9. Gonzalo N, Garcia-Garcia HM, Serruys PW, Commissaris KH, Bezerra H, Gobbens P, Costa M, Regar E (2009) Reproducibility of quantitative optical coherence tomography for stent analysis. EuroIntervention 5(2):224–232
10. Bahr GF, Bloom G, Friberg U (1957) Volume changes of tissues in physiological fluids during fixation in osmium tetroxide or formaldehyde and during subsequent treatment. Exp Cell Res 12(2):342–355
11. Suzuki Y, Ikeno F, Koizumi T, Tio F, Yeung AC, Yock PG, Fitzgerald PJ, Fearon WF (2008) In vivo comparison between optical coherence tomography and intravascular ultrasound for detecting small degrees of in-stent neointima after stent implantation. JACC Cardiovasc Interv 1(2): 168–173
12. Gonzalo N, Serruys PW, Garcia-Garcia HM, van Soest G, Okamura T, Ligthart J, Knaapen M, Verheye S, Bruining N, Regar E (2009) Quantitative ex vivo and in vivo comparison of lumen dimensions measured by optical coherence tomography and intravascular ultrasound in human coronary arteries. Rev Esp Cardiol 62(6):615–624
13. Murata A, Wallace-Bradley D, Tellez A, Alviar C, Aboodi M, Sheehy A, Coleman L, Perkins L, Nakazawa G, Mintz G, Kaluza GL, Virmani R, Granada JF (2010) Accuracy of optical coherence tomography in the evaluation of neointimal coverage after stent implantation. JACC Cardiovasc Imaging 3(1):76–84
14. Templin C, Meyer M, Muller MF, Djonov V, Hlushchuk R, Dimova I, Flueckiger S, Kronen P, Sidler M, Klein K, Nicholls F, Ghadri JR, Weber K, Paunovic D, Corti R, Hoerstrup SP, Luscher TF, Landmesser U (2010) Coronary optical frequency domain imaging (OFDI) for in vivo evaluation of stent healing: comparison with light and electron microscopy. Eur Heart J 31(14):1792–1801
15. Farb A, Kolodgie FD, Hwang JY, Burke AP, Tefera K, Weber DK, Wight TN, Virmani R (2004) Extracellular matrix changes in stented human coronary arteries. Circulation 110(8):940–947
16. Bruining N, Knaapen M, de Winter S, Van Langenhove G, Serruys PW, Hamers R, de Feijter PJ, Verheye S (2009) A

histological "fly-through" of a diseased coronary artery. Circ Cardiovasc Imaging 2(2):e8–e9
17. Kawase Y, Suzuki Y, Ikeno F, Yoneyama R, Hoshino K, Ly HQ, Lau GT, Hayase M, Yeung AC, Hajjar RJ, Jang IK (2007) Comparison of nonuniform rotational distortion between mechanical IVUS and OCT using a phantom model. Ultrasound Med Biol 33(1):67–73
18. Okamura T, Onuma Y, Garcia-Garcia H, Bruining N, Serruys P High-speed intracoronary optical frequency domain imaging: implications for three-dimensional reconstruction and quantitative analysis (submitted)
19. Sihan K, Botha C, Post F, De Winter S, Gonzalo N, Regar E, Serruys P, Hamers R, Bruining N (2010) Retrospective image-based gating of intracoronary optical coherence tomography: implications for quantitative analysis. EuroIntervention 6. [Epub ahead of print]
20. Okamura T, Gonzalo N, Gutierrez-Chico JL, Serruys P, Bruining N, de Winter S, Dijkstra J, Commossaris K, van Geuns RJ, van Soest G, Ligthart J, Regar E (2010) Reproducibility of coronary Fourier domain optical coherence tomography: quantitative analysis of in vivo stented coronary arteries using three different software packages. EuroIntervention 6:371–379

CHAPTER 5 THE APPLICATION OF OPTICAL COHERENCE TOMOGRAPHY IN THE CLINICAL EVALUATION OF BIORESORBABLE SCAFFOLDS

5.1 Head to head comparison of optical coherence tomography, intravascular ultrasound echogenicity and virtual histology for the detection of changes in polymeric struts over time: insights from the ABSORB trial.

Brugaletta S, Gomez-Lara J, Bruining N, **Radu MD**, van Geuns RJ, Thuesen L, McClean D, Koolen J, Windecker S, Whitbourn R, Oberhauser J, Rapoza R, Ormiston JA, Garcia-Garcia HM, Serruys PW.

EuroIntervention. 2012;8:352-8.

Head to head comparison of optical coherence tomography, intravascular ultrasound echogenicity and virtual histology for the detection of changes in polymeric struts over time: insights from the ABSORB trial

Salvatore Brugaletta[1,2], MD; Josep Gomez-Lara[1], MD; Nico Bruining[1], PhD; Maria D. Radu[1], MD; Robert-Jan van Geuns[1], MD, PhD; Leif Thuesen[3], MD; Dougal McClean[4], MD; Jacques Koolen[5], MD, PhD; Stephan Windecker[6], MD, PhD; Robert Whitbourn[7], MD; James Oberhauser[8], PhD; Richard Rapoza[8], PhD; John A. Ormiston[9], MBChB, PhD; Hector M. Garcia-Garcia[1,10], MD, PhD; Patrick W. Serruys[1]*, MD, PhD

1. Thoraxcenter, Erasmus MC, Rotterdam, The Netherlands; 2. Thorax Institute, Department of Cardiology, Hospital Clinic, Barcelona, Spain; 3. Skejby Sygehus, Aarhus University Hospital, Aarhus, Denmark; 4. Christchurch Hospital, Christchurch, New Zealand; 5. Catharina Hospital, Eindhoven, The Netherlands; 6. Bern University Hospital, Bern, Switzerland; 7. St Vincent's Hospital, Fitzroy, Australia; 8. Abbott Vascular, Santa Clara, CA, USA; 9. Auckland City Hospital, Auckland, New Zealand; 10. Cardialysis BV, Rotterdam, The Netherlands

KEYWORDS

- virtual histology
- OCT
- imaging

Abstract

Aims: To analyse and to compare the changes in the various optical coherence tomography (OCT), echogenicity and intravascular ultrasound virtual histology (VH) of the everolimus-eluting bioresorbable scaffold (ABSORB) degradation parameters during the first 12 months after ABSORB implantation. In the ABSORB study, changes in the appearance of the ABSORB scaffold were monitored over time using various intracoronary imaging modalities. The scaffold struts exhibited a progressive change in their black core area by OCT, in their ultrasound derived grey level intensity quantified by echogenicity, and in their backscattering ultrasound signal, identified as "pseudo dense-calcium" (DC) by VH.

Methods and results: From the ABSORB Cohort B trial 35 patients had paired OCT, echogenicity and VH assessment at baseline and at six- (n=18) or 12-months follow-up (n=17). Changes in OCT strut core area, hyperechogenicity and VH-derived DC were analysed and compared at the various time points. At six months, the change (median[IQR]) in OCT strut core area was –7.2% (–14.0–+0.9) (p=0.053), in hyperechogenicity –12.7% (–33.7–+1.4) (p=0.048) and VH-DC 22.1% (–10.8–+48.8) (p=0.102). At 12 months, all the imaging modalities showed a decrease in the various parameters considered (OCT: –12.2% [–17.5– –1.9], p=0.093; hyperechogenicity –24.64% [–36.6– –16.5], p=0.001; VH-DC: –24.66% [–32.0– –7.0], p=0.071). However, the correlation between the relative changes in these parameters was statistically poor (Spearman's rho <0.4).

Conclusions: OCT, echogenicity and VH were able to detect changes in the ABSORB scaffold struts, although the correlation between those changes was poor. This is likely due to the fact that each imaging modality interrogates different material properties on different length scales. Further studies are needed to explore these hypotheses.

**Corresponding author: Erasmus MC, Thoraxcenter, 's Gravendijkwal 230, NL-3015 CE Rotterdam, The Netherlands. E-mail: p.w.j.serruys@erasmusmc.nl*

Abbreviations

IVUS intravascular ultrasound
LLI LightLab Imaging
OCT optical coherence tomography
PDLLA poly(D,L-lactide)
PLA polylactide
PLLA poly(L-lactide)
VH virtual histology

Introduction

The everolimus-eluting bioresorbable ABSORB scaffold (Abbott Vascular, Santa Clara, CA, USA) represents a novel approach for the treatment of coronary lesions, providing transient luminal support and vessel wall drug delivery without the long-term limitations of conventional metallic drug-eluting stents[1-3].

In the ABSORB trials, multi-modality imaging techniques were applied, including optical coherence tomography (OCT), intravascular ultrasound (IVUS) greyscale and virtual histology (VH). These modalities have been extensively used, primarily to investigate geometric changes to the vessel wall and lumen and secondarily to assess changes in the appearance of the struts, as surrogate for changes in polymer microstructure caused by hydrolytic degradation of the polymer over time. OCT, for example, monitored the progressive integration of the scaffold into the vessel wall, with modification in the reflectivity of the strut core area and in the size of the black strut core area[3,4]; IVUS showed a progressive reduction in the grey level intensity of the polymeric struts over time, detected by change in hyperechogenicity[5], and VH reported changes in dense calcium areas (DC) as the struts are detected by the software as "pseudo dense-calcium"[2,3,6,7].

However, no systematic and serial comparison between these three intracoronary imaging modalities and their derived parameters, detecting the polymer microstructural changes, has been made. With this "pilot-study", we tried to quantitatively compare the material property changes of the scaffold as detected by OCT, echogenicity and VH *in vivo* at six and 12 months after ABSORB implantation.

Methods

STUDY POPULATION

The ABSORB Cohort B study enrolled 101 patients older than 18 years of age with a diagnosis of stable/unstable angina or silent ischaemia (Trial number: NCT00856856). Those patients were divided into two groups: the first group (Cohort B1) underwent invasive imaging including greyscale IVUS, IVUS-VH and OCT at six-month follow-up; the second group (Cohort B2) had the same invasive imaging at 12 months[3]. All lesions were *de novo*, in a native coronary artery with a reference vessel diameter of 3.0 mm, a percentage diameter stenosis ≥50% and <100%, a thrombolysis in myocardial infarction flow grade of ≥1, and were treated with implantation of an ABSORB scaffold (3.0×18 mm). Major exclusion criteria were: patients with an acute myocardial infarction, unstable arrhythmias or who had a left ventricular ejection fraction <30%, restenotic lesions, lesions located in the left main coronary artery, lesions involving a side branch ≥2 mm in diameter, and the presence of thrombus or other clinically significant stenoses in the target vessel. The local ethics committee at each participating institution approved the trial and each patient gave written informed consent before inclusion.

Only patients with paired IVUS-VH, echogenicity and OCT data were included in the present analysis.

ABSORB SCAFFOLD

The ABSORB scaffold is a fully bioresorbable intracoronary device made from semi-crystalline poly(L-lactide) (PLLA) coated with an amorphous poly(D,L-lactide) (PDLLA) copolymer that contains and controls the release of the antiproliferative drug everolimus. The primary mechanism for molecular weight degradation of both polylactide (PLA) materials is hydrolysis, a process in which the ester bonds present in the monomeric subunit of PLA molecules are progressively cleaved. Ultimately, PLLA and PDLLA degrade to lactic acid, which is readily converted to lactate and processed via both the Kreb's cycle (for L-lactate) and methylglycoxal metabolism (for D-lactate[1,2,8]). Based on preclinical studies, the time for complete resorption is assumed to be approximately two years[9].

The ABSORB Cohort A and Cohort B trials evaluated the ABSORB scaffold generation 1.0 and 1.1, respectively[1,2]. There are no differences in polymeric material, drug dose, drug release rate or strut thickness between the two generations. Of note, the ABSORB 1.1 has a smaller maximum circular unsupported surface area than the ABSORB 1.0[10]. Controls implemented in the manufacturing of ABSORB 1.1 have resulted in more prolonged luminal support post-implantation[3].

IVUS ACQUISITION

Treated vessels were examined post-procedure and at follow-up with 20 MHz phased array intravascular ultrasound (IVUS) Eagle-eye® catheters (Volcano Corporation, Rancho Cordova, CA, USA), using automated pullback at 0.5 mm per second after administration of 0.2 mg intracoronary nitroglycerine. IVUS analyses were performed by an independent core laboratory (Cardialysis BV, Rotterdam, The Netherlands).

IVUS-VH ANALYSIS

Backscattering of radiofrequency signals provides information on vessel wall tissue composition[11]. All IVUS-VH analyses were performed offline using the pcVH 2.1 software (Volcano Corporation, Rancho Cordova, CA, USA). Four tissue components (necrotic core: red; dense calcium: white; fibrous: green; and fibrofatty: light green) were identified with autoregressive classification systems[11,12]. Each individual tissue component was quantified, colour coded in all IVUS cross-sections and reported as absolute and relative areas[11]. As previously shown, the polymeric struts are normally classified as areas of "pseudo dense calcium" (DC)[2,3,6,7,13]. For this reason, we assessed the change in DC areas between post-implantation and follow-up as previously reported[1,2,6].

IVUS ECHOGENICITY ANALYSIS

Fully-automated quantitative echogenicity analysis software, previously developed in-house and validated, was used to quantify the hyperechogenicity in the treated segment[5,14]. Briefly, the mean grey value of the adventitia is used to classify tissue components as either hypo- or hyperechogenic. The adventitia circumscribing the coronary artery is defined as a layer extending from 0.2 to 0.5 mm outside the external elastic membrane. To minimise artefacts, tissue within acoustic shadowed areas is excluded and very high grey level pixels are identified as upper tissue[14]. After the tissue identification process, the relative fraction of hypo- versus hyperechogenic tissue volumes are calculated for the entire scaffold segment[5]. As the polymeric struts, due to a high grey value intensity, are identified as hyperechogenic tissue and show a continuous decrease of their grey level intensity during the degradation process, we therefore used changes in hyperechogenicity as a surrogate for scaffold degradation, as previously described[5,15,16].

OCT ACQUISITION AND ANALYSIS

OCT imaging was performed as an optional investigation in selected centres, using either time domain (M3 system; LightLab Imaging [LLI], Westford, MA, USA) or frequency domain OCT systems (C7XR system, LLI) at baseline and follow-up[10,17-21]. The OCT measurements were performed with proprietary software for offline analysis (LightLab Imaging). Adjusting for the pullback speed, the analysis of continuous cross-sections was performed at 1 mm longitudinal intervals within the treated segment.

The ABSORB scaffold shows important differences with respect to metallic stents when imaged by OCT. The optically translucent polymer allows imaging of both luminal and abluminal boundaries of the strut, which appears as a box with a black central core (strut core area) framed by highly reflective borders[3]. The second generation ABSORB 1.1 shows, up to 12 months, a progressive decrease in strut core area, and none of the changes in morphological strut appearance that were seen with the first generation ABSORB 1.0[1,2]. In this analysis, we therefore focus on the changes in the strut core area between post-implantation and follow-up, as a surrogate for scaffold degradation[3,4].

STATISTICAL ANALYSIS

Categorical variables are expressed as counts and percentages. Continuous variables are presented as mean±standard deviation or median and interquartile range, according to their normal or not normal distribution. Normality of the data was evaluated using the Kolmogorov-Smirnov test. The correlation between various parameters across all time points was performed with the Spearman's test, as the data were not normally distributed.

The percentage changes for VH-derived dense calcium, hyperechogenicity and strut core area by OCT were calculated for each scaffolded coronary segment as follows:

$$\frac{\text{(Follow-up - post ABSORB scaffold implantation)}}{\text{post ABSORB scaffold implantation}} \times 100\%$$

A two-tailed value of $p<0.05$ was considered statistically significant. Statistical analyses were performed with SPSS 16.0 software (SPSS Inc., Chicago, IL, USA).

Results

BASELINE CLINICAL AND ANGIOGRAPHIC CHARACTERISTICS

Overall, 35 patients had paired multi-modality imaging analyses post-implantation and at follow-up. Of these, 17 patients were followed up at six months, and the remaining 18 were followed up at 12 months. Clinical and angiographic characteristics are shown in **Table 1**.

Table 1. Clinical and angiographic baseline characteristics.

	Cohort B1 (n=17)	Cohort B2 (n=18)
Age (years) mean±SD (n)	61.0±9.0	60.0±9.1
Men, n (%)	13 (76)	13 (72)
Smokers, n (%)	4 (23)	5 (27)
Diabetes, n (%)	2 (12)	2 (11)
Hypertension requiring medication, n (%)	8 (47)	11 (61)
Hyperlipidaemia requiring medication, n (%)	15 (88)	11 (61)
Previous target vessel intervention, n (%)	4 (23)	3 (16)
Previous myocardial infarction, n (%)	8 (47)	2 (11)
Clinical presentation, n (%)		
Stable angina	14 (82)	13 (72)
Unstable angina	2 (12)	3 (16)
Silent ischaemia	0 (0)	2 (12)
Target vessel, n (%)		
Left anterior descending	6 (35)	11 (61)
Left circumflex	5 (30)	4 (22)
Right coronary artery	6 (35)	3 (17)
SD: standard deviation		

MULTI-IMAGING ANALYSES FROM OCT, IVUS-VH AND ECHOGENICITY AT SIX AND 12 MONTHS

Table 2 shows the mean strut core area, mean absolute and relative VH-DC area, mean absolute and relative hyperechogenicity values immediately after ABSORB implantation and at six and 12-month follow-up.

At six months, the change in strut core area by OCT was –7.25% (–14.07–+0.98) (p=0.053), in VH-DC 22.13% (–10.82–+48.85) (p=0.102) and in hyperechogenicity –12.71% (–33.70–+1.41) (p=0.048). At 12 months, the change in strut core area was –12.20% (–17.55– –1.98) (p=0.093), in VH-DC –24.66% (–32.07– –7.01) (p=0.071) and in hyperechogenicity –24.64% (–36.63– –16.51) (p=0.001) **(Figure 1)**.

CORRELATION BETWEEN OCT, IVUS-VH AND ECHOGENICITY

There was a poor correlation between the changes in the evaluated parameters both at six and at 12 months (six months: OCT vs. hyperechogenicity Spearman's rho= –0.361, p=0.141; OCT vs. VH-DC Spearman's rho=0.362, p=0.139; hyperechogenicity vs. VH-DC Spearman's rho=-0.218, p=0.385; 12 months: OCT vs.

Table 2. Multi-imaging data from both cohorts.

	Cohort B1 (n=17)			Cohort B2 (n=18)		
	Baseline	6-month	*p*-value	Baseline	12-month	*p*-value
Mean strut core area (mm²)	0.21±0.03	0.20±0.05	0.053	0.19±0.03	0.17±0.06	0.093
Mean DC area (mm²)	1.15±0.90	1.39±0.82	0.050	1.47±0.72	1.23±0.49	0.029
Mean DC (%)	14.10±7.08	16.27±6.67	0.102	17.38±5.62	13.75±3.92	0.071
Mean hyperechogenicity volume (mm³)	36.6±13.7	34.5±19.0	0.446	38.2±14.3	33.2±41.0	0.093
Mean hyperechogenicity (%)	23.1±9.4	19.2±8.9	0.048	24.4±10.5	18.2±8.9	0.001
DC: dense calcium						

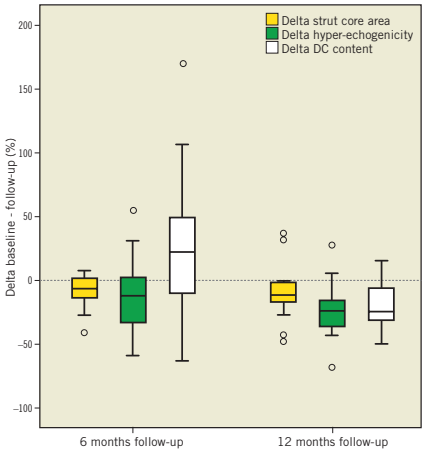

Figure 1. *Relative reduction in strut core area, hyperechogenicity and DC content between baseline and 6/12 months follow-up. DC: dense calcium*

hyperechogenicity Spearman's rho=0.262, p=0.309; OCT vs. VH-DC Spearman's rho=0.233, p=0.368; hyperechogenicity vs. VH-DC Spearman's rho=0.368, p=0.233). The correlation did not improve when considering the data from six and 12 months together (OCT vs. hyperechogenicity Spearman's rho= –0.038, p=0.830; OCT vs. VH-DC Spearman's rho=0.281, p=0.102; hyperechogenicity vs. VH-DC Spearman's rho=0.071, p=0.683) **(Figure 2)**.

Discussion

The main findings of the analysis are: 1) there appears to be a reduction in strut core area by OCT and in hyperechogenicity values both at six and 12-month follow-up; 2) VH detects contrasting changes in dense-calcium between six and 12 months; 3) at the patient level, the correlation between the various parameters detected by the three imaging modalities is poor.

One of the most interesting concepts of the ABSORB scaffold is the temporary lumen scaffolding: in contrast with metallic stents, the polymeric scaffold does not involve a permanent caging of the vessel, as it is bioresorbed over time[22,23]. In keeping with this concept, much interest has been focused on the use of intracoronary imaging techniques and their capabilities in detecting *in vivo* changes in scaffold material properties.

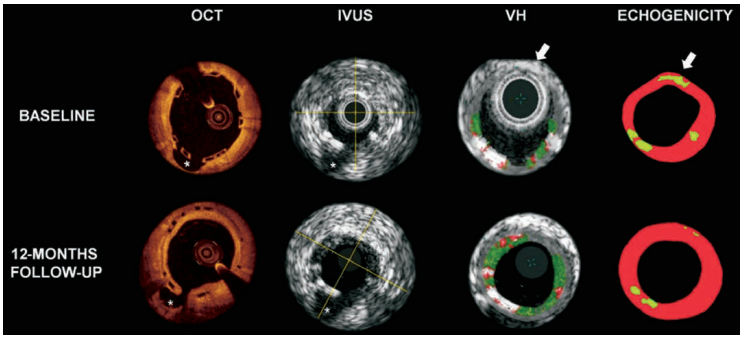

Figure 2. *Examples of OCT, IVUS, VH and echogenicity findings of corresponding cross-sectional images with a side branch (*) selected as an anatomical landmark. The white arrows indicate a hyperechogenic tissue in echogenicity analysis, hidden by the grey media stripe in the VH analysis. OCT: optical coherence tomography; IVUS: intravascular ultrasound; VH: virtual histology*

With regard to OCT, it is sensitive to refractive index changes on a length scale greater than the wavelength of the light emitted from the catheter. For this reason, it detects the polymeric struts as being highly reflective compared to the lumen and the vessel wall. Conversely, the black strut core area, despite the heterogeneity of the semi-crystalline polymer structure, has a light-poor signal after ABSORB implantation, indicating that changes in refractive index occur on a length scale less than that of the wavelength of the OCT light. However, as hydrolytic degradation progresses, it is reasonable to expect that this polymer microstructural heterogeneity coarsens, leading eventually to an increase in OCT reflectivity. For example, in the ABSORB Cohort A trial, testing the first generation ABSORB device, OCT showed that at six months, only 3% of the strut boxes kept the so-called "preserved box" appearance seen at post-implantation, whereas the remaining 97% changed their reflectivity, becoming "open box, dissolved bright box or dissolved black box[2]". Each of these OCT appearances was related to different histological characteristics in an animal study, where it was shown that reduction in strut core area and transition from preserved to open/dissolved box may represent indirect signs of scaffold degradation (e.g., polymer microstructural heterogeneity) and integration into the vessel wall[9]. Conversely, in the ABSORB Cohort B trial, using the second generation ABSORB device, the scaffold struts maintained the OCT-defined "preserved box" appearance both at six and at 12-month follow-up exhibiting a progressive reduction in black strut core area by OCT[3,24]. Concomitantly, IVUS greyscale showed a progressive reduction in the grey level intensity of the struts; this phenomenon was quantified by echogenic analysis, demonstrating a reduction in the hyperechogenicity values of the polymeric struts over time[5]. In the ABSORB Cohort A study, quantitative differential echogenicity was already applied to monitor *in vivo* changes of the scaffold by means of the acoustic property changes, showing an increase of hyperechogenic tissue immediately after the ABSORB implantation, which was back to pre-implantation values at the time of expected degradation and bioresorption (approximately two years[2,5]). At six months, the differences in hyperechogenic reduction between the ABSORB Cohort A and Cohort B (50% vs. 17%) were in line with the differences in the struts' OCT appearance and in the late loss (0.43 mm vs. 0.19 mm), further supporting differences in hydrolytic degradation rate characteristics between the two ABSORB devices[3].

At variance with these findings, a slight increase in the backscattering signal of the struts interpreted as dense calcium by VH was detected at six months with a subsequent decrease at 12 months. It should be kept in mind that not only the polymeric scaffold –with its presence and degradation– but also the tissue surrounding the struts contributes to the VH-derived dense calcium quantification, which may explain this contrasting finding[6,25]. In particular, our global evaluation of the area comprised between the lumen and the medial stripe integrates into our quantification of dense calcium also the backscattering signal not related to the sole struts, but, for instance, to the plaque behind the scaffold. Changes in composition of this plaque are therefore also detected by VH. In a porcine model some inflammatory cells, such as granuloma and giant cells, were found surrounding the polymeric struts in the early stages after implantation, before decreasing over time[9]. At six months, focusing on the VH appearance of the plaque behind the scaffold, we confirmed this observation in humans, finding a progression in the NC content[25]. Of note is that dense calcium is a frequent finding within the necrotic core region; in this case it is frequently "speckled" and can be due to calcification of a "nidus" of macrophages[26]. Changes over time in strut core area and in hyperechogenicity are instead probably less related to the plaque changes.

It is important to highlight that despite an overall agreement between hyperechogenicity and strut core area in terms of reduction of both parameters during the first 12 months, analysis at the patient level revealed that the correlation between these imaging parameters is poor. This is not surprising, since the optical and ultrasonic parameters reflect different aspects of scaffold degradation. From our animal experience, we learnt that the polymer is first hydrolysed into small oligomers digested by macrophages and that the strut voids initially occupied by the polymeric struts are then filled with proteoglycan and eventually integrated into the vessel wall. Hence, the changes in black strut core area by OCT do not reflect the molecular dissolution of the polylactide, as the polymer and the proteoglycan material have the same optical properties, but rather the filling of the strut voids by connective tissue ultimately making the struts undetectable by OCT and in histology[9]. Conversely, changes in the material properties of polylactide (e.g., crystallinity, molecular weight, stiffness, etc.) have previously been demonstrated to predominantly affect the acoustic properties of the material over time, and these can be detected by ultrasonic waves[15,16].

Although both echogenicity and VH data are based on the application of ultrasound, the correlation between them was also poor. This lack of correlation may be explained by the differences of methodologies used in these two techniques. Whilst the echogenicity software analyses the complete image and the echo intensity (envelope amplitude), which is normally used in the formation of the greyscale-IVUS image, the VH software analyses the frequency of the signal underlying the amplitude (radiofrequency backscattering). As the classification tree of VH was not validated for recognition of metallic/polymeric struts, the backscattering signal, derived from a stent/scaffold, was usually interpreted by the software as dense calcium, such as found in heavily calcified coronary segments[6,27]. Conversely, echogenicity analysis excluded from its tissue quantification the acoustically shadowed areas, resulting in a likely better discrimination between polymeric struts and calcified coronary segments. Another important point to consider in the VH detection of the polymeric struts is that some scaffold strut information may be missed because of the presence of the medial grey stripe and it is extremely dependent on the contours drawing[28,29] **(Figure 2)**. In addition no data are available to date correlating the backscattering signal changes with the physical and mechanical properties of polylactide.

Finally, it is important to note the difference in variability of the various changes explored by these techniques, with OCT exhibiting

the least variability **(Figure 1)**. The fundamental differences in the principles and spatial resolution of each technique should be taken into account in the interpretation of this variability and also of their poor correlation[30,31].

Limitations

A major limitation of our analysis is the small number of patients compared to the total number of patients enrolled in the trial. For this reason the p-values of the modification over time in the various parameters investigated have to be considered as exploratory. Nevertheless, limiting the analysis to only patients receiving all three imaging modalities allows a more accurate comparison between the various parameters investigated. Lack of data about the polylactide degradation has also to be taken into account as a possible limitation of our comparison. An *in vitro* or *ex vivo* study would be required to correlate these parameters with the scaffold/polymer degradation.

Conclusions

Our analysis showed that during the first 12 months after ABSORB scaffold implantation there is a reduction in black strut core area, as measured by OCT, and in the hyperechogenicity of the scaffold, representing independent signs of scaffold/polymer degradation. In contrast, VH only showed a reduction in "pseudo dense-calcium" at 12 months indicating some limitations in monitoring scaffold property changes.

Acknowledgements

The ABSORB Trial is sponsored and funded by Abbott Vascular, Santa Clara, CA, USA.

Conflict of interest statement

J. Oberhauser and R. Rapoza are employees of Abbott Vascular. None of the other authors have conflicts of interest relevant to the subject material in this paper.

References

1. Ormiston JA, Serruys PW, Regar E, Dudek D, Thuesen L, Webster MW, Onuma Y, Garcia-Garcia HM, McGreevy R, Veldhof S. A bioabsorbable everolimus-eluting coronary stent system for patients with single de-novo coronary artery lesions (ABSORB): A prospective open-label trial. *Lancet*. 2008;371:899-907.

2. Serruys PW, Ormiston JA, Onuma Y, Regar E, Gonzalo N, Garcia-Garcia HM, Nieman K, Bruining N, Dorange C, Miquel-Hebert K, Veldhof S, Webster M, Thuesen L, Dudek D. A bioabsorbable everolimus-eluting coronary stent system (ABSORB): 2-year outcomes and results from multiple imaging methods. *Lancet*. 2009;373:897-910.

3. Serruys PW, Onuma Y, Ormiston JA, de Bruyne B, Regar E, Dudek D, Thuesen L, Smits PC, Chevalier B, McClean D, Koolen J, Windecker S, Whitbourn R, Meredith I, Dorange C, Veldhof S, Miquel-Hebert K, Rapoza R, Garcia-Garcia HM. Evaluation of the second generation of a bioresorbable everolimus drug-eluting vascular scaffold for treatment of de novo coronary artery stenosis: Six-month clinical and imaging outcomes. *Circulation*. 2010;122:2301-2312.

4. Gomez-Lara J, Brugaletta S, Diletti R, Garg S, Onuma Y, Gogas BD, van Geuns RJ, Dorange C, Veldhof S, Rapoza R, Whitbourn R, Windecker S, Garcia-Garcia HM, Regar E, Serruys PW. A comparative assessment by optical coherence tomography of the performance of the first and second generation of the everolimus-eluting bioresorbable vascular scaffolds. *Eur Heart J*. 2011;32: 294-304.

5. Bruining N, de Winter S, Roelandt JR, Regar E, Heller I, van Domburg RT, Hamers R, Onuma Y, Dudek D, Webster MW, Thuesen L, Ormiston JA, Cheong WF, Miquel-Hebert K, Veldhof S, Serruys PW. Monitoring in vivo absorption of a drug-eluting bioabsorbable stent with intravascular ultrasound-derived parameters a feasibility study. *JACC Cardiovasc Interv*. 2010;3:449-456.

6. Garcia-Garcia HM, Gonzalo N, Pawar R, Kukreja N, Dudek D, Thuesen L, Ormiston JA, Regar E, Serruys PW. Assessment of the absorption proces s following bioabsorbable everolimus-eluting stent implantation: Temporal changes in strain values and tissue composition using intravascular ultrasound radiofrequency data analysis. A substudy of the ABSORB clinical trial. *EuroIntervention*. 2009;4:443-448.

7. Brugaletta S, Garcia-Garcia HM, Diletti R, Gomez-Lara J, Garg S, Onuma Y, Shin ES, Van Geuns RJ, De Bruyne B, Dudek D, Thuesen L, Chevalier B, McClean D, Windecker S, Whitbourn R, Dorange C, Veldhof S, Rapoza R, Sudhir K, Bruining N, Ormiston J, Serruys P. Comparison between the first and second generation bioresorbable vascular scaffolds: A six month virtual histology study. *EuroIntervention*. 2011;6:1110-6.

8. Ewaschuk JB, Naylor JM, Zello GA. D-lactate in human and ruminant metabolism. *J Nutr.* 2005;135:1619-1625.

9. Onuma Y, Serruys PW, Perkins LE, Okamura T, Gonzalo N, Garcia-Garcia HM, Regar E, Kamberi M, Powers JC, Rapoza R, van Beusekom H, van der Giessen W, Virmani R. Intracoronary optical coherence tomography and histology at 1 month and 2, 3, and 4 years after implantation of everolimus-eluting bioresorbable vascular scaffolds in a porcine coronary artery model: An attempt to decipher the human optical coherence tomography images in the ABSORB trial. *Circulation*. 2010;122:2288-2300.

10. Okamura T, Garg S, Gutierrez-Chico JL, Shin ES, Onuma Y, Garcia HM, Rapoza R, Sudhir K, Regar E, Serruys PW. In vivo evaluation of stent strut distribution patterns in the bioabsorbable everolimus-eluting device: an OCT ad hoc analysis of the revision 1.0 and revision 1.1 stent design in the ABSORB clinical trial. *EuroIntervention*. 2010;6:932-938.

11. Nair A, Kuban BD, Tuzcu EM, Schoenhagen P, Nissen SE, Vince DG. Coronary plaque classification with intravascular ultrasound radiofrequency data analysis. *Circulation*. 2002;106:2200-2206.

12. Nasu K, Tsuchikane E, Katoh O, Vince DG, Virmani R, Surmely JF, Murata A, Takeda Y, Ito T, Ehara M, Matsubara T, Terashima M, Suzuki T. Accuracy of in vivo coronary plaque morphology assessment: A validation study of in vivo virtual histology

compared with in vitro histopathology. *J Am Coll Cardiol.* 2006;47: 2405-2412.

13. Serruys PW, Onuma Y, Dudek D, Smits PC, Koolen J, Chevalier B, De Bruyne B, Thuesen L, McClean D, van Geuns RJ, Windecker S, Whitbourn R, Meredith C, Dorange C, Veldhof S, Miquel-Hebert K, Sudhir K, Garcia-Garcia HM, Ormiston JA. Evaluation of the second generation of a bioresorbable everolimus-eluting vascular scaffold for the treatment of de novo coronary artery stenosis: 12-month clinical and imaging outcomes. *J Am Coll Cardiol.* 2011;58:1578-88.

14. Bruining N, Verheye S, Knaapen M, Somers P, Roelandt JR, Regar E, Heller I, de Winter S, Ligthart J, Van Langenhove G, de Feijter PJ, Serruys PW, Hamers R. Three-dimensional and quantitative analysis of atherosclerotic plaque composition by automated differential echogenicity. *Catheter Cardiovasc Interv.* 2007;70: 968-978.

15. Wu HC, Shen FW, Hong X, Chang WV, Winet H. Monitoring the degradation process of biopolymers by ultrasonic longitudinal wave pulse-echo technique. *Biomaterials*. 2003;24:3871-3876.

16. Parker NG, Mather ML, Morgan SP, Povey MJ. Longitudinal acoustic properties of poly(lactic acid) and poly(lactic-co-glycolic acid). *Biomed Mater.* 2010;5:055004.

17. Sihan K, Botha C, Post F, de Winter S, Gonzalo N, Regar E, Serruys PJ, Hamers R, Bruining N. Fully automatic three-dimensional quantitative analysis of intracoronary optical coherence tomography: Method and validation. *Catheter Cardiovasc Interv.* 2009;74:1058-1065.

18. Prati F, Regar E, Mintz GS, Arbustini E, Di Mario C, Jang IK, Akasaka T, Costa M, Guagliumi G, Grube E, Ozaki Y, Pinto F, Serruys PW. Expert review document on methodology, terminology, and clinical applications of optical coherence tomography: Physical principles, methodology of image acquisition, and clinical application for assessment of coronary arteries and atherosclerosis. *Eur Heart J.* 2010;31:401-415.

19. Gonzalo N, Serruys PW, Okamura T, Shen ZJ, Onuma Y, Garcia-Garcia HM, Sarno G, Schultz C, van Geuns RJ, Ligthart J, Regar E. Optical coherence tomography assessment of the acute effects of stent implantation on the vessel wall: A systematic quantitative approach. *Heart*. 2009;95:1913-1919.

20. Regar E, Leeuwen AMGJv, Serruys PW. Optical coherence tomography in cardiovascular research. *Informa Healthcare*; 2007.

21. Gonzalo N, Serruys PW, Garcia-Garcia HM, van Soest G, Okamura T, Ligthart J, Knaapen M, Verheye S, Bruining N, Regar E. Quantitative ex vivo and in vivo comparison of lumen dimensions measured by optical coherence tomography and intravascular ultrasound in human coronary arteries. *Rev Esp Cardiol.* 2009;62:615-624.

22. Onuma Y, Serruys PW. Bioresorbable scaffold: The advent of a new era in percutaneous coronary and peripheral revascularization? *Circulation*. 2011;123:779-797.

23. Oberhauser JP, Hossainy S, Rapoza R. Design principles and performance of bioresorbable polymeric vascular scaffolds. *EuroIntervention.* 2009;5:F15-F22.

24. Brugaletta S, Garcia-Garcia HM, Garg S, Gomez-Lara J, Diletti R, Onuma Y, van Geuns RJ, McClean D, Dudek D, Thuesen L, Chevalier B, Windecker S, Whitbourn R, Dorange C, Miquel-Hebert K, Sudhir K, Ormiston JA, Serruys PW. Temporal changes of coronary artery plaque located behind the struts of the everolimus eluting bioresorbable vascular scaffold. *Int J Cardiovasc Imaging*. 2011;27:859-866.

25. Garcia-Garcia HM, Mintz GS, Lerman A, Vince DG, Margolis MP, van Es GA, Morel MA, Nair A, Virmani R, Burke AP, Stone GW, Serruys PW. Tissue characterisation using intravascular radiofrequency data analysis: Recommendations for acquisition, analysis, interpretation and reporting. *EuroIntervention*. 2009;5:177-189.

26. Kubo T, Maehara A, Mintz GS, Garcia-Garcia HM, Serruys PW, Suzuki T, Klauss V, Sumitsuji S, Lerman A, Marso SP, Margolis MP, Margolis JR, Foster MC, De Bruyne B, Leon MB, Stone GW. Analysis of the long-term effects of drug-eluting stents on coronary arterial wall morphology as assessed by virtual histology intravascular ultrasound. *Am Heart J.* 2010;159:271-277.

27. Shin ES, Garcia-Garcia HM, Garg S, Ligthart J, Thuesen L, Dudek D, Ormiston JA, Serruys PW. Assessment of the serial changes of vessel wall contents in atherosclerotic coronary lesion with bioresorbable everolimus-eluting vascular scaffolds using shin's method: An IVUS study. *Int J Cardiovasc Imaging.* 2011;27:931-7.

28. Mintz GS, Nissen SE, Anderson WD, Bailey SR, Erbel R, Fitzgerald PJ, Pinto FJ, Rosenfield K, Siegel RJ, Tuzcu EM, Yock PG. American college of cardiology clinical expert consensus document on standards for acquisition, measurement and reporting of intravascular ultrasound studies (ivus). A report of the american college of cardiology task force on clinical expert consensus documents. *J Am Coll Cardiol.* 2001;37:1478-1492.

29. Bezerra HG, Costa MA, Guagliumi G, Rollins AM, Simon DI. Intracoronary optical coherence tomography: A comprehensive review clinical and research applications. *JACC Cardiovasc Interv.* 2009;2:1035-1046.

CHAPTER 5 THE APPLICATION OF OPTICAL COHERENCE TOMOGRAPHY IN THE CLINICAL EVALUATION OF BIORESORBABLE SCAFFOLDS

5.2 Serial analysis of the malapposed and uncovered struts of the new generation of everolimus-eluting bioresorbable scaffold with optical coherence tomography.

Gomez-Lara J, **Radu M**, Brugaletta S, Farooq V, Diletti R, Onuma Y, Windecker S, Thuesen L, McClean D, Koolen J, Whitbourn R, Dudek D, Smits PC, Regar E, Veldhof S, Rapoza R, Ormiston JA, Garcia-Garcia HM, Serruys PW.

JACC Cardiovascular Interventions. 2011;4:992-1001.

Serial Analysis of the Malapposed and Uncovered Struts of the New Generation of Everolimus-Eluting Bioresorbable Scaffold With Optical Coherence Tomography

Josep Gomez-Lara, MD,* Maria Radu, MD,* Salvatore Brugaletta, MD,* Vasim Farooq, MBChB,* Roberto Diletti, MD,* Yoshinobu Onuma, MD,* Stephan Windecker, MD,† Leif Thuesen, MD,‡ Dougal McClean, MD,§ Jacques Koolen, MD, PhD,‖ Robert Whitbourn, MD,¶ Dariusz Dudek, MD,# Pieter C. Smits, MD, PhD,** Evelyn Regar, MD, PhD,* Susan Veldhof, RN,†† Richard Rapoza, PhD,‡‡ John A. Ormiston, MBChB, PhD,§§ Hector M. Garcia-Garcia, MD, PhD,* Patrick W. Serruys, MD, PhD*

Rotterdam and Eindhoven, the Netherlands; Bern, Switzerland; Aarhus, Denmark; Christchurch and Auckland, New Zealand; Fitzroy, Australia; Krakow, Poland; Diegem, Belgium; and Santa Clara, California

Objectives The aim of this study is to assess the serial changes in strut apposition and coverage of the bioresorbable vascular scaffolds (BVS) and to relate this with the presence of intraluminal masses at 6 months with optical coherence tomography (OCT).

Background Incomplete strut/scaffold apposition (ISA) and uncovered struts are related to a higher risk of scaffold thrombosis. Bioresorbable vascular scaffolds can potentially avoid the risk of scaffold thrombosis because of its complete resorption. However, during the resorption period, the risk of scaffold thrombosis is unknown.

Methods OCT was performed in 25 patients at baseline and 6 months. Struts were classified according to apposition, coverage, and presence of intraluminal masses. Persistent ISA was defined as malapposed struts present at baseline and follow-up, and late acquired ISA as ISA developing at follow-up, and scaffold pattern irregularities when the strut distribution suggested scaffold fracture.

Results At baseline, 3,686 struts were analyzed: 128 (4%) were ISA, and 53 (1%) were located over side-branches (SB). At 6 months, 3,905 struts were analyzed: 32 (1%) ISA, and 35 (1%) at the SB. Persistent ISA was observed more frequently than late acquired-ISA (81% vs. 16%, respectively; 3% were unmatchable). Late acquired ISA was associated with scaffold pattern irregularities, which were related to overstretching of the scaffold. Uncovered struts (63 struts, 2%) were more frequently observed in ISA and SB struts, compared with apposed struts (29% vs. 1%; $p < 0.01$). Intraluminal masses (14 cross-sections, 3%; in 6 patients, 24%) were more frequently located at the site of ISA and/or uncovered struts (39% vs. 2% and 13% vs. 2%, respectively; $p < 0.01$).

Conclusions The lack of strut apposition at baseline is related to the presence of uncovered struts and intraluminal masses at 6 month. An appropriate balloon/artery ratio respecting the actual vessel size and avoiding the overstretching of the scaffold can potentially decrease the risk of scaffold thrombosis. (ABSORB Clinical Investigation, Cohort B [ABSORB B]; NCT00856856) (J Am Coll Cardiol Intv 2011;4:992–1001) © 2011 by the American College of Cardiology Foundation

From the *Thoraxcenter, Erasmus Medical Center, Rotterdam, the Netherlands; †Swiss Cardiovascular Center, Bern, Switzerland; ‡Skejby Sygehus, Aarhus University Hospital, Aarhus, Denmark; §Christchurch Hospital, Christchurch, New Zealand; ‖Catharina Ziekenhuis, Eindhoven, the Netherlands; ¶St. Vincent's Hospital, Fitzroy, Australia; #Jagiellonian University, Krakow, Poland; **Maasstad Ziekenhuis, Rotterdam, the Netherlands; ††Abbott Laboratories, Ltd., Vascular, Diegem, Belgium; ‡‡Abbott Laboratories, Ltd., Vascular, Santa Clara, California; and the §§Auckland City Hospital, Auckland, New Zealand. The Absorb

Serial intravascular ultrasound (IVUS) imaging of metallic drug-eluting stents (DES) has shown that incomplete stent/strut apposition (ISA) at follow-up can be caused by the persistence of ISA observed at baseline or by the new appearance of late acquired incomplete scaffold/strut apposition (LAISA) (1,2). Recent reports suggest that strut apposition is important for the development of strut coverage, because malapposed struts are more frequently uncovered at follow-up, as compared with apposed struts (3,4). Furthermore, the absence of neointimal coverage as well as the presence of malapposed struts have been related to late stent thrombosis, even in patients treated with dual antiplatelet therapy (5,6).

The novel everolimus-eluting bioresorbable vascular scaffolds (BVS) are promising intravascular devices that can potentially circumvent the risk of malapposed and uncovered struts at follow-up. Notably, at 2 years after implantation, the polymeric material has been shown to be resorbed with the disappearance of struts that were initially malapposed or at side branches (SBs) (7). The first-generation BVS (version 1.0) demonstrated a high rate of malapposed struts before complete resorption, with a rate of malapposed struts at 6 months higher than at baseline (6% vs. 5%, respectively; $p < 0.01$). This uncommon phenomenon was caused by a low rate of resolved malapposed struts and by the occurrence of LAISA at 6-month follow-up (8). The late scaffold area reduction (shrinkage) observed at 6 months was the most plausible explanation for the higher rate of ISA observed at follow-up compared with baseline. Despite this, only 1% of struts remained uncovered at 6-month follow-up (8).

The new-generation BVS (version 1.1) uses a new platform design and a different processing of the polymer, as compared with the previous generation of BVS (version 1.0), resulting in an increased radial force and longer retention of mechanical integrity (9). Consequently, there is now no detectable loss in scaffold area at 6 months (10,11). Nevertheless, ISA and uncovered struts can still be detected with the new generation of BVS, but the fate of these struts is unknown.

The aim of our study is to describe the serial changes of ISA and uncovered struts at baseline and at 6-month follow-up of the new generation of BVS (version 1.1), as assessed by optical coherence tomography (OCT).

Methods

Population. The ABSORB Cohort B (A Clinical Evaluation of the Bioabsorbable Everolimus Eluting Coronary Stent System [BVS EECSS] in the Treatment of Patients With de Novo Native Coronary Artery Lesions) trial is a nonrandomized, multicenter, single-arm, efficacy-safety study (12). The study included 101 patients that were allocated to 6-month angiographic and intravascular imaging control (cohort B1) or 12-month angiographic and intravascular imaging control (cohort B2). All lesions were treated with a single-size device (3×18 mm) of the new generation of BVS (version 1.1). The OCT imaging was an optional investigation performed in selected participating centers. In brief, the common inclusion criteria were patients 18 years of age or older, with a diagnosis of stable, unstable, or silent ischemia that presented with a de novo lesion in a native coronary artery between 50% and 99% of the luminal diameter and a Thrombolysis In Myocardial Infarction flow grade of 1 or more. Exclusion criteria included patients with an evolving myocardial infarction, stenosis of the left main or ostial right coronary artery, presence of intracoronary thrombus, or heavy calcification.

The present study is a post hoc analysis of those patients included in the ABSORB cohort B1 that were serially imaged with OCT at baseline and at 6-month follow-up.

BVS. The BVS version 1.1 revision is a balloon-expandable device, consisting of a polymer backbone of poly-L-lactide coated with a thin layer of a 1:1 mixture of an amorphous matrix of poly-D,L-lactide polymer containing 100 $\mu g/cm^2$ of the antiproliferative drug everolimus. The implant is radiolucent but has 2 platinum markers at each edge, which allows visualization on angiography and other imaging modalities. Physically, the scaffold has struts with an approximate thickness of 150 μm arranged as in-phase zigzag hoops linked together by 3 longitudinal bridges.

Abbreviations and Acronyms

BVS = bioresorbable vascular scaffolds

DES = drug-eluting stents

ISA = incomplete scaffold/strut apposition

IVUS = intravascular ultrasound

LAISA = late acquired incomplete scaffold/strut apposition

OCT = optical coherence tomography

SB = side branch

Cohort B study has been funded by Abbott Vascular (Santa Clara, California). Dr. Windecker has received research grants from Abbott, Cordis, Medtronic, Biosensors, and Boston Scientific. Dr. Dudek has received research grants or served as consultant/advisory board member for Abbott, Adamed, AstraZeneca, Biotronik, Balton, Bayer, BBraun, BioMatrix, Boston Scientific, Boehringer Ingelheim, Bristol-Myers Squibb, Cordis, Cook, Eli Lilly, EuroCor, Glaxo, Invatec, Medtronic, The Medicines Co., MSD, Nycomed, Orbus-Neich, Pfizer, Possis, Promed, Sanofi-Aventis, Siemens, Solvay, Terumo, and Tyco. Dr. Smits has received travel fees from Abbott Vascular. Ms. Susan Veldhof and Dr. Rapoza are employees of Abbott Vascular. Dr. Ormiston is on the advisory board of and has received minor honoraria from Abbott Vascular and Boston Scientific. All other authors have reported that they have no relationships relevant to the contents of this paper to disclose.

Manuscript received November 30, 2010; revised manuscript received March 18, 2011, accepted March 28, 2011.

Treatment procedure. Lesions were treated with routine interventional techniques. As per protocol, pre-dilation with conventional balloons was mandatory. Pre-dilation balloons should be shorter than the length of the scaffold and 0.5-mm smaller in diameter than the reference vessel. The BVS implantation should not exceed the burst pressure as indicated by the product chart (16 atm). Post-dilation with a balloon shorter than the implanted device was allowed at the discretion of the operator but, when performed, should only be done with balloons sized to fit within the boundaries of the scaffold. Intravascular imaging techniques were performed when optimal BVS placement was obtained according to the judgment of the physician on the basis of angiographic results. In case of suboptimal deployment as assessed by intravascular imaging techniques, post-dilations were allowed at discretion of the operator until optimal stent placement was achieved (on the basis of angiography). After the last post-dilation, a new intravascular imaging acquisition was performed and was used for the study analysis.

OCT acquisition. The OCT imaging was performed with 2 different OCT systems (M3 Time-Domain System and C7XR Fourier-Domain System; LightLab Imaging, Westford, Massachusetts). The M3 OCT system used a standard intracoronary guidewire to cross the target lesion, and then a single-lumen (e.g., Transit, Cordis, Johnson and Johnson, Miami, Florida, or ProGreat, Terumo, Tokyo, Japan) or double-lumen catheter (0.023-inch TwinPass, Vascular Solutions, Inc., Minneapolis, Minnesota) was required to exchange the conventional wire with the LightLab Imaging ImageWire. Pullback was performed during continuous injection of contrast medium (1 to 3 ml/s, iodixanol 370; Visipaque, GE Healthcare, Cork, Ireland) through the guide catheter with an injection pump. The automated pullback was performed at 3 mm/s with a frame rate of 20 images/s.

The C7XR system used a conventional wire to cross the segment of interest. The OCT imaging catheter (Dragonfly, LightLab Imaging) was then advanced distally to the treated region. Pullback was performed during continuous injection of contrast medium (3 ml/s, iodixanol 370; Visipaque) through the guide catheter with an injection pump. The automated pullback rate was 20 mm/s, and the frame rate was 100 images/s.

OCT analysis. Offline OCT qualitative data analysis was carried out by 2 expert analysts with the proprietary software for offline analysis (LightLab Imaging). Both investigators were blinded to the patient, procedural, and clinical characteristics as well as to the clinical outcomes. Adjusting for the pullback speed, the analysis of contiguous cross-sections was performed at 1-mm longitudinal intervals within the treated segment (7 cross-sections/mm in case of M3 OCT system and 5 cross-sections/mm in case of C7 OCT system).

At baseline, embedded struts were defined as present when more than one-half thickness of the strut was impacted into the vessel wall; protruding struts were defined as struts being in contact with the vessel wall but with less than one-half strut thickness impacted into the vessel wall. Both embedded and protruding struts presented with different degrees of apposed struts at follow-up, but we made no distinction. At baseline and follow-up, malapposed struts were defined as struts where the abluminal surfaces were separated from the vessel wall by flush; and SB struts were defined as struts overlying the ostium of an SB (Fig. 1). It is noteworthy that, in contrast with metallic stents, the BVS allows the assessment of the structures located behind the struts without the usual shadowing of metallic struts. Therefore, strut malapposition can be easily assessed when the polymeric strut is separated from the vessel wall. At follow-up, the absence of strut coverage was defined when 1 of the strut corners preserved the right angle shape without signs of neointimal tissue (Fig. 1). Although strut apposition and coverage was measured as a consensus between 2 analysts, a total of 100 random images of 10 different patients were analyzed separately by 2 analysts to ensure the agreement of the qualitative assessments. Scaffold pattern irregularities were defined when struts were found in locations incongruent with the scaffold pattern. They were classified into 2 categories: 1) 2 struts overhanging each other in the same angular sector of the lumen perimeter, with or without malapposition; and/or 2) isolated struts located more or less at the center of the vessel without obvious connection to the expected adjacent strut pattern. At follow-up, protruding masses attached to the vessel wall or floating masses without contact with the vessel wall have been suggested to be thrombi (3). However, the distinction between thrombi and neointimal protrusions into the lumen is not always possible. Therefore, any irregular mass attached to the polymeric struts or floating into the lumen has been classified as intraluminal mass without distinction between thrombus and neointima.

With clear landmarks in the longitudinal OCT images, all cross-sections with at least 1 ISA or SB strut at baseline were matched with the corresponding image of all the possible cross-sections of the entire recording at follow-up (every 7 cross-sections/mm in case of M3 OCT system and every 5 cross-sections/mm in case of C7 OCT system). Every single ISA or SB strut at baseline was investigated at follow-up, to assess its apposition and the state of neointimal coverage. Similarly, those images with at least 1 ISA and/or uncovered struts at follow-up were matched to the corresponding image at baseline of all possible cross-sections of the entire recording at baseline and investigated to assess the original state of strut apposition.

Statistical analysis. Statistical analysis was performed with the SPSS software (version 15.0, SPSS, Inc., Chicago, Illinois). Discrete variables are presented as counts and percentages and continuous variables as mean ± SD. Comparisons of continuous variables between baseline and

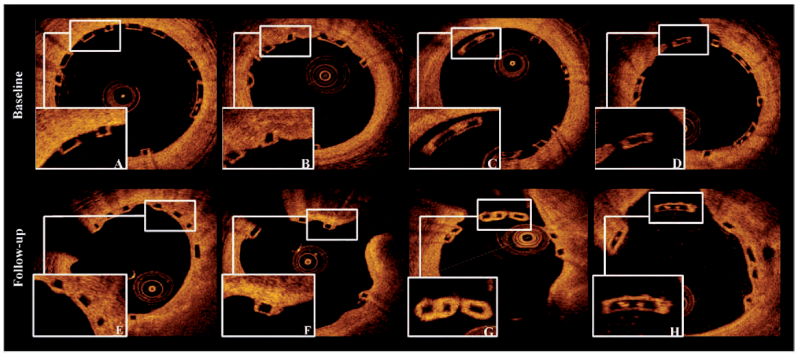

Figure 1. Strut Apposition and Coverage Assessment

Apposition assessment at baseline: **(A)** protruding struts: less than one-half thickness of the strut is impacted into the vessel wall; **(B)** embedded strut: more than one-half thickness of the strut is impacted into the vessel wall; **(C)** incomplete strut/scaffold apposition (ISA): the back-side of the strut is separated from the vessel wall; **(D)** side-branches (SB) strut: the strut is located in the take-off of an SB without any contact with the vessel wall. Strut coverage assessment at follow-up: **(E)** apposed and covered strut: the 4 corners of the polymeric strut have lost the right angle shape with signs of tissue coverage; **(F)** apposed and uncovered strut: 1 of the 2 endoluminal strut corners preserves the right angle shape without signs of tissue coverage; **(G)** ISA/SB and covered strut: the 4 strut corners have lost the right angle shape with signs of tissue coverage; **(H)** ISA/SB and uncovered: 1 of the 4 strut corners preserves the right angle shape without signs of tissue coverage.

follow-up have been estimated with the nonparametric Wilcoxon signed-rank test. Comparison of percentages of uncovered struts between apposed and nonapposed struts has been performed with the Mann-Whitney *U* test at strut level analysis. Adjustments for clustering data at the patient and frame level analysis have not been performed. A 2-sided p value $\leq$0.05 was considered statistically significant.

The interobserver agreement for qualitative measurements was quantified by the Cohen's kappa test for concordance (13). In accordance with previous publications, a value <0 indicates poor agreement, 0 to 0.20 indicates slight agreement, 0.21 to 0.40 indicates fair agreement, 0.41 to 0.60 indicates moderate agreement, 0.61 to 0.80 indicates good agreement, and 0.81 to 1.0 indicates excellent agreement (14).

Results

Population. The ABSORB Cohort B1 study included 45 patients, 28 of whom were imaged with OCT at baseline. Two patients were excluded due to suboptimal quality of the OCT recording (lack of imaging of the full length and/or perimeter of the implant); and 1 asymptomatic patient withdrew consent to invasive control at 6-month follow-up. The remaining 25 patients, all of whom were serially imaged with OCT at baseline and 6-month follow-up, were included in the present study. A total of 11 and 9 patients were imaged with the M3 OCT system at baseline and follow-up, respectively; whereas 14 and 16 patients were imaged with the C7 OCT system at baseline and follow-up, respectively. Only 2 patients were imaged with different OCT systems at baseline and follow-up.

Table 1. Baseline Clinical and Angiographic Characteristics (n = 25)

Male	20 (80.0)
Age (yrs)	62.4 ± 10.0
Hypertension	14 (56.0)
Hypercholesterolemia	24 (96.0)
Diabetes	2 (8.0)
Smokers	5 (20.0)
Prior MI	11 (44.0)
Prior PCI	6 (24.0)
Clinical indication	
Stable angina	21 (84.0)
Unstable angina	4 (16.0)
Number of vessel disease	
1	21 (84.0)
2	3 (12.0)
3	1 (4.0)
Target vessel	
Left anterior descending	11 (44.0)
Left circumflex	6 (24.0)
Right coronary artery	8 (32.0)

Values are count (%) or mean ± SD.
MI = myocardial infarction; PCI = percutaneous coronary intervention.

Table 2. Qualitative OCT Findings at Baseline (n = 25)

Number of struts	3,686
Protruding	2,554 (69.3%)
Embedded	951 (25.8%)
ISA	128 (3.5%)
SB	53 (1.4%)
Matched ISA at baseline that at 6 months became	128
Apposed + covered	97 (75.8%)
Apposed + uncovered	6 (4.7%)
Persistent ISA + covered	15 (11.7%)
Persistent ISA + uncovered	4 (3.1%)
Unmatchable	6 (4.7%)
Matched SB struts at baseline that at 6 months became	53
Apposed + covered	12 (22.7%)
Apposed + uncovered	1 (1.9%)
SB + covered	27 (50.9%)
SB + uncovered	5 (9.4%)
Unmatchable	8 (15.1%)

ISA = incomplete scaffold/strut apposition; OCT = optical coherence tomography; SB = side branch.

Baseline clinical and angiographic characteristics are shown in Table 1. Mean age was 62.4 years; 80% were men, and 8% were diabetic. The clinical indication of the index procedure was stable angina in 84% of patients. A total of 85% of patients had single-vessel disease.

Qualitative OCT findings at baseline. Qualitative OCT findings at baseline are shown in Table 2. At baseline, 3,686 struts in 424 frames were analyzed: 2,554 were classified as protruding (69.3%), 951 as embedded (25.8%), 128 as ISA (3.5%), and 53 struts were overlying an SB (1.4%). Figure 2 shows the distribution of malapposed and SB struts throughout the length of the BVS.

Matched cross-sections. A total of 80 of 90 baseline images with ISA and/or SB struts were properly matched with the corresponding frame at 6-month follow-up. Therefore, 95.3% of malapposed and 84.9% of SB struts were properly matched between time points. At follow-up, the fate of the malapposed struts observed at baseline was: 80.5% resolved into apposed struts, and 14.8% persisted as ISA (4.7% were unmatchable).

Qualitative OCT findings at 6-month follow-up. At 6 months, all polymeric struts were visible, remaining with the preserved box appearance. Qualitative OCT findings are shown in Table 3. At follow-up, 3,905 struts in 433 frames were analyzed: 3,838 were apposed (98.3%), 32 were malapposed (0.8%), and 35 were located over an SB (0.9%). Lack of tissue coverage was detected in 63 struts (1.6%). Distribution of ISA, SB, and uncovered struts throughout the length of the BVS is shown in Figure 2.

Strut coverage. A total of 43 of 3,838 apposed struts (1.1%) were uncovered, whereas 10 of 32 ISA struts (31.3%) and 10 of 35 SB struts (28.6%) were uncovered. The comparison of the rate of uncovered plus apposed struts (1.1%) with the rate of uncovered plus ISA or SB struts (29.0%) was statistically significant ($p < 0.01$) (Fig. 3).

Intraluminal masses. At 6 months, intraluminal masses were observed in 14 cross-sections (2.9%) in 6 patients (24.0%).

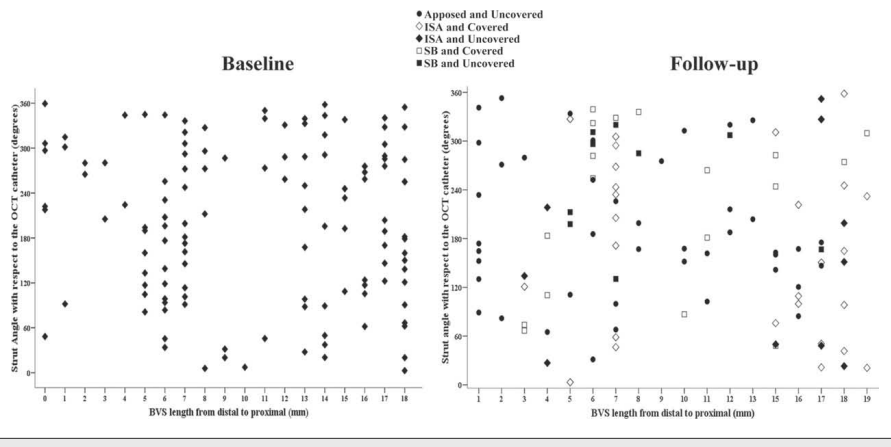

Figure 2. Distribution of Malapposed and Uncovered Struts

Strut distribution with respect to the optical coherence tomography (OCT) catheter (degrees) and location throughout the bioresorbable vascular scaffold (BVS) length (from distal to proximal) of malapposed, side-branch (SB), and uncovered struts. ISA = incomplete strut/scaffold apposition.

Table 3. Qualitative OCT Findings at 6-Month Follow-Up

Number of struts at 6 months	3,905
Apposed + covered	3,795 (97.2%)
Apposed + uncovered	43 (1.1%)
ISA + covered	22 (0.5%)
ISA + uncovered	10 (0.3%)
SB + covered	25 (0.6%)
SB + uncovered	10 (0.3%)
Number of struts with attached intraluminal masses at 6 months*	21 (0.5%)
Apposed + covered	9 (0.2%)
Apposed + uncovered	4 (9.3%)
ISA + covered	4 (18.2%)
ISA + uncovered	4 (40%)
SB + covered	0
SB + uncovered	0
Matched ISA struts at follow-up that at baseline were:	32 (0.8%)
ISA	26 (81.3%)
Protruding	5 (15.6%)
Embedded	0
Unmatchable	1 (3.1%)
Matched uncovered struts at follow-up that at baseline were:	63 (1.6%)
Protruding	36 (57.1%)
Embedded	4 (6.3%)
ISA	10 (15.9%)
SB	10 (15.9%)
Unmatchable	3 (4.8%)
Matched ISA + uncovered struts at follow-up that at baseline were:	10 (0.3%)
Protruding	5 (50.0%)
ISA	5 (50.0%)

N = 25. *Percentages are estimated according the total amount of each strut type. Abbreviations as in Table 2.

Notably, intraluminal masses were more often associated with malapposed and/or uncovered struts rather than apposed and covered struts. Of struts with attached intraluminal masses, 40.0% of struts were malapposed and uncovered, 18.2% were malapposed and covered, 9.3% were apposed and uncovered, and 0.9% were apposed and covered ($p < 0.01$).

Matched cross-sections. A total of 51 of 53 cross-sections with ISA or uncovered struts were properly matched with the corresponding image at baseline. Likewise, 97.1% of malapposed and 95.2% of uncovered struts were properly matched. The ISA was more frequently caused by persistent ISA (81.3%) rather than LAISA (15.6%); 3.1% of the struts were unmatchable. Late acquired ISA was only found in 2 patients (8.0%). Serial analysis of uncovered struts showed that, at baseline, 36 matched struts were classified as protruding (57.1%), 4 as embedded (6.3%), and 10 as ISA (15.9%), and 10 struts were overlying an SB (15.9%); 4.8% were unmatchable.

Clinical outcomes. At 6-month follow-up, no death, spontaneous acute myocardial infarction, scaffold thrombosis, or target lesion revascularization of the 25 patients included in the present study were documented. One patient experienced a periprocedural acute myocardial infarction at the time of the index procedure without any further complications. Another patient with suboptimal OCT imaging at baseline (and excluded from our study) presented with nonclinically driven target lesion revascularization at day 33. At that time, OCT imaging showed scaffold pattern irregularities demonstrating substantial structural distortion, with intraluminal masses attached to the malapposed struts. At the time of the index procedure, this patient was also treated with a post-dilation balloon that achieved a larger predicted diameter than the maximum limit recommended for the BVS.

Qualitative coverage agreement between the 2 analysts. Two analysts investigated, in separate analyses, 100 selected cross-sections of 10 different patients with 767 struts. Both analysts agreed in 710 and 35 covered and uncovered struts, respectively. The Kappa index was 0.75 (good agreement).

Discussion

The main findings of our study are: 1) with the BVS version 1.1, the number of malapposed struts decreased from baseline to 6-month follow-up; 2) 80% of the malapposed struts observed at baseline resolved into apposed struts at follow-up, with a relatively low rate of LAISA at 6 months; 3) as at baseline and follow-up, ISA and SB struts were associated with a lack of strut coverage at 6 months; and 4) intraluminal masses were rarely observed but were more frequently associated with ISA and uncovered struts.

Acute ISA. With metallic-DES, acute ISA ranged from 3.7% to 11.6% of the total amount of struts in patients without ST-segment elevation myocardial infarction

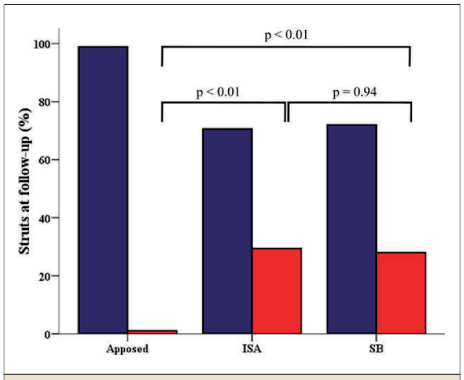

Figure 3. Strut Coverage at Follow-Up With Respect to Strut Apposition

Blue bars = covered; **red bars** = uncovered. ISA = incomplete scaffold/strut apposition; SB = side-branch strut.

(15,16). Patients with at least 1 malapposed strut ranged from 32% to 88% in the same clinical setting (17,18). Our study observed a rate of acute ISA of 3.5%; and 17 patients (68%) presented with at least 1 malapposed strut. These findings suggest that the BVS might have a similar rate of acute ISA, as compared with metallic-DES.

Figure 2 shows the distribution of the malapposed struts throughout the BVS length. According to this figure, malapposed struts were distributed with a particular pattern and were more frequently located at the 2 edges (especially at the proximal edge), with few malapposed struts being located in the central segments of the BVS. This is probably caused by the placement of the central segment of the BVS at the site of the minimal lumen area and by the use of post-dilation balloons (in 56% of patients), shorter than the length of the scaffold, applied at the central segment of the BVS. At baseline, 2 of 25 patients presented with scaffold pattern irregularities resulting in acute strut malapposition. Both patients were treated with post-dilation balloons immediately after the BVS implantation. In both cases, post-dilation balloons were inflated at pressures that resulted in predicted device diameters (according to the manufacturer's chart) larger than the recommended limits for the BVS implantation (3.3 mm for a 3.0-mm nominal diameter BVS). Scaffold pattern irregularities were located at the proximal edges and extended over 2 to 4 mm of the scaffold length. In these images, the number of ISAs were 2 and 5 struts, respectively. Additionally, no intraluminal mass was observed in these frames.

ISA at 6 months. Malapposed struts of different metallic-DES ranged from 0% to 15% of the total amount of struts at 6 months in non–ST-segment elevation myocardial infarction patients (19–21). In a single study comparing different metallic-DES, zotarolimus DES presented with lower rates of malapposed struts (0.0%), as compared with paclitaxel (0.7%) or sirolimus DES (1.9%) (19). All serial OCT imaging studies performed with metallic-DES have found a progressively decreasing amount of malapposed struts over time (21,22). Unfortunately, at the time of the present study, no OCT data were available for the everolimus DES at 6-month follow-up.

The healing process of the different metallic-DES is extremely heterogeneous, with little data being available with regard to the healing process of malapposed struts. Serial OCT imaging of sirolimus DES at baseline and 10-month follow-up showed a high rate of persistent malapposed struts, with 65% of ISA struts observed at baseline remaining malapposed at follow-up. Late acquired ISA was observed in 7.3% of malapposed struts at follow-up (3). Although there are many IVUS studies with serial strut analysis at baseline and at follow-up, the low sensitivity of IVUS to assess ISA—when compared with OCT—challenges the comparability of the results (23). Nevertheless, IVUS was able to identify some of the mechanisms involved in the appearance of LAISA with metallic-DES. Some patients experienced positive remodeling due to vessel and lumen enlargement without increasing the plaque area. In these cases, the vessel wall separated from the apposed strut causing LAISA. This mechanism was more frequently related to sirolimus DES (24,25) rather than paclitaxel DES (1,25), everolimus DES (26), or zotarolimus DES (27).

The first generation of the everolimus-eluting BVS (version 1.0) presented with more malapposed struts at 6 months than at baseline. A total of 78% of malapposed struts observed at baseline persisted at 6 months. Late acquired ISA was observed in 1.0% of the total amount of struts and represented 16% of the total amount of ISA at follow-up (8). The most plausible explanation for this phenomenon was the loss in scaffold area observed during the first 6 months, when the BVS version 1.0 had a premature loss of its radial force and structural continuity (10). This phenomenon caused the displacement of the scaffold into the lumen and probably delayed the healing of previously (baseline) malapposed struts. Likewise, this probably caused the appearance of new malapposed struts at follow-up that were apposed at baseline (LAISA). As assessed by IVUS (8), positive remodeling was not observed with the BVS (version 1.0), unlike what was previously reported in DES.

In our study, with the new generation of BVS (version 1.1), the percentage of malapposed struts at 6-month follow-up was inferior to that at baseline (0.8% vs. 3.5%, respectively; $p < 0.01$). Only 15% of the malapposed struts at baseline persisted at follow-up. Late acquired ISA was observed in 5 struts (1.0%) in 2 patients and represented 16% of malapposed struts at follow-up. The mechanism owing to LAISA in these 2 patients was the emergence of scaffold pattern irregularities not observed at baseline. Scaffold pattern irregularities were extended over 4 mm throughout the length of the BVS and were mainly located at the proximal edge. The IVUS analysis showed the absence of positive remodeling at the site of the external elastic membrane in those patients (data not shown). Figures 4 and 5 show matched OCT images from baseline to 6-month follow-up of the 2 patients with LAISA caused by the emergence of scaffold pattern irregularities. Although scaffold pattern irregularities were not observed in any of those patients at baseline, it is remarkable that the respective patients had been treated with post-dilation with balloons that over-stretched the BVS to larger diameters than the recommended maximum device diameter of 3.3 mm.

The matched images of the 7 struts with acute ISA due to acute scaffold pattern irregularities (at baseline) evolved to ISA + covered (3 struts) and to ISA + uncovered (4 struts) at 6 months. None of the cases were related to LAISA.

Strut coverage at 6-month follow-up. Strut coverage of different metallic-DES is extremely heterogeneous. At 6

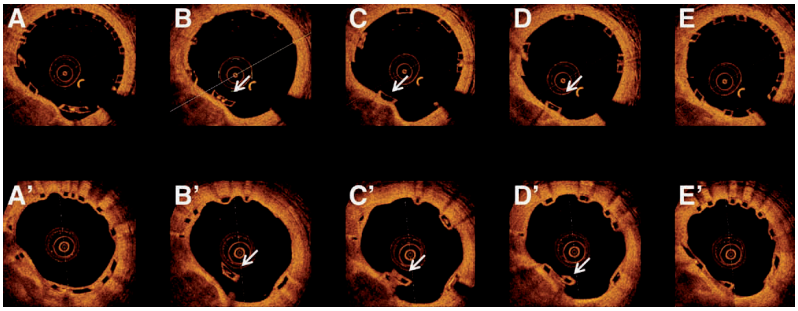

Figure 4. Late Acquired ISA

Consecutive, matched OCT images at baseline **(A to E)** and 6 months **(A′ to E′)** of 1 patient treated with excessive post-dilation (3.4 mm). At baseline, the scaffold pattern is regular. **B, C, and D** show 1 apposed strut at baseline **(arrows)** that at follow-up evolved to acquired malapposed strut **(arrows)** due to scaffold pattern irregularities. Abbreviations as in Figure 2.

months, sirolimus DES presented with a rate of uncovered struts from 8.7% to 15.0% (19–22). Uncovered struts with paclitaxel DES ranged from 2.7% to 5.0% (19,20), and zotarolimus DES presented with 0% of uncovered struts in a single report (19).

In our study, with the new generation of BVS (version 1.1), a total of 1.6% of struts were uncovered at 6-month follow-up. The distribution of uncovered struts throughout the BVS length did not show any particular pattern (Fig. 2). However, uncovered struts at follow-up were relatively more frequently found in struts that at baseline were ISA and SB struts rather than apposed struts. Similar results have been obtained with serial OCT imaging of sirolimus DES. Ozaki et al. (3) found a higher percentage of uncovered struts, at 10-month follow-up, in struts that were malapposed at baseline (65.4%) as compared with struts that were apposed (8.6%). The first generation of everolimus-eluting BVS (version 1.0) presented with 1.0% of uncovered struts at 6-month follow-up (8). Although the rate of ISA at 6 months was relatively high, uncovered struts were not commonly found. Moreover, the mean neointimal hyperplasia area was statistically higher with the BVS version 1.0 than with the BVS version 1.1 (10). There is no clear explanation for these findings. One hypothesis is that the advanced resorption state and the strut appearance changes observed with the BVS version 1.0 at 6 months as compared

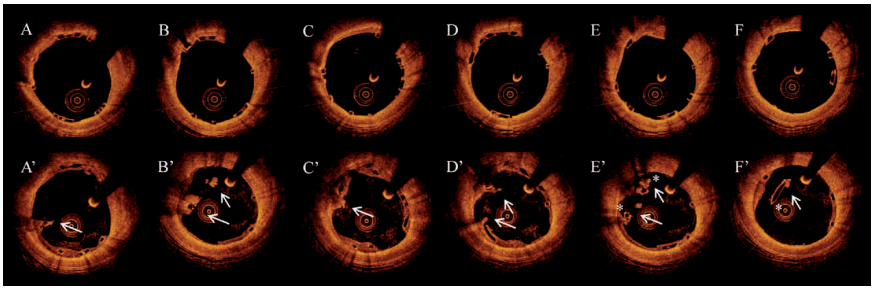

Figure 5. Late Acquired ISA With Attached IntraLuminal Masses

Consecutive, matched OCT images at baseline **(A to F)** and 6-month follow-up **(A′ to F′)**. At baseline, the scaffold was post-dilated up to 3.4 mm of predicted device diameter. The OCT images show all struts are apposed to the vessel wall without scaffold pattern irregularities. At 6 months, the scaffold presents with pattern irregularities resulting in strut malapposition and lack of tissue coverage **(*)**. Irregular intraluminal masses **(arrows)** with mild shadowing behind are attached to the malapposed and uncovered struts. Abbreviations as in Figure 2.

with the BVS 1.1 could trigger a higher neointimal response and strut coverage.

intraluminal masses at 6-month follow-up. Lack of neointimal coverage of different DES was proposed as the best predictor of late stent thrombosis in pathological studies (6). However, although sirolimus DES presented with a higher percentage of uncovered struts compared with paclitaxel DES, thrombi were more frequently found with paclitaxel DES (20). This observation supports the concept of a multicausal pathogenesis of late stent thrombosis, including malapposition, expansive vessel remodeling, and other factors that can initiate thrombus formation (28,29). Due to its high resolution, OCT is able to visualize, with great detail, many of the proposed predictors of late stent thrombosis in vivo (3,30). With sirolimus DES, Ozaki et al. (3) found 4.1% of frames with thrombi at 10-month follow-up; thrombi were more frequently observed in frames with ISA than in those without this feature (21% vs. 2%, respectively, $p < 0.01$). Our study found 14 cross-sections (2.9%) in 6 patients (24%) containing intraluminal masses at 6-month follow-up. Intraluminal masses were more frequently observed in cross-sections with ISA than without (39% vs. 2%; $p < 0.01$) and in cross-sections with uncovered struts than without (13% vs. 2%; $p < 0.01$), supporting that malapposition and absence of coverage can initiate thrombosis. However, whether this is of clinical importance needs to be further investigated. Figure 5 shows intraluminal masses attached to malapposed and uncovered struts in 1 patient with acquired scaffold pattern irregularities and LAISA at 6 months.

Clinical implications. In our study, the new generation of BVS presented with a lower rate of ISA, uncovered struts, and intraluminal masses as compared with sirolimus DES at 6-month follow-up. The polymeric nature of this new technology, however, could render it susceptible to iatrogenically induced scaffold pattern irregularities. These can lead to ISA and lack of strut coverage at 6-month follow-up. The 5 cases reported in our study were treated with aggressive post-dilations, probably resulting in overstretching of the scaffold at the time of the implantation. A third generation of the device is intended to raise the limit of deployment of the 3.0-mm nominal diameter device to 3.8 mm. Nevertheless, the previous generation of the BVS (version 1.0) showed a complete resorption of its components at 2-year follow-up without any malapposed or uncovered struts (7). Therefore, in this case, the treatment with dual antiplatelet therapy can become unnecessary. It is, however, currently uncertain whether the new generation of the BVS (version 1.1) will exhibit similar resorption characteristics at 2 years.

Study limitations. The first limitation of the present study is the limited number of patients. However, our report is 1 of the largest OCT studies with serial imaging of the same intracoronary device at baseline and at follow-up. The second limitation is the lack of statistical adjustment for clinical and anatomic covariables. The clustering essence of the OCT data (patient level, stent level, frame level, and strut level) needs a multilevel regression analysis not applied in our study. Moreover, the different OCT pullback speed, frame/rate, and quality of the image of the 2 OCT systems used in the present study hamper the matching of cross-sections between baseline and follow-up. A total of 12 cross-sections were unmatchable from baseline to follow-up or vice versa: 8 cross-sections were imaged with the M3 OCT system and 4 cross-sections were imaged with the C7 OCT system in both baseline and follow-up. Finally, the last limitation is the lack of results at very-long-term follow-up. The extrapolation of the 2-year follow-up results observed with the first generation of BVS (version 1.0) with the new generation of BVS (version 1.1) is purely speculative. However, all patients included in the ABSORB cohort B study will be reinvestigated at 2-year follow-up with invasive imaging techniques.

Conclusions

The new generation of BVS exhibited a low rate of acute, persistent, and late acquired incomplete strut/scaffold malapposition as well as uncovered struts. At baseline and follow-up, malapposed and SB struts were related to a lack of tissue coverage at 6 months. Scaffold pattern irregularities were the only cause observed in our study of late acquired malapposed struts and were also related to a lack of tissue coverage. Attached intraluminal masses occurred more frequently in malapposed and uncovered struts at 6 months. A more careful device implantation, with appropriate sizing of the vessel and respecting the deployment limits of inflation, will reduce the rates of acute ISA and scaffold pattern irregularities and, therefore, could circumvent most of the ISA, uncovered struts, and intraluminal masses observed at midterm follow-up.

Reprint requests and correspondence: Dr. Patrick W. Serruys, Thoraxcenter, Erasmus University Medical Center, 's-Gravendijkwal 230, Ba-583, 3015 CE Rotterdam, the Netherlands. E-mail: p.w.j.c.serruys@erasmusmc.nl.

REFERENCES

1. Tanabe K, Serruys PW, Degertekin M, et al. Incomplete stent apposition after implantation of paclitaxel-eluting stents or bare metal stents: insights from the randomized TAXUS II trial. Circulation 2005;111:900–5.
2. Degertekin M, Serruys PW, Tanabe K, et al. Long-term follow-up of incomplete stent apposition in patients who received sirolimus-eluting stent for de novo coronary lesions: an intravascular ultrasound analysis. Circulation 2003;108:2747–50.
3. Ozaki Y, Okumura M, Ismail TF, et al. The fate of incomplete stent apposition with drug-eluting stents: an optical coherence tomography-based natural history study. Eur Heart J 2010;31:1470–6.

4. Matsumoto D, Shite J, Shinke T, et al. Neointimal coverage of sirolimus-eluting stents at 6-month follow-up: evaluated by optical coherence tomography. Eur Heart J 2007;28:961–7.
5. Cook S, Wenaweser P, Togni M, et al. Incomplete stent apposition and very late stent thrombosis after drug-eluting stent implantation. Circulation 2007;115:2426–34.
6. Finn AV, Joner M, Nakazawa G, et al. Pathological correlates of late drug-eluting stent thrombosis: strut coverage as a marker of endothelialization. Circulation 2007;115:2435–41.
7. Serruys PW, Ormiston JA, Onuma Y, et al. A bioabsorbable everolimus-eluting coronary stent system (ABSORB): 2-year outcomes and results from multiple imaging methods. Lancet 2009;373:897–910.
8. Ormiston JA, Serruys PW, Regar E, et al. A bioabsorbable everolimus-eluting coronary stent system for patients with single de-novo coronary artery lesions (ABSORB): a prospective open-label trial. Lancet 2008; 371:899–907.
9. Okamura T, Garg S, Gutierrez-Chico JL, et al. In vivo evaluation of stent strut distribution patterns in the bioabsorbable everolimus-eluting device: an OCT ad hoc analysis of the revision 1.0 and revision 1.1 stent design in the ABSORB clinical trial EuroIntervention 2010;5: 932–8.
10. Gomez-Lara J, Brugaletta S, Diletti R, et al. A comparative assessment by optical coherence tomography of the performance of the first and second generation of the everolimus-eluting bioresorbable vascular scaffolds. Eur Heart J 2011;32:294–304.
11. Brugaletta S, Garcia-Garcia HM, Diletti R, et al. Comparison between the first and second generation bioresorbable vascular scaffolds: a six month virtual histology study. Euro Intervention 2010;6:1110–6.
12. Serruys PW, Onuma Y, Ormiston JA, et al. Evaluation of the second generation of a bioresorbable everolimus drug-eluting vascular scaffold for treatment of de novo coronary artery stenosis: six-month clinical and imaging outcomes. Circulation 2010;122:2301–12.
13. Cohen J. A coefficient of agreement for nominal scales. Educ Psychol Meas 1960;20:37–46.
14. Fleiss J. Statistical Methods for Rates and Proportions. 2nd edition. New York, NY: John Wiley, 1981.
15. Tanigawa J, Barlis P, Dimopoulos K, Dalby M, Moore P, Di Mario C. The influence of strut thickness and cell design on immediate apposition of drug-eluting stents assessed by optical coherence tomography. Int J Cardiol 2009;134:180–8.
16. Kim JS, Jang IK, Fan C, et al. Evaluation in 3 months duration of neointimal coverage after zotarolimus-eluting stent implantation by optical coherence tomography: the ENDEAVOR OCT trial. J Am Coll Cardiol Intv 2009;2:1240–7.
17. Kubo T, Imanishi T, Kitabata H, et al. Comparison of vascular response after sirolimus-eluting stent implantation between patients with unstable and stable angina pectoris: a serial optical coherence tomography study. J Am Coll Cardiol Img 2008;1:475–84.
18. Tanigawa J, Barlis P, Dimopoulos K, Di Mario C. Optical coherence tomography to assess malapposition in overlapping drug-eluting stents. EuroIntervention 2008;3:580–3.
19. Guagliumi G, Musumeci G, Sirbu V, et al. Optical coherence tomography assessment of in vivo vascular response after implantation of overlapping bare-metal and drug-eluting stents. J Am Coll Cardiol Intv 2010;3:531–9.
20. Murakami D, Takano M, Yamamoto M, et al. Advanced neointimal growth is not associated with a low risk of in-stent thrombus. Optical coherence tomographic findings after first-generation drug-eluting stent implantation. Circ J 2009;73:1627–34.
21. Katoh H, Shite J, Shinke T, et al. Delayed neointimalization on sirolimus-eluting stents: 6-month and 12-month follow up by optical coherence tomography. Circ J 2009;73:1033–7.
22. Ishigami K, Uemura S, Morikawa Y, et al. Long-term follow-up of neointimal coverage of sirolimus-eluting stents: evaluation with optical coherence tomography. Circ J 2009;73:2300–7.
23. Bouma BE, Tearney GJ, Yabushita H, et al. Evaluation of intracoronary stenting by intravascular optical coherence tomography. Heart 2003;89:317–20.
24. Ako J, Morino Y, Honda Y, et al. Late incomplete stent apposition after sirolimus-eluting stent implantation: a serial intravascular ultrasound analysis. J Am Coll Cardiol 2005;46:1002–5.
25. Hong MK, Mintz GS, Lee CW, et al. Late stent malapposition after drug-eluting stent implantation: an intravascular ultrasound analysis with long-term follow-up. Circulation 2006;113:414–9.
26. Tsuchiya Y, Lansky AJ, Costa RA, et al. Effect of everolimus-eluting stents in different vessel sizes (from the pooled FUTURE I and II trials). Am J Cardiol 2006;98:464–9.
27. Miyazawa A, Ako J, Hongo Y, et al. Comparison of vascular response to zotarolimus-eluting stent versus sirolimus-eluting stent: intravascular ultrasound results from ENDEAVOR. Am Heart J 2008;III:155: 108–13.
28. Oikawa Y, Yajima J, Costa M, et al. Intravascular ultrasound, angioscopic and histopathological characterization of heterogeneous patterns of restenosis after sirolimus-eluting stent implantation: insights into potential "thromborestenosis" phenomenon. EuroIntervention 2010;6: 380–7.
29. Joner M, Finn AV, Farb A, et al. Pathology of drug-eluting stents in humans: delayed healing and late thrombotic risk. J Am Coll Cardiol 2006;48:193–202.
30. Otake H, Shite J, Ako J, et al. Local determinants of thrombus formation following sirolimus-eluting stent implantation assessed by optical coherence tomography. J Am Coll Cardiol Intv 2009;2:459–66.

Key Words: bioresorbable scaffolds ■ incomplete stent ■ late acquired incomplete stent ■ optical coherence tomography ■ strut apposition ■ uncovered struts.

CHAPTER 5 THE APPLICATION OF OPTICAL COHERENCE TOMOGRAPHY IN THE CLINICAL EVALUATION OF BIORESORBABLE SCAFFOLDS

5.3 Circumferential evaluation of the neointima by optical coherence tomography after ABSORB bioresorbable vascular scaffold implantation: can the scaffold cap the plaque?

Brugaletta S, **Radu MD**, Garcia-Garcia HM, Heo JH, Farooq V, Girasis C, van Geuns RJ, Thuesen L, McClean D, Chevalier B, Windecker S, Koolen J, Rapoza R, Miquel-Hebert K, Ormiston J, Serruys PW.

Atherosclerosis. 2012;221:106-12.

Circumferential evaluation of the neointima by optical coherence tomography after ABSORB bioresorbable vascular scaffold implantation: Can the scaffold cap the plaque?

Salvatore Brugaletta[a,b], Maria D. Radu[a], Hector M. Garcia-Garcia[a,b,c], Jung Ho Heo[a], Vasim Farooq[a], Chrysafios Girasis[a], Robert-Jan van Geuns[a], Leif Thuesen[d], Dougal McClean[e], Bernard Chevalier[f], Stephan Windecker[g], Jacques Koolen[h], Richard Rapoza[i], Karine Miquel-Hebert[j], John Ormiston[k], Patrick W. Serruys[a,*]

[a] *Thoraxcenter, Erasmus MC, Rotterdam, The Netherlands*
[b] *Department of Cardiology, Thorax Institute, Hospital Clinic, University of Barcelona, Barcelona, Spain*
[c] *Cardialysis B.V., Rotterdam, The Netherlands*
[d] *Skejby Sygehus, Aarhus University Hospital, Aarhus, Denmark*
[e] *Christchurch Hospital, Christchurch, New Zealand*
[f] *Institut Cardiovasculaire Paris Sud, Massy, France*
[g] *Bern University Hospital, Bern, Switzerland*
[h] *Catharina Hospital, Eindhoven, The Netherlands*
[i] *Abbott Vascular, Santa Clara, CA, USA*
[j] *Abbott Vascular, Diegem, Belgium*
[k] *Auckland City Hospital, Auckland, New Zealand*

ARTICLE INFO

Article history:
Received 12 October 2011
Received in revised form 3 December 2011
Accepted 5 December 2011
Available online 13 December 2011

Keywords:
OCT
Neointima
Bioresorbable vascular scaffold

ABSTRACT

Objective: To quantify the circumferential healing process at 6 and 12 months following scaffold implantation.
Background: The healing process following stent implantation consists of tissue growing on the top of and in the space between each strut. With the ABSORB bioresorbable vascular scaffold (BVS), the outer circumference of the scaffold is detectable by optical coherence tomography (OCT), allowing a more accurate and complete evaluation of the intra-scaffold neointima.
Methods: A total of 58 patients (59 lesions), who received an ABSORB BVS 1.1 implantation and a subsequent OCT investigation at 6 ($n = 28$ patients/lesions) or 12 ($n = 30$ patients with 31 lesions) months follow-up were included in the analysis. The thickness of the neointima was calculated circumferentially in the area between the abluminal side of the scaffold and the lumen by means of an automated detection algorithm. The symmetry of the neointima thickness in each cross section was evaluated as the ratio between minimum and maximum thickness.
Results: The neointima area was not different between 6 and 12 months follow-up ($1.57 \pm 0.42\ mm^2$ vs. $1.64 \pm 0.77\ mm^2$; $p = 0.691$). No difference was also found in the mean thickness of the neointima (median [IQR]) between the two follow-up time points (210 μm [180–260]) vs. 220 μm [150–260]; $p = 0.904$). However, the symmetry of the neointima thickness was higher at 12 than at 6 months follow-up (0.23 [0.13–0.28] vs. 0.16 [0.08–0.21], $p = 0.019$).
Conclusions: A circumferential evaluation of the healing process following ABSORB implantation is feasible, showing the formation of a neointima layer, that resembles a thick fibrous cap, known for its contribution to plaque stability.

1. Introduction

The aim of percutaneous treatment of a coronary lesion with an intracoronary scaffolding device is to acutely restore the geometry of the coronary lumen, alleviating its flow-limiting character. Thereafter, the reaction of the vessel wall to the implanted stent initiates a healing process resulting in the growth of intra-scaffold

* Corresponding author at: Interventional Cardiology Department Erasmus MC, Thoraxcenter, 's Gravendijkwal 230,3015 CE Rotterdam, The Netherlands.
Tel.: +31 10 4635260; fax: +31 10 4369154.
E-mail address: p.w.j.c.serruys@erasmusmc.nl (P.W. Serruys).

0021-9150/$ – see front matter © 2011 Elsevier Ireland Ltd. All rights reserved.
doi:10.1016/j.atherosclerosis.2011.12.008

neointima [1,2]. Growth of this neo-tissue on top of a vulnerable thin-cap fibroatheroma may generate a new "fibrous cap" which may potentially increase the thickness of the cap [3–5]. This biological process may be of particular interest in cases where scaffolds have been implanted on top of a necrotic core, abutting the lumen.

Nevertheless, autopsy studies have suggested that metallic struts embedded in necrotic core may remain uncovered even at long-term, and thus be potentially a trigger for stent thrombosis [4].

The bioresorbable vascular scaffolds, which in the long-term are completely replaced by connective tissue and smooth muscle cells – overcoming the problem of metal persistence into the coronary vessel wall – can ensure the formation of a neointima layer [6,7]. In addition as the polymeric struts are translucent and do not create an optical shadow, an optical coherence tomography (OCT) evaluation of the neointima growth can be performed in a more refined way in the scaffold than in the metallic stents [8].

The aim of this analysis was to assess and to quantify the circumferential distribution of the intra-scaffold neo-intima tissue during the first year after ABSORB implantation.

2. Methods

2.1. Study population

The ABSORB Cohort B trial (NCT00856856) is a multicentre single-arm trial assessing the safety and performance of the ABSORB BVS (Abbott Vascular, Santa Clara, USA). The details of this trial have been previously reported [8,9].

In total, 101 patients were enrolled in the ABSORB Cohort B trial, subdivided in two subgroups of patients: the first group of 45 patients (Cohort B1) randomized to invasive imaging at 6 and 24 months; the second group of the remaining 56 patients (Cohort B2) randomized to the same invasive imaging at 12 and 36 months. OCT was realized as an optional investigation in some of these patients without any inclusion/exclusion criteria.

The present study is a post hoc analysis of the patients receiving an OCT investigation at the various follow-up time points.

2.2. ABSORB BVS

The ABSORB BVS is a fully bioresorbable intra-coronary device made of semi-crystalline poly (L-lactide) (PLLA) coated with an amorphous poly (D,L-lactide) (PDLLA) copolymer that contains and controls the release of the anti-proliferative drug everolimus. At the time of implantation, the total strut thickness is 156 μm. The primary mechanism for molecular weight degradation of both polylactide (PLA) materials is hydrolysis, a process in which the ester bonds between repeating lactide molecules are progressively cleaved by water. Ultimately, PLLA and PDLLA degrade into lactic acid, which is readily converted to lactate and processed via both the Kreb's cycle (for L-lactate) and methylglycoxal metabolism (for D-lactate) [7,10,11]. Based on preclinical studies, the time for complete bioresorption is assumed to be approximately 2 years [6].

2.3. OCT acquisition and analysis

OCT imaging was performed as an optional investigation at selected centers, using either time domain [M3 system, Light Lab Imaging (LLI), Westford, MA, USA] or frequency domain OCT systems (C7XR system, LLI) at baseline and follow-up [12–17]. The OCT measurements were performed with proprietary software for offline analysis (Light Lab Imaging, Westford, MA, USA). Adjusting for the pullback speed, the cross-sectional analysis was performed at 1 mm longitudinal intervals within the treated segment.

When imaged with OCT, the ABSORB BVS presents important differences compared to the metallic stents. The optically translucent polymeric struts appear as black boxes (strut core area) framed by light-scattering borders that do not produce dorsal shadows, thus allowing for a complete imaging of the strut thickness [8]. As the strut is entirely visible throughout its entire thickness, the main quantitative measurements (strut core area, strut area, lumen area, scaffold area, incomplete scaffold apposition area and neointima area) required different analysis rules than with the metallic stents, as previously described [8,9]. In particular, the neointima area has been previously calculated as [scaffold area – lumen area – strut core area] and the thickness of the coverage has been measured for every strut between the abluminal side of the strut core and the lumen [8,9].

At variance with this previous analysis, the strut core area is now included in the neointima area assessment, in order to perform a circumferential measurement of the neointima thickness by means of an automated contour detection algorithm available in the Light Lab proprietary software. The size and the thickness of the neo-intima area, delimitated by the scaffold (as outer reference, drawn at the abluminal side of the struts) and the lumen contours (as inner reference), were measured in each frame (Fig. 1). Frames containing malapposed struts were excluded from the analysis, as the area included between the scaffold and the lumen does not contain in these cases any neointimal tissue, but represents incomplete scaffold apposition (ISA) area. The neointima area was estimated as scaffold area – lumen area. The neointima area was normalized per scaffold size as "in-scaffold area obstruction" and estimated as: [neointima area/scaffold area] × 100. The symmetry of the neointima thickness in each cross-section was evaluated as a ratio between the minimum and the maximum thickness of neointima in that cross-section [18,19].

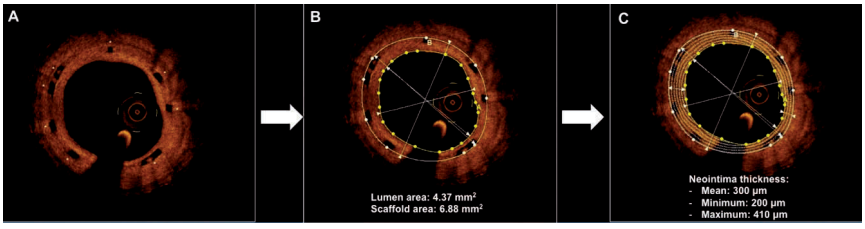

Fig. 1. Circumferential assessment of neointima for ABSORB BVS. Panel A shows the circumferential distribution of the polymeric struts (*) in a cross-section. After drawing the lumen and scaffold contours (Panel B), the neointima thickness is calculated (Panel C). The minimum and maximum diameters of lumen and scaffold areas are also drawn.

2.4. Statistical analysis

Continuous variables are expressed as mean ± standard deviation (SD) or median and interquartile range, depending on their distribution. The distribution normality of the variables was tested using the Kolgomorov–Smirnov test. Dichotomous variables are reported as numbers and percentages. Comparison between groups was done by means of the non-parametric Mann–Whitney test. Adjustment for clustering data at cross section level was performed using a generalized estimating equations approach [20]. A two-tailed p-value < 0.05 was considered statistically significant. Statistical analyses were performed with SPSS statistical package, version 17.0 (SPSS Inc., Chicago IL, USA).

3. Results

3.1. Patient population

A total of 58 patients (59 lesions) received an OCT investigation at 6 (n = 28 patients/lesions) or 12 (n = 30 patients with 31 lesions) months follow-up after ABSORB BVS implantation, and all were included in the present analysis. (see Supplementary material for baseline clinical characteristics).

3.2. OCT analysis of neointimal area at 6 and 12 months follow-up

A total of 1083 cross sections were analyzed (531 and 552 at 6 and 12 months, respectively). Forty-nine cross sections were excluded from the analysis due to the presence of ISA (23 and 26 at 6 and 12 months follow-up, respectively).

At a cross-section level, lumen and scaffold areas tended to be smaller, while the minimum neointima thickness tended to be larger at 12 as compared to 6 months. However, the mean neointima area was not different between the two time points (Table 1). Fig. 2A shows the bimodal distribution histogram of the mean neointima thicknesses, pooling the 6 and the 12 months follow-up data. There was a significant relationship between the mean neointima thickness measured at the minimum lumen area frame and the angiographic late loss (r = 0.624, p = 0.003) (Fig. 2B).

At a lesion level, lumen and scaffold area also tended to be smaller at 12 months follow-up and the minimum neointima thickness tended to be larger at 12 than at 6 months follow-up (Table 1).

The symmetry of the neointima thickness (more homogeneous distribution of neointima) was significantly higher at 12 than at 6 months follow-up both at cross-section and at lesion level (Fig. 3).

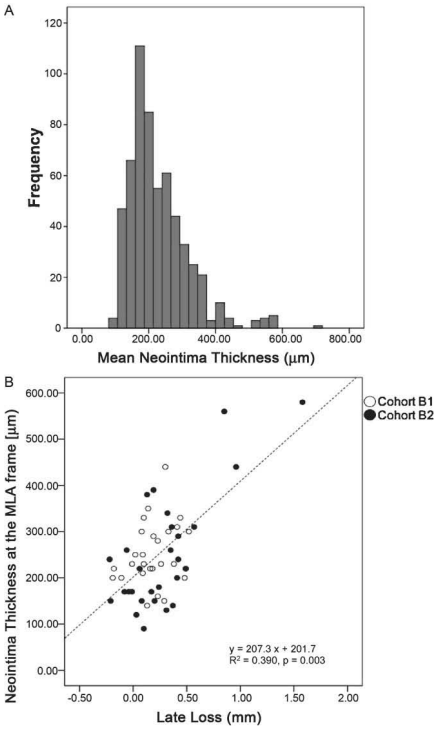

Fig. 2. Neointima thickness: histogram distribution and correlation with angiographic late loss. Panel A: Histogram distribution of the neointima thickness at cross-sectional level (1034 cross-section). The ABSORB BVS scaffold has a median (interquartile range) of 210 μm (160–270 μm) with a bimodal distribution. Panel B: the mean neointima thickness at the site of minimum lumen area (MLA) is significantly correlated with the angiographic late loss.

4. Discussion

The main findings of the present analysis are: (1) the methodology for measuring the neointima thickness circumferentially by OCT is feasible with translucent bioresorbable scaffolds and allows for the measurement of the neointima on top and between the struts; (2) the neointima at 6 and 12 months does not differ in terms of thickness but appears to be more symmetric at 12 than at 6 months.

It is known that in the pathogenesis of acute coronary syndromes a major role is played by coronary plaque rupture and erosion with subsequent local thrombosis [21]. In particular, pathological studies have documented that these plaques are mostly represented by thin-cap fibroatheromas (TCFA), which are lipid core plaques covered by a thin fibrous cap (<65 μm) [22,23]. The PROSPECT study has further demonstrated that IVUS-VH derived TCFA are independent predictors of coronary events in patients after an acute coronary syndrome at a median follow-up of 3.4 years [24]. Nevertheless, it has not been yet demonstrated which of these plaques are going to be the cause of events. Of note is that the majority of the events in the PROSPECT study were progressive angina, caused probably by plaque growth and not acute coronary syndromes that could be attributed to the rupture of a vulnerable plaque. In addition to this, TCFA were identified in the PROSPECT study by IVUS-VH, which has a limited resolution to measure the thickness of the cap. For these reasons, more natural history studies with more precise techniques for the detection of TCFAs are needed before the interventional treatment of these lesions can be recommended.

Pharmacological and mechanical treatments aimed to stabilize TCFA are, however, a current topic of research. Takarada et al. [25] showed that pharmacological treatment, such as statins, enables to significantly increase the fibrous-cap thickness of coronary plaques. The pilot SECRITT trial attempted to address for the first time the question whether a mechanical preventive treatment of such kind of plaques by means of self-expandable metallic stent ("Shield") may be feasible and safe [3]. The percutaneous treatment of a TCFA by a metallic stent, especially bare-metal, triggers

Table 1
Neointima thickness analysis by OCT.

Cross section level			
	6 month (508 cross sections)	12 months (526 cross sections)	*p*-value
Mean lumen area (mm^2)	6.26 ± 1.72	5.63 ± 1.48	0.071
Mean scaffold area (mm^2)	7.86 ± 1.63	7.31 ± 1.38	0.095
Mean neointima thickness (μm)	230 [190–280]	190 [150–270]	0.410
Minimum neointima thickness (μm)	40 [10–105]	60 [30–120]	0.096
Maximum neointima thickness (μm)	330 [280–410]	310 [240–410]	0.648
Neointima area (mm^2)	1.60 ± 0.62	1.68 ± 0.77	0.517
In-scaffold area obstruction (%)	21.37 ± 9.44	23.46 ± 11.24	0.284
Symmetry of neointima thickness	0.10 [0.03–0.24]	0.20 [0.09–0.30]	0.005
Patient level			
	6 months (n = 28)	12 months (n = 31)	*p*-value
Mean lumen area (mm^2)	6.42 ± 1.40	5.64 ± 1.41	0.050
Mean scaffold area (mm^2)	7.98 ± 1.52	7.28 ± 1.08	0.031
Mean neointima thickness (μm)	210 [180–260]	220 [150–260]	0.904
Minimum neointima thickness (μm)	50 [30–80]	80 [40–120]	0.071
Maximum neointima thickness (μm)	335 [300–410]	340 [280–420]	0.912
Neointima area (mm^2)	1.57 ± 0.42	1.64 ± 0.77	0.691
In-scaffold area obstruction (%)	20.66 ± 7.47	23.38 ± 11.73	0.322
Symmetry of neointima thickness	0.16 [0.08–0.21]	0.23 [0.13–0.28]	0.019

Data are reported as median and interquartile range or mean ± standard deviation, according to their distribution.

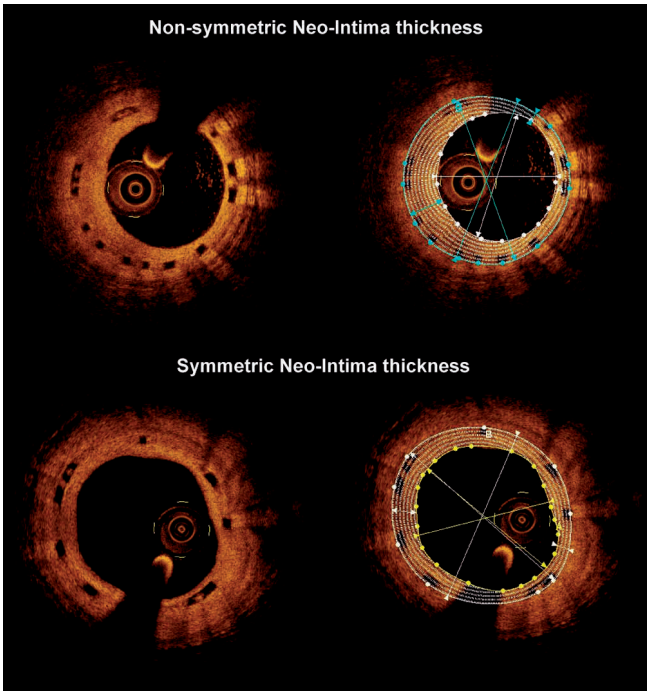

Fig. 3. Symmetry of the neointima. Examples of non-symmetric (6 months follow-up) and symmetric (12 months follow-up) neointima thickness. The minimum and maximum diameter of the lumen and scaffold contours are drawn.

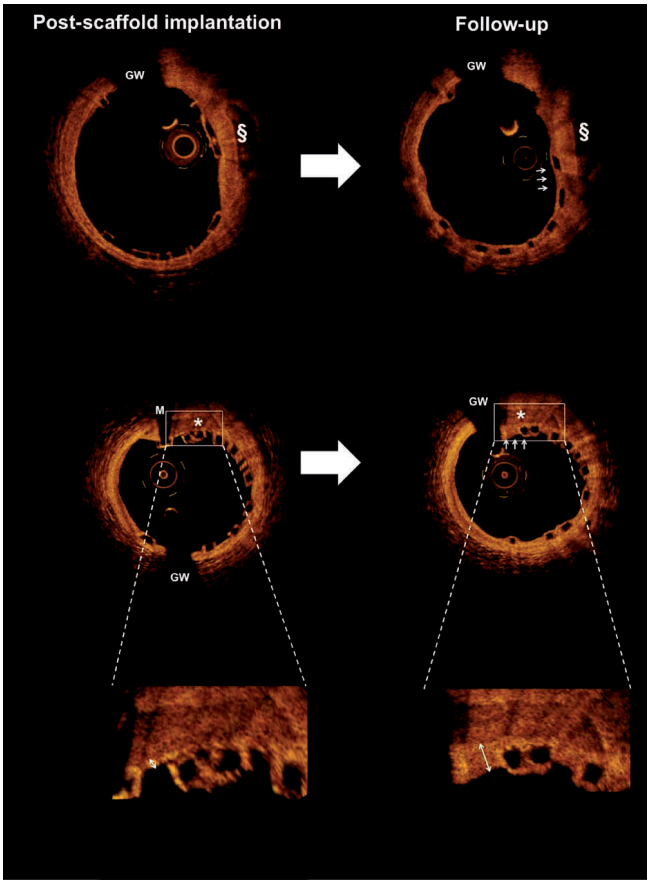

Fig. 4. Neointima layer covering coronary plaques. Examples of the formation of a neointima layer over two coronary plaques (indicated as § and *), scaffolded by an ABSORB BVS device. At follow-up a neo-tissue is visible not only on the top of the polymeric struts, but also in the space between two adjacent struts (white arrows), thickening the cap of the plaque originally treated (see the enlargement on the bottom). GW = shadow of the guidewire. M = shadow of the radio-opaque marker, present at the scaffold edge (note: the shadow of the marker at follow-up is hidden by the guidewire shadow).

the formation of a fibrotic layer (more or less thick) on the top of the thin cap covering the lipid pool, potentially reducing therefore the probability of plaque rupture/erosion. However, the persistence of metal and/or non-degradable polymers into the vessel wall can have some detrimental effects (e.g., permanent presence of foreign body, etc.) [26]. With regards to ABSORB bioresorbable vascular scaffold, it has been established that at approximately 2 years the polymeric material has been fully degraded and replaced by proteoglycans. At 4 years, the initial location of the struts in the vessel wall is no longer identifiable by histology or OCT and the neointimal layer built up on the scaffolding structure becomes thereby a "*de novo*" cap, which cannot be distinguished from a fibrotic cap, normally seen in fibroatheroma [6,10,27] (Fig. 4). The formation of a symmetric neo-tissue with a mean thickness of 220 μm without remnants of polymeric struts, when the device is completely bioresorbed, may therefore favor the use of a bioresorbable device for the treatment of thin-cap fibroatheromas [10]. Based on the findings of our previous pre-clinical studies, we have established that the main component of the neointima following ABSORB BVS implantation is fibrous tissue, whereas fibrin and granulomatous cells are scarce at long-term follow-up [6].

Of note is that in our analysis the thickness of the neointima was on average not different between 6 and 12 months follow-up. Only the minimum neointima thickness exhibited some tendency to be larger at 12 than at 6 months follow-up. This observation suggests that the healing process following an ABSORB BVS implantation is

almost completed 6 months after the device implantation, without further increase of neointima overtime. Conversely, the symmetry of the neointima, although far away from the value of 1, which potentially represents a highly symmetric neointima, significantly increases from 6 to 12 months follow-up, reflecting a more circumferentially homogenous distribution of tissue capping the original plaque. A symmetric distribution of neointima thickness ensures more likely the presence of a "thick cap" on the top of the plaque originally treated, regardless of its circumferential location in the vessel wall.

It is noteworthy that the comparison between 6 and 12 months represents an unpaired comparison so that the tendency toward a reduction in lumen and scaffold areas should be carefully interpreted. In the paired comparison, previously reported, there was not reduction in scaffold area by OCT at 6 and 12 months [8,9]. The histogram distribution of the neointima thickness seems to have a bimodal distribution, which is consistent with the DES late loss distribution, previously observed [28]. Of note is that the angiographic late loss appeared to be significantly correlated with the thickness of the neointima at the site of MLA [29,30]. The difference in resolution between the two imaging techniques and other factors, such as remodeling of the vessel, should be taken into account for explaining this relationship. It is also known that the level of neointima proliferation may affect the correlation between late loss by QCA and neointima thickness by OCT that is high in presence of a high late loss [30]. The small number of patients did not allow us this kind of sub-analysis and will require further studies.

5. Limitations

Our analysis may have some limitations. The first is that the assessment of the intra-scaffold neointima area incorporates the area of the strut core in the quantification of the neointima area, at variance with the method previously described [8,9]. However, from animal studies, it may be argued that that each polymeric strut is ultimately replaced by proteoglycan and connective tissue: for this reason, the inclusion of the strut core area into the neointima area more correctly reflects the thickness of the tissue covering the plaque originally treated [6] (See Fig. 1 in Supplementary material).

Another important consideration is about the small sample size at the two time points. Nevertheless, these patients represent the unique cohort of patients received an ABSORB implantation and an OCT analysis.

The presence of ISA is another limitation of our methodology, as the automatic detection software algorithm of the software recognizes this area as neointima. However, the segments with ISA can be excluded and analyzed using conventional methodology.

6. Conclusions

An accurate and circumferential quantification of the healing process following implantation of bioresorbable scaffolds is allowed. The formation of a thick neointimal layer, without remnants of polymeric struts, creates a "*de novo*" cap, which may be used to seal a thin-cap fibroatheroma.

Acknowledgment

The ABSORB trial is sponsored and funded by Abbott Vascular, Santa Clara, California, USA.

Appendix A. Supplementary data

Supplementary data associated with this article can be found, in the online version, at doi:10.1016/j.atherosclerosis.2011.12.008.

References

[1] Garg S, Serruys PW. Coronary stents: looking forward. J Am Coll Cardiol 2010;56:S43–78.
[2] Garg S, Serruys PW. Coronary stents: current status. J Am Coll Cardiol 2010;56:S1–42.
[3] Ramcharitar S, Gonzalo N, van Geuns RJ, Garcia-Garcia HM, Wykrzykowska JJ, Ligthart JM, et al. First case of stenting of a vulnerable plaque in the secritt i trial-the dawn of a new era? Nat Rev Cardiol 2009;6:374–8.
[4] Joner M, Finn AV, Farb A, Mont EK, Kolodgie FD, Ladich E, et al. Pathology of drug-eluting stents in humans: delayed healing and late thrombotic risk. J Am Coll Cardiol 2006;48:193–202.
[5] Finn AV, Joner M, Nakazawa G, Kolodgie F, Newell J, John MC, et al. Pathological correlates of late drug-eluting stent thrombosis: strut coverage as a marker of endothelialization. Circulation 2007;115:2435–41.
[6] Onuma Y, Serruys PW, Perkins LE, Okamura T, Gonzalo N, Garcia-Garcia HM, et al. Intracoronary optical coherence tomography and histology at 1 month and 2, 3, and 4 years after implantation of everolimus-eluting bioresorbable vascular scaffolds in a porcine coronary artery model: an attempt to decipher the human optical coherence tomography images in the absorb trial. Circulation 2010;122:2288–300.
[7] Serruys PW, Ormiston JA, Onuma Y, Regar E, Gonzalo N, Garcia-Garcia HM, et al. A bioabsorbable everolimus-eluting coronary stent system (absorb): 2-year outcomes and results from multiple imaging methods. Lancet 2009;373:897–910.
[8] Serruys PW, Onuma Y, Ormiston JA, de Bruyne B, Regar E, Dudek D, et al. Evaluation of the second generation of a bioresorbable everolimus drug-eluting vascular scaffold for treatment of de novo coronary artery stenosis: six-month clinical and imaging outcomes. Circulation 2010;122:2301–12.
[9] Serruys PW, Onuma Y, Dudek D, Smits PC, Koolen J, Chevalier B, et al. Evaluation of the second generation of a bioresorbable everolimus-eluting vascular scaffold for the treatment of de novo coronary artery stenosis 12-month clinical and imaging outcomes. J Am Coll Cardiol 2011;58:1578–88.
[10] Ormiston JA, Serruys PW, Regar E, Dudek D, Thuesen L, Webster MW, et al. A bioabsorbable everolimus-eluting coronary stent system for patients with single de-novo coronary artery lesions (absorb): a prospective open-label trial. Lancet 2008;371:899–907.
[11] Ewaschuk JB, Naylor JM, Zello GA. D-lactate in human and ruminant metabolism. J Nutr 2005;135:1619–25.
[12] Sihan K, Botha C, Post F, de Winter S, Gonzalo N, Regar E, et al. Fully automatic three-dimensional quantitative analysis of intracoronary optical coherence tomography: method and validation. Catheter Cardiovasc Interv 2009;74:1058–65.
[13] Prati F, Regar E, Mintz GS, Arbustini E, Di Mario C, Jang IK, et al. Expert review document on methodology, terminology, and clinical applications of optical coherence tomography: physical principles, methodology of image acquisition, and clinical application for assessment of coronary arteries and atherosclerosis. Eur Heart J 2010;31:401–15.
[14] Gonzalo N, Serruys PW, Okamura T, Shen ZJ, Onuma Y, Garcia-Garcia HM, et al. Optical coherence tomography assessment of the acute effects of stent implantation on the vessel wall: a systematic quantitative approach. Heart 2009;95:1913–9.
[15] Okamura T, Garg S, Gutierrez-Chico JL, Shin ES, Onuma Y, Garcia HM, et al. In vivo evaluation of stent strut distribution patterns in the bioabsorbable everolimus-eluting device: an oct ad hoc analysis of the revision 1.0 and revision 1.1 stent design in the absorb clinical trial. EuroIntervention 2010:932–8.
[16] Regar E, Leeuwen AMGJv, Serruys PW. Optical coherence tomography in cardiovascular research. Informa Healthcare 2007.
[17] Gonzalo N, Serruys PW, Garcia-Garcia HM, van Soest G, Okamura T, Ligthart J, et al. Quantitative ex vivo and in vivo comparison of lumen dimensions measured by optical coherence tomography and intravascular ultrasound in human coronary arteries. Rev Esp Cardiol 2009;62:615–24.
[18] Brugaletta S, Gomez-Lara J, Diletti R, Farooq V, Jan van Geuns R, de Bruyne B, et al. Comparison of in vivo eccentricity and symmetry indices between metallic stents and bioresorbable vascular scaffolds: Insights from the absorb and spirit trials. Catheter Cardiovasc Interv 2011. Epub ahead of print.
[19] de Jaegere P, Mudra H, Figulla H, Almagor Y, Doucet S, Penn I, et al. Intravascular ultrasound-guided optimized stent deployment. Immediate and 6 months clinical and angiographic results from the multicenter ultrasound stenting in coronaries study (music study). Eur Heart J 1998;19:1214–23.
[20] Guagliumi G, Costa MA, Sirbu V, Musumeci G, Bezerra HG, Suzuki N, et al. Strut coverage and late malapposition with paclitaxel-eluting stents compared with bare metal stents in acute myocardial infarction: optical coherence tomography substudy of the harmonizing outcomes with revascularization and stents in acute myocardial infarction (horizons-ami) trial. Circulation 2011;123:274–81.
[21] Shah PK. Mechanisms of plaque vulnerability and rupture. J Am Coll Cardiol 2003;41:15S–22S.
[22] Virmani R, Burke AP, Farb A, Kolodgie FD. Pathology of the vulnerable plaque. J Am Coll Cardiol 2006;47:C13–8.
[23] Burke AP, Farb A, Malcom GT, Liang YH, Smialek J, Virmani R. Coronary risk factors and plaque morphology in men with coronary disease who died suddenly. N Engl J Med 1997;336:1276–82.
[24] Stone GW, Maehara A, Lansky AJ, de Bruyne B, Cristea E, Mintz GS, et al. A prospective natural-history study of coronary atherosclerosis. N Engl J Med 2011;364:226–35.

[25] Takarada S, Imanishi T, Kubo T, Tanimoto T, Kitabata H, Nakamura N, et al. Effect of statin therapy on coronary fibrous-cap thickness in patients with acute coronary syndrome: assessment by optical coherence tomography study. Atherosclerosis 2009;202:491–7.
[26] Holmes Jr DR, Kereiakes DJ, Garg S, Serruys PW, Dehmer GJ, Ellis SG, et al. Stent thrombosis. J Am Coll Cardiol 2010;56:1357–65.
[27] Khattab A, Windecker S. Vascular restoration therapy: what should the clinical and angiographic measures for success be? EuroIntervention 2009;5(Supplement F):F49–57.
[28] Farooq V, Gogas BD, Serruys PW. Restenosis: delineating the numerous causes of drug-eluting stent restenosis. Circ Cardiovasc Interv 2011;4:195–205.
[29] Kim BK, Kim JS, Ko YG, Choi D, Jang Y, Hong MK. Correlation of angiographic late loss with neointimal coverage of drug-eluting stent struts on follow-up optical coherence tomography. Int J Cardiovasc Imaging 2011.
[30] Kim JS, Wallace-Bradley D, Alviar CL, Conditt G, Milewski K, Afari ME, et al. Correlation of angiographic late loss with neointimal proliferation in stents evaluated by oct and histology in porcine coronary arteries. JACC Cardiovasc Imaging 2011;4:1002–10.

CHAPTER 6 METHODOLOGICAL CONSIDERATIONS IN THE USE OF OPTICAL COHERENCE TOMOGRAPHY TO EVALUATE ATHEROSCLEROSIS

6.1 Atherosclerosis visualised with optical coherence tomography.

Räber L*, **Radu MD***, Garcia-Garcia HM, Akasaka T, Banz Y, Kume T, Windecker S, Serruys PW.

The Clinical Atlas of OCT. PCR Publishing. May 2012.

Please see separate electronic application, chapter 3

CHAPTER 6 METHODOLOGICAL CONSIDERATIONS IN THE USE OF OPTICAL COHERENCE TOMOGRAPHY TO EVALUATE ATHEROSCLEROSIS

6.2 In search of vulnerable features of coronary plaques with optical coherence tomography: is it time to rethink the current methodological concepts?

Radu MD, Falk E.

European Heart Journal. 2012;33:9-12.

In search of vulnerable features of coronary plaques with optical coherence tomography: is it time to rethink the current methodological concepts?

Maria D. Radu[1]* and Erling Falk[2]

[1]Rigshospitalet, Copenhagen University Hospital, DK-2100 Copenhagen, Denmark; and [2]Aarhus University Hospital Skejby, Aarhus, Denmark

This editorial refers to 'Thin-cap fibroatheroma and microchannel findings in optical coherence tomography correlate with subsequent progression of coronary atheromatous plaques', by S. Uemura *et al.*, doi:10.1093/eurheartj/ehr284

Intravascular optical coherence tomography (OCT) is increasingly being used to assess coronary vessel pathology *in vivo* due to its unrivalled high resolution of 10–20 μm. Previous reports have shown that OCT is capable of visualizing thin-cap fibroatheromas (TCFAs),[1] which are thought to be the precursor lesions of ruptured plaques responsible for the majority of thrombosis-mediated sudden death.[2] In addition, OCT is able to identify features that have been related to the advancement of atherosclerotic lesions, including neovascularization[3,4] and macrophage infiltration.[5,6] It is against this background that Uemura and colleagues describe the baseline OCT morphological characteristics of angiographically non-significant, non-culprit coronary lesions exhibiting rapid progression over a period of 6–9 months.[7] At a median follow-up of 7 months, 13 (19%) of the 69 studied lesions showed angiographic progression from a mean diameter stenosis of 28.8–61.4%, compared with 28.9–29.3% in the remaining lesions. Progression was clinically silent in all but three patients. OCT at baseline suggested a higher incidence of TCFAs, intraplaque microchannels, lipid pools, macrophages, intimal lacerations, and intraluminal thrombi in the progressed lesions, thus being in line with pathology-driven hypotheses of the role of these features in the progression of coronary atherosclerosis.[7]

The study is intriguing in that it reports for the first time the innovative concept of using OCT to evaluate potential markers of rapid plaque progression. Nevertheless, the results should be interpreted with caution: first due to the small size and possible selection bias in the evaluated cohort; and secondly, in view of the current methodological concepts. Concerning the former, lesions were selected from the angiogram by the identification of a focal discrete non-significant stenosis (<50% diameter stenosis), thus disregarding important information about the plaque (total burden) at baseline, as this can be visualized neither by the angiographic lumenogram nor by OCT in view of its limited tissue penetration. By the selection of only a very short segment (10 mm of length), other non-significant regions were excluded, thus making it somewhat difficult to generalize the results. In relation to the latter, the study indirectly draws attention to the challenges of developing a methodological approach that accounts for the limitations of present OCT embodiments in characterizing plaque-related features—in particular those of TCFAs. These challenges merit further consideration and will be the focus of this editorial.

Pitfalls in the OCT interpretation of TCFAs

Given the assumed importance of TCFAs in causing clinical events, there is a strong desire in the interventional community to identify and treat these lesions before they cause harm. TCFAs, with their lipid-rich/necrotic cores and thin fibrous caps,[8] visualized by OCT as diffusely demarcated signal-poor regions with overlying thin signal-rich layers (*Figure 1A* and *C*),[1] are often diagnosed with confidence, although there is emerging evidence of several factors that may obscure a correct diagnosis.

First is the intrinsic capability of OCT to distinguish lipid from non-lipid plaques. This capability was shown to be very high in the landmark validation study from 2002 where Yabushita *et al.* observed an excellent sensitivity and specificity (90–94% and 90–92%, respectively) of OCT for detecting lipid plaques.[1] However, subsequent reports have shown conflicting results, which can in part be attributed to the heterogeneity between studies in terms of vessel types (coronary vs. carotid vs. aortic),

* Corresponding author. Tel: +45 35 45 9769, Fax: +45 35 45 2705, Email: maria.radu@rh.regionh.dk

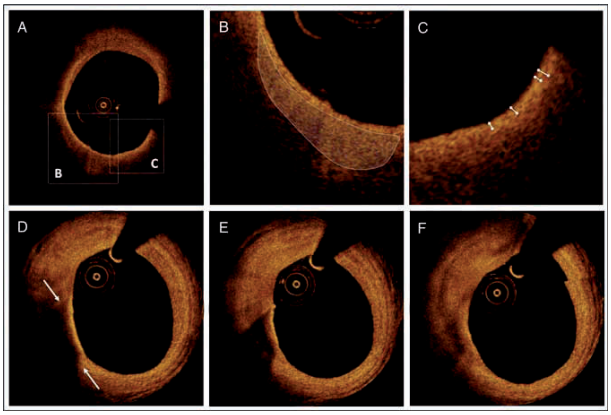

Figure 1 (*A–C*) An OCT cross-section from a non-culprit vessel of a patient with ST-elevation myocardial infarction. (*A*) From 1 to 11 o'clock, a relatively signal-rich layer is seen covering a signal-poor region. This layer becomes thinner from 4 up to 8 o'clock. Of note, the underlying signal-poor region is diffusely demarcated at 4–6 o'clock but slightly marked at 6–8 o'clock (white shaded area in the magnification in *B*), suggestive of a lipid pool and calcific pool, respectively (according to criteria by Yabushita *et al.*[1]). (*C*) *A* magnification of the diffusely demarcated signal-poor region in *A*, illustrating the difficulty in manually measuring the thickness of the overlying fibrous cap (white traces). The results of the measurements from left to right are 60, 80, 70, and 130 μm. Given that the first measurement has been placed correctly, the lesion can be diagnosed as a TCFA using the current criteria. (*D–F*) Three consecutive frames with findings consistent with luminal macrophage accumulation. In *D*, there is a signal-rich band from 7 to 9 o'clock, with strong light attenuation creating an underlying signal-poor region, which is relatively sharply demarcated laterally (arrows). The appearance as a whole is reminiscent of a TCFA; however, inspection of adjacent frames (*E* and *F*, 0.4 mm apart) suggests that there is no typical lipid pool/necrotic core as would be expected in a TCFA having a large necrotic core. Instead, the attenuated area becomes somewhat 'transparent', with even sharper borders in *E*, and disappears in *F*, revealing a relatively homogeneous, bright tissue composition, consistent with a fibrous plaque. The high light attenuation in *D* can thus be attributed to shadowing from the luminal signal-rich band, which in conclusion probably represents macrophage infiltration. The images are derived from the imaging substudy of the COMFORTABLE-AMI trial. Courtesy of Professor Stephan Windecker and Dr Lorenz Räber, Bern University Hospital, Bern, Switzerland.

sample sizes, previous experience of OCT observers, and plaque dimensions (small vs. large; superficial vs. deep).[9–11] Nevertheless, most studies showed a varying degree of misclassification of fibrous plaques into lipid-rich as well as fibrocalcific plaques. Recent data have proposed that the accuracy of plaque characterization with OCT, and then in particular the detection of lipid pools and necrotic cores, may be increased by combining OCT with other intracoronary modalities, such as intravascular ultrasound-virtual histology (IVUS-VH).[11] Additional improvement in tissue characterization by OCT may also be expected from the application of quantitative analysis techniques involving the measurement of signal attenuation and backscatter intensity.[12]

A second factor to be considered as differential diagnosis of the TCFA is the presence of macrophages. OCT displays macrophages as punctate, highly backscattering (i.e. signal-rich) structures with significant signal attenuation.[6] Given the similarities in optical properties, thin bands of accumulated macrophages close to the luminal surface can mimic the appearance of TCFAs (*Figure 1D–F*).[13] Recent studies, including the one by Uemura *et al.*,[7] point to the fact that macrophage infiltrations are becoming a target of interest in the search for markers of vulnerability. For the time being, the incidence of macrophage accumulations, and to what extent they affect the TCFA diagnosis, remains unknown. However, considering that they are being assessed in parallel with TCFAs, it is highly desirable to identify means that can aid in the differentiation of the two, as well as to assess the reproducibility. The latter would in particular have been interesting to know in the study by Uemura and colleagues.[7]

Artefacts represent a third issue that may complicate the correct diagnosis of a TCFA. The most relevant artefacts include those related to the luminal marginalization of the imaging light source, namely 'attenuation in the line-of-sight' and tangential signal drop-out, which typically occur when the light beam travels more or less parallel to the vessel wall.[11] Insights into the technical background of OCT image display is crucial for identifying these features. Their occurrence and, more importantly, how often they cause misinterpretation are presently unknown but certainly deserve further investigation.

Challenges in the quantification of the fibrous cap

An additional concern related to the diagnosis of a TCFA is the partly quantitative aspect of the assessment. On the one hand

there is the cut-off value of the thin fibrous cap, which continues to be a matter of dispute; and on the other hand there is the subjective, manual delineation of this layer. The often used cut-off to indicate a thin cap and thus vulnerability is based on autopsy reports and is 65 μm, as 95% of ruptured fibrous caps causing sudden coronary death were below this threshold.[2] It could be argued that this value may be inappropriate for non-ruptured TCFAs considering that they have less necrotic core, cholesterol clefts, and macrophage infiltration than ruptured plaques,[8] but also because histological processing techniques may cause up to 20% tissue shrinkage. Recent *in vivo* OCT data from Yonetsu and colleagues support the latter, as they found that 95% of ruptured fibrous caps (visualized as thin signal-rich flaps in relation to cavities) had a minimum thickness of 80 μm,[14] suggesting that this may be a more appropriate value for ruptured plaques. However, a suitable cut-off for non-ruptured plaques still needs to be defined. In this regard, we need first to scrutinize the methods for quantifying the thickness of intact caps.

The current approach is to measure the distance from the arterial lumen to the inner border of the lipid pool at the point where the fibrous cap thickness is considered minimal.[7,14,15] To the best of our knowledge, the only available validation study of cap thickness measurement is the one from 2006 by Kume *et al.* who found a good agreement (mean difference -24 ± 44 μm) between OCT and histology in 35 lipid-rich plaques with histology-derived cap thicknesses between 10 and 450 μm (mean: 138 μm), out of which ~ 7–8 were histology-defined TCFAs according to the correlation plot.[15] The interobserver variability was low, with a mean difference of 20 ± 59 μm. However low, this difference may be of crucial importance for classifying a lesion as a TCFA or not, in particular for cap thicknesses in the range 45–100 μm, depending on the cut-off value used (65 vs. 80 μm).[2,14]

Further, the process of delineating the cap also deserves some attention: This involves initially the identification by eye-balling of the 'thinnest point' selected from 'TCFA-looking' areas within the longitudinal and circumferential direction, followed by the manual measurement, where a line is traced from the relatively well demarcated lumen contour to the lipid border, which by definition is diffuse.[1] The subjectivity of both steps suggests that this may not be as straightforward as previously anticipated—something that is illustrated in *Figure 1C*. The additional challenge to assess the same location in a blinded fashion at a later time point, in order to assess progression or regression of the cap thickness, needs no further mention. Bearing in mind that Uemura *et al.* found TCFAs to be highly correlated with subsequent disease progression, it would have been interesting to know the reproducibility and distribution of cap thickness measurements in the two assessed groups, as well as to what extent a consideration of different cut-off values would have influenced the results.[7]

Rethinking the current methodological concepts

With the above in mind, we can conclude that the issues complicating the TCFA diagnosis require attention; both because prior studies need to be interpreted with caution, and because a number of OCT studies involving the assessment of TCFAs are under way. Considering the mentioned points, the diagnosis of TCFAs could possibly be made more reliable by implementing a phenomenological approach consisting of a number of inclusion as well as exclusion criteria. These could be complemented by semi-automatic techniques to measure cap thicknesses in order to, on the one hand, increase the reproducibility, and, on the other hand, to take full advantage of the large amount of data provided by OCT. For the latter, this could involve the extension of cap thickness measurement to larger areas of the lesion rather than only one specific point, which would provide interesting information about the lesion in general. This information may, together with other assessed features, help us to better understand why some TCFAs cause events while others do not.[16] Moreover, validation of the specific entity of OCT-defined TCFA as well as that of the necrotic core needs to be considered, as this has not yet been performed.

Additional refinements of our methodological concepts should suggestively involve a revision of the manner in which the qualitative findings are reported. In this regard, it may be argued that a semi-quantitative expression of the data may reflect the effect of a certain feature more accurately than a mere binary approach—something that may be important for the further interpretation of the results, as well as for the comparison with other studies. Accordingly, it would have been interesting to know the percentage of frames with TCFA in the two groups studied by Uemura *et al.*, and whether a semi-quantitative rather than a binary reporting of the data could have influenced the final results.

Taken together, an awareness of the limitations of current methodological concepts will allow us to develop ways to circumvent these in order to be able to use the large amount of information provided by OCT more accurately. This may eventually allow us to take full advantage of what OCT can offer in order to better understand the diagnostic benefits of this wonderful high-resolution modality.

Conflict of interest: none declared.

References

1. Yabushita H, Bouma BE, Houser SL, Aretz HT, Jang IK, Schlendorf KH, Kauffman CR, Shishkov M, Kang DH, Halpern EF, Tearney GJ. Characterization of human atherosclerosis by optical coherence tomography. *Circulation* 2002; **106**:1640–1645.
2. Burke AP, Farb A, Malcom GT, Liang YH, Smialek J, Virmani R. Coronary risk factors and plaque morphology in men with coronary disease who died suddenly. *N Engl J Med* 1997;**336**:1276–1282.
3. Moreno PR, Purushothaman KR, Sirol M, Levy AP, Fuster V. Neovascularization in human atherosclerosis. *Circulation* 2006;**113**:2245–2252.
4. Vorpahl M, Nakano M, Virmani R. Small black holes in optical frequency domain imaging matches intravascular neoangiogenesis formation in histology. *Eur Heart J* 2010;**31**:1889.
5. Falk E, Shah PK, Fuster V. Coronary plaque disruption. *Circulation* 1995;**92**:657–671.
6. Tearney GJ, Yabushita H, Houser SL, Aretz HT, Jang IK, Schlendorf KH, Kauffman CR, Shishkov M, Halpern EF, Bouma BE. Quantification of macrophage content in atherosclerotic plaques by optical coherence tomography. *Circulation* 2003;**107**:113–119.
7. Uemura S, Ishigami K, Soeda T, Okayama S, Sung JH, Nakagawa H, Somekawa S, Takeda Y, Kawata H, Horii M, Saito Y. Thin-cap fibroatheroma and microchannel findings in optical coherence tomography correlate with subsequent progression of coronary atheromatous plaques. *Eur Heart J* doi:10.1093/eurheartj/ehr284. Published online ahead of print 10 August 2011.
8. Virmani R, Kolodgie FD, Burke AP, Farb A, Schwartz SM. Lessons from sudden coronary death: a comprehensive morphological classification scheme for atherosclerotic lesions. *Arterioscler Thromb Vasc Biol* 2000;**20**:1262–1275.

9. Kawasaki M, Bouma BE, Bressner J, Houser SL, Nadkarni SK, MacNeill BD, Jang IK, Fujiwara H, Tearney GJ. Diagnostic accuracy of optical coherence tomography and integrated backscatter intravascular ultrasound images for tissue characterization of human coronary plaques. *J Am Coll Cardiol* 2006;**48**:81–88.
10. Manfrini O, Mont E, Leone O, Arbustini E, Eusebi V, Virmani R, Bugiardini R. Sources of error and interpretation of plaque morphology by optical coherence tomography. *Am J Cardiol* 2006;**98**:156–159.
11. Goderie TP, van Soest G, Garcia-Garcia HM, Gonzalo N, Koljenovic S, van Leenders GJ, Mastik F, Regar E, Oosterhuis JW, Serruys PW, van der Steen AF. Combined optical coherence tomography and intravascular ultrasound radio frequency data analysis for plaque characterization. Classification accuracy of human coronary plaques *in vitro*. *Int J Cardiovasc Imaging* 2010;**26**:843–850.
12. Xu C, Schmitt JM, Carlier SG, Virmani R. Characterization of atherosclerosis plaques by measuring both backscattering and attenuation coefficients in optical coherence tomography. *J Biomed Opt* 2008;**13**:034003.
13. van Soest G RE, Goderie TP, Gonzalo N, Koljenovic S, van Leenders GJ, Serruys PW, van der Steen AF. Pitfalls in plaque characterisation by optical coherence tomography: image artifacts in native coronary arteries. *JACC Cardiovasc Imaging* 2011;**4**:810–813.
14. Yonetsu T, Kakuta T, Lee T, Takahashi K, Kawaguchi N, Yamamoto G, Koura K, Hishikari K, Iesaka Y, Fujiwara H, Isobe M. *In vivo* critical fibrous cap thickness for rupture-prone coronary plaques assessed by optical coherence tomography. *Eur Heart J* 2011;**32**:1251–1259.
15. Kume T, Akasaka T, Kawamoto T, Okura H, Watanabe N, Toyota E, Neishi Y, Sukmawan R, Sadahira Y, Yoshida K. Measurement of the thickness of the fibrous cap by optical coherence tomography. *Am Heart J* 2006;**152**:755 e751–754.
16. Stone GW, Maehara A, Lansky AJ, de Bruyne B, Cristea E, Mintz GS, Mehran R, McPherson J, Farhat N, Marso SP, Parise H, Templin B, White R, Zhang Z, Serruys PW. A prospective natural-history study of coronary atherosclerosis. *N Engl J Med* 2011;**364**:226–235.

CHAPTER 6 METHODOLOGICAL CONSIDERATIONS IN THE USE OF OPTICAL COHERENCE TOMOGRAPHY TO EVALUATE ATHEROSCLEROSIS

6.3 Off-line fusion of co-registered intravascular ultrasound and frequency domain optical coherence tomography images for the analysis of human atherosclerotic plaques.

Räber L, Heo JH, **Radu MD**, Garcia-Garcia HM, Stefanini GG, Moschovitis A, Kelbaek H, Windecker S, Serruys PW.

EuroIntervention. 2012;8:98-108.

Offline fusion of co-registered intravascular ultrasound and frequency domain optical coherence tomography images for the analysis of human atherosclerotic plaques

Lorenz Räber[1,2], MD; Jung Ho Heo[1,3], MD; Maria D. Radu[1,4], MD; Hector M. Garcia-Garcia[1], MD, PhD; Giulio G. Stefanini[2], MD; Aris Moschovitis[2], MD; Jouke Dijkstra[5], MD; Henning Kelbaek[4], MD, DMSci; Stephan Windecker[2], MD; Patrick W. Serruys[1]*, MD, PhD

1. Department of Cardiology, Thoraxcenter, Erasmus Medical Center, Rotterdam, The Netherlands; 2. Department of Cardiology, Bern University Hospital, Bern, Switzerland; 3. Department of Cardiology, Kosin University Hospital, Busan, Korea; 4. Department of Cardiology, Rigshospitalet, Copenhagen, Denmark; 5. Division of Image Processing (LKEB), University Medical Center, Leiden, The Netherlands

L. Räber and J. Ho Heo contributed equally to this work.

KEYWORDS

- optical coherence tomography
- intravascular ultrasound
- fusion
- co-registration
- atherosclerosis

Abstract

Aims: To demonstrate the feasibility and potential usefulness of an offline fusion of matched optical coherence tomography (OCT) and intravascular ultrasound (IVUS)/virtual histology (IVUS-VH) images.

Methods and results: A total of nine matched OCT, IVUS, and IVUS-VH cross-sections were fused according to a methodology described in this report. On the basis of the fused images, an OCT-IVUS-VH tissue classification algorithm is proposed taking into account the individual strength of both techniques.

Conclusions: Offline fusion of co-registered IVUS and OCT is feasible and combines the strengths of both imaging modalities, potentially improving the diagnostic accuracy of plaque characterisation.

**Corresponding author: Thoraxcenter, Erasmus MC, 's-Gravendijkwal 230, 3015 CE, Rotterdam, The Netherlands. E-mail: p.w.j.c.serruys@erasmusmc.nl*

Introduction

The gold standard for the assessment of human coronary atherosclerosis is histology. By nature, histology remains restricted to post-mortem studies and animal models, which do not reflect anatomy under pressurised conditions *in vivo* and does not provide longitudinal information as it relates to disease progression or regression within the same individual and lacks transferability of animal data to humans[1]. Therefore, *in vivo* imaging modalities that allow a diagnostic accuracy similar to histology are in demand. Intravascular imaging techniques currently provide the highest resolution of all available coronary imaging modalities[2] and can contribute to the understanding of mechanisms underlying the progression of coronary artery disease; evaluate pharmaceutical effects on progression and regression of atherosclerosis[3]; and can potentially guide interventional therapy with the aim of improving outcomes[4].

Editorial, see page 19

Two intracoronary technologies are predominantly used for research and clinical application, namely intravascular ultrasound (IVUS) and optical coherence tomography (OCT), both of which have previously been validated against histology[5-11]. The applied imaging physics differ fundamentally: IVUS, which has been available since the early 1990s, is based on the backscattering of ultrasound waves at a frequency of millions of cycles per second. When extracting information from the ultrasonic signal, two physical characteristics can be utilised: first, the amplitude of the reflected ultrasound wave, which is used to create the greyscale (GS) image; and second, the radio-frequency signal, which is the basis for virtual histology (IVUS-VH), a technique that aims to assess plaque composition, also validated in previous studies[7]. The axial resolution of IVUS is in the range of 80-200 μm depending on the sound frequency, and the penetration depth amounts to 8-10 mm. As opposed to IVUS, OCT is a relatively novel technique, available for clinical use since 2005 (CE approval of time-domain OCT). It is based on the use of near-infrared light, with a wavelength specifically chosen of around 1,300 nm in order to reduce the light absorption of different tissues to a minimum. The axial resolution of OCT is in the range of 10 μm, an order of magnitude higher than IVUS, allowing for the identification of certain features shown to be related to plaque vulnerability. The high resolution, however, comes at the cost of a limited tissue penetration, which amounts to 1-2 mm[11,12]. Consequently, OCT provides a detailed assessment of features close to the lumen surface, whereas IVUS offers a cross-section of the entire vessel wall. In view of the fundamental differences in imaging physics resulting in different information gained by IVUS and OCT, a combination of these techniques may improve the assessment of coronary atherosclerosis in a synergistic manner. As the sensitivity and specificity for assessing the tissue composition of atherosclerotic lesions varies for the two technologies, a combined approach may further enhance the diagnostic precision. At present, there is neither a dedicated imaging probe that would allow a simultaneous *in vivo* IVUS-OCT assessment, nor specific software enabling an offline fusion of matched IVUS and OCT images. It is against this background that we describe here our methodological approach to fuse co-registered IVUS and OCT images, in order to achieve a comprehensive *in vivo* assessment of human atherosclerosis.

Methods

DEFINITIONS

CO-REGISTRATION Co-registration refers to the recording of an identical region of interest (ROI) within a coronary artery by two different imaging technologies. To date, a simultaneous co-registration of IVUS and OCT images, using a single bimodal imaging catheter, cannot be obtained *in vivo*. Consequently, separate acquisition of IVUS and OCT images in a serial fashion is necessary. Serial imaging, however, impacts importantly on the matching process, as common landmarks have to predefined and identified.

MATCHING Matching relies on the identification of corresponding frames from two separately acquired pullbacks. Matching is initiated by the identification of common landmarks, such as side branches, bifurcations or large calcifications, and the precision of the matching increases with the number of common landmarks identified. Matching can be achieved manually, or semi-automatically using dedicated software[13].

FUSION Fusion refers to the offline merging of two fully matched cross-sections that were acquired using two different imaging techniques. In this report we describe the methodological procedures and feasibility of manual matching and fusion of IVUS (IVUS-GS or IVUS-VH) and OCT images to create combined tissue maps, which in the future may lead to the development of dedicated fusion software to analyse co-registered images.

IMAGE ACQUISITION

OCT images were acquired using the C7 frequency domain OCT system (LightLab Imaging/St. Jude Medical, Westford, MA, USA). The Dragonfly™ OCT catheter (LightLab Imaging/St. Jude Medical) was advanced over a conventional guidewire, distal to the distal landmark of interest (typically a side branch), and care was taken to document the catheter position angiographically. After intracoronary administration of 100 μg nitroglycerine, blood was displaced using a non-ionic contrast agent (Xenetics®; Guerbet S.A., Villepinte, France) at 4-6 ml/sec. When sufficient blood clearance was achieved, imaging pullback was initiated at a rate of 20 mm/sec. After successful OCT imaging and verification of target landmarks on the OCT pullback, the Eagle-Eye® Gold 20 MHz IVUS probe (Volcano Corp., San Diego, CA, USA) was positioned at the same starting point, which was documented angiographically. After another administration of 100 μg nitroglycerine, catheter pullback was initiated at a standard rate of 0.5 mm/sec, and continued beyond the proximal landmark. Images were stored for later offline analysis.

POST-ACQUISITION IMAGE PROCESSING

MATCHING OF PULLBACKS AND DEFINITION OF ROI The OCT data was loaded into a dedicated offline workstation with proprietary software from LightLab Imaging/St. Jude, whereas IVUS data was loaded into the QCU-CMSTM software (Medis, Leiden, The Netherlands) on a separate computer next to the OCT worksta-

tion. As a first step, the most proximal side branch was identified in both OCT and IVUS pullbacks, and the cross-sectional rotation of the OCT pullback was adapted according to the orientation of the IVUS pullback. Subsequently, as many common side branches as possible were identified, and the most proximal and distal common side branches were used to define the matched ROI.

MATCHING OF CROSS-SECTIONS Within the matched ROI, a subsegment of interest (coronary artery plaque) was identified by OCT, and side branches within or adjacent to this segment were located in both OCT and IVUS pullbacks. Subsequently, matched cross-sections of interest were identified, again using common landmarks such as: small side branches; a certain position and configuration of calcifications; and/or a characteristic lumen shape and circumferential profile of the plaque thickness. Finally, a 1 mm calibration line was inserted in order to allow for size adaptation prior to the fusion, and the selected cross-sections were exported in JPEG format.

FUSION OF CROSS-SECTIONS Cross-sections were uploaded in Adobe® Photoshop® (Adobe Systems Incorporated, San Jose, CA, USA) and the matched IVUS-GS, IVUS-VH and OCT images placed next to each other. Thereafter, the following steps were undertaken:

1. The size of OCT and IVUS images was adjusted by matching the calibration line of 1 mm.
2. The two-dimensional orientation of the cross-sections was fine-tuned by rotating the images using cross-sectional landmarks according to the following hierarchy: a) side branch; b) calcification; c) lumen shape; d) circumferential plaque configuration (distance between lumen and external elastic membrane).
3. To optimise the overlay of IVUS on top of OCT images, the transparency function of Adobe Photoshop was used to allow the simultaneous visibility of the structures in the underlying OCT image. As a suitable default setting for overlaying IVUS on top of OCT images, a transparency of 60-70% for the IVUS-GS images, and 70-80% for the IVUS-VH images, was used **(Figure 1, Figure 3 and Figure 5)**.
4. Using information from the matched original OCT and IVUS-VH images **(Figure 2A, Figure 4A and Figure 6A)**, the contours of all visible tissue compartments as well as the external elastic membrane (EEM) were delineated and coloured using the following colour codes: white=calcific tissue by OCT/dense calcium by IVUS-VH; green=fibrous tissue by OCT/fibrous and fibro-fatty tissue by IVUS-VH; red=necrotic/lipid tissue by OCT/necrotic core by IVUS-VH; and grey=media by OCT/media stripe, i.e., EEM, by IVUS-VH **(Figure 2B, Figure 4B and Figure 6B)**. The tissue composition in OCT images was assessed using previously validated criteria[14].
5. The delineated compartments derived from the two technologies were then superimposed and displayed simultaneously in a fused schematic image **(Figure 2C, Figure 4C and Figure 6C)**.
6. For the final presentation of the schematic fused cross-sections, the information from the technology having a "superior" accuracy for a respective feature outweighed the information from the technology with the "inferior" accuracy, and was placed on top of it. The algorithm considered is outlined in **Table 1**.

Results

We selected in total three matched coronary artery cross-sections showing various plaque morphologies from co-registered IVUS and OCT pullbacks obtained from patients undergoing a study

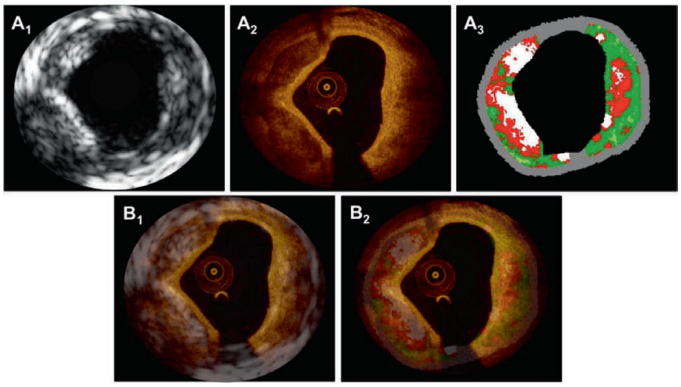

Figure 1. *In panels A_{1-3} matched cross-sections obtained by IVUS-GS (A_1), OCT (A_2) and IVUS-VH (A_3) depict fibrocalcific plaque in the left half of the vessel, and a necrotic core/lipid pool at the opposite side of the calcification. Superimposition of IVUS-GS on top of OCT and IVUS-VH on top of OCT is presented in panels B_1 and B_2, respectively.*

Table 1. Algorithm for fusion of manually delineated tissue contours based on OCT and IVUS-VH.

	OCT-defined contours are followed:	IVUS-VH-defined contours are followed:
Calcification Has to be confirmed by both technologies, otherwise, re-evaluation* is needed.	– When borders of calcifications are clearly demarcated	
Fibrous tissue In case of disagreement between technologies within the same quadrant, re-evaluation* is needed.	– As long as fibrous tissue is visible, which is typically when it is located superficially	– When fibrous tissue lies deep and thus is not visible by OCT (>300-400 micrometre)
Lipid pool/necrotic core In case of disagreement between technologies within the same quadrant, re-evaluation* is needed.	– When border of lipid pool/necrotic core is superficially located	– When luminal border of necrotic core lies deep and thus is not visible by OCT (>300-400 µm) – When delineating the abluminal border of lipid pool/necrotic core, as this is seldom visible by OCT
Fibrous cap	– Always to delineate the fibrous cap	
Cap rupture and erosion	– Always to delineate ruptures and OCT-defined erosions	
EEM	– When tunica media is visible	– When tunica media is not visible by OCT
EEM: external elastic membrane; * A review of the correctness of the matching process, of consistency between consecutive frames, as well as evaluation of potential artefacts		

including both IVUS and OCT (NCT00962416). Below follows an explanation of the findings from the isolated and fused images.

EXAMPLE 1. CALCIFIED THICK-CAP FIBROATHEROMA

UNFUSED MATCHED IMAGES The OCT cross-section in **Figure 1A$_2$** shows two sharply delineated signal-poor, low-attenuation foci at 6-9 and 9-11 o'clock, suggestive of calcific pools. The cores of these calcifications exhibit a homogeneous appearance and are covered by a relatively thin (80 µm) homogeneous signal-rich layer of even thickness, consistent with fibrous tissue. Opposite the calcification, a diffusely demarcated signal-poor zone with high light attenuation is seen, indicative of a lipid pool. This is covered by

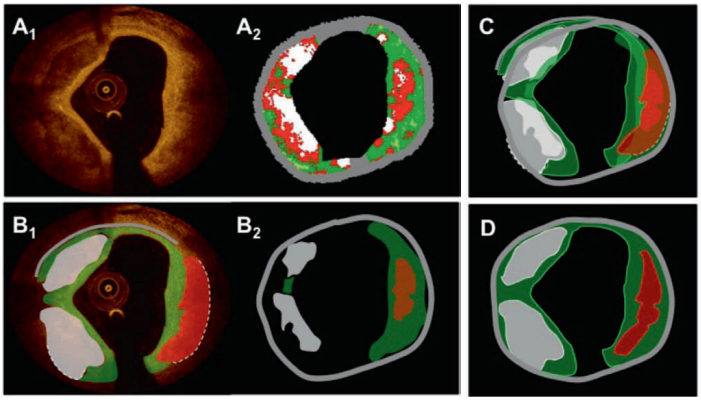

Figure 2. *Panels A_1 and A_2 show the same matched OCT and IVUS-VH images as in Figure 1. Panels B_1 and B_2 show the resulting tissue maps after delineation of the visible tissue compartments according to validated criteria. Green indicates fibrous/fibro-fatty tissue; white, calcific tissue; red, lipid tissue/necrotic core; and grey, media/EEM. The dotted lines in the OCT image in panel B_1 indicate that the deep contours of the lipid/necrotic region at 1-5 o'clock and the calcific pool at 6-9 o'clock cannot be accurately delineated. Of note, the necrotic tissue displayed by the software behind the calcifications in panel A_2 has been excluded in the tissue map in panel B_2, as it is known that this information is not reliable. Panel C shows the superimposed tissue maps from panels B_{1-2} in which many features coincide; however, they have different sizes and shapes due to different imaging physics. Of note, the IVUS-VH displays a necrotic core with direct contact to the lumen suggestive of an IVUS-VH TCFA, which is in contradiction with the OCT that displays a thick fibrous cap, suggesting an OCT ThCFA. As OCT is considered to be superior in terms of superficially-located tissue, the final diagnosis using a fused approach is a calcified ThCFA. The final fused result after weighting of the individual components in the tissue maps, according to the algorithm in Table 1, is shown in panel D.*

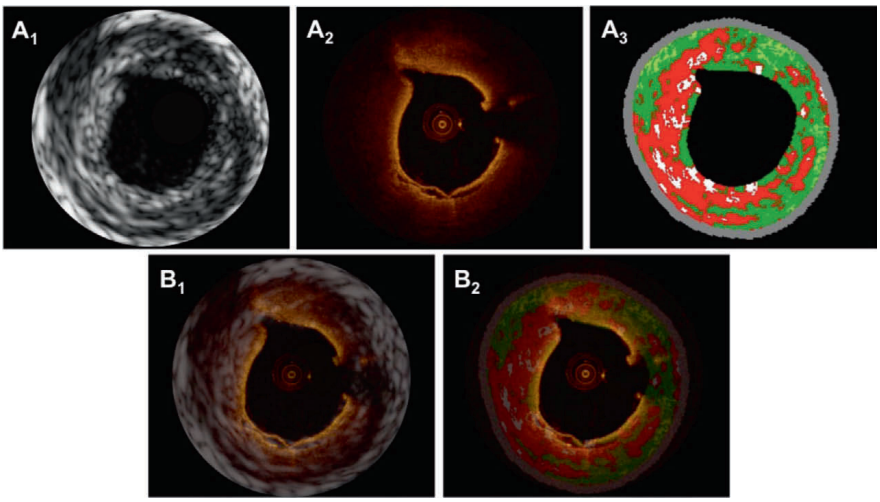

Figure 3. *In panels A_{1-3}, matched cross-sections obtained by IVUS-GS (A_1), OCT (A_2) and IVUS-VH (A_3) show a thin-cap fibroatheroma (TCFA) with a large necrotic core/lipid pool abutting to the lumen in panel A_3, and rupture of the thin fibrous plaque at 6 o'clock in panel A_2. Superimposition of IVUS-GS on top of OCT and IVUS-VH on top of OCT is presented in panels B_1 and B_2, respectively.*

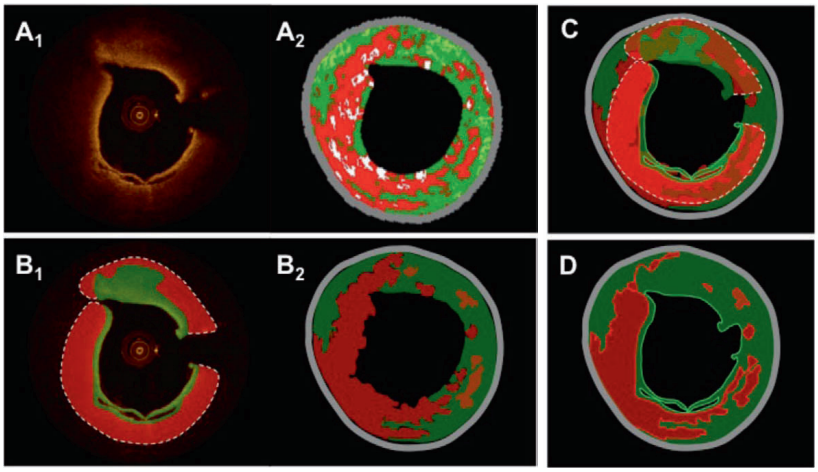

Figure 4. *Panels A_1 and A_2 show the same matched OCT and IVUS-VH images as in Figure 3. Panels B_1 and B_2 show the resulting tissue maps after manual delineation of the visible tissue compartments according to validated criteria. Green indicates fibrous/fibro-fatty tissue; red, lipid tissue/necrotic core; and grey, media/EEM. The dotted line in the OCT image in panel B_1 indicates that the deep contour of the lipid/necrotic region cannot be accurately delineated. Panel C shows the superimposed tissue maps from panel B_{1-2} in which the necrotic core and parts of fibrous features coincide. The final fused result after weighting of the individual components and contours in the tissue maps, according to the algorithm in Table 1, is shown in panel D.*

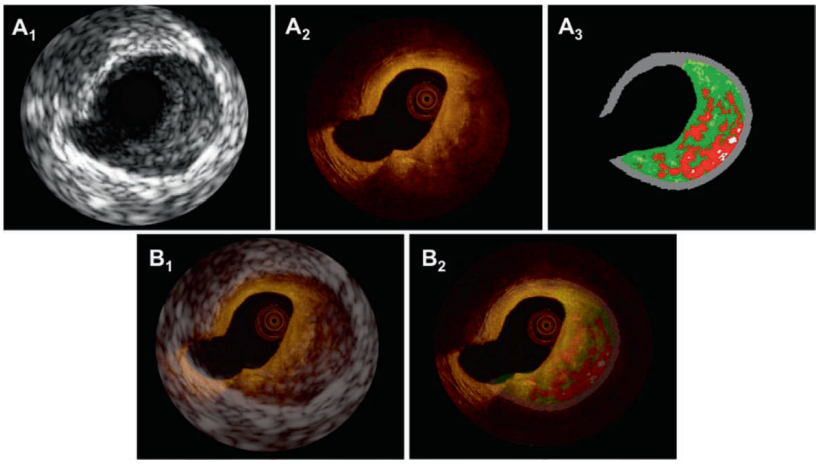

Figure 5. *In panels A_{1-3}, matched cross-sections obtained by IVUS-GS (A_1), OCT (A_2) and IVUS-VH (A_3) display a thick-cap fibroatheroma (ThCFA) with a necrotic core/lipid pool covered by a thick cap (>200 µm by OCT) at 4 o'clock. Superimposition of IVUS-GS on top of OCT and IVUS-VH on top of OCT is shown in panels B_1 and B_2, respectively.*

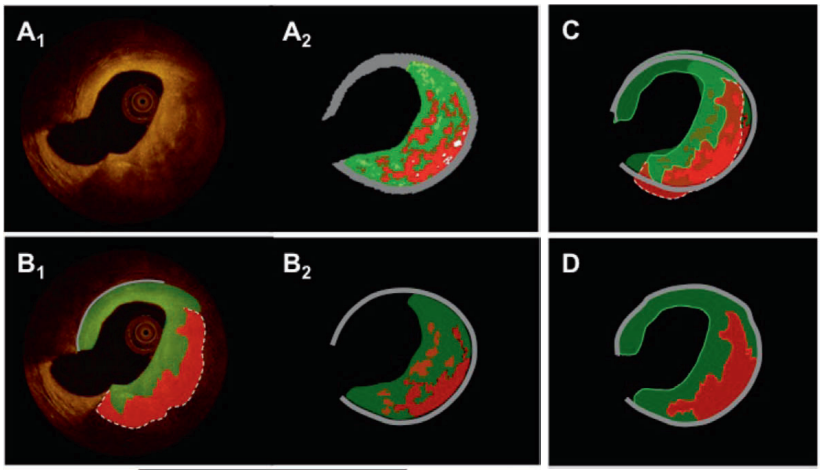

Figure 6. *Panels A_1 and A_2 show the same matched OCT and IVUS-VH images as in Figure 5. Panels B_1 and B_2 show the resulting tissue maps after manual delineation of the visible tissue compartments according to validated criteria. Green indicates fibrous/fibro-fatty tissue; red, lipid tissue/necrotic core; and grey, media/EEM. The dotted line in the OCT image in panel B_1 indicates that the deep contour of the lipid/necrotic region cannot be reliably traced. Panel C shows the superimposed tissue maps from panels B_{1-2} in which the necrotic core and parts of fibrous features coincide. The final fused result after weighting of the individual components and contours in the tissue maps, according to the algorithm in Table 1, is shown in panel D. Similar cross-sections as in Figure 5 are shown (OCT and IVUS-VH). A colour-coded tissue map was derived from the original OCT image. (B_1). The dotted line indicates that the abluminal border zone of the necrotic core/lipid pool is not precisely traceable. In panel C, the tissue maps of OCT and IVUS-VH are fused and in panel D the final fusion is executed under the assumptions made in Table 1.*

a signal-rich fibrous cap that measures >200 μm, defining this part of the cross-section as an OCT-derived calcified thick-cap fibroatheroma.

Figure 1A$_1$ shows the matched IVUS-GS image depicting two hypoechoic pools suggesting calcific areas. Of note, the calcific pool at 6-9 o'clock is inducing an acoustic shadowing which prevents visualisation of the deep contour of the calcification. With the exception of the region with acoustic shadowing, the external elastic membrane delineating the plaque border is clearly visible throughout the circumference.

Based on the radio-frequency signal, the corresponding IVUS-VH cross-section in **Figure 1A$_3$** displays the two calcific pools in white. Depending on the extent of acoustic shadowing, tissue characterisation using radio-frequency data from behind the calcifications is less reliable[8]. The zone at the opposite side of the calcification is displayed as necrotic core with direct contact to the lumen, indicative of an IVUS-VH derived calcified thin-cap fibroatheroma, which challenges the findings by OCT.

FUSED IMAGES In this example, matching and fusion was facilitated by the presence of the two calcific pools as well as the specific lumen shape and characteristic plaque thickness profile (thin intima from 11-1 o'clock). Superimposition of IVUS-GS/VH on top of OCT is shown in **Figure 1B$_{1-2}$**. Of note, both the lumen shape and size, and the calcific pools overlay each other with a high agreement. The information that is added by OCT as compared to IVUS includes the following: firstly, the fibrous cap overlying the calcific pools cannot be visualised using IVUS as the thickness is below the resolution of the technique; secondly, the abluminal border of the calcific pools and therefore the area of the calcification is not assessable using IVUS due to the acoustic shadowing, which is however in part possible with OCT. Conversely, the limited penetration of the optical signal does not allow for the visualisation of the EEM, when it is in the far-field of the source of light (**Figure 1A$_2$**, 7-8 o'clock) or concealed behind highly attenuating tissue (**Figure 1A$_2$**, 1-6 o'clock). OCT therefore precludes the determination of the total plaque volume and of the remodelling index (information that is available by IVUS). **Figure 2** shows how the schematic tissue information can be combined and fused by individual weighting of the information obtained by OCT and IVUS-VH according to the steps described above and the algorithm presented in **Table 1**. IVUS-VH displays a thin-cap fibroatheroma with necrotic core in contact to the lumen, whereas a thick fibrous cap (>200 μm) is depicted by OCT, suggesting an OCT-derived thin-cap fibroatheroma (TCFA). According to a combined algorithm (see also discussion section), the final diagnosis corresponds to a VH-OCT derived calcified thick-cap fibroatheroma.

EXAMPLE 2. THIN-CAP FIBROATHEROMA (TCFA)

UNFUSED MATCHED IMAGES **Figure 3A$_2$** shows an OCT cross-section displaying a circumferential signal-poor region, diffusely demarcated luminally, with a fast signal drop-off, suggestive of lipid/necrotic tissue. The region is covered by a highly reflective thin layer (minimal thickness 40 μm) – a thin fibrous cap – which is fissured at 6 o'clock and lifted from the underlying tissue from 5-8 o'clock. Taken together, the findings suggest a ruptured TCFA. IVUS-GS in **Figure 3A$_1$** shows concentric plaque with a zone of relatively high echogenicity from 6-12 o'clock. The corresponding IVUS-VH confirms a large area of confluent necrotic core from 6-1 o'clock, abutting the lumen at >30 degrees, thus corresponding to a VH-derived TCFA.

FUSED IMAGES In this case, cross-sectional fusion was facilitated by the presence of the small side branch at 11 o'clock, together with the oval lumen shape. The superimposed OCT and IVUS images are shown in **Figure 3B$_{1,2}$**. This example illustrates the limitation of OCT in visualising the EEM behind a thick highly light-attenuating lipid/necrotic core. At the same time, however, the figures demonstrate that the combination of OCT with IVUS allows for delineation of the EEM and thus assessment of the total plaque volume. IVUS, on the other hand, is limited by its resolution, which is clearly evident in this example by the inability to visualise the thin fibrous cap and, specifically, the site of plaque rupture. Nevertheless, the superimposed image demonstrates that the IVUS-VH derived necrotic core is in contact with the lumen at the localisation of the ruptured plaque, indicating that the technology has the capability to recognise a TCFA although a detailed surface assessment is not possible. In the OCT image at three o'clock, there is a discontinuity in the fibrous cap, which is partially obscured by the shadowing of the guidewire. **Figure 4** shows the delineation of tissue compartments in OCT creating a schematic tissue map, which is then fused with that provided by IVUS-VH. Of note, the deep border of the lipid/necrotic core cannot be delineated by OCT, which is highlighted with a dotted line. For the final fused image in **Figure 4D**, the delineation of lipid/necrotic core features was based on OCT for the luminal contour and on IVUS-VH for the abluminal border, while the information on deeply located fibrous tissue and EEM border was derived from IVUS-VH, all according to the algorithm presented in **Table 1**.

EXAMPLE 3. THICK-CAP FIBROATHEROMA (ThCFA)

UNFUSED MATCHED IMAGES The OCT cross-section in **Figure 5A$_2$** reveals a deeply located low-signal area at 2-6 o'clock covered by a thick homogeneous signal-rich layer, suggestive of an OCT-derived ThCFA. Due to the limited tissue penetration, the media can only be appreciated at the site of the discrete intimal thickening from 9-1 o'clock. IVUS-GS, however **(Figure 5A$_1$)**, provides a well-defined overview of the deeper parts of the vessel wall allowing for the assessment of the EEM area. IVUS-VH indicates plaque composed of >10% confluent necrotic core without contact with the lumen, suggesting an IVUS-VH derived ThCFA.[15] Of note, the intimal thickening as seen by OCT between 9-1 o'clock is not displayed by IVUS-VH, as the thickness of the intima (~200 μm by OCT) does not exceed the default setting of the thickness of the medial stripe on IVUS-VH (250 μm)[16].

FUSED IMAGES Cross-sectional matching, superimposition **(Figure 5B$_{1,2}$)** and fusion **(Figure 6)** were, in this example, facilitated by the presence of a large side branch at 7-9 o'clock in conjunction with the eccentric profile of the plaque. The information added by IVUS-GS in this example mainly includes the delineation of the EEM, but also the indication of necrotic core/lipid pool at the site corresponding to the signal-poor region in OCT, thus further supporting the diagnosis of a ThCFA. This is of importance as, whether the signal-poor region in the OCT image is mainly caused by light attenuation by the thick fibrotic layer, or is rather due to the attenuating effects of deep lipid/necrotic core, can be discussed. Both may play a role in this case, the argument for the latter being that a slight increase in the signal can be appreciated deep in the vessel wall around 3-4 o'clock, indicating that light still reaches this part of the vessel wall and that attenuation is thus caused by both. **Figure 6** shows schematically how tissue compartments were delineated by OCT, and how the combined OCT and IVUS-VH information was weighed to create a fused tissue map, based on the algorithm shown in **Table 1**.

Discussion

To our knowledge, this is the first report demonstrating the feasibility of an offline fusion of co-registered OCT and IVUS-GS/VH images. A few studies have been published on the combined use of IVUS and OCT for the assessment of coronary atherosclerosis, yet none of them used an offline fusion approach[17-19]. The examples presented here illustrate the advantages of combining complementary information from two technologies with differing physical properties, resulting in an optimised assessment of volumetric and structural characteristics of human atherosclerosis. Consequently, fusing co-registered matched IVUS and OCT images offers the following advantages.

IDENTIFICATION OF TUNICA MEDIA AND ASSESSMENT OF PLAQUE VOLUME

The identification of the medial layer by OCT relies on the penetration of light through the entire intima, which is determined by several factors. First, tissue penetration in general relates to the intrinsic properties of the OCT light such that increasing the wavelength would increase the penetration depth; however, this would come at the cost of resolution. Second, the penetration depth of OCT depends on the optical properties of the tissues, namely absorption and backscatter, which determine to what degree light is attenuated along the scan line. Accordingly, lipid and necrotic tissue attenuate the light significantly, whereas fibrous and calcified tissues allow a deeper penetration. However, the extent of the vessel wall finally visualised also depends on the thickness of the plaque. Third, the imaging depth is to some extent also affected by the position of the imaging catheter in the lumen, which is related to vessel tortuosity. Consequently, marginalisation of the catheter results in a poorer delivery of light to the part of the vessel circumference located farthest away[20].

As opposed to OCT, IVUS technology uses longer wavelengths, which, in the absence of large calcifications, enables it to detect the interface (i.e., the external elastic membrane) between the media and adventitia. In this way, IVUS permits assessment of the total plaque volume as well as vessel remodelling, which is of particular importance in the study of plaque progression and regression[21]. In **Figure 3** and **Figure 5** we demonstrated how the overlay of IVUS on top of OCT facilitates the location of the EEM behind highly attenuating tissue in the OCT cross-section.

LIPID POOLS AND NECROTIC CORES

Lipid pools and necrotic cores are recognised by OCT as diffusely demarcated signal-poor regions. In addition to precluding delineation of the media, they also prevent the evaluation of other potentially present tissues types. This is illustrated in **Figure 5** where evaluation of the deep tissue at 1-7 o'clock is not possible by OCT **(Figure 5A$_2$)**. However, IVUS-VH **(Figure 5A$_3$)** suggests that fibrous tissue is present behind the necrotic core at 2 o'clock. Fusion of OCT and IVUS-VH information in this example offers a more accurate characterisation of the vessel wall composition. Notwithstanding, we wish to emphasise that additional studies need to compare directly a fused analysis of co-registered IVUS and OCT images against histology in order to determine whether this technique results in higher diagnostic precision, and whether it can eliminate misinterpretations of OCT related to the limited penetration depth. We would also like to mention that, for the fusion of OCT and IVUS-VH images showing lipid/necrotic content, a general requirement should include the co-localisation of this feature to some extent in both technologies. In case of disagreement, potential causes, such as imaging artefacts or insufficient matching, should be excluded prior to fusion of the images.

CALCIFICATIONS

IVUS has a high sensitivity and specificity for the detection of calcifications[8]. However, as calcium is a potent ultrasound reflector, calcific deposits produce an acoustic shadowing, preventing the assessment of the configuration as well as the thickness and volume of calcific pools[22]. Occasionally, dense fibrous tissue may, by IVUS, produce an echo-dense signal and mimic a calcification. By OCT, calcific pools are in general well-defined and not associated with shadowing. This allows an accurate delineation and volumetric assessment, as long as they are not located too deep, as demonstrated in **Figure 1** and **Figure 2**. In addition, the differentiation between dense fibrous tissue and calcifications is readily possible, as the attenuation and backscattering signal of the two tissue types are quite different[10]. However, when deeply located, calcifications may be confused with lipid pools and vice versa, as suggested by Manfrini and co-workers[23] and, in these cases, IVUS may potentially aid in differentiation of the two. Taken together, fusion of the complementary information added by IVUS and OCT may improve the accuracy for the detection and quantification of calcium.

ASSESSMENT OF VULNERABILITY

One of the major objectives in cardiovascular medicine is the prospective identification of lesions that may later cause myocardial infarction or cardiac death. The histological lesion type suggested

to be responsible for the majority of thrombosis-related cardiac deaths is the ruptured TCFA, composed of a necrotic core with an overlying thin fibrous cap, measuring <65 µm in 95% of these TCFA[21]. While the detection of lipid and necrotic tissue is unreliable with IVUS-GS due to a high inter- and intra-observer variability[22], analysis of radio-frequency data (IVUS-VH) has proved to be useful for the identification of necrotic core[8]. As visualisation of the fibrous cap is not possible due to a limited resolution, a consensus was reached, stating that a TCFA can be diagnosed by IVUS-VH when the amount of confluent necrotic core exceeds 10% and is in direct contact with the lumen for >30 degrees of the circumference[15,24].

As compared to IVUS, OCT has sufficient axial resolution to assess directly the cap thickness overlying signal-poor diffusely demarcated lipid pools/necrotic cores[14,25], as well as to allow the evaluation of the structural integrity of the cap, as illustrated in **Figure 3**. Nevertheless, it should not be neglected that several features can obscure a correct TCFA diagnosis, including plaque-related components (e.g., macrophage accumulation) and various artefacts, which can mimic the appearance of a TCFA.

The fused approach in the setting of detecting TCFA potentially permits a more specific identification of this vulnerable plaque type, and may therefore increase the prognostic accuracy for future events. In this regard, the following criteria may be requested for the combined diagnosis of a vulnerable TCFA following fusion of OCT and IVUS: 1) IVUS-VH – presence of >10% confluent necrotic core; 2) OCT – presence of a diffusely demarcated signal-poor region, covered by a signal-rich fibrous cap <65 µm thick; 3) the findings of necrotic core by VH and lipid pool/necrotic core by OCT should naturally coincide within the same quadrant. It remains to be defined whether a summary of additional vulnerability criteria within the fused image (e.g., IVUS: remodelling index[26], calcific nodules[27]; OCT: micro-channels[28], calcific nodules, intra-plaque haemorrhages[29], plaque rupture and erosions[30]) could further increase the accuracy to predict future events.

COMBINED OCT-IVUS PROBES

The major limitation of the methodology applied for fusion of IVUS and OCT is related to the sequential assessment of OCT and IVUS using two separate probes, as this necessitates a laborious matching procedure prior to offline fusion. Simultaneous assessment with the use of a combined IVUS-OCT catheter has recently been reported by Yin et al[31,32]. This group of engineers have demonstrated the feasibility of a simultaneous IVUS-OCT assessment, a "true" co-registration, in pathology specimens free of blood. To date, the need for full blood clearance during the OCT image acquisition constitutes the main limiting step for *in vivo* application of a combined IVUS-OCT probe for simultaneous acquisition. While blood prevents light transmission, it serves as an ideal medium to transmit ultrasound waves. Consequently, as blood clearance during the OCT pullback requires a short pullback time (to date 20 mm/sec) in order to reduce ischaemia, IVUS necessitates a much slower pullback speed (0.5-1.0 mm/sec).

Limitations

The images presented in this report were selected on the basis of their illustrative and didactic character, and it remains to be shown whether fusion is feasible in a broad spectrum of co-registered, matched cross-sections. As the imaging was performed *in vivo*, we were unable to investigate the diagnostic accuracy of a fused approach in comparison with histology. Finally, we have not used any imaging software specifically validated to create fused images. Therefore, the display of the presented images is purely exploratory, but may serve as a preamble for the further development of a dedicated software application. The distinction between necrotic core and lipid pool using OCT has not yet been validated. For this reason, we do not attempt to differentiate between the two tissue types, accepting that the fusion of VH necrotic core and OCT lipid pool/necrotic core cannot entirely correspond.

Conclusion

Offline fusion of co-registered IVUS and OCT is feasible and combines the strengths of both imaging modalities, potentially improving the diagnostic accuracy of plaque characterisation and offering an ideal platform to elaborate on new diagnostic algorithms that consider the individual strengths of both technologies. Offline fusion demonstrates the potential usefulness of a combined IVUS-OCT device that would allow for a simultaneous image acquisition and an online fusion.

Acknowledgements

L. Räber is the recipient of a research fellowship (SPUM) funded by the Swiss National Science Foundation, Bern, Switzerland. All images are courtesy of S. Windecker and L. Räber, Bern University Hospital, Bern, Switzerland.

Conflict of interest statement

The authors have no conflict of interest to declare.

References

1. Lafont A, Faxon D. Why do animal models of post-angioplasty restenosis sometimes poorly predict the outcome of clinical trials? *Cardiovasc Res*. 1998;39:50-59.

2. Garcia-Garcia HM. Novel intravascular imaging technologies. Imaging in Clinical Management. Jones and Bartlett. 2009.

3. Nissen SE, Tuzcu EM, Schoenhagen P, Crowe T, Sasiela WJ, Tsai J, Orazem J, Magorien RD, O'Shaughnessy C, Ganz P. Statin therapy, LDL cholesterol, C-reactive protein, and coronary artery disease. *N Engl J Med*. 2005;352:29-38.

4. Park SJ, Hong MK, Lee CW, Kim JJ, Song JK, Kang DH, Park SW, Mintz GS. Elective stenting of unprotected left main coronary artery stenosis: effect of debulking before stenting and intravascular ultrasound guidance. *J Am Coll Cardiol.* 2001;38: 1054-1060.

5. Kimura BJ, Bhargava V, DeMaria AN. Value and limitations of intravascular ultrasound imaging in characterizing coronary atherosclerotic plaque. *Am Heart J.* 1995;130:386-396.

6. Van Herck J, De Meyer G, Ennekens G, Van Herck P, Herman A, Vrints C. Validation of in vivo plaque characterisation by virtual histology in a rabbit model of atherosclerosis. *EuroIntervention.* 2009;5:149-156.

7. Nair A, Margolis MP, Kuban BD, Vince DG. Automated coronary plaque characterisation with intravascular ultrasound backscatter: ex vivo validation. *EuroIntervention*. 2007;3:113-120.

8. Nasu K, Tsuchikane E, Katoh O, Vince DG, Virmani R, Surmely JF, Murata A, Takeda Y, Ito T, Ehara M, Matsubara T, Terashima M, Suzuki T. Accuracy of in vivo coronary plaque morphology assessment: a validation study of in vivo virtual histology compared with in vitro histopathology. *J Am Coll Cardiol*. 2006;47:2405-2412.

9. Tobis JM, Mallery J, Mahon D, Lehmann K, Zalesky P, Griffith J, Gessert J, Moriuchi M, McRae M, Dwyer ML, et al. Intravascular ultrasound imaging of human coronary arteries in vivo. Analysis of tissue characterizations with comparison to in vitro histological specimens. *Circulation*. 1991;83:913-926.

10. Jang IK, Tearney GJ, MacNeill B, Takano M, Moselewski F, Iftima N, Shishkov M, Houser S, Aretz HT, Halpern EF, Bouma BE. In vivo characterization of coronary atherosclerotic plaque by use of optical coherence tomography. *Circulation*. 2005;111: 1551-1555.

11. Jang IK, Bouma BE, Kang DH, Park SJ, Park SW, Seung KB, Choi KB, Shishkov M, Schlendorf K, Pomerantsev E, Houser SL, Aretz HT, Tearney GJ. Visualization of coronary atherosclerotic plaques in patients using optical coherence tomography: comparison with intravascular ultrasound. *J Am Coll Cardiol*. 2002;39: 604-609.

12. Kawasaki M, Bouma BE, Bressner J, Houser SL, Nadkarni SK, MacNeill BD, Jang IK, Fujiwara H, Tearney GJ. Diagnostic accuracy of optical coherence tomography and integrated backscatter intravascular ultrasound images for tissue characterization of human coronary plaques. *J Am Coll Cardiol*. 2006;48:81-88.

13. Tu S, Holm NR, Koning G, Huang Z, Reiber JH. Fusion of 3D QCA and IVUS/OCT. *Int J Cardiovasc Imaging*. 2011;27: 197-207.

14. Tearney GJ, Regar E, Akasaka T, Adriaenssens T, Barlis P, Bezerra HG, Bouma B, Bruining N, Cho JM, Chowdhary S, Costa MA, de Silva R, Dijkstra J, Di Mario C, Dudeck D, Falk E, Feldman MD, Fitzgerald P, Garcia H, Gonzalo N, Granada JF, Guagliumi G, Holm NR, Honda Y, Ikeno F, Kawasaki M, Kochman J, Koltowski L, Kubo T, Kume T, Kyono H, Lam CC, Lamouche G, Lee DP, Leon MB, Maehara A, Manfrini O, Mintz GS, Mizuno K, Morel MA, Nadkarni S, Okura H, Otake H, Pietrasik A, Prati F, Räber L, Radu MD, Rieber J, Riga M, Rollins A, Rosenberg M, Sirbu V, Serruys PW, Shimada K, Shinke T, Shite J, Siegel E, Sonada S, Suter M, Takarada S, Tanaka A, Terashima M, Troels T, Uemura S, Ughi GJ, van Beusekom HM, van der Steen AF, van Es GA, van Soest G, Virmani R, Waxman S, Weissman NJ, Weisz G. Consensus standards for acquisition, measurement, and reporting of intravascular optical coherence tomography studies: a report from the international working group for intravascular optical coherence tomography standardization and validation. *J Am Coll Cardiol*. 2012;59:1058-72.

15. Rodriguez-Granillo GA, Garcia-Garcia HM, Mc Fadden EP, Valgimigli M, Aoki J, de Feyter P, Serruys PW. In vivo intravascular ultrasound-derived thin-cap fibroatheroma detection using ultrasound radiofrequency data analysis. *J Am Coll Cardiol*. 2005;46: 2038-2042.

16. Brugaletta S, Garcia-Garcia HM, Garg S, Gomez-Lara J, Diletti R, Onuma Y, van Geuns RJ, McClean D, Dudek D, Thuesen L, Chevalier B, Windecker S, Whitbourn R, Dorange C, Miquel-Hebert K, Sudhir K, Ormiston JA, Serruys PW. Temporal changes of coronary artery plaque located behind the struts of the everolimus eluting bioresorbable vascular scaffold. *Int J Cardiovasc Imaging*. 2011;27:859-866.

17. Sawada T, Shite J, Garcia-Garcia HM, Shinke T, Watanabe S, Otake H, Matsumoto D, Tanino Y, Ogasawara D, Kawamori H, Kato H, Miyoshi N, Yokoyama M, Serruys PW, Hirata K. Feasibility of combined use of intravascular ultrasound radiofrequency data analysis and optical coherence tomography for detecting thin-cap fibroatheroma. *Eur Heart J*. 2008;29:1136-1146.

18. Gonzalo N, Garcia-Garcia HM, Regar E, Barlis P, Wentzel J, Onuma Y, Ligthart J, Serruys PW. In vivo assessment of high-risk coronary plaques at bifurcations with combined intravascular ultrasound and optical coherence tomography. *JACC Cardiovasc Imaging*. 2009;2:473-482.

19. Diletti R, Garcia-Garcia HM, Gomez-Lara J, Brugaletta S, Wykrzykowska JJ, van Ditzhuijzen N, van Geuns RJ, Regar E, Ambrosio G, Serruys PW. Assessment of coronary atherosclerosis progression and regression at bifurcations using combined IVUS and OCT. *JACC Cardiovasc Imaging*. 2011;4:774-780.

20. Prati F, Regar E, Mintz GS, Arbustini E, Di Mario C, Jang IK, Akasaka T, Costa M, Guagliumi G, Grube E, Ozaki Y, Pinto F, Serruys PW. Expert review document on methodology, terminology, and clinical applications of optical coherence tomography: physical principles, methodology of image acquisition, and clinical application for assessment of coronary arteries and atherosclerosis. *Eur Heart J*. 2010;31:401-415.

21. Burke AP, Farb A, Malcom GT, Liang YH, Smialek J, Virmani R. Coronary risk factors and plaque morphology in men with coronary disease who died suddenly. *N Engl J Med*. 1997;336: 1276-1282.

22. Mintz GS, Nissen SE, Anderson WD, Bailey SR, Erbel R, Fitzgerald PJ, Pinto FJ, Rosenfield K, Siegel RJ, Tuzcu EM, Yock PG. American College of Cardiology Clinical Expert Consensus Document on Standards for Acquisition, Measurement and Reporting of Intravascular Ultrasound Studies (IVUS). A report of the American College of Cardiology Task Force on Clinical Expert Consensus Documents. *J Am Coll Cardiol*. 2001;37: 1478-1492.

23. Manfrini O, Mont E, Leone O, Arbustini E, Eusebi V, Virmani R, Bugiardini R. Sources of error and interpretation of plaque morphology by optical coherence tomography. *Am J Cardiol.* 2006;98:156-159.

24. Garcia-Garcia HM, Goedhart D, Schuurbiers JC, Kukreja N, Tanimoto S, Daemen J, Morel MA, Bressers M, van Es GA,

Wentzel JJ, Gijsen F, van der Steen AF, Serruys PW. Virtual histology and remodelling index allow in vivo identification of allegedly high-risk coronary plaques in patients with acute coronary syndromes: a three vessel intravascular ultrasound radiofrequency data analysis. *EuroIntervention*. 2006;2:338-344.

25. Kume T, Akasaka T, Kawamoto T, Okura H, Watanabe N, Toyota E, Neishi Y, Sukmawan R, Sadahira Y, Yoshida K. Measurement of the thickness of the fibrous cap by optical coherence tomography. *Am Heart J*. 2006;152:755.e1-4.

26. Nakamura M, Nishikawa H, Mukai S, Setsuda M, Nakajima K, Tamada H, Suzuki H, Ohnishi T, Kakuta Y, Nakano T, Yeung AC. Impact of coronary artery remodeling on clinical presentation of coronary artery disease: an intravascular ultrasound study. *J Am Coll Cardiol*. 2001;37:63-69.

27. Mintz GS. Atlas of Intracoronary Ultrasound. Taylor & Francis; 2005.

28. Kitabata H, Tanaka A, Kubo T, Takarada S, Kashiwagi M, Tsujioka H, Ikejima H, Kuroi A, Kataiwa H, Ishibashi K, Komukai K, Tanimoto T, Ino Y, Hirata K, Nakamura N, Mizukoshi M, Imanishi T, Akasaka T. Relation of microchannel structure identified by optical coherence tomography to plaque vulnerability in patients with coronary artery disease. *Am J Cardiol*. 2010;105:1673-1678.

29. Virmani R, Kolodgie FD, Burke AP, Finn AV, Gold HK, Tulenko TN, Wrenn SP, Narula J. Atherosclerotic plaque progression and vulnerability to rupture: angiogenesis as a source of intraplaque hemorrhage. *Arterioscler Thromb Vasc Biol*. 2005;25:2054-2061.

30. Michel JB, Virmani R, Arbustini E, Pasterkamp G. Intraplaque haemorrhages as the trigger of plaque vulnerability. *Eur Heart J*. 2011;32:1977-1985.

31. Yang HC, Yin J, Hu C, Cannata J, Zhou Q, Zhang J, Chen Z, Shung KK. A dual-modality probe utilizing intravascular ultrasound and optical coherence tomography for intravascular imaging applications. *IEEE Trans Ultrason Ferroelectr Freq Control*. 2010;57:2839-2843.

32. Yin J, Li X, Jing J, Li J, Mukai D, Mahon S, Edris A, Hoang K, Shung KK, Brenner M, Narula J, Zhou Q, Chen Z. Novel combined miniature optical coherence tomography ultrasound probe for in vivo intravascular imaging. *J Biomed Opt*. 2011;16:060505.

SUMMARY AND CONCLUSIONS

SUMMARY

Without doubt, optical coherence tomography (OCT) has brought us closer than any other imaging modality to a histology-like visualisation of the coronary vessel wall. By enabling the identification *in vivo* of features thought to be the main causes of athero- and stent thrombosis, namely thin-cap fibroatheromas (TCFA) and incompletely covered and malapposed struts, OCT offers a prerequisite to study these lesions and determine ways to prevent and modify them, potentially impacting on patient morbidity and mortality. The fruitful use of the powerful capabilities of OCT demands from the interventional cardiologist knowledge about the pathophysiology of atherothrombosis and stent failure; as well as the understanding of the principles and methods of OCT imaging. This thesis offers significant insights into these, and provides important data regarding the safety of OCT and the vascular healing of metallic and bioresorbable vascular scaffolds.

UNDERSTANDING OPTICAL COHERENCE TOMOGRAPHY

In ***chapter 1.1***, we described the technical principles of OCT, with emphasis on the different factors that may influence the image resolution as well as the limitations related to the need to clear the vessel of blood during image acquisition. Although the latter is inevitable, we showed in ***chapter 1.2*** that this does not constitute a major clinical challenge since three-vessel imaging with both OCT and intravascular ultrasound-virtual histology (IVUS-VH) can be performed at the same occasion even in high-risk ST-elevation myocardial infarction patients, with a high success-rate and safely in both the short and long term.

When it comes to understanding the OCT image, we have seen in ***chapter 1.3*** that the signal intensity in the final output image and concurrently the penetration depth of the technique, depends on how the OCT light is attenuated, absorbed and scattered on its way from the catheter through the vessel wall – to an extent that depends on the composition of the scanned tissue. The various artefacts that can influence the correct representation of the targeted lesion can be divided into: those related to disturbances in the OCT signal – notably suboptimal vessel flushing, thrombi and macrophage infiltrations; artefacts that are caused by catheter marginalisation and cardiac motion; and artefacts associated with the preparation of the catheter.

METHODOLOGICAL CONSIDERATIONS FOR EVALUATING METALLIC STENTS

As described in ***chapter 2.1***, a limitation of OCT in the evaluation of strut apposition is the inability of the infrared light to penetrate the metal platforms of conventional stents. Therefore, OCT visualises only the endoluminal surfaces of metallic struts, which appear as bright spots with dorsal shadowing. When the actual strut thickness is known, apposition can be assessed either by reconstructing the true strut thickness and comparing it with the luminal vessel boundary; or by measuring the distance from the endoluminal surface of the strut to the luminal vessel contour and comparing it with the actual strut thickness. In either case, the high resolution of OCT allows the classification of strut apposition into categories previously not assessable with IVUS.

The stent area is measured by connecting the endoluminal or abluminal surfaces of struts with a trace line. Although the former is more straightforward, it was the latter that brought our attention to a morphological configuration of the vessel wall not previously described (***chapter 2.2***). By reconstructing the abluminal boundary of the stent such that it allows the assessment of the *outer* boundary of the stent circumference similar to what is customary with translucent polymeric scaffolds [1], the abluminal stent area represents the circumferential "point of contact" between the stent and the vessel wall when the stent is completely apposed. By using this method, we noted that the luminal contour between struts in some stents was located outside this abluminal stent contour although these struts were not malapposed. These were termed *pseudoapposed* in order not to confuse them with the *protruding* struts which at that time (2007) referred to apposed struts that were not completely embedded in the vessel wall at baseline. [2] These pseudoapposed struts, which we later renamed "protruding" (***chapter 2.3***), often co-located with malapposed struts. By an initial exploratory analysis we found that malapposed and protruding struts were more frequently associated with acute coronary syndrome and angiographically visible dissections at stent implantation; and that these types of struts tended to have lesser strut coverage compared to apposed struts. From these results we hypothesised that the protruding struts and their associated vessel bulgings were a manifestation of an abnormal vessel response to the respective stents.

CORONARY EVAGINATIONS AND EDGE DISSECTIONS

We continued to study the abovementioned morphological features in ***chapter 3.1***, with particular attention to the vessel bulgings which were termed *coronary evaginations*. Per definition, these were present when the depth of the outward bulge between struts exceeded the actual strut thickness. Since evaginations sometimes extended over several

consecutive cross-sections, creating an ectatic vessel appearance by 3D reconstruction, we assessed the presence of *major* evaginations (ME) which were at least 3 mm of length with a minimal depth of 10% of the nominal stent diameter. We studied 254 lesions treated with five different drug-eluting stents (DES) assessed with OCT at one, two and five years following implantation. OCT-detected ME were specifically related to early-generation sirolimus-eluting stents (SES), being smaller and generally less frequent in newer-generation DES. Malapposed and uncovered struts were significantly more common in lesions with vs. without ME, as was subclinical thrombus. One of the cohorts offered serial data with both OCT and IVUS at baseline and one-year follow-up, showing that intra-stent dissections and tissue protrusions present after stent implantation were associated with an increased risk of evaginations at follow-up. The paired IVUS-analyses suggested positive remodeling as the mechanism of coronary evaginations.

It is remarkable that positive vessel remodeling in SES has been associated with chronic eosinophilic inflammation deep in the vessel wall – in animal studies as well as in human autopsy material from cases of late stent thrombosis. [3-5] Similarly, IVUS-assessed vessel remodeling, predominantly after implantation of SES, has been correlated with eosinophils in thrombus aspirates from patients with very late stent thrombosis. [6] The similarity in patterns between our findings and those of previous studies altogether support the notion that OCT-detected ME represent a pathological vessel reaction particularly related to SES.

Even though our study included one of the largest OCT cohorts to date, it was too small for an evaluation of the clinical impact of ME in terms of the rare event very late stent thrombosis. We therefore used fluid dynamic simulations to assess the haemodynamics of these lesions and found that the presence of evaginations caused local flow disturbances with a change in flow which increased with the evagination size (***chapter 3.2***). Whether this may be one of the mechanisms of the subclinical thrombi found in the above study, and part of the pathophysiology of clinical stent thrombosis would be interesting to assess further.

In ***chapter 3.3***, we revisited a highly debated topic, namely the natural history of OCT-detected non-flow-limiting edge dissections following DES-implantation. A total of 22 edge dissections (flaps in most cases) were studied at baseline and one year after implantation. The median (IQR) longitudinal length was 2.9 (1.6-4.2) mm, and the circumferential extension, 1.2 (0.9-1.7) mm. The dissections extended into the media and adventitia in around half the lesions, and were angiographically visible in only two cases. At follow-up, 90% of edge dissections were completely healed by OCT. The two

cases with persistent dissection had the longest flaps at baseline. Altogether, there were no clinical events up to one year. Together with results from other studies, OCT-detected non-flow-limiting edge dissections seem to constitute a benign phenomenon that can be left untreated. [7-9]

METHODOLOGICAL CONSIDERATIONS FOR EVALUATING BIORESORBABLE VASCULAR SCAFFOLDS

Due to the polymeric composition, bioresorbable vascular scaffolds (BVS) have unique characteristics when imaged with OCT in that the optically translucent polymer allows complete imaging of the strut thickness without shadowing of the underlying vessel wall, such that the BVS struts appear as boxes with black cores framed by light-scattering borders. How this unique appearance by OCT affects the methods for assessing main quantitative measurements as compared to metallic stents, has previously been described for lesions implanted with a single scaffold. [1] In ***chapter 4.1***, we focused on lesions in which multiple BVS were implanted in an overlap fashion and saw that endothelialisation in porcine coronaries was delayed at these sites – notably in the presence of multiple stacked struts (each 300 µm thick). Due to the potential clinical importance of these findings, and due to the complex appearance by OCT of these regions, we first explored the different types of overlap that can potentially be achieved in human implantation with two scaffolds as assessed in phantom models. Of note, these same patterns were found in human clinical case examples. Subsequently, we defined methods for assessing in a constant manner relevant quantitative OCT parameters at the overlap, taking into account the type of overlap, scaffold apposition, and the time point of implantation.

Even though BVS struts by OCT per definition appear as boxes with black cores framed by light-scattering borders, the translucency can be seen altered in some instances, namely as focal intense signals in the black core without apparent contact with the strut borders. In ***chapter 4.2*** we found that these "white dots" by OCT at baseline as well as at six months follow-up were located exclusively at hinge points of the scaffold, strongly suggesting that these are caused by crazing of the polymer during the manufacturing process when the scaffold is crimped onto a delivery balloon, rather than induced by the degradation process.

In ***chapter 4.3***, we compared various quantitative measures obtained with OCT and histology from the BVS at two years after implantation in porcine coronary arteries. Even though the measurements correlated somehow by being in the same order of

magnitude, histology systematically overestimated all measurements. As discussed, there are several potential explanations for this, with the most plausible involving an unsatisfactory correspondence of cross-sections. This report not only illustrates the challenges with validation studies where histology is used as *gold standard*, but also highlights important differences between *in vivo* OCT and *post mortem* histology which are relevant to consider when using extrapolated results and hypotheses from autopsy studies to clinical examinations with OCT.

OCT TO ASSESS VASCULAR HEALING IN BIORESORBABLE SCAFFOLDS

By definition, the polymeric structure of the BVS changes with degradation as opposed to the non-erodible platform of metallic stents. OCT, IVUS and IVUS-VH can be used to assess not only the geometrical changes in BVS with time but also changes in the appearance of the struts as surrogate for changes in polymer microstructure caused by hydrolytic degradation. In ***chapter 5.1***, we compared quantitative changes in BVS struts of the scaffold revision 1.1 evaluated with OCT, IVUS and IVUS-VH at baseline, six and twelve months. We found a trend for a reduction in strut core area by OCT, and decrease in hyperechogenicity by IVUS, at both six and twelve months. IVUS-VH showed inconclusive changes in dense calcium. The correlation between techniques was poor, which is not surprising considering that each technique is fundamentally different and interrogates material- and tissue composition based on different properties (optical- (OCT), echogenic- (IVUS echogenicity) and radiofrequency (IVUS-VH)) – each at individual scale lengths.

Considering the thick struts of the BVS together with the relative fragility of the scaffold structure, requiring caution during implantation and post-dilatation, it is of interest to evaluate the occurrence and natural history of incompletely apposed struts. ***Chapter 5.2*** showed by serial analysis at baseline and 6 months that incompletely apposed struts were rare (128 struts, 3.5%) immediately after implantation, and healed within 6 months into apposed struts in the majority of cases (75.8%) by means of tissue coverage. Among the incompletely apposed struts seen at follow-up (32 struts, 0.8%), only 5 were late acquired, and displayed scaffold pattern irregularities suggestive of scaffold fracture, which was not detectable at baseline. Interestingly, the respective two patients were at baseline treated with post-dilatation up to higher diameters than recommended. The few (2%) uncovered struts and the rare presence of intra-luminal masses (3% of cross-sections) at follow-up were more frequently observed in incompletely apposed compared to completely apposed struts.

A closer investigation of the strut coverage at the frame level showed in ***chapter 5.3*** that the thickness of the coverage was well-developed at six months and remained stable up to twelve months follow-up. The circumferential distribution expressed as the ratio of the minimum and maximum thickness of coverage in the respective cross-section, was more symmetric at twelve months. Considering the homogeneous and bright appearance of the coverage, suggestive of a fibrous neointima, it is exciting to speculate whether this can, once the scaffold is resorbed, fulfil the function of a de novo fibrous cap to stabilise vulnerable thin-cap fibroatheromas by increasing the fibrous cap thickness.

METHODOLOGICAL CONSIDERATIONS FOR USING OCT TO EVALUATE ATHEROSCLEROSIS

In addition to the assessment of coronary devices by means of quantitative parameters, OCT enables the qualitative evaluation of coronary atherosclerosis. As emphasised in ***chapter 6.1***, the histological diagnosis of atherosclerosis is based on the direct visualisation of microstructural composition. In contrast to this, OCT characterises atherosclerosis based on the optical properties of the three main tissue types. Although a similar nomenclature is being used with the two modalities, the simplified classification offered by OCT means that the same term used with OCT not necessarily reflects the exact same histopathological lesion. The subject is further complicated by the occasional utilisation of contrasting nomenclature between OCT and histology for the same type of lesion, for example fibrous plaque by OCT, which corresponds to pathological intimal thickening by histology. Although these issues have not been previously highlighted, they should be considered because they not only cause confusion but may also lead to important misinterpretation of results and incorrect extrapolation of conclusions between non-corresponding pathology- and OCT studies. We have reviewed the current histological classification of atherosclerotic plaques, and in the best possible way corresponded terminology and plaque definitions between histology, OCT and IVUS-VH, based on qualitative criteria combined with arbitrary quantitative criteria, where necessary.

The thin-cap fibroatheroma (TCFA), thought to be the precursor lesion of ruptured plaques responsible for the majority of thrombosis-mediated sudden deaths [10], represents the main motive for using OCT in the clinical evaluation of coronary atherosclerosis. In ***chapter 6.2*** we focused on the various factors that may influence a correct OCT-diagnosis of TCFAs comprising those related to the intrinsic capabilities of OCT to distinguish qualitatively lipid from non-lipid plaques and other structures; different artefacts related to light phenomena; as well as factors related to the quantitative aspect of the assessment. Based on the previous proposition that the accuracy of plaque characterisation

with OCT may be increased by combining OCT with IVUS-VH data, we demonstrated in ***chapter 6.3*** the feasibility of the off-line fusion of co-registered OCT, IVUS-greyscale and IVUS-VH following the definition of an algorithm that takes into account the individual strengths of both techniques. The presented examples illustrate how the combination of these modalities can optimise the structural and volumetric assessment of human atherosclerosis. Whether this combined information can in addition reduce the rate of misclassification of different plaques remains to be settled.

CONCLUSIONS

This thesis comprehensively reflects the many considerations related to the research and clinical use of OCT, as well as the diverse contributions of OCT to interventional cardiology. I believe this thesis is of value as it has particularly:

- Offered a comprehensive guide to a systematic OCT image interpretation related to coronary stents and atherosclerosis, through the elaboration of The Clinical Atlas of OCT;
- Provided important insights into the methodological considerations behind the OCT evaluation of metallic stents, bioresorbable scaffolds, and atherosclerosis; and
- Presented new data on the feature coronary evagination; the clinical impact of edge dissections; and the vascular responses to the implantation of bioresorbable scaffolds.

SAMENVATTING EN CONCLUSIES

SAMENVATTING

Optische coherentie tomografie (OCT) heeft ons, zonder twijfel, dichter bij gebracht naar een op histologie-gelijkende visualisatie van de kransvatwand dan andere beeldvormende technieken. OCT kan *in vivo* de belangrijkste karakteristieken van de hoofdoorzaken van atherosclerose en stent trombose identificeren zoals "thin-cap fibroatheroma" (TCFA) en niet complete weefsel bekleding van de stent "struts" en malappositie van de stent "struts". Zodoende kan men met behulp van OCT deze laesies bestuderen en kunnen we mogelijke maatregelen worden ontdekt die modificatie of zelfs preventie toelaten, en die dientengevolge een verbetering kunnen geven van de morbiditeit en mortaliteit. Echter het nuttige gebruik van OCT vereist van de interventie cardioloog niet alleen kennis van de pathofysiologie van atherosclerose en stent disfunctie, maar ook begrip van de principes en methodes van OCT. Dit proefschrift draagt bij aan het verkrijgen van belangrijke inzichten. Bovendien worden belangrijke gegevens verschaft betreffende veiligheid van OCT, het vaatwand genees proces na implantatie van metalen stent of BVS.

DE PRINCIPES VAN OPTISCHE COHERENTIE TOMOGRAFIE

In ***hoofdstuk 1.1*** beschrijven we de technische principes van OCT met de nadruk op verschillende factoren die de beeld resolutie kunnen be-invloeden en de beperkingen ten gevolge van de noodzaak om het bloedvat vrij te maken van stromend bloed gedurende de acquisitie van de beelden. Dit laatste is echter geen majeur probleem en het is mogelijk om zowel OCT als IVUS-VH onderzoek te doen in alle drie de kransvaten in een zitting zelfs bij patienten met een STEMI (***hoofdstuk 1.2***). Dit blijkt veilig te zijn met geen nadelige gevolgen op korte of langere termijn.

In ***hoofdstuk 1.3*** beschrijven we dat de OCT signaal intensiteit en de penetratie diepte afhankelijk zijn hoe het OCT lichtsignaal door absorptie, attenuatie en spreiding wordt veranderd gedurende de reis van de katheter en door de vaatwand afhankelijk van de weefsel compositie van de onderzochte vaatwand. Verschillende artefacten kunnen de correcte representatie van de te onderzoeken laesie in de weg staan zoals: verstoringen van het OCT signaal door b.v. niet optimale vaat schoonspoeling, trombus, en macrofagen infiltratie; marginalisatie van de katheter en cardiale contractie; en onzorgvuldige voorbereiding van de katheter.

EVALUATIE METALEN STENTS

In ***hoofdstuk 2.1*** worden de tekortkomingen van OCT besproken met betrekking tot de evaluatie van stent appositie omdat infrarood licht niet penetreert door het metaal

van de conventionele stent. Daardoor kan OCT alleen maar het endoluminale oppervlak van de stent "struts" afbeelden, die er uit zien als heldere stippen met daarachter een schaduw. Indien de actuele dikte van de "strut" bekend is kan de appositie bepaald worden door enerzijds reconstructie van de echte "strut"dikte en deze vergelijken ten opzichte van de vaatwand grens of anderzijds door het meten van de afstand tussen het endoluminale oppervlak van de "struts" en de luminale vaatwand contour en dit te vergelijken met de actuele "strut" dikte. Door de grote resolutie van OCT is het mogelijk de stent appositie nauwkeurig te classificeren hetgeen niet mogelijk was met IVUS.

Het stent oppervlak kan worden gemeten door een lijn te trekken door ofwel de endoluminale ofwel de abluminale kant van de stent. De endoluminale meting is recht toe recht aan, maar door de abluminale metingen kregen we een totaal nieuw, niet eerder beschreven inzicht betreffende de morfologische configuratie van de vaatwand (***hoofdstuk 2.2***). Reconstructie van de abluminale grens van de stent betekent vaststelling van de buitengrens van de stent omtrek hetgeen lijkt op de situatie met een translucente polymeer "scaffold". [1] Dit betekent dat de stent in complete appositie is wanneer het abluminale stent oppervlak (de buitengrens) gelijk is aan het endoluminale vaatwand grens oppervlak. Zo ontdekten we dat de luminale vaatwand contour tussen de "struts" van sommige stents gelokaliseerd was buiten de abluminale stent contour, alhoewel deze "struts" geen malappositie hadden. Dit noemden we "pseudo apposition", niet te verwarren met "protruding stents" die toentertijd refereerden naar appositie van stents die niet volledig waren ingebed in de vaatwand na implantatie. [2] Deze "pseudo apposed struts" werden herbenoemd tot "protruding struts" (***hoofdstuk 2.3***). Het bleek dat de stents met goede appositie en "protruding struts" vaker geassocieerd waren met ACS en angiografisch zichtbare dissectie na stent implantatie. Dit type stent "struts" neigt naar een mindere "strut" bekleding vergeleken met stents met goede appositie. Op basis van deze resultaten concludeerden we dat "protruding struts" en de samengaande uitstulpingen een uiting zijn van een abnormale vaatwand reactie op deze stents.

CORONARY EVAGINATIONS EN STENT RAND DISSECTIES

In ***hoofdstuk 3.1*** worden "protruding struts" kenmerken verder bestudeerd met speciale aandacht voor de vaatwand uitstulpingen die we "coronary evaginations" hebben genoemd. Coronaire uitstulpingen zijn aanwezig indien de grootte van de uitstulping naar buiten tussen de stent "struts" meer is dan de actuele dikte van de "struts". Deze uitstulpingen strekken zich soms uit over verschillende dwarsdoorsneden, waardoor de vaatwand met een 3D reconstructie lijkt op een "ectatic" vat. We onderzochten de frequentie van grote uitstulpingen (GU) die gedefinieerd waren als tenminste 3 mm lang

en met minimale diepte van 10% van de nominale stent diameter. We onderzochten 254 laesies die werden behandeld met 5 verschillende DES en die werden onderzocht met OCT 1, 2 en 5 jaar na implantatie. OCT GU kwamen vaker voor bij eerste generatie "sirolimus-eluting stent" (SES) en ze waren kleiner en minder vaak voorkomend bij nieuwe generatie DES. Malappositie en niet beklede stent "struts" en subklinische trombus kwamen significant vaker voor bij laesies met GU, vergeleken met laesie zonder deze uitstulpingen. In een cohort patienten die serieel onderzocht werden met OCT en IVUS onmiddellijk na implantatie en 1 jaar later zagen we dat de "intrastent dissecties" en weefsel uitstulpingen na stent implantatie samengingen met een verhoogd risico op uitstulpingen 1 jaar later. De gepaarde IVUS analyse suggereert dat de positieve vaatwand remodelering de oorzaak kan zijn van deze uitstulpingen.

Het is opvallend dat positieve vaatwand remodelering met SES samengaat met chronische eosinofiele ontsteking van de diepe delen van de vaatwand zoals kan worden vastgesteld in dier studies en autopsie materiaal van patienten met late stent trombose. [3-5] Ditzelfde fenomeen werd ook gezien in patienten met zeer late stent trombose die een positieve vaatwand remodelering hadden met IVUS waar ook eosinofiele cellen werden gevonden in trombus aspiraten. [6] De overeenkomsten tussen onze bevindingen en die gemeld in de bovenstaande studies onderschrijven het idee dat met OCT gedetecteerde GU kunnen worden toe geschreven aan een pathologische vaatwand reactie voornamelijk voorkomend na SES implantatie.

Onze studie was te klein, alhoewel het een van de grootste OCT cohort was, om te kunnen vaststellen dat deze uitstulpingen gepaard gaan met een klinisch waarneembare complicatie zoals b.v. de zelden voorkomende zeer late stent trombose. Daarom hebben we een ander studie opzet gekozen. In een stroom dynamisch model hebben we de hemodynamische effecten van deze uitstulpingen bestudeerd. We zagen dat deze uitstulpingen lokale stroom verstoringen veroorzaakten en dat hoe groter deze uitstulpingen waren des te groter was de verstoring van de stroom (***hoofdstuk 3.2***). Verdere studies moeten uitwijzen of het ontstaan van subklinische trombus vorming onderdeel is van de pathofysiologie van stent trombose.

In ***hoofdstuk 3.3*** bespreken we een heet hangijzer, namelijk wat is het natuurlijke beloop van OCT gedetecteerde niet stroom belemmerende rand dissectie na DES implantatie. Twee en twintig rand dissecties (flappen in de meeste gevallen) ontstaan onmiddellijk na implantatie en na 1 jaar later werden onderzocht. De mediane (IQR) longitudinale lengte was 2.9 (1.6-4.2) mm en de grootte van de circumferentie 1.2 (0.9-1.7)

mm. Deze dissecties liepen door tot in de media of adventitia in 50% van de gevallen en in 2 gevallen waren deze ook angiografisch zichtbaar. Na 1 jaar vervolg onderzoek bleek 90% volledig genezen te zijn bij OCT. Twee gevallen met persisterende scheur hadden de grootste scheur na implantatie. Er traden geen klinische complicaties op gedurende het 1 jaar vervolg onderzoek. We kunnen dan ook concluderen op basis van onze en andere onderzoeken dat de met OCT vastgestelde niet doorstroming belemmerende rand dissecties een goedaardig fenomeen zijn die geen behandeling behoeven. [7-9]

EVALUATIE VAN BIORESORBEERBARE VASCULAIRE "SCAFFOLDS"

De BVS zijn samengesteld uit polymeren met unieke karakteristieken. Met OCT kunnen we, doordat de polymeren optische doorlaatbaar zijn, de hele "strut" dikte zonder schaduw van de onderliggende vaatwand afbeelden. De BVS ziet er met OCT uit als een doosje met een zwarte kern in een lijst met lichte rand. De unieke afbeelding met OCT van de BVS vereist andere kwantitatieve metingen dan die met metalen stents. [1] In ***hoodstuk 4.1*** concentreerden we ons op laesies in varkens die werden behandeld met multipele overlappende BVS en we constateerden dat de endothelialisatie was vetraagd – met name op de plaatsen met "strut" overlap (BVS stent "strut" 300 µm dik). Dit kan potentieel klinische consequenties hebben indien BVS overlappend in patienten worden ge-implanteerd. Daarom hebben we eerst in een fantoom de potentieel verschillende overlap types bestudeerd die met OCT complexe beelden weergeven. Deze types werden ook gevonden bij overlappende BVS implantatie in patienten. Vervolgens hebben we methodes ontwikkeld die op een constante manier relevante kwantitatieve OCT parameters meten, ook op het niveau van de overlap, daarbij rekening houdend met het type overlap, "scaffold" appositie en tijdstip van implantatie.

We zagen dat met OCT de overlappende "scaffolds" andere beelden gaven dan de vrij liggende "struts", doordat de doorlaatbaarheid in sommige gevallen veranderde waardoor focale intense signalen, de "white dots", ontstonden in de zwarte kern van de "strut" zonder dat er een duidelijk contact was met de grenzen van de "struts". In ***hoofdstuk 4.2*** beschrijven we dat deze "white dots" met OCT zowel bij implantatie als na 6 maanden vervolg uitsluitend waren gelokaliseerd op de scharnier punten van de "scaffolds" daarmee suggererend dat dit eerder wordt veroorzaakt door beschadiging van de polymeer ten tijde van het maken van de "scaffold" wanneer deze geklemd wordt op de ballon en niet door het intrinsieke degradatie proces van de "scaffolds".

In ***hoofdstuk 4.3*** beschrijven we de resultaten van de verschillende kwantitatieve metingen met OCT in vergelijking met histologie van de BVS 2 jaar na implantatie in varkens.

Alhoewel de metingen met beide methoden min of meer hetzelfde waren, bleek het dat de metingen met histologie systematisch hoger waren. Hiervoor zijn verschillende redenen aan te geven, maar de meest plausibele lijkt een onbevredigende correspondentie van de dwarsdoorsneden te zijn. Dit illustreert niet alleen de uitdagingen met validatie studies met histologie als referentie standaard, maar belicht ook de belangrijke verschillen tussen *in vivo* OCT en *post mortem* histologie. Dit is met name relevant indien resultaten en hypothesen van autopsie studies worden geextrapoleerd naar klinisch onderzoek met OCT.

EVALUATIE MET OCT VAN VASCULAIRE GENEZING NA BVS IMPLANTATIE

Met behulp van OCT, IVUS en IVUS-VH kunnen we de degradatie in de tijd van de polymeren van de BVS volgen door de optredende geometrische veranderingen en de OCT beeld veranderingen van de "struts". Deze dienen als surrogaat voor de veranderingen in de polymeer microstructuur die veroorzaakt wordt door degradatie ten gevolge van hydrolyse. In ***hoofdstuk 5.1*** beschrijven we de kwantitatieve veranderingen van de BVS "struts" van de BVS revisie 1.1 gemeten met OCT, IVUS en IVUS-VH, zowel onmiddellijk na implantatie en na 6 en 12 maanden. Met OCT zagen we een reductie van het oppervlak van de kern van de "strut" en een afname van de hyper-echoreflectie met IVUS zowel na 6 en 12 maanden. Met IVUS-VH werden niet overtuigende veranderingen gezien van de calcium neerslagen. De correlatie tussen de verschillende technieken was niet goed maar dat was te verwachten gezien de fundamentele verschillen van de onderzoek technieken die gebruikt werden voor het onderzoek van het "scaffold" materiaal en weefsel compositie: OCT – licht, IVUS – geluidsreflectie, en IVUS-VH – radiofrequentie.

We vonden het interessant om het voorkomen van en het natuurlijk beloop van incomplete appositie van de BVS "struts" te bestuderen vanwege het gegeven dat de BVS een relatief fragiele structuur heeft. In ***hoofdstuk 5.2*** toonden we aan met serieel analyse onmiddellijk na implantatie en 6 maanden later dat incomplete appositie van "struts" zeldzaam is (128 "struts", 3.5%) onmiddellijk na implantatie, terwijl na 6 maanden de meerderheid van deze "struts" nu in een goede appositie (75.8%) verkeerd door genezing met weefselbekleding. Van de "struts" met incomplete appositie na 6 maanden (32 "struts", 0.8%) waren 5 later ontstaan. Deze toonden onregelmatige patronen van de "scaffold" die verdacht waren voor fractuur, die niet aanwezig was bij implantatie. Bij 2 van de patienten kan dit verklaard worden doordat de "scaffold" ten tijde van de ballon dilatatie een grotere diameter heeft gekregen dan wordt aanbevolen. De weinige "struts" (2%) die niet met weefsel bekleed zijn en de zeldzame aanwezigheid van intra-

luminale massa (3% dwarsdoorsnede) na 6 maanden kwamen vaker voor bij incomplete appositie van de "struts" in vergelijking met complete appositie.

In ***hoofdstuk 5.3*** worden de resultaten weergegeven van een nauwkeurig onderzoek naar de bekleding van de "struts". Na 6 maanden is de dikte van de bekleding goed ontwikkeld en dit blijft stabiel tot na 12 maanden. De circumferentiele distributie van de bekleding uitgedrukt als de verhouding tussen minimale en maximale dikte was meer symmetrisch na 12 maanden. De bekleding is homogeen en helder en daarmee suggestief dat er een fibreuse neointima is ontstaan. Het is interessant om te speculeren dat deze neointima, nadat de BVS volledig is geresorbeerd, kan fungeren als een de novo fibreuse kap die de dunne kap van een TCFA kan stabiliseren doordat de dikte van de kap toeneemt.

EVALUATIE VAN ATHEROSCLEROSE MET OCT

Met OCT kan ook coronaire atherosclerose kwalitatief beoordeeld worden. De histologische diagnose van atherosclerose is gebaseerd op de directe visualisatie van de micro structurele samenstelling (***hoofdstuk 6.1***). Dit contrasteert met OCT die atherosclerose baseert op de optische eigenschappen van de 3 voornaamste weefsel types. Alhoewel een identieke nomenclatuur wordt gebezigd door de 2 modaliteiten, betekent het niet dat de gesimplificeerde classificatie met OCT noodzakelijkerwijs dezelfde histologische typering geeft. Dit alles wordt nog versterkt doordat soms niet dezelfde nomenclatuur wordt gehanteerd tussen OCT en histologie. Zo is b.v. een fibreuse plaque met OCT een intima verdikking met histologie. Deze problemen werden in het verleden niet benoemd, maar toch is het van belang hier aandacht aan te besteden omdat anders verwarring kan optreden dat kan resulteren in belangrijke misinterpretatie en onjuiste extrapolatie van conclusies. We hebben de huidige classificatie van atherosclerotische plaques opnieuw beoordeeld en op de best mogelijke manier gebruik gemaakt van dezelfde terminologie en plaque definities als OCT, histologie en IVUV-VH, waarbij we ons baseerden op kwalitatieve criteria gecombineerd waar nodig met arbitraire criteria.

OCT is goed in de diagnose van TCFA de laesie die wordt beschouwd als zijnde de voorloper van een geruptureerde plaque die samen gaat met intracoronaire trombose en het optreden van plotse dood. [10] In ***hoofdstuk 6.2*** bespreken we verschillende factoren die kunnen leiden tot een onjuiste OCT diagnose van TCFA. OCT heeft problemen met het maken van een duidelijk onderscheid tussen een lipide en niet lipide plaque. Verschillende artefacten kunnen worden gerelateerd aan licht fenomenen, maar ook kwantitatieve aspecten van de beoordeling kunnen problemen geven. Echter de

correcte karakterisering van de plaque met OCT kan worden verbeterd door OCT te combineren met IVUS-VH. In ***hoofdstuk 6.3*** demonstreren we de mogelijkheid van "off-line" fusie van coregistratie beelden met OCT, IVUS en IVUS-VH door gebruik te maken van een algoritme dat rekening houdt met de individuele sterkte van elke techniek. De gepresenteerde voorbeelden illustreren dat de combinatie van deze modaliteiten de structurele en volumetrische beoordeling van atherosclerose in vivo kan worden verbeterd. Verdere studies zijn nodig om aan te tonen dat de combinatie van informatie in staat is om de frequentie van misclassificatie van coronaire plaques terug te dringen.

CONCLUSIES

Het proefschrift biedt een overzichtelijk neerslag van de vele problemen die gepaard gaan met onderzoek en klinische toepassing van OCT, maar ook van de vele bijdragen van OCT aan de interventie cardiologie. Het proefschrift is waardevol omdat het:

- Geeft een overzichtelijke handleiding om systematisch OCT beelden te interpreteren van coronaire stents en atherosclerose, zoals te zien is in met zorg uitgevoerde Clinical Atlas of OCT;
- Verstrekt belangrijke inzichten in de methodologische beschouwingen omtrent OCT evaluatie van metalen stents, bioresorbeerbare "scaffolds" en atherosclerose; en
- Verschaft nieuwe data betreffende een speciaal probleem de "coronary evaginations"; en bespreekt het klinisch belang van stent rand dissectie; en de vasculaire reacties na de implantatie van een bioresorbeerbare "scaffold".

REFERENCES

1. Serruys PW, Onuma Y, Ormiston JA, de Bruyne B, Regar E, Dudek D, Thuesen L, Smits PC, Chevalier B, McClean D, Koolen J, Windecker S, Whitbourn R, Meredith I, Dorange C, Veldhof S, Miquel-Hebert K, Rapoza R, Garcia-Garcia HM. Evaluation of the second generation of a bioresorbable everolimus drug-eluting vascular scaffold for treatment of de novo coronary artery stenosis: six-month clinical and imaging outcomes. *Circulation.* 2010;122(22):2301-2312.
2. Tanigawa J, Barlis P, Di Mario C. Intravascular optical coherence tomography: optimisation of image acquisition and quantitative assessment of stent strut apposition. *EuroIntervention.* 2007;3(1):128-136.
3. Virmani R, Guagliumi G, Farb A, Musumeci G, Grieco N, Motta T, Mihalcsik L, Tespili M, Valsecchi O, Kolodgie FD. Localized hypersensitivity and late coronary thrombosis secondary to a sirolimus-eluting stent: should we be cautious? *Circulation.* 2004;109(6):701-705.
4. John MC, Wessely R, Kastrati A, Schomig A, Joner M, Uchihashi M, Crimins J, Lajoie S, Kolodgie FD, Gold HK, Virmani R, Finn AV. Differential healing responses in polymer- and nonpolymer-based sirolimus-eluting stents. *JACC Cardiovasc Interv.* 2008;1(5):535-544.
5. Wilson GJ, Nakazawa G, Schwartz RS, Huibregtse B, Poff B, Herbst TJ, Baim DS, Virmani R. Comparison of inflammatory response after implantation of sirolimus- and paclitaxel-eluting stents in porcine coronary arteries. *Circulation.* 2009;120(2):141-149, 141-142.
6. Cook S, Ladich E, Nakazawa G, Eshtehardi P, Neidhart M, Vogel R, Togni M, Wenaweser P, Billinger M, Seiler C, Gay S, Meier B, Pichler WJ, Juni P, Virmani R, Windecker S. Correlation of intravascular ultrasound findings with histopathological analysis of thrombus aspirates in patients with very late drug-eluting stent thrombosis. *Circulation.* 2009;120(5):391-399.
7. Kume T, Okura H, Miyamoto Y, Yamada R, Saito K, Tamada T, Koyama T, Neishi Y, Hayashida A, Kawamoto T, Yoshida K. Natural history of stent edge dissection, tissue protrusion and incomplete stent apposition detectable only on optical coherence tomography after stent implantation. *Circ J.* 2012.
8. Chamie D, Bezerra HG, Attizzani GF, Yamamoto H, Kanaya T, Stefano GT, Fujino Y, Mehanna E, Wang W, Abdul-Aziz A, Dias M, Simon DI, Costa MA. Incidence, predictors, morphological characteristics, and clinical outcomes of stent edge dissections detected by optical coherence tomography. *JACC Cardiovasc Interv.* 2013;6(8):800-813.
9. De Cock D, Bennett J, Ughi GJ, Dubois C, Sinnaeve P, Dhooge J, Desmet W, Belmans A, Adriaenssens T. Healing course of acute vessel wall injury after drug-eluting stent implantation assessed by optical coherence tomography. *Eur Heart J Cardiovasc Imaging.* 2014;15(7):800-809.
10. Burke AP, Farb A, Malcom GT, Liang YH, Smialek J, Virmani R. Coronary risk factors and plaque morphology in men with coronary disease who died suddenly. *N Engl J Med.* 1997;336(18):1276-1282.

ACKNOWLEDGEMENTS

This thesis for the degree of *Philosophiae Doctor* was carried out at the Thoraxcenter, Erasmus University Medical Centre in Rotterdam, between July 2010 and December 2011. I am convinced that no part of it would have been achieved without the generous help of a lot of people. I am therefore deeply grateful to all my colleagues, friends and family for providing their experience and support, and for sharing both the good and challenging times. I wish in particular to thank:

Prof. Patrick Serruys, the promoter of this thesis. It has been a great honour and privilege to work with one of the pioneers and shapers of interventional cardiology; to be able to personally experience your outstanding innovative mind which has enabled you to lead not one but four revolutions in interventional cardiology; your amazing ability to orchestrate a multitude of international projects simultaneously; your unbelievably hard work and your enthusiasm for new epic projects; your indefatigable energy; your incredible memory enabling you to retain an impressive amount of information far beyond your 1800 publications; your attentiveness to perfection and detail without losing the helicopter view; and your capability to continuously attract a large number of international fellows whom you generously accept into your successful team. Thank you for being a tremendous source of inspiration; for granting me invaluable insights into planning and performance of everything from clinical trials and manuscript writing, to fund raising, congresses and editorial work; for all the interesting studies I had the opportunity to work with you on, out of which the Clinical Atlas of OCT was surely one of the most pleasurable. I will always be proud of having been your fellow, and hope to be able to continue our collaboration.

Dr. Henning Kelbæk, my co-promoter, for firmly believing in me and always encouraging my development as a researcher and clinician, not only at home in Copenhagen but also during my entire stay in Rotterdam. Thank you for being a huge source of inspiration: for continuously helping me with my clinical studies and teaching me how to practically organise and manage my clinical projects at home, even when far away; for always providing me with good advice when needing it; for importantly showing me how research can be kept alive alongside clinics; for your continuous and generous support not least financially; for your much appreciated friendship; for showing me that humility and world reputation are indeed compatible; and for always making me feel welcome in the cath lab at Rigshospitalet. I am deeply grateful for the years I had the privilege to work with you thus far, and hope that there are many more to come.

Dr. Hector García-García, my co-promotor, with whom I had many interesting discussions on intracoronary imaging, and with whom I had the pleasure to collaborate on the Clinical Atlas of OCT. Thank you for guiding me in lots of practical things, especially for swiftly helping me to make the necessary connections when being a newcomer in Rotterdam; for facilitating my collaboration with Cardialysis; and for being available during my acquaintance with the Medis software. Thank you also for the friendship I made with you and your lovely family, and for the unforgettable barbeques in the park.

Dr. Kari Saunamäki, my supervisor in Copenhagen. It was you who initially opened the door for me to the grand world of interventional cardiology. Thank you for stimulating my curiosity and staying there afterwards to guide me on the right paths; for helping to make our projects in Copenhagen financially and practically possible, not least for your invaluable help with the inclusion of patients into our studies. Thank you for your much appreciated friendship; for always being available for me, patiently listening to my concerns; and for helping me out with excellent advice. I admire you greatly for being such an interesting person, and for teaching me that life is more than just work. I hope to have the privilege to continue our eight-year-long collaboration, not least through your continued guidance in PCI procedures, and our enjoyable meetings in Snowmass.

Dr. Erik Jørgensen and **Dr. Steffen Helqvist**: Thank you for the appreciated collaboration with our studies in Copenhagen; for your patient help and always good advice; for being such excellent examples in the art of PCI, and for encouraging me to follow my heart.

My fellow research colleagues and friends in Rotterdam:

Lorenz: you have been and still are one of my most appreciated friends and colleagues. Thank you for teaching me a lot about research and life; for the many endless, exhausting yet still enjoyable hours spent to prepare the Atlas of OCT; for your always generous help and encouragement during my stay in Rotterdam, which I will never forget. I sincerely admire your intelligence, extremely hard work, unbelievably organisational mind, and how all this fits in a kind and humble person. I hope that our excellent collaboration and friendship will continue for many years.

Bill: I cannot tell you how much I have appreciated our friendship. You have felt practically like family to me during my time in Rotterdam. Thank you for all the happy moments we had together, our nice talks, the BVS histology paper we worked intensively

on, and the unforgettable Sunday dinners after church. I am so happy for you that you have found the conditions you were seeking.

Vasim: I have really appreciated the many hours we spent together in the same working room, all the good laughs you have stimulated in me, our friendship, and for always being a caring person, not least when it came to fruit and delicious cookies and cakes. I will never forget the hilarious sushi-session we had together with Bill at my place.

Josep: thank you for your always polite manners, for our friendship, for the nice paper we did together, and for introducing me to delicious Catalan grilled onions.

Salvatore: you truly impressed me with your calmness, diplomacy and remarkably productivity. It felt like every time we turned our backs, you had written another paper. Thank you for your appreciated friendship and for always being ready for a nice dinner or a good party.

Yoshinobu-sensei: thank you for your kind friendship and good advice in various situations. I highly admire you for your hard work, incredible energy, and humility. I sincerely wish you success, should it be in Rotterdam or Japan.

Takashi-sensei: together with your wife Yuko, you have both been such honest and dear friends. I am truly grateful for your invaluable help with the IVUS analysis in the evagination paper, where you laid aside all your other projects just to help me – something I will never forget. I appreciate very much that our friendship still continues, and hope to be able to welcome you and Yuko again in Copenhagen.

Roberto: thank you for all the good talks we had during my stay in Rotterdam, and for allowing me to trick you into setting up a jogging team with me – it was great fun. To be more serious, I was very impressed by the incredible strength you showed during your father's illness, and how you continued to cope with all the different projects in spite of this.

Jung Ho: Dr. Heo, we had so much fun together. Thank you for your appreciated friendship, for introducing me to South Korean "kimchi", and for demonstrating to us all the incredible art of powernap. I am happy for you that you are back home now with your wife and daughter that you missed so much.

Il Soo: Dr. Lee, you astonished us all when you and your wife invited us for an incredibly memorable and moving evening at your place with delicious food, words of wisdom, and ancient South Korean tea. I greatly admire your kindness, humility and always-calm-disposition, and truly appreciate our warm friendship.

Juan-Luis: although our time in Rotterdam only overlapped for a short period of time, I am grateful for the good advice you gave me before coming to Rotterdam and at the beginning of my stay. I am convinced that with your intelligence, you will prosper in any department in Europe.

Alexander: although we didn't have any common projects, it was interesting to hear about your work and to see your commitment within the field of nanotechnology.

I wish importantly to thank **Sylvie Lhoste** who is also one of my paranimfs: you were and still are a one of my dearest friends. Thank you so much for always being there for me, for taking so good care of me, and for all the happy moments we shared not only in Rotterdam but also in San Francisco, Paris, Barcelona and Copenhagen. You have such a big heart and I sincerely wish you all the best, and that our friendship will continue to grow.

Paul Cummins: I am sincerely grateful for your always true and honest friendship, and for never hesitating to help me out in any situation, even at 10 pm. Thank you for still being there for me and for sharing memorable moments in Rotterdam as well as Copenhagen.

Nico Bruining: thank you for all the good discussions we had both in Rotterdam and abroad, and for all your appreciated advice.

You were all my family during my stay in Rotterdam and it would never have been the same without you. I will never forget our happy time together.

Hanny Boutkan: as Professor's secretary, you are overwhelmed not only with your duties, but also with all kinds of requests from the fellows – yet, you always carry them out with excellence. Thank you so much for helping me out with all kinds of things, not least in tricky situations. I really appreciate your kind friendship and warm heart.

Marie-Angel Morel: thank you very much for your practical advice on many different things during my entire stay, and for the good moments we shared outside of work.

Prof. Stephan Windecker from Bern: thank you for granting me access to the SIRTAX-LATE OCT data and for your appreciated help in manuscript writing. I truly admire the perfection of your hard work, and envy the excellent role model that Lorenz has in you. I look very much forward to continuing our collaboration on various projects.

Bindu Kalesan from Bern: thank you for your invaluable contribution to the evagination paper by performing the complex statistical analysis. During the numerous hours we spent together by skype and during my visits to Bern, I came to admire your amazing capability to work endlessly and without exhaustion – I do not understand how you do it. I appreciate your friendship and generous hospitality.

Prof. Peter Jüni from Bern: thank you very much for supporting the statistical analysis of the evagination paper and for the interesting discussions with had.

Aloïs Pfenniger from Bern: thank you for the good collaboration we had on the fluid dynamic simulation study; for your great patience with all my questions by skype and while in Bern; and for the many hours you spent on the time-consuming simulations.

Frédéric Doncieux and Véronique Deltort from PCR Publishing: thank you for an excellent and truly pleasant collaboration on the Atlas of OCT. I appreciate all our moments together, both with producing the Atlas and enjoying it, and look forward to future collaborations. Also thank you to your **co-workers**, and the **iPad team** lead by **David Fairand**.

Company collaborations: thank you to Terumo, St. Jude, Biotronik and Stentys for making the publication of the Atlas of OCT possible through their financial support; and thank you to Richard Rapoza from Abbott Vascular, for providing me with useful insights into various aspects of the BVS.

Giulio and **Masanori-sensei** from Bern: it has been a pleasure to get to know both of you and to spend nice moments in Bern and around the world. Thanks to Giulio for a nice collaboration on the Atlas of OCT, and to Masa for the collaboration on the IBIS-4 safety paper.

I owe a special thank you to **Prof. Pim de Feyter** for kindly and swiftly translating into Dutch the introduction, summary and conclusion of my thesis.

I wish to thank all the **committee members** for kindly agreeing to evaluate my thesis.

Thank you to **Nadia**: my dear friend in Copenhagen who has during my entire fellowship abroad been a great support in soul and by skype.

Last but certainly not least, I am eternally indebted to my wonderful parents **Mihai** and **Constanta Radu** and my brothers **Mikael** and **Dacius** for their never-ending love and support, for always believing in me and making me feel special, and for faithfully sharing both joy and hardship. Thank you for having raised me with strong belief, hope and love, and for teaching me good values and work ethics from childhood. None of what I have in my life today would ever have been possible without your infinite support! I love you all very much!

The work of this thesis was financially supported by:
Dr. Henning Kelbæk
Dr. Kari Saunamäki
The Heart Centre Rigshospitalet Research Foundation
Copenhagen University Travel Grant
Astra Zeneca Travel Grant

CURRICULUM VITAE

Name Maria D. Radu
Date of birth 12th October 1978
Place of birth Stockholm, Sweden
Citizenship Swedish
E-mail maria_d_radu@yahoo.com

EDUCATION AND DEGREES

1997 – 2003 ***Master of Arts, solo piano***
Lund University
Malmö Academy of Music
Malmö, Sweden

1999 – 2006 ***Degree in Medicine and Surgery (MD)***
University of Copenhagen
Faculty of Medicine
Copenhagen, Denmark

2004 ***Clinical Fellowship in Otolaryngology, Dermatology and Ophthalmology***
Vanderbilt University
Faculty of Medicine
Nashville, Tennessee, USA

2007 – 2010 ***PhD Research Fellowship***
University of Copenhagen, Faculty of Medicine, and
Copenhagen University Hospital, Rigshospitalet
Promotor: Dr. Kari Saunamäki
Copenhagen, Denmark

2010 – 2012 ***PhD Research Fellowship***
Erasmus Medical Center
Faculty of Medicine
Promotor: Prof. Patrick W. Serruys
Rotterdam, The Netherlands

2006 – 2007 ***Clinical Internship in Internal medicine and Surgery***
Slagelse Hospital
Slagelse, Denmark

2012 – (2017) ***Clinical Fellowship in Internal Medicine and Cardiology***
Herlev University Hospital, and
Copenhagen University Hospital, Rigshospitalet
Copenhagen, Denmark

OTHER ACTIVITIES

Editor-in-Chief and author of the Clinical Atlas of OCT, together with editors Lorenz Räber, Hector Garcia-Garcia and Prof. Patrick W. Serruys (PCR Publishing): Dec 2010 – May 2012

Board member of the EAPCI Young interventionalists committee, under the European Association of Percutaneous Coronary Interventions: Aug 2011 – Aug 2014

Co-Chair of the EAPCI Young interventionalists committee, under the European Association of Percutaneous Coronary Interventions: May 2014 – May 2016

Member of the International Working Group for Standardization of OCT: Dec 2009 – present. Active participant of the Subgroup for Standardization of stent and atherosclerosis measurements: Nov 2012 – present

International Associate Editor of the Eurointervention Journal: Jun 2010 – present

Member of the Editorial Board of PCR online: May 2010 – present

Reviewer for the Eurointervention Journal; European Heart Journal; European Heart Journal Cardiovascular Imaging; Journal of the American College of Cardiology; Journal of the American College of Cardiology Cardiovascular Interventions; and Scandinavian Cardiovascular Journal: Feb 2010 – present

Abstract grader for the EuroPCR congress 2012 – 2014

Member of the EAPCI Women's Committee: May 2014 – present

***Society memberships*:**

Danish Society of Cardiology; Swedish Society of Cardiology; European Society of Cardiology

PUBLICATIONS

Radu MD, Kelbæk H, Jørgensen E, Helqvist S, Løjmand B, Engstrøm T, Saunamäki K. Intracoronary optical coherence tomography: Insights from clinical research – What do we need to learn? *In press Curr Cardiov Imag Rep*.

Murray SW, Cooper RM, Appleby C, McCann C, Binukrishnan S, **Radu MD**, Stables R. Double jeopardy: Multi-modality imaging of monozygotic "twin" and thick-cap fibroatheromas. *In Press Atherosclerosis*.

Dridi NP, Johansson PI, Lønborg JT, Clemmensen P, **Radu MD**, Qayyum A, Pedersen F, Helqvist S, Saunamäki K, Kelbæk H, Jørgensen E, Engstrøm T, Holmvang L. Tailored antiplatelet therapy to improve prognosis in patients exhibiting clopidogrel low-response prior to percutaneous coronary intervention. *Platelets. 2014 Aug 28:1-9. [Epub ahead of print]*

Dridi NP, Johansson PI, Clemmensen P, Stissing T, **Radu MD**, Qayyum A, Pedersen F, Helqvist S, Saunamäki K, Kelbæk H, Jørgensen E, Engstrøm T, Holmvang L. Prasugrel or double-dose clopidogrel to overcome clopidogrel low-response–the TAILOR (Thrombocytes And IndividuaLization of ORal antiplatelet therapy in percutaneous coronary intervention) trial. Platelets. 2013 Nov 18. [Epub ahead of print].

Radu MD, Räber L. Cautionary approach recommended when interpreting images obtained with optical coherence tomography. Lancet. 2014;383:1887.

Radu MD, Pfenniger A, Räber L, de Marchi S, Obrist D, Serruys PW, Vogel R. Flow disturbances in stent-related coronary evaginations – A computational fluid-dynamic simulation study. EuroIntervention. 2014 May;10(1):113-23.

Radu MD, Räber L, Kalesan B, Muramatsu T, Kelbæk H, Heo J, Jørgensen E, Helqvist S, Farooq V, Brugaletta S, Garcia-Garcia HM, Jüni P, Saunamäki K, Windecker W, Serruys PW. Coronary evaginations are caused by positive vessel remodeling and are nearly absent following implantation of newer-generation drug-eluting stents: An optical coherence tomography and intravascular ultrasound study. Eur Heart J. 2014 Mar;35(12):795-807.

Radu MD, Räber L, Heo JH, Jørgensen E, Kelbæk H, Muramatsu T, Helqvist S, Gogas BD, Farooq V, Garcia-Garcia HM, Windecker S, Saunamäki K, Serruys PW. Natural history of

optical coherence tomography-detected edge dissections following drug-eluting stent implantation. EuroIntervention. EuroIntervention. 2014 Jan 22;9(9):1085-94.

Muramatsu T, García-García HM, Onuma Y, Zhang Y, Bourantas C, Diletti R, **Radu MD**, Ozaki Y, Serruys PW. Intimal flaps detected by optical frequency domain imaging in the proximal segments of native coronary arteries - An innocent bystander? Insights from the TROFI trial. Circ J. 2013;77(9):2327-33.

Farooq V, Serruys PW, Heo JH, Gogas BD, Perkins LE, Onuma Y, Diletti R, **Radu MD**, Räber L, Bourantas CV, van Remortel E, Pawar R, Rapoza RJ, Powers JC, van Beusekom H, Garcìa-Garcìa HM, Virmani R. Intracoronary Optical Coherence Tomography and Histology of Overlapping Everolimus-Eluting Bioresorbable Vascular Scaffolds in a Porcine Coronary Artery Model: The Potential Implications for Clinical Practice. JACC Cardiovasc Interv. 2013 May;6(5):523-32.

Dridi NP, Lønborg JT, **Radu MD**, Clemmensen P, Engstrøm T, Kelbæk H, Jørgensen E, Helqvist S, Saunamäki K, Christensen TH, Baeres FM, Johansson PI, Holmvang L. Hypercoagulation Assessed by Thromboelastography is Neither Related to Infarct Size nor to Clinical Outcome After Primary Percutaneous Coronary Intervention. Clin Appl Thromb Hemost. 2013 Apr 23. Clin Appl Thromb Hemost. 2013 May 1. [Epub ahead of print]

Farooq V, Gogas BD, Okamura T, Heo JH, Magro M, Gomez-Lara J, Onuma Y, **Radu MD**, Brugaletta S, van Bochove G, van Geuns RJ, Garcìa-Garcìa HM, Serruys PW. Three-dimensional optical frequency domain imaging in conventional percutaneous coronary intervention: the potential for clinical application. Eur Heart J. 2013;34(12):875-85.

Brugaletta S, Garcia-Garcia HM, Gomez-Lara J, **Radu MD**, Pawar R, Khachabi J, Bruining N, Sabaté M, Serruys PW. Reproducibility of qualitative assessment of stent struts coverage by optical coherence tomography. Int J Cardiovasc Imaging. 2013;29(1):5-11.

Räber L, **Radu MD**. Optimising cardiovascular outcomes using optical coherence tomography-guided percutaneous coronary interventions. EuroIntervention 2012;8(7):765-771.

Gogas BD, Serruys PW, Diletti R, Farooq V, Brugaletta S, **Radu MD**, Heo JH, Onuma Y, van Geuns RJ, Regar E, De Bruyne B, Chevalier B, Thuesen L, Smits PC, Dudek D, Koolen J, Windecker S, Whitbourn R, Miquel-Hebert K, Dorange C, Rapoza R, Garcia-Garcia HM,

McClean D, Ormiston JA. Vascular response of the segments adjacent to the proximal and distal edges of the ABSORB everolimus-eluting bioresorbable vascular scaffold: 6-month and 1-year follow-up assessment: a virtual histology intravascular ultrasound study from the first-in-man ABSORB cohort B trial. JACC Cardiovasc Interv. 2012;5(6):656-65.

Prati F, Guagliumi G, Mintz GS, Costa M, Regar E, Akasaka T, Barlis P, Tearney GJ, Jang IK, Arbustini E, Bezerra HG, Ozaki Y, Bruining N, Dudek D, **Radu M**, Erglis A, Motreff P, Alfonso F, Toutouzas K, Pinto F, Serruys PWJC, Di Mario C. Expert review document, part 2. Methodology, terminology and clinical applications of OCT for assessment of interventional procedures. Eur Heart J. 2012;33(20):2513-20.

Radu MD, Räber L, van Soest G, Garcia-Garcia HM, Serruys PW. Chapter 1. Principles of intravascular optical coherence tomography. The Clinical Atlas of OCT. PCR Publishing. May 2012.

Radu MD, Räber L, Serruys PW. Chapter 2. Artefacts with intracoronary optical coherence tomography. The Clinical Atlas of OCT. PCR Publishing. May 2012.

Räber L, **Radu MD**, Garcia-Garcia HM, Akasaka T, Banz Y, Kume T, Windecker S, Serruys PW. Chapter 3. Atherosclerosis visualised with optical coherence tomography. The Clinical Atlas of OCT. PCR Publishing. May 2012.

Radu MD, Räber L, Gomez-Lara J, Kelbæk H, Stefanini G, Jørgensen E, Helqvist S, Tellez A, Granada J, Saunamäki K, Serruys PW, Windecker S. Chapter 4. Optical coherence tomography for the assessment of intracoronary stents. The Clinical Atlas of OCT. PCR Publishing. May 2012.

Gogas BD, **Radu M**, Onuma Y, Perkins L, Powers JC, Gomez-Lara J, Farooq V, Garcia-Garcia HM, Diletti R, Rapoza R, Virmani R, Serruys PW. Evaluation with in vivo optical coherence tomography and histology of the vascular effects of the everolimus-eluting bioresorbable vascular scaffold at two years following implantation in a healthy porcine coronary artery model: implications of pilot results for future pre-clinical studies. Int J Cardiovasc Imaging. 2012;28(3):499-511.

Räber L, Heo JH, **Radu MD**, Garcia-Garcia HM, Stefanini GG, Moschovitis A, Kelbaek H, Windecker S, Serruys PW. Off-line fusion of co-registered intravascular ultrasound and

frequency domain optical coherence tomography images for the analysis of human atherosclerotic plaques. EuroIntervention. 2012;8(1):98-108.

Tearney GJ, Regar E, Akasaka T, Adriaenssens T, Barlis P, Bezerra HG, Bouma B, Bruining N, Cho JM, Chowdhary S, Costa MA, de Silva R, Dijkstra J, Di Mario C, Dudeck D, Falk E, Feldman MD, Fitzgerald P, Garcia H, Gonzalo N, Granada JF, Guagliumi G, Holm NR, Honda Y, Ikeno F, Kawasaki M, Kochman J,Koltowski L, Kubo T, Kume T, Kyono H, Lam CC, Lamouche G, Lee DP, Leon MB, Maehara A, Manfrini O, Mintz GS, Mizuno K, Morel MA, Nadkarni S, Okura H,Otake H, Pietrasik A, Prati F, Räber L, **Radu MD**, Rieber J, Riga M, Rollins A, Rosenberg M, Sirbu V, Serruys PW, Shimada K, Shinke T, Shite J, Siegel E,Sonada S, Suter M, Takarada S, Tanaka A, Terashima M, Troels T, Uemura S, Ughi GJ, van Beusekom HM, van der Steen AF, van Es GA, van Soest G, Virmani R, Waxman S, Weissman NJ, Weisz G. Consensus standards for acquisition, measurement, and reporting of intravascular optical coherence tomography studies: a report from the international working group for intravascular optical coherence tomography standardization and validation. J Am Coll Cardiol. 2012;59(12):1058-72.

Brugaletta S, **Radu MD**, Garcia-Garcia HM, Heo JH, Farooq V, Girasis C, van Geuns RJ, Thuesen L, McClean D, Chevalier B, Windecker S, Koolen J, Rapoza R, Miquel-Hebert K, Ormiston J, Serruys PW. Circumferential evaluation of the neointima by optical coherence tomography after ABSORB bioresorbable vascular scaffold implantation: can the scaffold cap the plaque? Atherosclerosis. 2012;221(1):106-12.

Brugaletta S, Gomez-Lara J, Bruining N, **Radu MD**, van Geuns RJ, Thuesen L, McClean D, Koolen J, Windecker S, Whitbourn R, Oberhauser J, Rapoza R, Ormiston JA, Garcia-Garcia HM, Serruys PW. Head to head comparison of optical coherence tomography, intravascular ultrasound echogenicity and virtual histology for the detection of changes in polymeric struts over time: insights from the ABSORB trial. EuroIntervention. 2012;8(3):352-8.

Gutierrez-Chico JL, **Radu MD**, Diletti R, Sheehy A, Glauser T, Harrington J, Rapoza R, Onuma Y, Serruys PW. Spatial distribution and temporal evolution of optical coherence tomography "white dots" in the poly-L-lactide backbone of an intracoronary bioresorbable scaffold: association to polymer crazes during crimping of the device. Circ J. 2012;76(2):342-50.

Radu MD, Onuma Y, Rapoza RJ, Diletti R, Serruys PW. In vivo visualisation by three-dimensional optical coherence tomography of stress crazing of a bioresorbable vas-

cular scaffold implanted for treatment of human coronary stenosis. EuroIntervention. 2012;7(12):1461-3.

Radu MD, Falk E. In search of vulnerable features of coronary plaques with optical coherence tomography: is it time to rethink the current methodological concepts? Eur Heart J. 2012;33(1):9-12.

Farooq V, Heo JH, Räber L, Brugaletta S, **Radu MD**, Gogas BD, Diletti R, Onuma Y, Garcia-Garcia HM, Serruys PW. Tools & Techniques: Risk stratification and diagnostic tools in left main stem intervention. EuroIntervention. 2011;7(6):747-53.

Gomez-Lara J, **Radu M**, Brugaletta S, Farooq V, Diletti R, Onuma Y, Windecker S, Thuesen L, McClean D, Koolen J, Whitbourn R, Dudek D, Smits PC, Regar E, Veldhof S, Rapoza R, Ormiston JA, Garcia-Garcia HM, Serruys PW. Serial analysis of the malapposed and uncovered struts of the new generation of everolimus-eluting bioresorbable scaffold with optical coherence tomography. JACC Cardiovasc Interv. 2011;4(9):992-1001.

Farooq V, Okamura T, Gogas BD, Heo JH, Magro M, Gomez-Lara J, Brugaletta S, Onuma Y, **Radu M**, Garcìa-Garcìa HM, Serruys PW. 3D Reconstructions of Optical Frequency Domain Imaging to Improve Understanding of Conventional PCI. JACC Cardiovasc Imaging. 2011;4(9):1044-6.

Gogas BD, Farooq V, Onuma Y, Magro M, **Radu MD**, van Geuns RJ, Regar E, Serruys PW. 3-dimensional optical frequency domain imaging for the evaluation of primary percutaneous coronary intervention in ST-segment elevation myocardial infarction. Int J Cardiol. 2011;151(1):103-5.

Farooq V, Onuma Y, **Radu M**, Okamura T, Gomez-Lara J, Brugaletta S, Gogas BD, van Geuns RJ, Regar E, Schultz C, Windecker S, Lefèvre T, Brueren BR, Powers J, Perkins LL, Rapoza RJ, Virmani R, García-García HM, Serruys PW. Optical coherence tomography (OCT) of overlapping bioresorbable scaffolds: from benchwork to clinical application. EuroIntervention. 2011;7(3):386-99.

Radu M, Jørgensen E, Kelbæk H, Helqvist S, Skovgaard L, Saunamäki K. Optical coherence tomography at follow-up after percutaneous coronary intervention: relationship between procedural dissections, stent strut malapposition and stent healing. EuroIntervention. 2011;7(3):353-61.

Radu MD, Räber L, Saunamäki KI, Serruys PW. How does optical coherence tomography visualize coronary atherosclerotic pool? Card Interv Today 2011, March/April.

Gogas BD, Parissis JT, Iliodromitis EK, Tsiodras S, **Radu M**, Paraskevaidis IA, Theodoropoulos SP, Kremastinos DT, Yacoub MH. Left ventricular assist device vegetation: "cure" without device explantation. Hellenic J Cardiol. 2010;51(6):549-51.

Radu M, Jørgensen E, Kelbaek H, Helqvist S, Skovgaard L, Saunamäki K. Strut apposition after coronary stent implantation visualised with optical coherence tomography. EuroIntervention. 2010 May;6(1):86-93.

Radu MD, Jørgensen E, Saunamäki K. [Optical coherence tomography for coronary visualisation]. Ugeskr Laeger. 2009 Aug 24;171(35):2466-7. Danish.